Modeling and optimization of power losses in poly-V belt transmissions : Application to the Front Engine Accessory Drive of trucks

Carlos Alexandre Ferreira Da Silva

Numéro d'ordre : 2018LYSEI079 Année 2018

THESE

MODELING AND OPTIMIZATION OF POWER LOSSES IN POLY-V BELT TRANSMISSIONS : APPLICATION TO THE FRONT ENGINE ACCESSORY DRIVE OF TRUCKS

Présentée devant
l'Institut National de Sciences Appliquées (INSA) de Lyon

Pour obtenir
le **GRADE DE DOCTEUR** en **GENIE MECANIQUE**

Ecole Doctorale des Sciences de l'Ingénieur de Lyon :
Mécanique, Energétique, Génie Civil, Acoustique (MEGA, ED 162)

Par
Carlos Alexandre FERREIRA DA SILVA
Double diplôme d'ingénieur en Génie Mécanique
Université Fédérale d'Uberlândia (Brésil) et INSA de Lyon (France)

Soutenue le 6 Novembre 2018 devant la commission d'examen :

Jury MM.

G. Parker, Robert	Professeur des Universités	Virginia Tech	Rapporteur
Boltezar, Miha	Professeur des Universités	Univ of Ljubljana	Rapporteur
Rémond, Didier	Professeur des Universités	INSA de Lyon	Directeur
Manin, Lionel	Maître de Conférences	INSA de Lyon	Co-Directeur
Michon, Guilhem	Professeur des Universités	ISAE Toulouse	Examinateur
Baranger N., Thouraya	Professeur des Universités	Université Lyon 1	Examinatrice
Ameil, Julien	Ingénieur leader MDEP	Volvo Trucks	Invité

Département FEDORA – INSA Lyon - Ecoles Doctorales – Quinquennal 2016-2020

SIGLE	ECOLE DOCTORALE	NOM ET COORDONNEES DU RESPONSABLE
CHIMIE	**CHIMIE DE LYON** **http://www.edchimie-lyon.fr** Sec. : Renée EL MELHEM Bât. Blaise PASCAL, 3e étage **secretariat@edchimie-lyon.fr** INSA : R. GOURDON	M. Stéphane DANIELE Institut de recherches sur la catalyse et l'environnement de Lyon IRCELYON-UMR 5256 Équipe CDFA 2 Avenue Albert EINSTEIN 69 626 Villeurbanne CEDEX **directeur@edchimie-lyon.fr**
E.E.A.	**ÉLECTRONIQUE, ÉLECTROTECHNIQUE, AUTOMATIQUE** **http://edeea.ec-lyon.fr** Sec. : M.C. HAVGOUDOUKIAN **ecole-doctorale.eea@ec-lyon.fr**	M. Gérard SCORLETTI École Centrale de Lyon 36 Avenue Guy DE COLLONGUE 69 134 Écully Tél : 04.72.18.60.97 Fax 04.78.43.37.17 **gerard.scorletti@ec-lyon.fr**
E2M2	**ÉVOLUTION, ÉCOSYSTÈME, MICROBIOLOGIE, MODÉLISATION** **http://e2m2.universite-lyon.fr** Sec. : Sylvie ROBERJOT Bât. Atrium, UCB Lyon 1 Tél : 04.72.44.83.62 INSA : H. CHARLES **secretariat.e2m2@univ-lyon1.fr**	M. Philippe NORMAND UMR 5557 Lab. d'Ecologie Microbienne Université Claude Bernard Lyon 1 Bâtiment Mendel 43, boulevard du 11 Novembre 1918 69 622 Villeurbanne CEDEX **philippe.normand@univ-lyon1.fr**
EDISS	**INTERDISCIPLINAIRE SCIENCES-SANTÉ** **http://www.ediss-lyon.fr** Sec. : Sylvie ROBERJOT Bât. Atrium, UCB Lyon 1 Tél : 04.72.44.83.62 INSA : M. LAGARDE **secretariat.ediss@univ-lyon1.fr**	Mme Emmanuelle CANET-SOULAS INSERM U1060, CarMeN lab, Univ. Lyon 1 Bâtiment IMBL 11 Avenue Jean CAPELLE INSA de Lyon 69 621 Villeurbanne Tél : 04.72.68.49.09 Fax : 04.72.68.49.16 **emmanuelle.canet@univ-lyon1.fr**
INFOMATHS	**INFORMATIQUE ET MATHÉMATIQUES** **http://edinfomaths.universite-lyon.fr** Sec. : Renée EL MELHEM Bât. Blaise PASCAL, 3e étage Tél : 04.72.43.80.46 Fax : 04.72.43.16.87 **infomaths@univ-lyon1.fr**	M. Luca ZAMBONI Bât. Braconnier 43 Boulevard du 11 novembre 1918 69 622 Villeurbanne CEDEX Tél : 04.26.23.45.52 **zamboni@maths.univ-lyon1.fr**
Matériaux	**MATÉRIAUX DE LYON** **http://ed34.universite-lyon.fr** Sec. : Marion COMBE Tél : 04.72.43.71.70 Fax : 04.72.43.87.12 Bât. Direction **ed.materiaux@insa-lyon.fr**	M. Jean-Yves BUFFIÈRE INSA de Lyon MATEIS - Bât. Saint-Exupéry 7 Avenue Jean CAPELLE 69 621 Villeurbanne CEDEX Tél : 04.72.43.71.70 Fax : 04.72.43.85.28 **jean-yves.buffiere@insa-lyon.fr**
MEGA	**MÉCANIQUE, ÉNERGÉTIQUE, GÉNIE CIVIL, ACOUSTIQUE** **http://edmega.universite-lyon.fr** Sec. : Marion COMBE Tél : 04.72.43.71.70 Fax : 04.72.43.87.12 Bât. Direction **mega@insa-lyon.fr**	M. Jocelyn BONJOUR INSA de Lyon Laboratoire CETHIL Bâtiment Sadi-Carnot 9, rue de la Physique 69 621 Villeurbanne CEDEX **jocelyn.bonjour@insa-lyon.fr**
ScSo	**ScSo*** **http://ed483.univ-lyon2.fr** Sec. : Viviane POLSINELLI Brigitte DUBOIS INSA : J.Y. TOUSSAINT Tél : 04.78.69.72.76 **viviane.polsinelli@univ-lyon2.fr**	M. Christian MONTES Université Lyon 2 86 Rue Pasteur 69 365 Lyon CEDEX 07 **christian.montes@univ-lyon2.fr**

*ScSo : Histoire, Géographie, Aménagement, Urbanisme, Archéologie, Science politique, Sociologie, Anthropologie

To my parents who, through their efforts, allowed me to make my dreams come true.

Disce quasi semper victurus vive quasi cras moriturus

Acknowledgments

I would like to thank God for giving me knowledge, strength, ability and opportunity to undertake this work and to persevere and complete it satisfactorily.

Thanks to my family for always standing by my side.

Thanks to LaMCoS for hosting me throughout the thesis.

Thanks to my thesis director, Didier Remond, and my thesis co-director, Lionel Manin, for giving me the opportunity to undertake this work.

I would especially like to thank my advisor, Lionel Manin, who guided me and gave me his support with patience and pedagogy throughout this professional experience.

Thanks to my teammates, Lionel Manin, Marie-Ange Andrianoely, Etienne Besnier and colleague Renaud Rinaldi, for the support and the valuable contribution.

Thanks to my interns, Xiaowen Li, Selven Ayasamy and Clement Santini for the valuable contribution and for giving me the opportunity to learn more than I might imagine.

Thanks to my fellow lab mates for the valuable discussions and moments spent in their vivacious and always stimulating company.

Thanks to Volvo Trucks for hosting us during the EDIT consortium meetings.

Thanks to Julien Ameil and Elie Garcia for providing us with support whenever required.

Thanks to the Auvergne Rhone Alpes council and Volvo Trucks who supported this work.

Thanks to the thesis committee members for accepting the invitation to review this work.

Abstract

This work is a part of the Efficient Distribution Truck (EDIT, FUI 19) project, led by Volvo Trucks, whose objective is to reduce distribution vehicles' fuel consumption for 2020 by 13% when compared with the current production vehicle EURO-6. The EDIT project targets five areas of research and technical solutions, one of which consists of obtaining an optimized poly-V belt transmission concerning the power losses. In terms of lifetime of the mechanical components, reduction of noise and vibrations, the Front Engine Accessory Drives (FEADs) are currently one of the most technologically sophisticated systems. However, further improvements can be made to make the vehicles more energy efficient. This thesis, which aims at investigating possibilities for reducing and optimizing the power losses in the FEADs, is composed of three main parts: the characterization of the viscoelastic materials of the poly-V belts via Dynamic Mechanical Analysis (DMA) and the FEAD components; the modeling, the optimization and the implementation of the power loss models in a simulation tool; and their experimental validation through a test bench. The power losses occurring in a FEAD are of several types: poly-V internal losses (hysteresis of the belt-rubber), poly-V external losses (belt/pulley slip) and losses from the accessory drives (friction inside the bearings). These power losses can be quantified and optimized thanks to the models developed throughout this thesis. These models have been validated and implemented in a simulation tool (PLFead, Power Loss Front engine accessory drive), which has been developed to optimize the power losses taking into consideration the design parameters and operating conditions of the FEAD.

Key-words: Poly-V belt transmission. Power losses. FEAD. Optimization. Test bench. Characterization. Viscoelastic material. Modeling. Experimental validation. Simulation.

Résumé

Ces travaux s'inscrivent dans le cadre du projet EDIT(Efficient Distribution Truck, FUI19), piloté par le groupe Volvo Trucks, dont l'objectif de réduction de consommation pour 2020 est fixé à 13% par rapport à un véhicule actuel EURO-6. Le projet EDIT porte sur cinq axes techniques d'amélioration dont un consiste en l'obtention d'un système optimisé de transmission par courroie poly-V au regard des pertes de puissance. Actuellement les faces avant de moteur sont perfectionnées sur le plan mécanique ; cela signifie que la durée de vie de ses composants est optimisée, et que les nuisances vibratoires sont réduites. Par contre, des améliorations peuvent être apportées sur le plan énergétique. Cette thèse, qui a pour objectif d'investiguer les possibilités de réduction et d'optimisation des pertes de puissance sur les façades accessoires, se décline en trois parties : une caractérisation par l'analyse mécanique dynamique des matériaux viscoélastiques des courroies poly-V et des composantes de façade ; une modélisation, une optimisation et une implémentation logicielle des modèles de pertes de puissance ; validées par une dernière partie expérimentale sur banc d'essais. Les pertes de puissances dans une face avant moteur sont de plusieurs types : des pertes internes à la courroie poly-V (hystérésis du caoutchouc), des pertes externes à la courroie (glissement poulie/courroie) et des pertes internes aux composants (frottement dans les roulements). Ces pertes peuvent désormais être quantifiées et optimisées grâce aux modèles développés durant cette thèse. Ces modèles ont été validés et implémentés dans un outil de simulation (PLFead, Power Loss Front engine accessory drive), qui a été développé pour optimiser les pertes de puissance en tenant compte des paramètres de *design* et de fonctionnement des faces avant moteur.

Mots-clés : Transmission par courroie poly-V. Pertes de puissance. Faces avant moteur. Optimisation. Caractérisation. Matériau viscoélastique. Modélisation. Validation sur banc d'essais. Simulation.

Resumo

Este trabalho se insere no âmbito do projeto EDIT (Efficient Distribution Truck, FUI 19), pilotado pelo grupo Volvo Trucks, cujo o objetivo de redução de consumação para 2020 é fixado em 13% em relação ao veículo atual EURO-6. O projeto EDIT se concentra em cinco áreas de pesquisa e soluções técnicas, na qual uma destas consiste na obtenção de um sistema otimizado de transmissão por correia poly-V no que diz respeito as perdas de potência. Atualmente as faces dianteiras de motores são aperfeiçoadas em relação aos seus mecanismos, isso significa que a vida útil dos seus componentes é otimizada e que o nível de vibrações é reduzido. No entanto, melhorias podem ser feitas para aumentar a eficiência enérgetica. Esta tese, que tem o objetivo de investigar possibilidades de redução e otimização de perdas de potência das faces dianteiras de motores, se divide em três partes : uma caracterização experimental através da análise mecânica dinâmica dos materiais viscoelásticos das correias poly-V e dos componentes de faces dianteiras de motores ; uma modelagem, uma otimização e uma implementação dos modelos de perda de potência em uma ferramenta de simulação ; validadas por uma ultima parte experimental em bancada de ensaios. As perdas de potência nas faces dianteiras de motores são de vários tipos : perdas internas à correia poly-V (histerese da borracha), perdas externas à correira (escorregamento polia/correia) e perdas internas aos componentes (atrito nos rolamentos). Estas perdas de potência podem à partir de agora ser quantificadas e otimizadas graças aos modelos desenvolvidos durante esta tese. Estes modelos foram validados e implementados em uma ferramenta de simulação (PLFead, Power Loss Front engine accessory drive), que foi desenvolvida para otimizar as perdas de potência levando em conta paramêtros de *design* e de funcionamento das faces dianteiras de motores.

Palavras-chave : Transmissão por correias poly-V. Perdas de potência. Faces dianteiras de motores. Otimização. Caracterização. Material viscoelástico. Modelagem. Validação em bancada de ensaios. Simulação.

Contents

Nomenclature

B	Belt width	i, p	i^{th} , p^{th} pulley of the poly-V belt transmission
B_d	Width of one V (belt-rib)	ϕ_p	Individual wrap angles, with $p = 1, 2, \dots, np$
n	Number of ribs composing the poly-V belt	ω_p	Individual pulley angular speed, with $p = 1, 2, \dots, np$
d_b	Poly-V belt setting diameter	$\square_R$	Refers to the driver pulley (s), e.g. ϕ_R , ω_R , etc.
H	Thickness of the poly-V belt	$\square_N$	Refers to the driven pulley (s), e.g. ϕ_N , ω_N , etc.
H_t	Thickness of the top (backside) layer	V_b	Belt linear velocity ($V_b = V = \omega R$)
H_b	Thickness of the middle layer	ρ_b	Belt mass per unit length
H_c	Thickness of the ribs layer	C_p	Torque imposed to a generic pulley p
ϕ	Belt-pulley wrap angle	R_p	Pulley pitch radius, $R_p = r_p$ with $p = 1, 2, \dots, np$
ϕ_a	Belt-pulley adhesion angle	d_p	Pulleys' diameters, $d_p = 2\, r_p$ with $p = 1, 2, \dots, np$
ϕ_s	Belt-pulley sliding angle	$\square_s$	Refers to the slack belt-span (s) or sliding angle (s)
T	Belt span tension	$\square_t$	Refers to the tight belt-span (s)
T_t	Belt span tight tension	$\square_a$	Refers to the adhesion angle (s)
T_s	Belt span slack tension	$\varepsilon_{a_{bend}}^{max}$	Maximum strain amplitude due to bending
T_c	Centrifugal action	$W_{h_{bend}}$	Energy lost by bending-hysteresis
T_o	Belt setting (initial, static) tension	$E_{Ht}^{"}$	Appropriate top layer $E^{"}$(plain strain conditions)
$T_{0_{min}}$	Minimum belt setting tension	$E_{Hb}^{"}$	Appropriate middle layer $E^{"}$(plain strain conditions)
μ	Belt-pulley friction coefficient	$E_{Hc}^{"}$	Loss modulus of the ribs layer material
μ_g	Belt-pulley global friction coefficient	$W_{h_{st}}$	Energy lost by stretching-hysteresis
μ_l	Belt-pulley local friction coefficient	$E_{Belt}^{"}$	Longitudinal loss modulus of the full belt
α	Wedge angle of the ribs/pulley contact surface	$\varepsilon_{a_{st}}$	Strain amplitude due to belt stretching
PL_{FEAD}	FEAD total power loss	A	Belt cross-sectional area
PL_{hys}	Total Hysteresis power loss	$c\ (EA)$	Tensile modulus or strain stiffness along the belt
PL_{bear}	Total bearings power loss	k	k^{th} belt member: top, middle, cord or ribs
PL_{slip}	Total belt-pulleys power loss	$E_{Ht}^{'}$	Appropriate top layer $E^{'}$(plain strain conditions)
PL_{vib}	Total belt-vibration power loss	$E_{cord}^{'}$	Storage modulus of the belt tension cords
$PL_{belt-hys}$	Total belt-hysteresis power loss	$E_{Hb}^{'}$	Appropriate middle layer $E^{'}$(plain strain conditions)
$PL_{tens-hys}$	Total tensioner-hysteresis power loss	$E_{Hc}^{'}$	Storage modulus of the ribs layer material
W_h	Energy loss by hysteresis	A_{Ht}	Cross-sectional area of the belt top-layer
E^*	Complex modulus of the poly-V belt/TVD	A_{cord}	Cross-sectional area of the tension-cords layer
E'	Storage modulus of the poly-V belt/TVD	A_{Hb}	Cross-sectional area of the belt middle-layer
E''	Loss modulus of the poly-V belt/TVD	A_{Hc}	Cross-sectional area of the belt ribs-layer
$\mathcal{Z}$	Loss factor of the viscoelastic material	ν	Poisson ratio of the belt elastomer (rubber)
$\varepsilon\ [\varepsilon_a]$	Dynamic strain [dynamic strain amplitude]	P_c	Pulley-belt contact pressure
$\sigma\ [\sigma_a]$	Dynamic stress [dynamic stress amplitude]	$W_{h_{fc}}$	Energy lost by flank-compression-hysteresis
j	Imaginary unit or j^{th} belt-span of the FEAD	$\varepsilon_{a_{fc}}$	Strain amplitude due to belt flank compression
θ_{exp}	Temperature experienced by the belt/TVD	A_{1V}	Cross-sectional area of one V (belt-rib)
f_{exp}	Frequency experienced by the belt/TVD	P_z	Horizontal component of P_c
ε_{exp}	Strain amplitude experienced by the belt/TVD	P_v	Vertical component of P_c
$\varepsilon_{a_{bend}}$	Strain amplitude due to belt bending	dS	Infinitesimal element of the belt contact surface
x	Through-thickness distance from neutral axis	$W_{h_{rc}}$	Energy lost by radial-compression-hysteresis
R	Radius of the curved belt, usually, $R = R_p$	$\varepsilon_{a_{rc}}$	Strain amplitude due to belt radial compression
x_{eq}	Arbitrary x in the rib layer	$\square_H$	Refers to the properties belonging to the layer "H"
B_{eq}	Equivalent B in the rib layer	$\square_{Ht}$	Refers to the poly-V belt top layer properties
d_{cord}	Diameter of a tension member (small cords)	$\square_{Hb}$	Refers to the poly-V belt middle layer properties
np	Number of pulleys	$\square_{Hc}$	Refers to the poly-V belt ribs layer properties

Nomenclature

H_{sh}	Thickness of the sheared layer	$L3$	Distance from the front-bearing to the pulley
H_c^*	Hypothetical thickness of the sheared-layer in H_c	$\vec{D}$	Seating-Unseating distance vector
$W_{h_{sh}}$	Energy lost by shear-hysteresis	$s\ ,u$	Seating-Unseating points
G^*	Complex modulus of belt or TVD material (shear)	$\vec{W_i}$	Weight vector of the pulley "i"
G'	Storage modulus of belt or TVD material (shear)	$\vec{G}$	Unit vector representing the gravity
G''	Loss modulus of the belt or TVD material (shear)	$\vec{\mu}_{T_i}$	Unit vector in the belt-span T_i direction
$\gamma_{a_{sh}}$	Shear angle along the adhesion arc ($R\ \phi_a$)	$\vec{T}_i$	i^{th} belt-span vector
A_{sh}	Cross-sectional area of the sheared layer	$\lvert\vec{T}_i\rvert$	Belt-span tension, $\lvert T_i\rvert = T_i = \mathrm{norm}(\vec{T}_i)$
τ_{sh}	Shear stress proportional to $\gamma_{a_{sh}}$	$\vec{F}_r$	Belt/pulley resultant radial force
ϖ	Deflection due to cyclic shear loading	$\vec{F}_{r\_k}$	k^{th} $\vec{F}_r$ of a FEAD containing k shafts
ΔV_T	Belt-pulley speed difference for driver pulleys	$\vec{F}_{r\_k\_f}$	Component of $\vec{F}_{r\_k}$ acting on the front bearing
ΔV_S	Belt-pulley speed difference for driven pulleys	$\vec{F}_{r\_k\_r}$	Component of $\vec{F}_{r\_k}$ acting on the rear bearing
y	Sum of increments along the arc of contact	$P\ ,C\ ,\omega$	Power, Torque, angular velocity
ε_s	Strain at the belt-pulley seating point	$f_P, f_C\ , f_\omega$	Power, Torque, Speed loss factors
G_*	Dimensionless quantity used in shear losses	s_i	Slip ($s = f_\omega$) quantity on a generic pulley i
L	Belt theoretical length (≈ size of the FEAD path)	ε	Strain in the belt longitudinal direction
E^*_{cord}	Complex modulus of the belt tension cords	$V_t\ , V_s$	Belt linear velocity at tight and slack free spans
$E^{"}_{cord}$	Loss modulus of the belt tension cords	r_{cp}	radius after belt radial compression
E^*_{Belt}	Longitudinal complex modulus of the poly-V belt	x_{cp}	Belt radial compression
E'_{Belt}	Longitudinal storage modulus of the poly-V belt	K_h	Arbitrary radial stiffness of a generic layer h
E''_{Belt}	Longitudinal loss modulus of the poly-V belt	$V_b\ , V_p$	Belt and pulley linear velocities
Φ_{Ht}	Volume fraction of the top layer material	V_{sl}	Sliding velocity between the belt and the pulley
Φ_{cord}	Volume fraction of the cords layer material	C_*	Dimensionless quantity used in slip losses
Φ_{HbHc}	Volume fraction of middle + ribs layers materials	ω_{CS}	Crankshaft angular speed
Φ_{Belt}	Volume fraction of the poly-V belt, equal to 1	P_i	Power transmitted by the pulley i
T_{ref}	Temperature of reference for the master curves	W_{span_j}	Belt-hysteresis energy loss in the span j
a_T	Master curves, data shifting, constant coefficients	PL_{span_j}	Belt-hysteresis power loss in the span j
θ_t	Tensioner rotation angle	$\Delta\varepsilon_j$	Variation of strain in the span j
θ_{t_0}	Initial tensioner rotation angle	ΔT_j	Variation of tension in the span j
θ_{t_eq}	Tensioner rotation angle at equilibrium	λ	Number of complete hysteresis loops
$\Delta\theta_t$	Variation of the tensioner arm angle	x_c	Pulley center‘s x-coordinate of the test bench
C_{fc}	Tensioner frictional torque	y_c	Pulley center‘s y-coordinate of the test bench
k_t	Tensioner arm stiffness	F_f	Fitness function (function to be minimized)
$W_{tens-hys}$	Tensioner-energy loss for 1 cycle	x_i	Pulley center‘s x-coordinate of the pulley i
Ω_t	Tensioner oscillation frequency	X	Vector containing all x_i, i.e. $X = [x_1, x_2, \dots, x_{np}]'$
PL_b	Bearing power loss	y_i	Pulley center‘s y-coordinate of the pulley i
M_b	Bearing total frictional moment	Y	Vector containing all y_i, i.e. $Y = [y_1, y_2, \dots, y_{np}]'$
n_b	Bearing rotational speed	Σ_ρ	Power loss model constant values
M_{rr}	Rolling frictional moment	X_{opt}	Optimized center X-coordinates
M_{sl}	Sliding frictional moment	Y_{opt}	Optimized center Y-coordinates
M_{seal}	Frictional moment of bearing seals	$T_{0_{opt}}$	Optimized belt-setting tension
M_{drag}	Frictional moment due to drag	O_1	Center of the pulley 1 (crankshaft)
ns	Number of shafts	O_i	Center of a generic pulley i
PL_{b_i}	Total power loss of the ith bearing	$T^*_{0_{min}}$	Minimum belt setting tension to transmit power
$PL_{b\_i\_F}$	Power loss of the ith front bearing	$T_{0_{max}}$	Maximum belt setting tension
$PL_{b\_i\_R}$	Power loss of the ith rear bearing	ng	Number of generations used for optimizing via GA
$L2$	Distance from the rear-bearing to the pulley	t	Generic generation of the GA optimization / time

Nomenclature and Abbreviations

$G1$	Part of the *t* that is selected to *t+1*	EDIT	Efficient DIstribution Truck
$G2$	Part of the *t* that is recombined, then be part of *t+1*	FUI	Single Inter-Ministry Fund
$G3$	Part of the *t* that is mutated, then be part of *t+1*	EURO-6	European emission standard No 459/2012
Z	Individual criterion of a DP optimization problem	FEAD	Front Engine Accessory Drive
S	State of each DP sub-problem	DMA	Dynamic Mechanical Analysis
U	Decision variables acting on each DP sub-problem	PLFead	Power Losses Fead, simulation tool
x_{min}	Minimum x_i reached by GA or DP optimization	MATLAB	MATrix LABoratory, software
x_{max}	Minimum x_i reached by GA or DP optimization	TVD	Torsional Vibration Damper
y_{min}	Minimum y_i reached by GA or DP optimization	PK, PJ, …	Types of poly-V belt profile
y_{max}	Maximum y_i reached by GA or DP optimization	PET	Poly Ethylene Terephthalate
v , w	DP intermediate standard sub-problem examples	EPDM	Ethylene Propylene Diene Monomer
si	Generic step from 2 to sn when optimizing by DP	MT, HT	Mechanical, Hydraulic Tensioners
sn	Number of steps when optimizing using DP	DR, DN	DriveR, DriveN pulleys
V_{si}	DP state of the step si, composed of X , Y , T_0 , Σ_ρ	PL	Power Loss or Power Losses
F	DP function to be optimized ($\approx$ F_f of GA)	BC	Boundary Conditions
x_d	Displacement of the system used to identify EA	GABO	Dynamic Mechanical Analysis machine
m_d	Mass of the 1DOF system used to identify EA	PLMap(s)	Power Loss Map (s)
k_d	Stiffness of the 1DOF system used to identify EA	SKF	Bearing manufacturing company
c_d	Damping of the 1DOF system used to identify EA	CS	CrankShaft
l_d	Generic belt-span length used to identify EA	AD	Accessory Drive
F_{ext}	External force applied to the 1DOF system	PLS	Power Loss Simulated
X_d	Absolute value of the displacement x_d	PLM	Power Loss Measured
c_c	Critical damping of a mass-spring-damper model	BF	Brute Force method
f_n	Natural frequency of the belt testing system/TVD	DP	Dynamic programming method
ω_n	Radian frequency of the belt testing system/TVD	GA(s)	Genetic Algorithm(s)
ω_0	Radian frequency of the undamped system	Multi-DP	Multi Decision Process
α_d	Damping factor of a given vibration signal	RAM	Random Access Memory
n_{vib}	Number of periods (n) of a vibration signal	CPU	Central Processing Unit
δ_d	Logarithmic decrement of a vibration signal	PS	Power Supplied
P_x	Normal load applied to poly-V belt sample	PC	Power Consumed
T_{max}	Traction force applied to poly-V belt sample	WP	Water Pump
K_{cst}	Constant stiffness of the TVD rubber-ring	ALT	ALTernator
R_{rr}	External radius of the TVD rubber-ring	AC	Air Conditioner
L_{rr}	Width of the TVD rubber -ring	PG	Power Generated
e_{rr}	Thickness of the TVD rubber -ring	GUI	Graphical User Interface
I_n	Inertia of the TVD corresponding to f_n	Ra	Roughness average
ξ	Damping ratio of the TVD rubber-ring	DOF	Degree of Freedom
ω_{acy}	Radian frequency of the engine torque fluctuation	FRF	Frequency Response Function
θ_{CS}	Harmonic excitation motion from the engine (CS)	FEA	Finite Element Analysis
θ_{amp}	Amplitude of the harmonic excitation motion	F(x)	Function of " x "
θ_1	Angular lag and the TVD angular DOF	MS	Measuring System
C_{cst}	Constant damping of the TVD rubber-ring		
I_1	Inertia of the TVD outer-ring		
K_{var}	Varying stiffness of the TVD rubber-ring		
C_{var}	Varying damping of the TVD rubber-ring		
K, C	Varying/Constant stiffness and damping of the TVD rubber-ring		
η	Structural loss factor of the TVD rubber-ring		

Chapter 1

INTRODUCTION

Contents

1.1 MOTIVATION

Over the last years, significant research effort has been directed towards developing vehicle transmissions more energy efficient. This effort has been a direct consequence of the new environmental regulations encouraging truck and car manufacturers to reduce the power losses of their engines. Recently, for example, the European Union have set penalties for car manufacturers of 95 euros per gram of CO_2/km for each new vehicle sold from 2019 exceeding this emission limit. Hence, modeling and optimizing the power losses in the transmissions of vehicles is extremely important to attain emission reduction goals. Moreover, for development purposes and in design of power transmissions, it is worth predicting the potential power losses before manufacturing. Thus, to predict the power losses in poly-v belt transmissions, theoretical models have been developed taking into consideration different types of power loss in a Front Engine Accessory Drive (FEAD). These losses have several origins: from the poly-V belt or from the mechanical components of the system (bearings, tensioners). In the first case, energy is dissipated inside the belt due to the hysteretic behavior of the belt constitutive elastomer (internal losses or torque losses). However, energy is also dissipated inside bearings and at the surface of the belt due to belt-pulleys slip (external losses or speed losses). Next, optimizing the power losses coming from the FEAD of vehicles helps reducing the engine fuel consumption and the emission of greenhouse gases. Thus, an optimization method based on a genetic algorithm has also been applied, i.e. principles of real life (natural selection, cross-over and mutation) applied to computations have been used to minimize power losses, since genetic algorithms are commonly used in optimization because of their adaptability to handle complex engineering problems (FEADs). For comparison purposes, the dynamic programming which is a technique based on the principle of sub-problematization has also been implemented. The optimization-problem consists in minimizing the power loss function representing the power losses taking place in a front engine accessory belt drive or the emissions of polluting gases. Results have shown in this thesis that the total power losses can be reduced by tens of percent by adjusting both the positions of the engine accessories (geometric parameters) and the belt setting tension (operating parameters). Experimental results confirm these numerical predictions from theoretical power loss models implemented in a simulation tool with exceptional characteristics. Thus, this thesis is motivated by the environmental questions about saving energy, the vehicle manufacturers' interrogations about how to improve their engines and my determination to carry forward the science and technology.

EDIT project

This thesis has been achieved within the frame of the EDIT (Efficient Distribution Truck) collaborative industry project. Indeed, Renault Trucks has been leading a collaborative industry project aiming to reduce the fuel consumption of distribution trucks compared with the current production vehicle EURO-6. Six industry partners have been working on the EDIT project alongside Renault Trucks, they are: Valeo, Lamberet, Michelin, BeNomad, INSA Lyon (LaMCoS) and IFSTTAR (LICIT).

Using a Renault Range D Wide truck with refrigerated body as a prototype (Fig. 1.1), the project aimed to design and develop a demonstration refrigerated vehicle consuming 13% less fuel than the reference Euro-6 distribution truck.

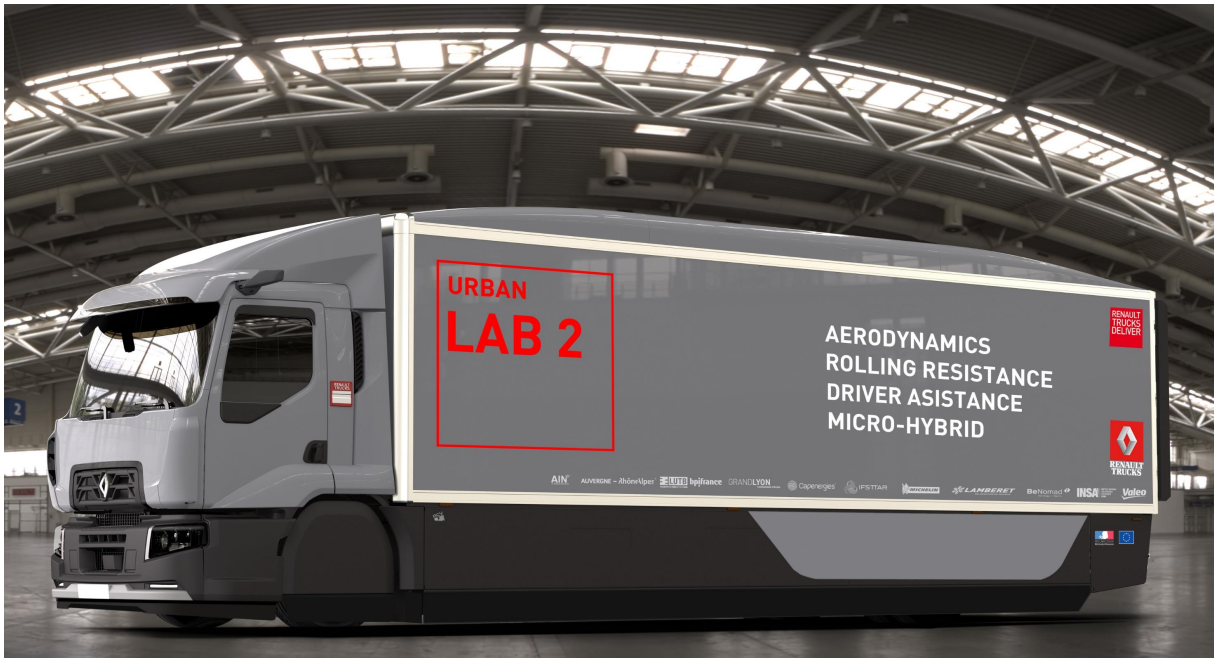

Figure 1.1 – Renault Range D Wide truck (Urban Lab 2).

Urban Lab 2 uses technologies, to which each partner have been contributing with their expertise, focusing on the key areas: aerodynamics, tyres, connectivity and hybridization/ optimization of the engine. Indeed, according to Renault Trucks Press Releases:

Aerodynamics

To reduce the aerodynamic drag of the Urban Lab 2 - and therefore its fuel consumption - engineers worked on airflow throughout the vehicle. Lamberet and Renault Trucks adapted the cab, chassis and refrigerated body to the recommendations of aerodynamic specialists, whilst meeting the regulatory and operating requirements of controlled temperature transport. The first step involves reducing the front surface area: "The refrigeration unit is normally located above the cab", explained François Savoye, Energy Efficiency Strategy Manager at Renault Trucks. "On Urban Lab 2, we decided to position it in the wheelbase of the vehicle to free up space overhead and optimize the body/tractor link to lower the body and improve airflow. This meant we could incorporate a roof deflector shaped to provide seamless continuity with the body. Redesigning the interior architecture of the refrigerated body has made a marked improvement in the shape of the roof, without adding to the height. As for the sides of the vehicle, these are fitted with textile side deflectors. "We have used a PVC-coated textile for the first time", François Savoye added. "When stretched and fitted on the side protectors, it provides a light, effective and economic system."

Lateral airflow is also boosted by streamlined wheels and the fitting of rear deflectors that are perfectly in keeping with the architecture and continuity of the tailgate. These deflectors are angled so as to reduce depression in the slipstream of the vehicle and do not require any manual operation when handling the doors. The access step is completely covered thanks to a mobile guard opened by door extensions that provides a seamless continuity between the upper and lower sections of the cab. Ground clearance is optimized by the addition of flexible components, thus optimizing air flow in the under-structure. Lastly, replacing wing mirrors with a system of profiled cameras and internal feedback screens also helps reduce vehicle air resistance.

Tyres

Michelin has been working with Renault Trucks to develop energy-saving tyres specially designed for distribution vehicles. "The objective of these tyres is to further reduce rolling resistance, without negatively impacting other performance criteria, such as safety, grip or longevity", explained Jean-François Cordonnier, Truck Pre-development Manager at Michelin. To this end, Michelin has deployed its wide range of technologies, in particular Infini-Coil technology, to guarantee tyre endurance and safety. Firstly, the self-generating tread ensures a lasting grip throughout the life of the tyre and secondly, silica is used as a reinforcing agent in the tread to improve the compromise between longevity and rolling resistance.

Connectivity

For Renault Trucks, drivers play a key role in reducing fuel consumption. This is why Urban Lab 2 features technology to help them with their driving by connecting the vehicle to infrastructures. Working with the company BeNomad, engineers have developed special navigation software that provides this connectivity. For each journey, the GPS proposes the route that is the most efficient and uses the least fuel, estimating both the predicted journey time and fuel consumption. This software has been configured to take not only fuel consumption into account, but also, and above all, the operational constraints of a distribution vehicle. Lastly, Urban Lab 2 is connected to infrastructures to optimize driving through green lights. When Urban Lab 2 approaches traffic lights, it receives information from the lights and the system calculates if it is more efficient to brake or accelerate, when conditions and regulations allow it to do so. This therefore limits the amount of stop-start driving, which has a highly negative impact on fuel consumption. Also, the traffic modeling expertise of LICIT has helped Renault Trucks to effectively integrate the effect of traffic on fuel consumption.

Hybridization

To reduce fuel consumption, Urban Lab 2 also proves innovative in its engine design, with a system combining Stop&Start and micro-hybrid technology, developed in partnership with Valeo. The Stop&Start system switches off the engine when the vehicle comes to a halt, at a red light for example, thereby reducing fuel consumption. In addition, the micro-hybrid system recovers "free" energy, such as energy generated during foot lift or braking, via a high-power (48 V) reversible electric machine. This energy can be used to drive the electrical accessories of the vehicle or reduce the mechanical power required by the thermal engine.

Renault Trucks has also been working with LaMCoS to reduce power loss in the front face of the engine in order to optimize the overall efficiency of the micro-hybrid system.

Finally, Renault Trucks and its partners have set themselves an ambitious target and have recently achieved the reducing fuel consumption of 12.8% compared to an equivalent Renault Trucks D Wide Euro-6. This amount was confirmed by measurements in practice.

Renault Trucks has even won the "Low Emissions Drivetrain Award" for its laboratory distribution vehicle (Urban Lab 2). This prize, awarded by the LUTB Transport and Mobility Systems cluster and the PFA Automotive Industry and Mobilities, as part of the Solutrans Innovation Awards, was presented to the manufacturer at the Lyon Chamber of Commerce and Industry on 21 November 2017.

1.2 LITERATURE REVIEW

Serpentine belts: Several recent studies have mainly focused on serpentine belt drive systems (see Fig. 1.2). Hawker [1] considered the belt longitudinal deflection and pulleys rotational vibrations in the analysis of free and forced response. Hwang et al [2] proposed a model to examine rotational vibration of a serpentine belt drive and the prediction of belt slip. Kraver et al [3] used a similar model to examine tensioner pivot dry friction using an equivalent viscous damper. Beikmann et al [4] demonstrated that the operating equilibrium is determined by an iteration of the nonlinear, time-invariant equations of motion. Beikmann et al also considered transverse and torsional belt vibrations [5] [6]. Parker [7] presented an efficient method to calculate the natural frequencies, vibration modes, and dynamic response of serpentine belt drive systems and to analytically formulate the eigensensitivities to system parameters. Chowdhury et al [8], in addition to the modeling of the dynamics of the belt, added the shaft on which the pulleys are mounted, they attempted to analytically determine the effect of the vibration of the flexible shaft-pulley system on the tension fluctuation of the attached belt span. These studies provide a good basis of relevant contributions and the serpentine belt drive dynamic responses detailed in some of these works are of great importance for the belt-vibrations power loss theory presented in this thesis.

Modelling and optimization of the power losses in poly-V belt transmissions: Regarding belt transmission systems, most of the works are generally related to their dynamics, e.g., Pan et al [9] have made efforts to model realistically the dynamics and the belt-pulley coupling in belt transmissions, Chowdhury and Yedavalli [8] studied the dynamics of belt-pulley-shaft systems, the slippage at the belt-pulley interfaces is ignored - which is often the case. However, sometimes the power losses (or their effects) have been indirectly studied (considered) through the friction or the slippage between the belt and the pulley, for example, Srivastava [10] and Haque reviewed the state-of-the-art research on dynamic modeling and control of friction-limited continuously variable transmissions and Lubarda [11] considered the mechanics of belt-friction (power loss) before the state of gross slip and determined the belt force before the pulley-belt slipping, etc. Most of the works directly related to power losses in belts transmission were mainly initiated by Amijima [12], [13], Gerbert [14], Childs and Cowburn [15]. However, only flat and V belts were considered. Furthermore, constant elastomeric properties of the belt rubber (storage and loss moduli) were used even though polymeric materials are known for exhibiting complex time and temperature dependent hysteretic properties [16]. Several authors such as Chen et al. [17], Almeida et al. [18] studied the global efficiency of belt transmission and therefore the global power loss. In the case of poly-V belts, experimental studies were carried out on the analysis of the pulley-belt slip (Manin et al. [19]) and on the identification of the friction coefficient between the belt and the pulley (Cepon et al. [20]). Recently, the speed and torque losses in poly-V belt drives with two equal-sized pulleys have been studied by Balta et al. in [21] and [22], respectively. Regarding the power losses in poly-V belts, a first model related to the hysteresis dissipation of the poly-V belt submitted to dynamic loading, was originally developed by Manin et al. [23]. Moreover, with respect to the optimization of power losses in poly-V belt transmissions, there is not much literature on this topic, except the studies of (1) Zhu et al [24] which have obtained the dynamic response of a FEAD and optimized the belt vibrations; and (2) Balta et al. [21] which proposed a design optimization procedure emerged from their experiments. Finally, most of the works related to the account for the rubber viscoelastic behavior in the structural components (belt, pulley, dampers) of the FEAD are about the impact of the poly-V belt viscoelasticity on its different vibration modes [25] [26] [27] [28] [29].

1.3 POLY-V BELT TRANSMISSION

Belts are commonly used in power transmission systems. In many of these systems there is a flexible element (belt) subjected to initial tension and moving in its axial direction. Indeed, there are essentially three types of belts, flat, trapezoidal and poly-V (V-ribbed) belts. They are used in mechanical systems such as textile and spinning machines, conveyors, industry fans, etc [14]. In this work, we are focusing on poly-V belts which are nowadays widely used in the automotive and truck industries as an essential part of the power transmission of vehicles (Fig. 1.2).

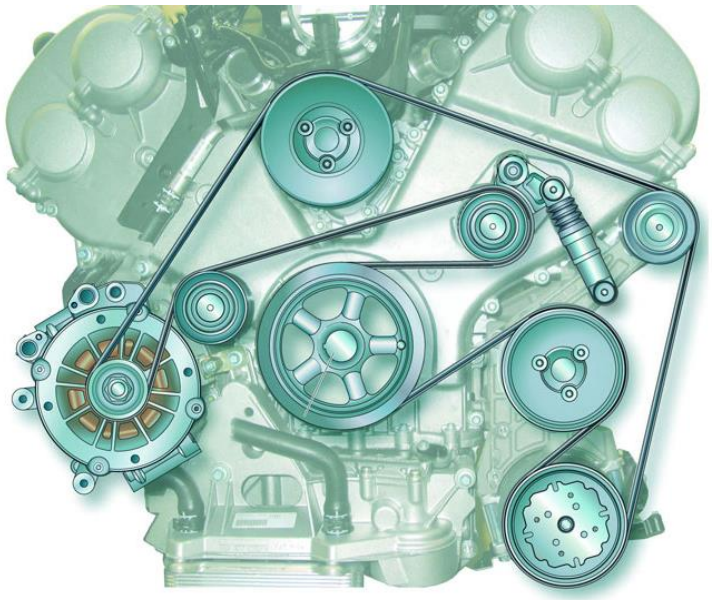

Figure 1.2 – Typical poly-V belt accessory drive system.

Poly-V belts are generally fabricated with composite materials that combine synthetic rubber backing (flexibility), polyester cords (longitudinal rigidity) and some fibrous polychloroprene base compounds which interacts directly with the pulley surface (Fig. 1.3).

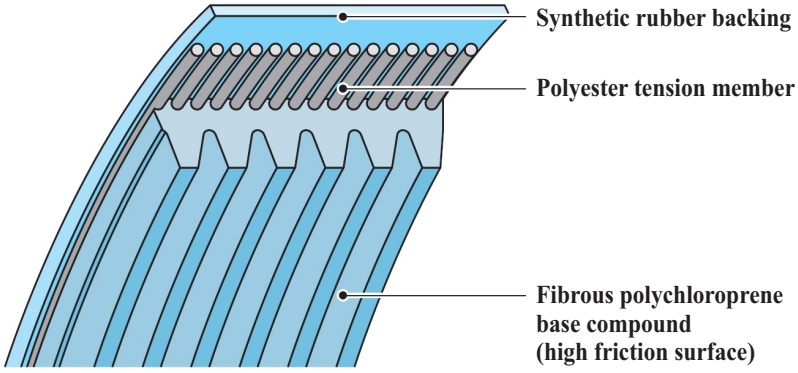

6 PK 1980

6 Number of ribs
PK Profile designation / spacing the ribs 3.56 mm
1980 Effective length [mm]

Figure 1.3 – Poly-V belt components [30].

1.4 FRONT ENGINE ACCESSORY DRIVE

In most cases, on the front engine of vehicles, power is delivered with a single poly-V (v-ribbed) belt from the crankshaft to the individual accessories such as the compressor, the alternator, the water and steering pump, etc. The belt transmission system including all the individual accessories is commonly named Front Engine Accessory Drive (FEAD). A Renault-Trucks FEAD (hereafter considered in the analyses) is presented in Fig. 1.4. In addition, an automatic tensioning device whose function is to adjust the belt slack span tension value over a wide range of operating conditions is also used (Fig. 1.4, left).

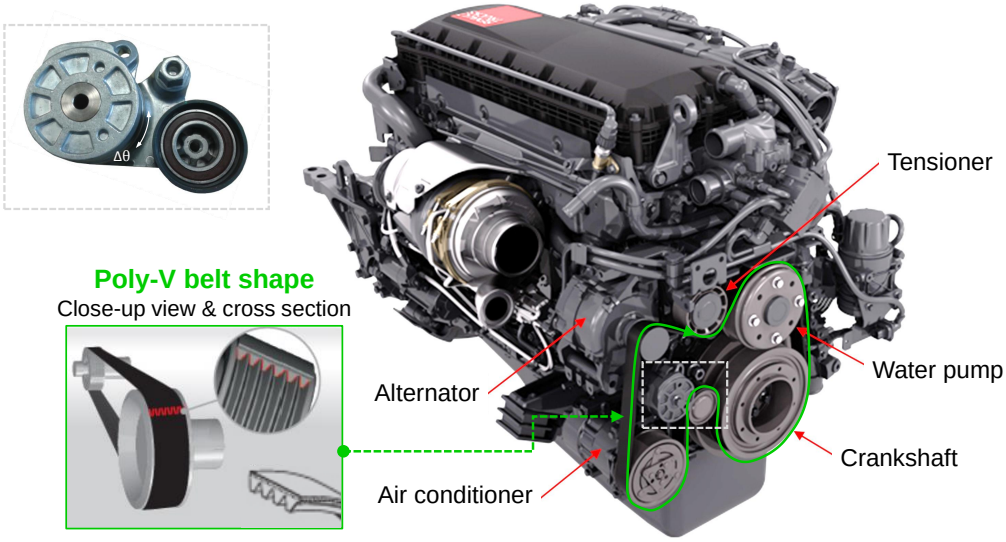

Figure 1.4 – EURO-6 Renault-Trucks FEAD with focus on the Poly-V Belt (inset).

Based on various areas of research, e.g. the hybridization of engines, new prototypes of FEADs have emerged. In Fig. 1.5 the FEAD of the Urban Lab 2 laboratory vehicle is presented. As previously mentioned, this is one of the technical solutions used to reduce fuel consumption. This prototype of FEAD is hereafter also considered in the analyses.

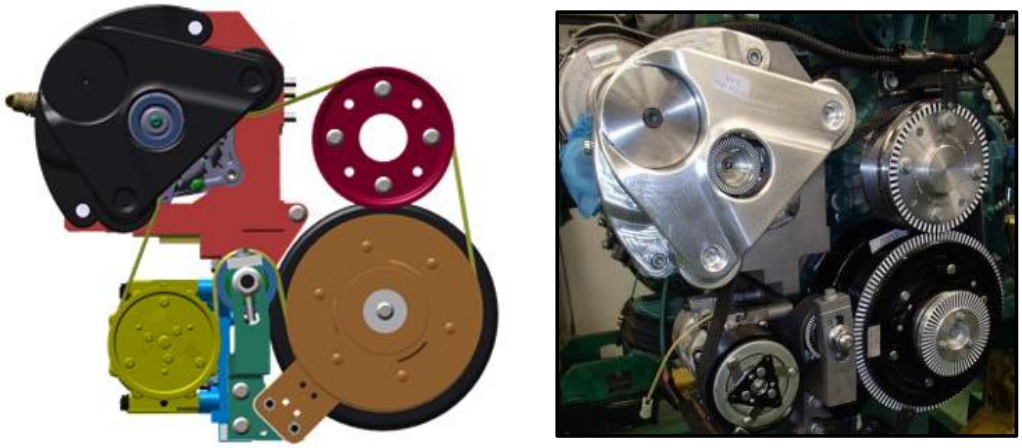

Figure 1.5 – Prototype of the Efficient Distribution Truck FEAD.

1.5 POLY-V BELT

The poly-V belt considered throughout this work has a PK profile chosen among four different types: PJ, PK, PL and PM which have dimensions as in Fig. 1.6.

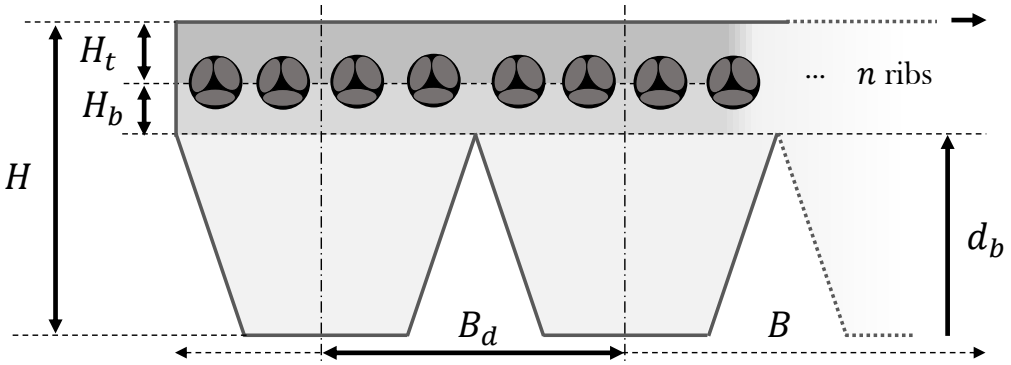

Dimensions (mm)	PJ	PK	PL	PM
H	3.8	5	9/7.5	14.5
H_t	1.1	1.5	1.5	2
H_b	1.2	1.5	3	4
B_d	2.34	3.56	4.7	9.4
d_b minimum	20	45	75	180

Figure 1.6 – Dimensions of the standard profiles of poly-V belts.

In most cases the belt profiles above are selected with the help of charts provided by the belt manufacturers (e.g. Hutchinson, Dayco, etc.) and they are chosen as a function of the power transmitted and the rotation speed of the smallest FEAD's pulley.

1.5.1 Material

Poly-V belts must be easy to bend to be effective in running on and off the pulleys. They must also be stiff in the longitudinal direction to support the traction force and to prevent excessive sliding against the pulleys [14]. To accomplish these properties, high power capacity poly-V belts are mostly designed with

- A tension member
- An elastomer
- A high friction surface

The tension member is a flexible cord layer of high modulus fibers, i.e. PET, polyester as shown in Fig. 1.3, aramid (kevlar) or glass. Sometimes the fibers are directly mixed into an elastomer to get a high modulus matrix.

The tension member is also surrounded by a highly flexible elastomer, i.e. synthetic rubber as in Fig. 1.3, rubber EPDM, polychloroprene or polyurethane. Also fibers are included in the elastomer and oriented so that to increase the load supporting capacity.

The friction surface is the outermost layer directly in contact with the pulley. Either an additional thin layer of some high friction coating (e.g. fibrous polychloroprene base compound as shown in Fig. 1.3) is attached to the belt or the elastomer itself has sufficient friction when it works directly on the pulley.

1.5.2 Design

Poly-V belts are more and more employed and they replace progressively other traditional designs, because of their compactness and their contact surface area up to 2.5 times larger than the contact surface area of flat belts and V-belts (Fig. 1.7).

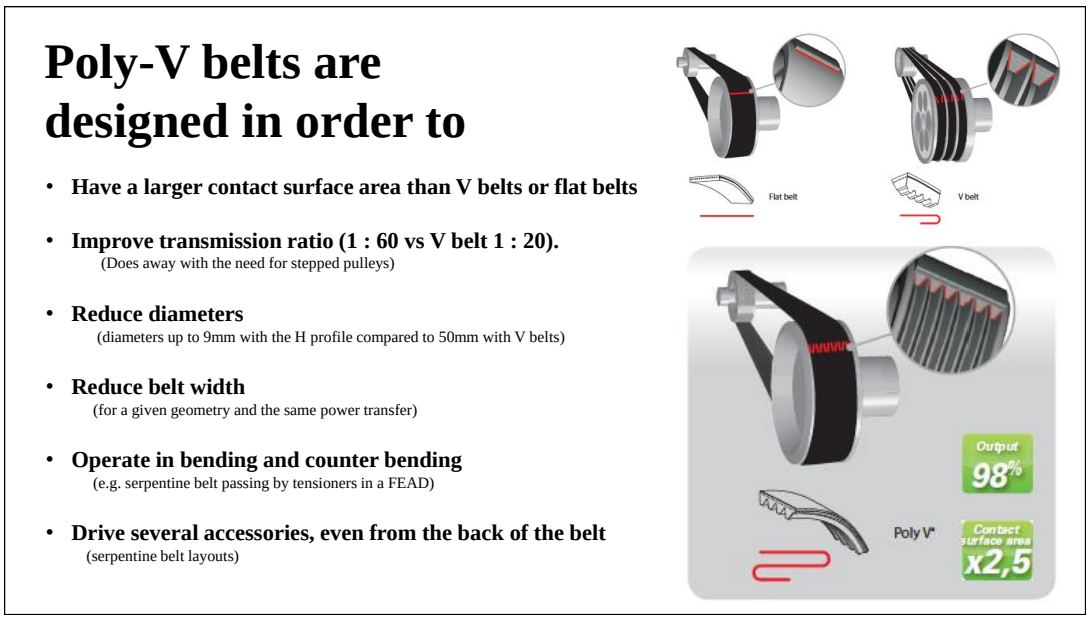

Figure 1.7 – Benefits of the use of poly-V belts instead of other designs of belts [31].

According to Fig. 1.7, the poly-V belt is not only an improved belt model, but it is also designed to be a combination with the best characteristics of flat belts and V-belts.

From microscopic analyses of the cross-section of the poly-V (Fig. 1.8), a physical model of the poly-V belt is adopted to be used across this work, mainly in the power losses modeling (chapter 2) where the models are based on the assumptions bellow.

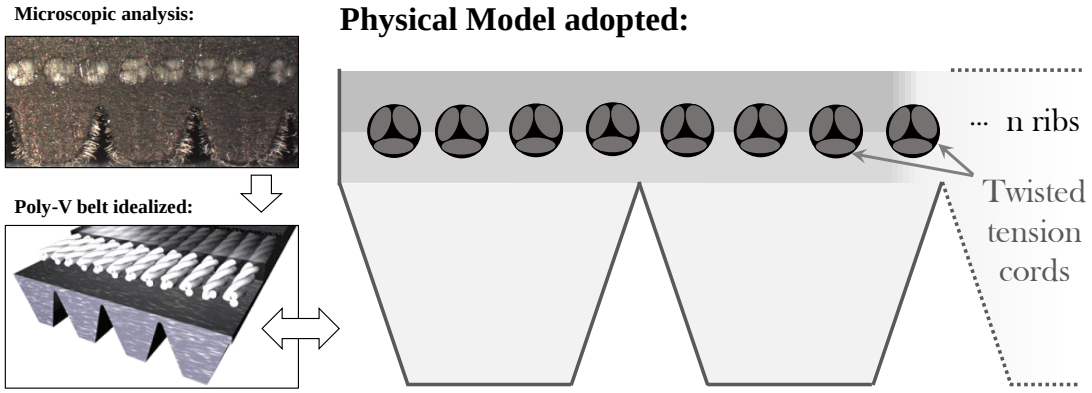

Figure 1.8 – Poly-v belt cross section microscopic analysis and its physical model.

- The poly-V ribs are assumed to be trapezoidal;
- The poly-V tension member is assumed to be composed of several cords, each one with small cords rolled spirally against each other;
- A poly-V belt may be idealized as an assembly of two flat belts and several small V-belts corresponding to the number of ribs.

1.6 ACCESSORIES

In internal combustion engines, accessories are almost exclusively driven by poly-V belts.

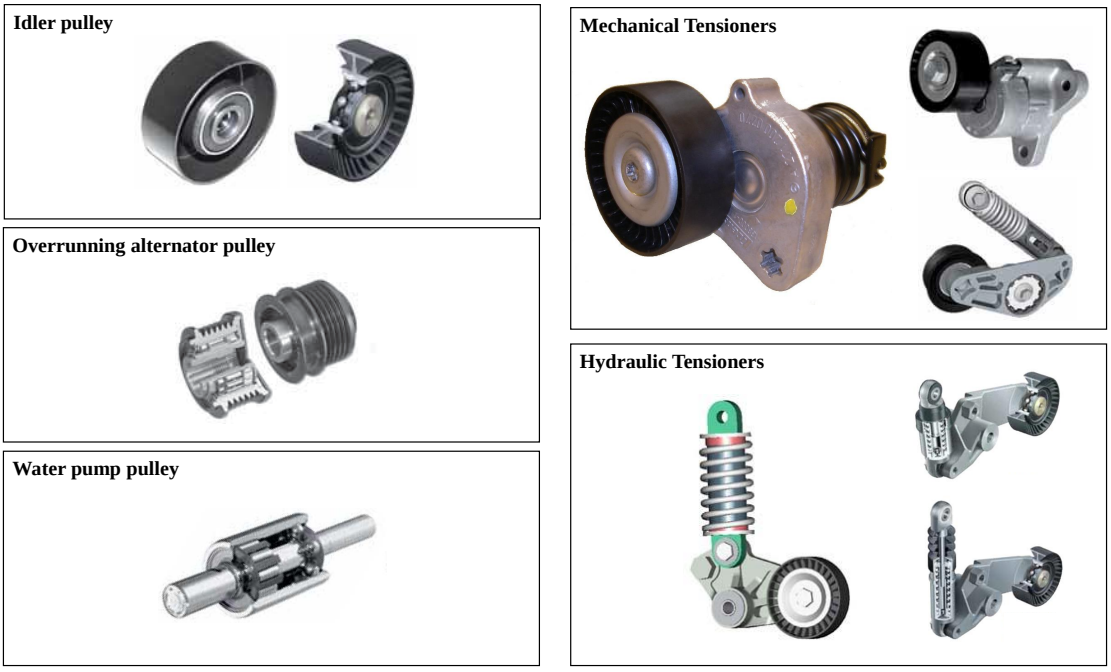

Figure 1.9 – Examples of FEAD components: pulleys and tensioners [32].

According to Schaeffler [32], the primary requirements for accessory drive systems and their automated tensioning systems are listed below:

- Self belt force adjustment during initial installation and maintenance of the FEAD and components including the belt (tolerance compensation of drive components);
- Nearly consistent belt force during operation and the entire life of the transmission (compensation of the belt elongation and wear);
- Reduction of dynamic belt force peaks;
- Minimization of slip, noise and belt wear;
- Rating life increase for the entire belt drive system;
- Optimal reliability of the overall belt drive system;
- Minimization of friction loss in the overall system, and so forth.

FEAD components can be from simple idler-pulleys equipped with grooved ball/roller bearings to more complex mechanical and hydraulic tensioning systems (Fig. 1.9).

1.6.1 Poly-V pulley

In Fig. 1.10, it is presented several types of pulleys, possibly made of different materials, which may be used to transmit power with a poly-V belt. The manufacturing process of the (poly-V) pulleys which fit the poly-V belt is also shown on the left (Fig. 1.10).

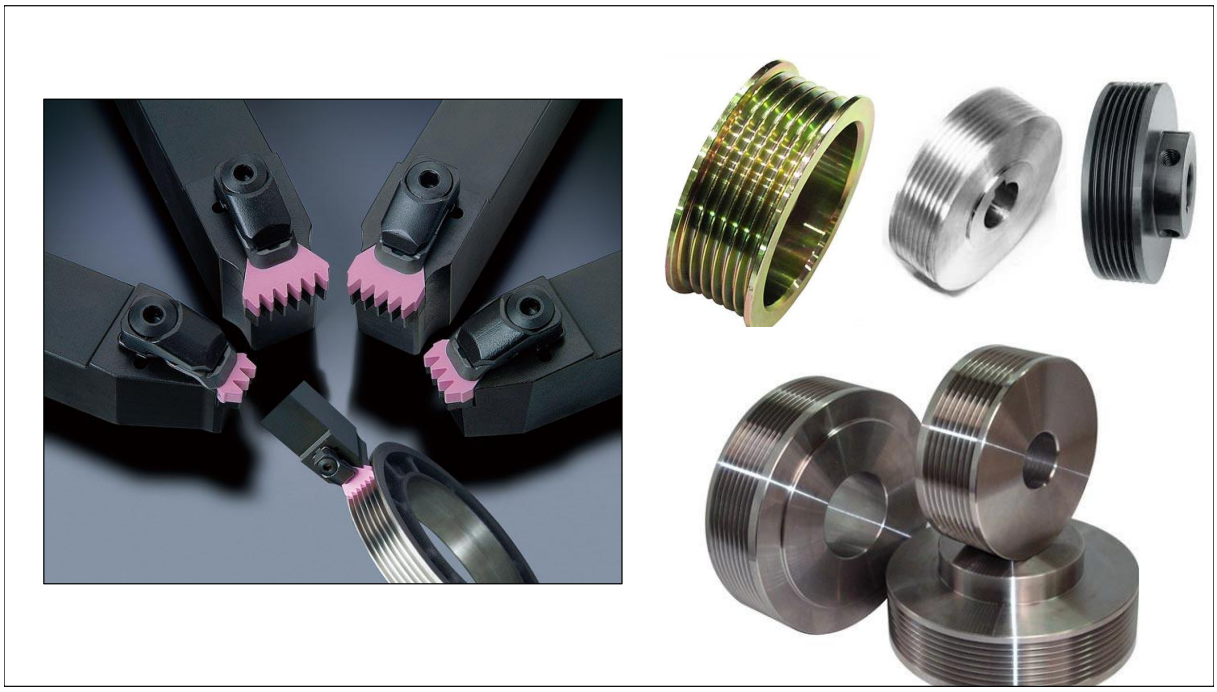

Figure 1.10 – Examples of different types of poly-V pulleys.

The poly-V pulley is a special type of grooved pulley designed to transmit more power than other (e.g. flat or V) models.

Poly-V pulleys have clear advantages over the use of conventional pulleys which are the same as those presented in Fig. 1.7.

According to the intended application, poly-V pulleys can be made of steel, aluminum, brass, etc. They can also be of different diameters, widths and form with splined or bolted shaft couplings. In addition, there exist many possibilities to manufacture them producing various sizes (number of ribs) and profiles as in Fig. 1.10. The width of the poly-v belt is adapted to the power to be transmitted.

1.6.2 Torsional Vibration Damper pulley

Internal combustion engines and especially diesel engines when firing produce torsional crankshaft vibrations. These vibrations are partly due to the cyclic rod forces working on the crankshaft combined with its proper rotation; it results in an irregular rotation speed. These torsional vibrations could lead to excessive belt wear, noise and transverse belt vibrations. That is why it is important to dampen them. For this purpose, a poly-V driving pulley is adapted to be a Torsional Vibration Damper (TVD) for the crankshaft. The principle is to separate into two (or more) mechanical parts the crankshaft pulley and to insert a rubber ring between them, a vibration absorber is therefore obtained (e.g. Fig. 1.11), with the same principle as a TMD (Tuned Mass Damper).

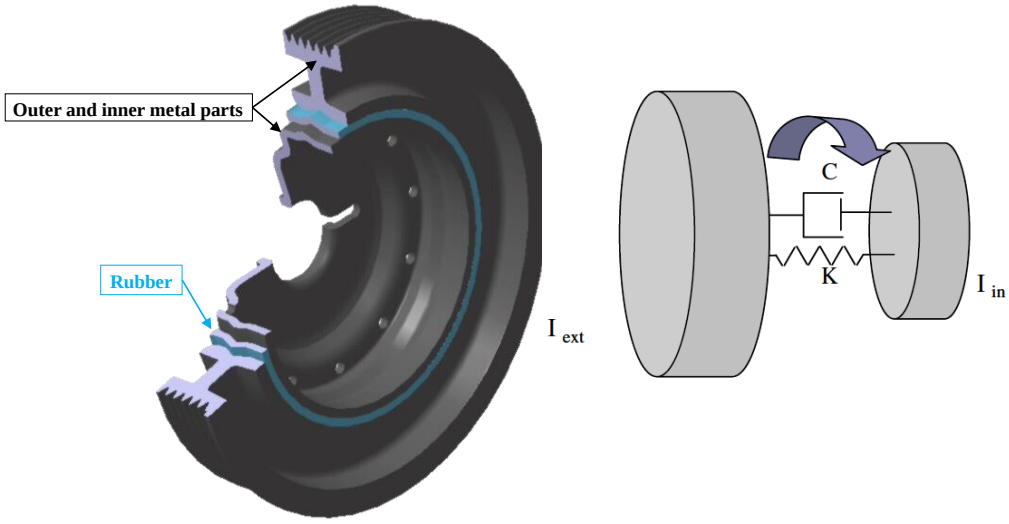

Figure 1.11 – Single-mass rubber TVD pulley [33].

The most common types of TVD are the single (Fig. 1.11) and dual mass rubber TVD which filters the vibrations from the crankshaft with an additional rubber ring (Fig. 1.12).

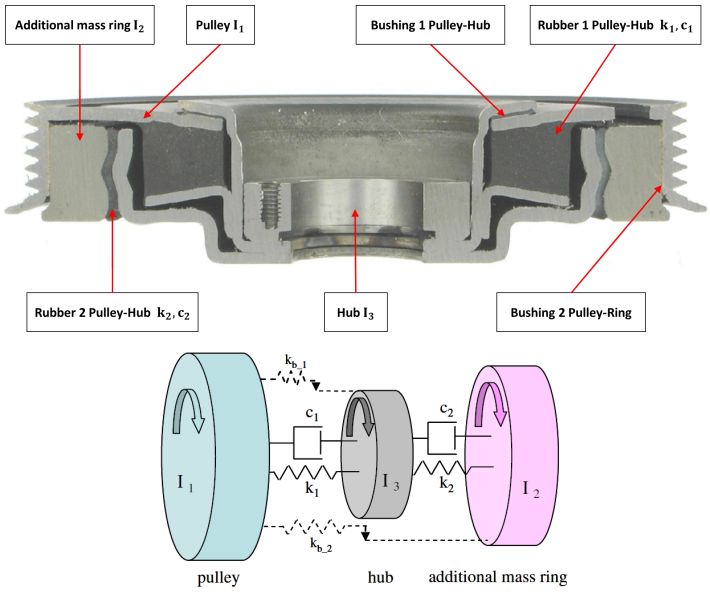

Figure 1.12 – Dual-mass rubber TVD pulley [33].

TVDs are mechanical assemblies which dampen the vibrations engendered by the engine torque fluctuations and are generally composed of at least three elements: the hub, a rubber ring and an inertia steel ring with V-ribs on its outer diameter (used as a pulley).

1.7 TENSIONERS

FEAD tensioners can be subdivided into two types. They can be fixed or mobile and belong to two categories, mechanical and hydraulic tensioners. Idler-pulley, mechanical and hydraulic tensioners are briefly presented hereafter.

1.7.1 Idler-pulley

The simplest tensioner, the idler pulley is responsible for guiding and maintaining tension with the drive belt. Examples of this type of tensioner are presented in Fig. 1.13.

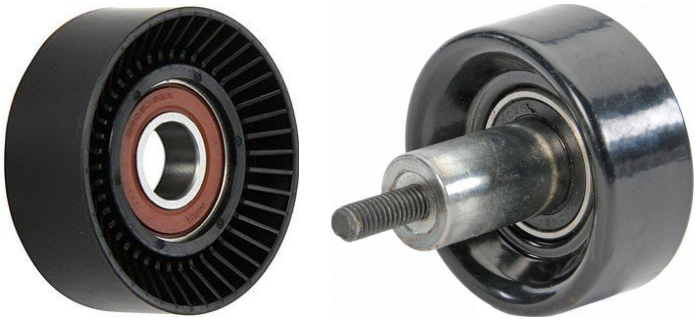

Figure 1.13 – Examples of idler-pulleys.

Moreover, there are several interests of introducing an idler pulley: vibration and noise reduction in critical belt spans, prevent collision with the surrounding parts as shown in Fig. 1.14, increase of wrap angles on neighboring pulleys and therefore decrease of setting tension and increasing belt durability.

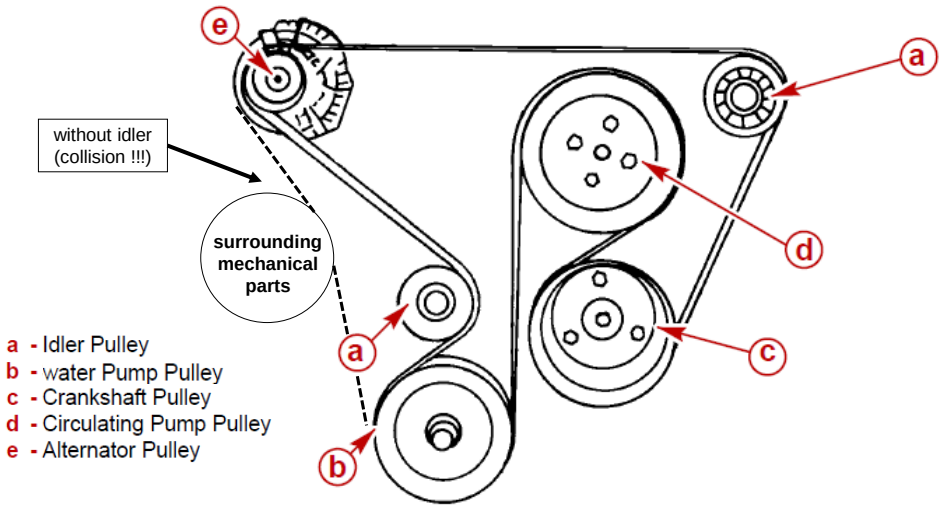

Figure 1.14 – Role of an idler-pulley in a FEAD

The idler-pulleys have similar rating life and noise development requirements as the belt tensioning systems presented in the following sections.

1.7.2 Mechanical tensioner

The Mechanical Tensioner (MT) is an articulated system composed by an idler-pulley attached to a mobile part (arm) connected to the FEAD by a torsion spring (Fig. 1.15).

This type of tensioner is a good cost-optimized solution to automatically maintain poly-V belt drives tensioned. The required belt pre-load force is usually generated by the arm of the lever, the tension pulley as well as the torque exerted by a torsion spring.

A mechanical tensioner can be modeled either by a friction element [34], or by a spring and a damper in parallel. This consists in a friction element (disk, ring and cone) pre-loaded by a torsion spring similar to that in Fig. 1.15.

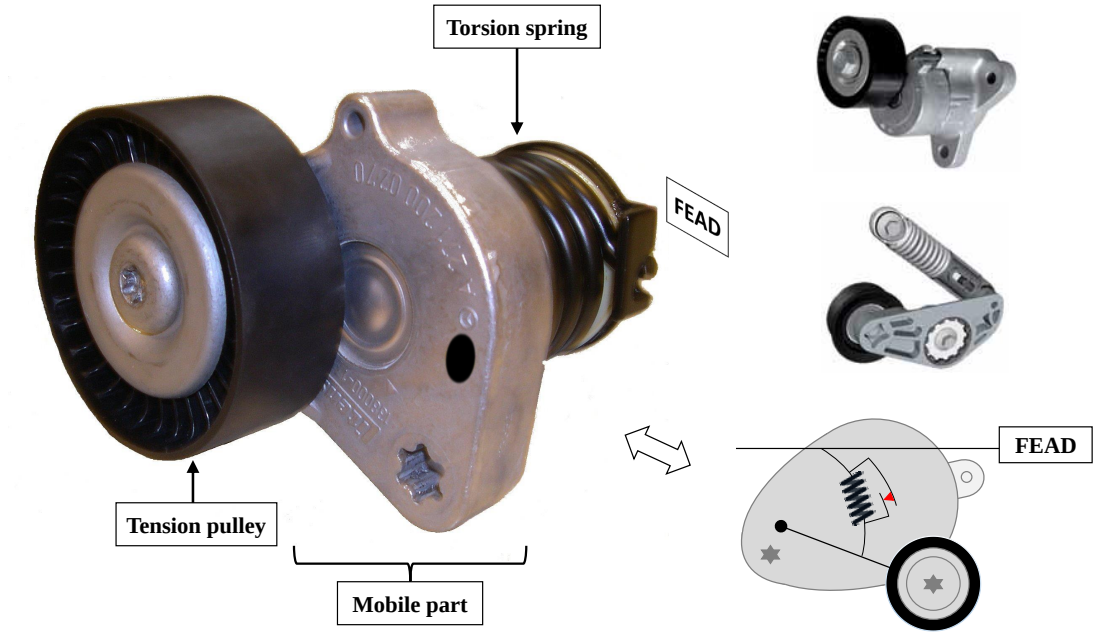

Figure 1.15 – Example of MT with its parts (left) and other types (right).

With respect to the damping function of the mechanical tensioner, the principle is simple: as the lever arm moves, a relative motion between two surfaces in contact takes place generating friction, and consequently, damping. The belt pre-load force thanks to the spring torque and damping are adjusted to match the mechanical tensioner application.

Depending on the application and power to be transmitted, the mechanical tensioner can generally be optimized (optimal tensioner-arm length and spring stiffness are employed) in order to reduce belt transverse vibrations and also to increase belt durability.

1.7.3 Hydraulic tensioner

Similar to the mechanical ones, Hydraulic Tensioners (HT) have fixed and mobile parts (Fig. 1.16). They are mainly considered when the system demands a solution with high requirements: significant tensioning force and belt-tensioning/tensioner-size ratio.

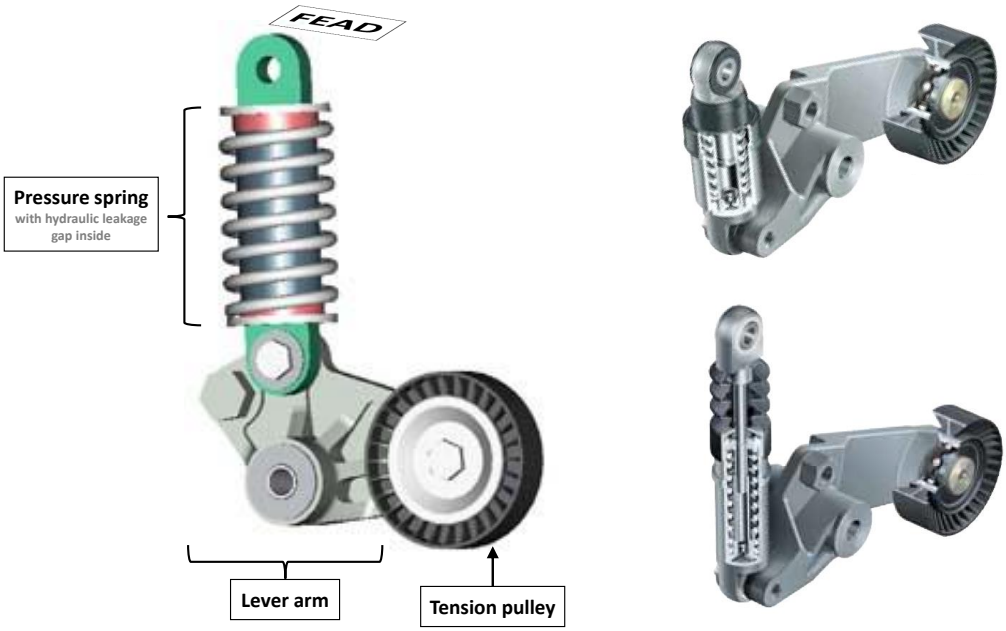

Figure 1.16 – Example of HT with its parts (left) and other types (right).

This type of tensioner consists of a hydraulic component with an integrated compression spring and hydraulic leakage gap damping as well as a lever arm with an attached idler pulley (Fig. 1.16, left). The hydraulic leakage gap damping acts in a controlled way and in proportion to the speed generating damping only when needed.

The optimal adjustment of the required belt pre-load force to the relevant application is performed by the HT integrated pressure spring and the converted lever ratio. The required damping is set by adjusting the leakage gap.

The properties of the lubricant (viscosity, compressibility, ...) used inside the hydraulic tensioners ensure the lowest possible damping temperature dependency in combination with excellent resistance to act without hardly wear. This may be one of the biggest advantages of using the hydraulic tensioner. Two design examples (right) of hydraulic tensioner and its constitutive parts (left) are shown in Fig. 1.16.

More details on belt drive systems can be found in [32].

After introducing the power transmission system studied in this thesis, the poly-V belt, the FEAD and its components, let us introduce the minimum necessary to understand the modeling of the power losses developed in chapter 2.

The geometry of the transmission, the belt-span tension, the belt setting tension, the adhesion and the sliding arcs are parameters directly involved in the FEAD power losses. Thus, let us briefly get into a basic theorization of their concepts.

1.8 KEY ENTRY TOPICS

1.8.1 Geometry

To calculate the geometrical parameters of a 2-pulleys belt transmission the formulas in Fig. 1.17 from [30] can be used. They relate the belt theoretical length (L) to the pulley's diameters (d) and the center distance (e) between the pulleys.

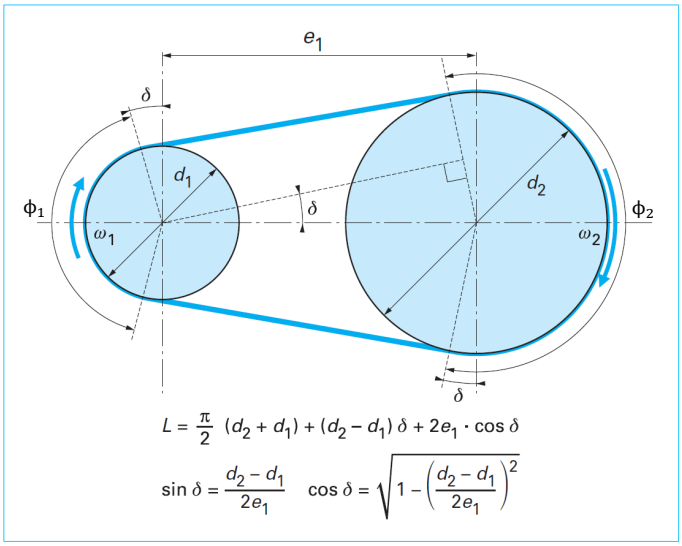

Figure 1.17 – Geometry of a belt transmission composed of two pulleys [30].

If the belt transmission has several pulleys (at least 3 pulleys) as in the case of the Front Engine Accessory Drives (FEADs), the formulas in Fig. 1.18 from [30] and [35] can be used, as is the case in this thesis.

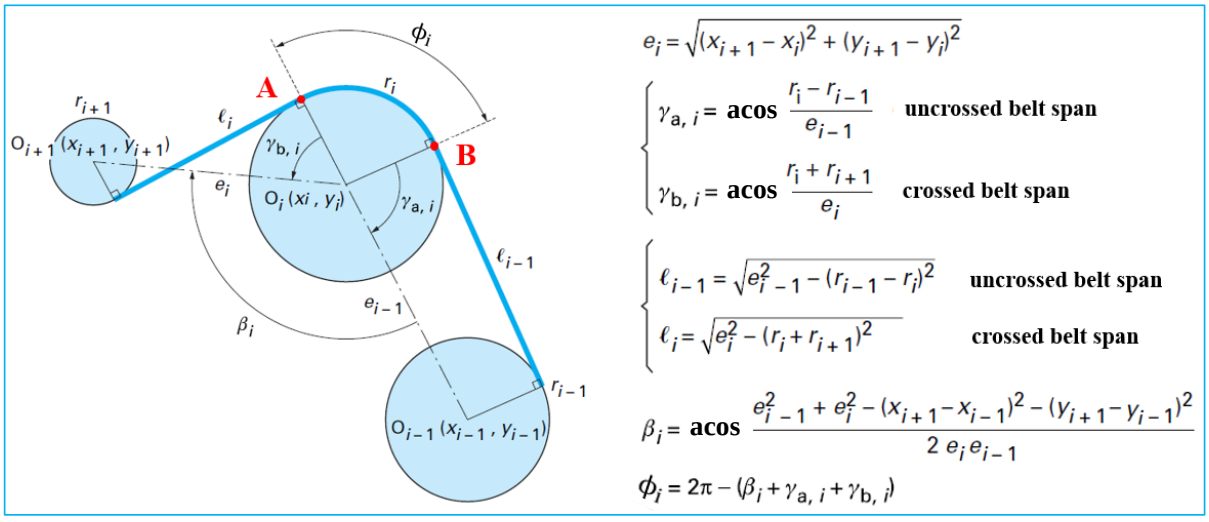

Figure 1.18 – Geometry of a belt transmission composed of several pulleys (FEAD) [30].

1.8.2 Belt span tensions

In a FEAD, power is often transmitted from a DriveR (DR) pulley to several DriveN (DN) pulleys by means of friction between the belt and the pulleys. Consequently, the tension varies in the belt. Let us consider the belt transmission system in Fig. 1.19.

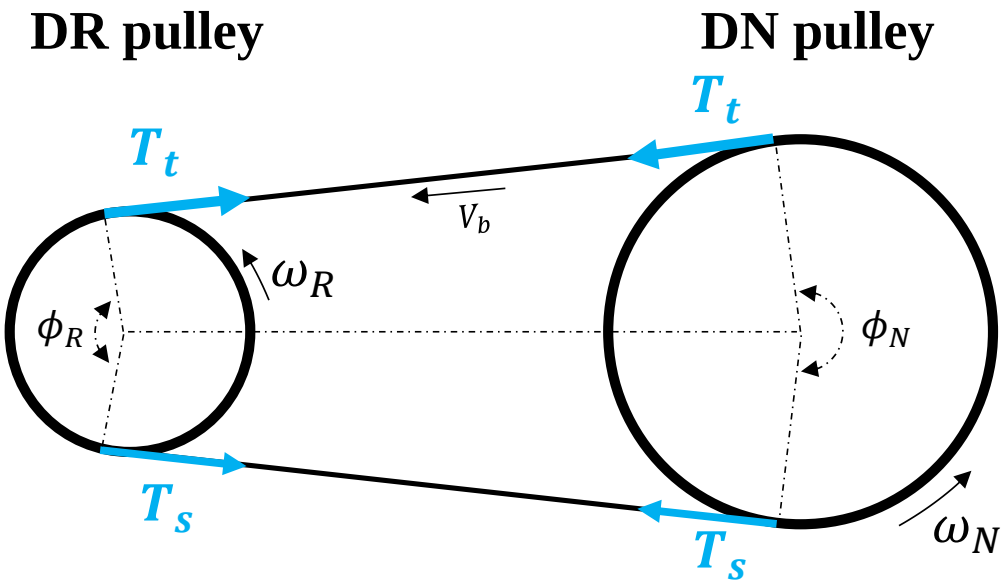

Figure 1.19 – Belt transmission system with a DR and a DN pulley.

When it is running, some variation of tension occurs along the angle of contact ϕ, it means that the belt is pulled on one side and pushed (lack of pulling) on the other side of the DR pulley, giving rise to the tight T_t and slack T_s side tensions. The effective pull $(T_t - T_s)$ is transmitted between the pulleys via the free spans of the belt.

In the same direction of rotation (i.e. V_b direction), similar to what happens around the DR pulley, a variation of tension also happens along the DN pulley, but in this case with tensions increasing from T_s to T_t instead of decreasing from T_t to T_s as along the DR pulley. This is a consequence of the driving and resisting torques imposed by the crankshaft and accessory-drive shafts, respectively.

The phenomenon described above happens similarly in a Front Engine Accessory Drive with the particularity that, in this case, along the FEAD path the effective pull from the crankshaft is partially distributed to all the accessory driven pulleys.

To summarize, the belt-span tension always changes around a pulley transmitting power from a slack to a tight side or vice-versa, the only difference is if the change in the belt tension corresponds theoretically to all (Fig. 1.19) or part (FEADs) of the effective pull generated by the crankshaft. Also, another parameter that changes with changing the belt-span tension is the magnitude of the adhesion ϕ_a and sliding ϕ_s angles constituting the wrap angle ϕ $(\phi_a + \phi_s)$ of the pulleys [14]. The angle ϕ of all pulleys in a FEAD can be determined from the geometry (Fig. 1.18). The adhesion ϕ_a and sliding ϕ_s angles/arcs are explained in the next sections.

1.8.3 Belt setting tension

The setting tension T_0 is the tension existing in all belt-spans when the system is at rest. This tension must be sufficiently high to guarantee the power transmission on all pulleys when the system is running, i.e. $T_0 \geq T_{0\,min}$ as in Fig. 1.20, and therefore, ensuring that the full pulley/belt slip (gross slip) does not occur.

From the above statement, let us consider the 2-pulleys belt transmission in Fig. 1.19. The calculation of the belt setting tension is also indicated in Fig. 1.19, where T_0 is the belt setting tension and is always calculated considering the smallest pulley in the transmission [30]. Indeed, if the non-slippage is ensured on the smallest pulley, it will also be ensured on the other pulleys of the transmission. Similarly, in a FEAD, it is also necessary to ensure the non-slippage of the belt on all pulleys.

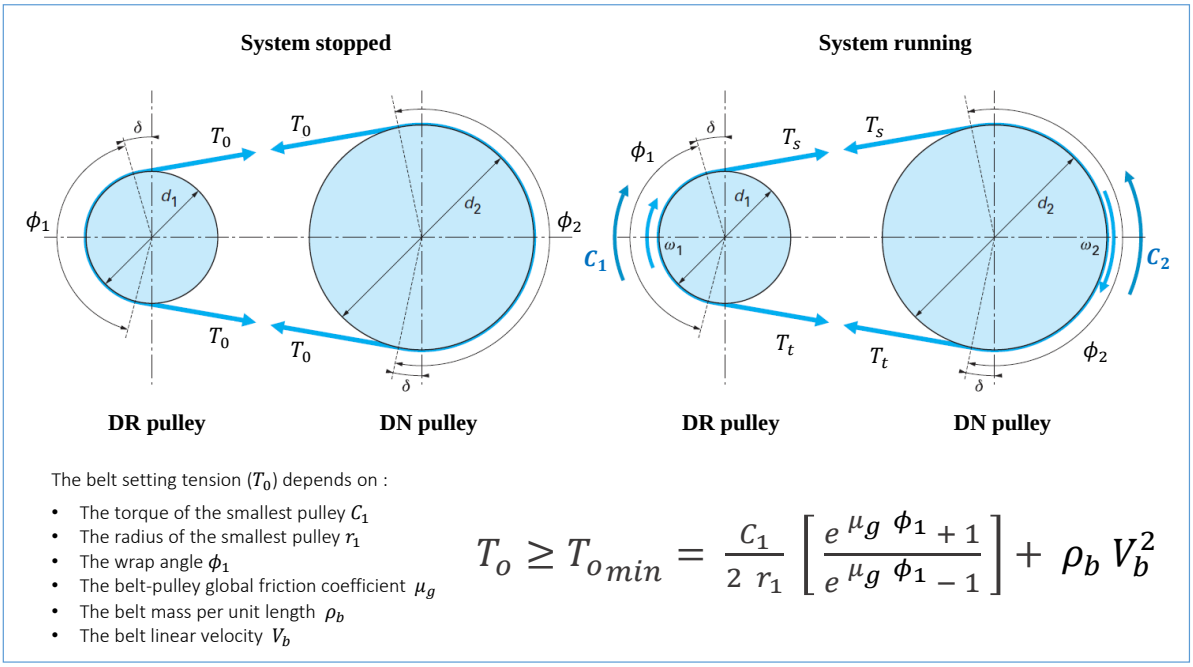

Figure 1.20 – Belt setting tension for a 2-pulleys belt transmission system [30].

In this regard, a minimum belt setting tension $T_0 \geq T_{0\,min}$ for each component of the system can be estimated as in Fig. 1.19 considering the driving and resisting torques from the engine and accessory drives. Thus, the tension is the (highest) setting tension which ensures the power transmission on all accessories of the FEAD.

In practice, the belt manufacturer guide/catalog do not use directly the equation to find T_0 as in Fig. 1.19. The guides for selecting belts consider different correction factor of the power to be transmitted to take into account the diameter of the smallest pulley, the belt/pulley wrap angles smaller than 180 degrees, the type of the driven machine, the transmission utilization rate per day, the length of the free belt-spans, etc.

1.8.4 Sliding and adhesion arcs

Still considering a 2-pulleys belt transmission system as in Fig. 1.21, when the system is running the belt span tension does not vary continuously over the whole arc of contact (ϕ) from slack to tight side or vice-versa, but according to Grashof [36] ϕ is divided into two angles (arcs): the sliding angle ϕ_s and the adhesion angle ϕ_a. Moreover, according to Gerbert [14] the tension in the belt varies along the sliding angle ϕ_s and remains constant along the adhesion angle ϕ_a. Also, in the sliding arc there is a relative motion in the longitudinal direction between the poly-V belt and the pulley surface.

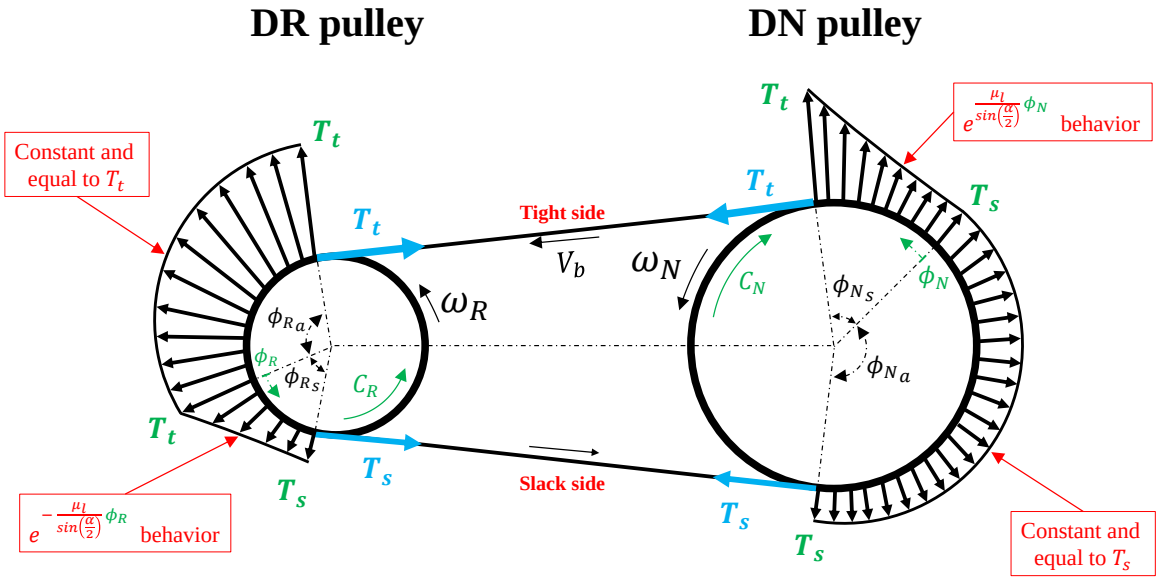

Figure 1.21 – Variation of tension in the belt along the contact arcs of a simple transmission.

Belt transmissions with 2, 3 or more pulleys have tension distribution profiles similar to that in Fig. 1.21, because the belt tension member is extensible and thin. Thus, there is an extensible belt subjected to varying tension running on stiff pulleys (rigid bodies). This implies that the belt slides on the pulley and the friction is fully developed within the sliding angle ϕ_s. In contrast, within the adhesion angle the belt adheres to the pulley. In this case, no shear occurs since the belt is assumed to be thin, so the tension is constant and no friction exist [14].

In Fig. 1.21, the sliding arc, corresponding to the sliding angle ϕ_s, is located towards the unseating region (where the belt leaves the pulley). Consequently, the adhesion arc, corresponding to the adhesion angle ϕ_a, is located towards the seating region [14] (where the belt meets the pulley), both at the DR and DN pulleys.

Assuming that in poly-V belts no radial sliding occurs (besides circumferential sliding), the magnitude of both DR (ϕ_{Rs}) and DN (ϕ_{Ns}) sliding angles in Fig. 1.21 are determined from Eqs. 1.1 and 1.2.

Applying the Capstan formula [37] on the DN pulley of Fig. 1.21 gives the varying force $T_N(\phi)$ (Eq. 1.1) which results in a varying contact pressure (Appendix $A2$) and ranges from T_s to T_t along the sliding arc.

$$\frac{T_N(\phi) - T_c}{T_s - T_c} = e^{\frac{\mu_l}{sin(\frac{\alpha}{2})}\,\phi_N} = e^{\,\mu_g\,\phi_N} \tag{1.1}$$

Similarly, applying the Capstan formula on the DR pulley of Fig. 1.21 gives the varying force $T_R(\phi)$ (Eq. 1.2) which results in a varying contact pressure (Appendix $A2$) and ranges from T_t to T_s along the sliding arc.

$$\frac{T_R(\phi) - T_c}{T_t - T_c} = e^{-\frac{\mu_l}{sin(\frac{\alpha}{2})}\,\phi_R} = e^{-\mu_g\,\phi_R} \tag{1.2}$$

Where

- $T_c = \rho_b\, V_b^2$ represents the centrifugal action;
- α represents the poly-V belt wedge angle;
- μ_l is the belt-pulley local friction coefficient.
- μ_g is the belt-pulley global friction coefficient.

Note that along the contact arc between the belt and the DN pulley (Eq. 1.1) the sliding angle ϕ_N varies from where it was indicated in Fig. 1.21 to ϕ_{Ns} which is a constant value.

Similarly, along the contact arc between the belt and the DR pulley (Eq. 1.2) the sliding angle ϕ_R varies from where it was indicated in Fig. 1.21 to ϕ_{Rs} (constant value).

As briefly mentioned earlier, from sliding angles ϕ_{Ns} and ϕ_{Rs} (Eqs. 1.1 and 1.2) the following relations can be used to obtain the adhesion angles ϕ_{Na} and ϕ_{Ra}.

$$\phi = \phi_s + \phi_a \tag{1.3}$$

Moreover, in Eqs. 1.1 and 1.2 to determine the angles ϕ_{Ns} and ϕ_{Rs} the belt-pulley friction coefficient μ, i.e. μ_l or μ_g, is needed.

In chapter 6, two methods are presented for determining the belt/pulley friction coefficients μ_l and μ_g. A method from [20] which uses the concept of gross slip, i.e. when the sliding arc is equal to the arc of contact ϕ between the belt and the pulley, and another method which considers the belt/pulley contact from a tribological approach.

1.9 OBJECTIVES

The mains objectives of this work are:

- To present a theory for research topics, i.e. modeling and optimization of the power losses taking place in poly-v belt transmissions, and particularly in the Front Engine Accessory Drives of vehicles, which have rarely been explored before and have only few studies in the literature.
- To contribute for the advance of science improving models initially developed by other scientists.
- To provide a scientific approach to understand where energy is lost in a FEAD and the nature of the corresponding power losses: hysteresis, dry friction, etc.
- To quantify the FEAD power losses in order to have a function to be optimized.
- To apply and validate the power losses modeling and the application of optimization methods for the case of the FEAD used in truck engines.
- To present a test bench and a practical method used for determining the FEAD power losses experimentally.
- To propose a simulation tool practical and effective for predicting and optimizing the FEAD power losses.
- To provide representative data for simulations on:
  - the poly-V belt viscoelastic material properties (obtained via DMA[1]);
  - the pulley/belt friction coefficient;
  - the tensioners hysteretic behavior of Volvo Trucks;
- To propose an easy-to-use methodology for characterizing (using master curves) and implementing (in simulations) the viscoelastic material behavior of the poly-V belts and the torsional vibration damper used on the crankshaft.
- To give some insights, conclusions and perspectives to go further.

[1]Dynamic Mechanical Analysis (DMA, section 2.3.7) is an experimental technique used to characterize materials. Further details on DMA technique can be found in chapter 2.

1.10 TASK OUTLINE

This thesis is divided into seven chapters and associated appendices:

- **Chapter 1** introduces the working context giving a brief review of the considered power transmission and its components. This chapter gives key entry topics needed to better understand theory afterwards. It also presents the motivations for this work, the main objectives, the outline of this thesis, the contributions of this work, and finally, a review of the literature.
- **Chapter 2** presents in detail the modeling of the power losses occurring in FEADs. Simulations and associated experimental verifications that permits sustaining the modeling are also presented in this chapter.
- **Chapter 3** presents the optimization of the power losses of a FEAD example using the genetic algorithm and the dynamic programming methods. This chapter also gives the specificities of each method when they are applied to the case of FEADs. Simulations and associated experimental verifications that permits extending the optimization to industrial applications are also presented in this chapter.
- **Chapter 4** is devoted to the presentation of the test fixture used in development tests and to test industrial FEAD layouts, respectively, throughout and at the end of the thesis. Comparisons between simulation and experiments that still permit sustaining the power loss modeling are also observed for industrial applications.
- **Chapter 5** presents the simulation tool PLFead, which implements the developed power loss theory and applies the optimization methods. This chapter also exposes the way in which PLFead is organized, some examples of the interfaces of PLFead, and the conclusions about this tool.
- **Chapter 6** describes the experimental identification of the parameters used in all of the simulations and some side research.
- **Chapter 7** discusses the achievements of this work, states the conclusions and suggests future work.
- **Appendices** provides support for the thesis manuscript with additional details on modeling, experiments and optimization algorithms.

1.11 CONTRIBUTIONS

The main contributions or novelties of this work are :

- The presentation of a full, detailed and improved modeling of the original (bending, flank and radial compression) power loss models developed by Manin et al. [23];
- The modeling of additional power loss phenomena, i.e. belt-hysteresis (stretching and shear), tensioner-hysteresis, and the implementation of the bearings power loss in order to obtain a FEAD representative model of the power losses taking place in poly-V belt transmissions (FEADs);
- The effective application (and exemplification) of optimization methods (applied) to reduce FEAD power losses;
- The implementation of a practical and effective tool (PLFead), mainly for predicting an optimizing the FEAD power losses;
- The provision of experimental/simulation data on
  - Belt and TVD elastomers viscoelastic properties obtained via DMA;
  - Properties such as the tensile modulus, stiffness and damping of the belt used in Volvo FEADs;
  - Pulley/belt friction coefficients for several operating conditions;
  - Hysteresis curves of the tensioners used in EDIT and EURO-6 FEADs;
  - FEAD power losses to serve as reference for future developments.
- The proposition/statement of
  - An easy and practical way to do a diagrammatic representation (Power Loss Maps) of the FEAD power losses;
  - A testing methodology based on the thermo-simplicity principle to determine the viscoelastic properties of the belt and TVD elastomers;
  - An analysis of the TVD used in the Volvo FEADs to inspire further research;
  - Clarifications on important viscoelastic effects (Mullins, Payne) possibly taking place in belt transmissions (Appendix $A4$);
  - Remarks over an enhanced analysis (Appendix $A5$) to improve future research.
- The oral clarifications of the present work at the
  - Regional conferences [A] and [B];
  - International conferences [C], [D], [E] and [F];
- The written contributions in the form of research papers ([G], [H], [I], [J] and [K]).

Details on the last items of the above list can be found in the next page.

Regional conferences

[*A*] Modelisation des pertes de puissance dans les tranmissions par courroie poly-V: influence des parametres de conception, Journees Transmissions Mecaniques (JTM), Villeurbanne, France, 11-12 July 2016.

[*B*] Dynamics of poly-V belts: power loss analysis, Journees Jeunes Chercheurs en vibrations, Acoustique et Bruit (JJCAB), Paris, France, 16-17 November 2017.

International conferences

[*C*] Modeling of power losses in Poly-V belt transmissions: influence of design parameters, proceedings of the International Conference on Power Transmissions 2016 (ICPT 2016), Chongqing, P.R. China, 27-30 October 2016.

[*D*] Modeling of power losses in poly-v belt transmissions: hysteresis phenomena, proceedings of the JSME International Conference on Motion and Power Transmissions 2017 (MPT 2017), Kyoto, Japan, February 28 - March 3 2017.

[*E*] Distribution of power losses in serpentine belt-drive: application to FEAD, proceedings of the International Gear Conference (IGC), Lyon, France, 27-29 August 2018.

[*F*] Dynamics of torsional vibration damper pulley: implementation of elastomeric constitutive law, proceedings of the International Conference on Noise and Vibration Engineering 2018 (ISMA 2018), Leuven, Belgium, 17-19 September 2018.

Research papers

Published:

[*G*] C. A. F. Silva, L. Manin, R. G. Rinaldi, D. Remond, E. Besnier, M. A. Andrianoely, Modeling of power losses in poly-v belt transmissions: hysteresis phenomena (standard analysis), JSME 11 (2017) 1–15. doi: 10.1299/jamdsm.2017jamdsm0085.

[*H*] C. A. F. Silva, L. Manin, R. G. Rinaldi, D. Remond, E. Besnier, M. A. Andrianoely, Modeling of power losses in poly-v belt transmissions: hysteresis phenomena (enhanced analysis), Mech. Mach. Theory 121 (2018) 373–397.
doi: 10.1016/j.mechmachtheory.2017.10.008.

[*I*] C. A. F. Silva, M. A. Andrianoely, L. Manin, S. Ayasamy, C. Santini, E. Besnier, D. Remond, Optimization of power losses in poly-v belt transmissions via genetic algorithm and dynamic programming, Mech. Mach. Theory 128 (2018) 169–190.
doi: 10.1016/j.mechmachtheory.2018.05.016.

Under review:

[*J*] C. A. F. Silva, L. Manin, M. A. Andrianoely, E. Besnier, D. Remond, Power losses distribution in serpentine belt-drive: modelling and experiments (2018).

[*K*] C. A. F. Silva, L. Manin, R. G. Rinaldi, E. Besnier, M. A. Andrianoely, J. Ameil, D. Remond, Dynamics of Torsional Vibration Damper (TVD) pulley: account for the elastomeric yet dissipative behavior, simulations and experiments (2018).

Chapter 2

FEAD POWER LOSSES MODELING

Contents

2.1 FEAD POWER LOSS MODEL

The energy lost by a functioning FEAD has several origins (Eq. 2.1). Overall, energy can be dissipated by the poly-V belt or by the mechanical components of the system (bearings, tensioners). In the first case, energy is dissipated as heat at the surface of the belt due to friction and sliding between the belt and the pulley groove (external losses, speed losses). However, energy (power) is also dissipated inside the belt due to the hysteretic behavior of the belt constitutive elastomer (internal losses, torque losses).

$$PL_{FEAD} = PL_{hys} + PL_{bear} + PL_{slip} + PL_{vib} \tag{2.1}$$

The power loss model PL_{FEAD} represented by Eq. 2.1 suggests that in a poly-V belt transmission as in Fig. 1.4 energy is dissipated by:

1. Hysteresis PL_{hys}
2. Friction inside the bearings PL_{bear}
3. Slip between the poly-V belt and the pulleys PL_{slip}
4. Vibrations in the belt-spans PL_{vib}

In (1), one part of the energy is dissipated inside of the belt due to the hysteretic behavior of its constitutive elastomer $PL_{belt-hys}$, and another part, dissipated outside of the belt due to the tensioner hysteretic behavior $PL_{tens-hys}$;

In (4), belt-hysteresis power losses are induced by tension fluctuations in the belt free and wrapped spans of the FEAD. Tension fluctuations result from the engine acyclism and the variability of the accessory torques.

The various power loss models (Eq. 2.1) are now discussed throughout this chapter.

2.2 HYSTERESIS LOSSES

The power (loss PL_{hys}) dissipated by hysteresis in a FEAD may be of two types, from the poly-belt and from the tensioner (Eq. 2.2).

$$PL_{hys} = PL_{belt-hys} + PL_{tens-hys} \tag{2.2}$$

Where $PL_{belt-hys}$ is the belt-hysteresis power loss characterized by the belt-elastomer (viscoelastic material [38]), internal friction and $PL_{tens-hys}$ the tensioner-hysteresis power loss due to the dry friction (hysteretic behavior) existing at the tensioner pivot.

2.3 HYSTERESIS POWER LOSSES OF BELTS

Throughout one complete loading and unloading cycle, dynamic loads are periodically applied and removed leading to energy dissipation as illustrated in Fig. 2.1.

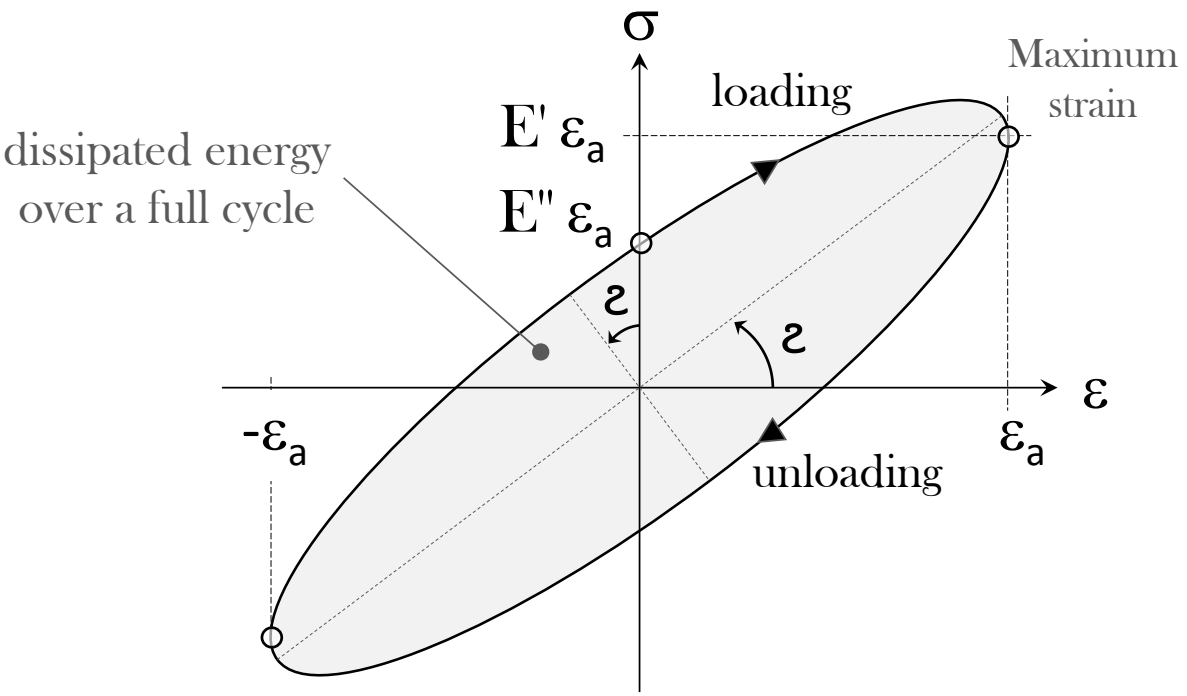

Figure 2.1 – Typical Strain-Stress hysteretic behavior of a linearly viscoelastic material.

From linear viscoelasticy theory [38], the amount of energy dissipated over one full cycle W_h corresponds to $\oint \sigma \cdot d\varepsilon$ (the stored energy being zero) and, according to Gerbert [14] and Eq. 1.14 (See Appendix A1), is equal to:

$$W_h = \pi \cdot E'' \cdot \varepsilon_a^2 \tag{2.3}$$

Where E'' is the loss modulus and ε_a the maximum strain endured during a cycle.

The loss modulus E'' in Eq. 2.3 is the imaginary part of the complex modulus E^* which, for viscoelastic materials (Hooke's law in Eq. 2.4 [38]), mainly depends on the frequency f_{exp}, the temperature θ_{exp} and the strain amplitude ε_{exp} so that Eq. 2.5 is considered.

$$\sigma = E^* \, \varepsilon \tag{2.4}$$

$$E^* = E' + j \cdot E'' = F(\theta_{exp}, f_{exp}, \varepsilon_{exp}) \tag{2.5}$$

Where E' is the storage modulus and the real part of E^*.

Finally, the dissipated energy (power) depends on both the material intrinsic property and the loading state experienced by the belt as it runs along the FEAD path.

Poly-V belt cyclic loading modes

With respect to the belt-hysteresis losses, energy (power) is dissipated inside the belt due to the hysteretic behavior of the belt constitutive elastomer. These losses are generated every time the belt, made of a viscoelastic material [38], e.g. EPDM-PET, is subjected to cyclic loading, i.e. the belt is cyclically bent and stretched on and off the pulleys [14]. The poly-V belt also has its different layers subjected to compression and shear.

(1) Bending In a FEAD, each time that the belt passes by a pulley a piece of it is bent, then unbent. It means that due to the belt transmission geometry and its radii of curvature corresponding to each pulley, bending loads are applied, then removed. This phenomenon is named bending-hysteresis, since by measuring the relationship between the bending-moment and bending-angle during bending loading and unloading cycle, a corresponding hysteresis loop occurs.

(2) Flank and (3) radial compression Every time the poly-V belt passes by a pulley a portion of the belt has its parts compressed and uncompressed cyclically. This compression comes from the contact between the pulley groove and the belt flanks. Moreover, not only the belt-flanks are cyclically compressed and uncompressed by the belt-pulley contact-pressure, but also the other layers of the belt, its middle and its backside. These phenomena are named flank and radial compression hysteresis.

(4) Stretching and (5) shear Along the arc of contact between the belt and the driven pulleys the belt is stretched and sheared proportionally to the resisting torque of each driven pulley, then it is suddenly unstretched and unsheared on the crankshaft pulley, passing from the tight span to the slack span of the belt. The shear loading is due to the torque (power) transmission, the belt and the pulley move at different speeds and there always exists a layer which the belt is sheared and unsheared [14] cyclically. Indeed, when the engine is running, the FEAD path is traveled by the belt, and consequently, a corresponding loading and unloading cycle occurs. The stretch is due to the nature of the materials used for belt manufacturing. In traction belts, polymers (i.e. viscoelastic materials) are often used, which stretch, then unstretch when corresponding loads (torques) are applied, then removed. These phenomena are named stretching and shear hysteresis.

In this chapter, the bending, stretching, shear, flank and radial compression hysteresis power losses have been identified and the associated models are developed thereafter.

These losses, also called torque losses [22], represent in a belt transmission the main causes for internal losses [14].

Method

System definition A power loss model of the FEAD such as in Fig. 1.4 is defined, it describes the belt internal (hysteresis) losses induced by belt bending, stretching, shear, flank and radial compression. Assumptions used in developing this model include:

1. The complex modulus E^* (Eq. 2.5) depends heavily and exclusively on the temperature and the frequency. Indeed, according to experiments the complex modulus E^* of the elastomeric belt does not change much within the realistic range of the strain theoretically experienced by the belt, so its variation as a function of strain is neglected (Appendix $A4$).

2. There exists a neutral axis in the cross section of the poly-V belt and it is located in the center of the tension cord layer.

3. Stretching and shear hysteresis losses are theoretically assumed not to take place on idler or tensioner pulleys, since tensioners are designed to impose no resisting torque (i.e. $\Delta T = 0$ and (or) $\Delta V = 0$ in Eqs. 2.14, 2.40, 2.41 and 2.42).

4. The poly-V belt is considered to be an assembly of two thin flat belts of cross-section area $H_t \cdot B$ and $H_b \cdot B$ in Fig. 2.3, and n (no. of ribs) small V-belts with only belt-flanks/pulley-groove contact (Fig. 2.5).

5. The belt geometry is not substantially changed in response to the *cyclic loading modes*. In this work, the equations are formulated according to linear elasticity because of the characteristics of the belt transmission. It means that in the poly-V belt longitudinal direction there are stiff (high storage modulus) cords which prevent deforming the belt elastomer. In other directions, the belt elastomer (rubber) is also considered to be isotropic and sufficiently stiff to avoid large deformations. Consequently, small and linear deformations are assumed and the belt deformed configuration is not appreciably different from the undeformed configuration.

6. As an initial step in the calculation of internal losses, isolated hysteresis phenomena are considered. It means, different parts (layers) of the poly-V belt are assumed to be independently loaded and unloaded by forces which provide through the law of Hooke corresponding strain amplitudes. These amplitudes are used to calculate the power losses, after this an enhanced analysis is proposed to improve the accuracy of the results.

7. Similar to Newtonian fluids, in the case of shear loading, along the sheared layer a linear relationship between stress and strain rate is assumed (Eq. 2.37).

8. The radial sliding and the associated power losses are assumed here to be much smaller (negligible) than the circumferential sliding and associated power losses. Indeed, when transmitting power, while the motion of the poly-V belt is limited in the radial direction by the surfaces in contact, the sliding in the circumferential (belt longitudinal) direction is not negligible. The circumferential sliding is implicit in the functional role of the poly-V belt and a direct consequence of its design.

The following statements shall be considered throughout this work.

1. The energy loss equation 2.3 describes the energy loss associated with a cycle where the strain magnitude ε_a varies from strain $-\varepsilon_a$ (compression) to $+\varepsilon_a$ (traction). Nevertheless, the belt loading state differs from this conventional description. For instance, when the belt is lying inside (with its ribs inside the pulley groove.), in the belt backside, the strain varies from the null value of strain, at its neutral axis, to a positive value of strain $+\varepsilon_a$ (traction), at its backside surface. Thus, if the classical traction-compression strain range in Fig. 2.1 from $-\varepsilon_a$ to $+\varepsilon_a$ would be changed to an null-traction (or compression) interval i.e. $[0 \ \ +\varepsilon_a]$, the strain magnitude used to calculate the energy lost has also to be changed to $\frac{+\varepsilon_a}{2}$. Thus, in the energy loss equation, the $\frac{1}{4}$ factor appears leading to Eq. 2.6.

$$W_h = \frac{1}{4} \cdot \pi \cdot E'' \cdot \varepsilon_a^2 \tag{2.6}$$

2. When calculating the hysteresis losses the sliding ϕ_s and adhesion ϕ_a angles are needed. According to Gerbert [14] and based on the assumption that there is no belt-pulley radial sliding, the capstan equation from [37] can be applied to calculate the magnitude of the sliding angle ϕ_s of each pulley of the belt transmission as in Eq. 2.7 (centrifugal action T_c included).

$$T_t = T_s \ e^{\mu_g \ \phi_s} \quad \rightarrow \quad \phi_s = \frac{1}{\mu_g} \ \ln\left(\frac{T_t - T_c}{T_s - T_c}\right) \tag{2.7}$$

   Once the sliding angle ϕ_s is found using the capstan equation, then the adhesion angle ϕ_a comes from the relation $\phi_a = \phi - \phi_s$, since due to the geometry of the system the belt-pulley wrap angle ϕ is a priori known.

The various loading modes and their hysteresis-energy-loss equation are now developed in the next paragraphs.

2.3.1 Bending losses

Bending is the deformation mode that results from the belt bending on the pulleys [14]. The loading and unloading cycle in Fig. 2.2 amounts to a typical hysteresis loop as in Fig. 2.1 which represents a power loss. This power loss only depends on the FEAD geometry (layout) and the belt loss modulus, it does not depend on the belt tension T, and therefore, on the torque (power) transmitted.

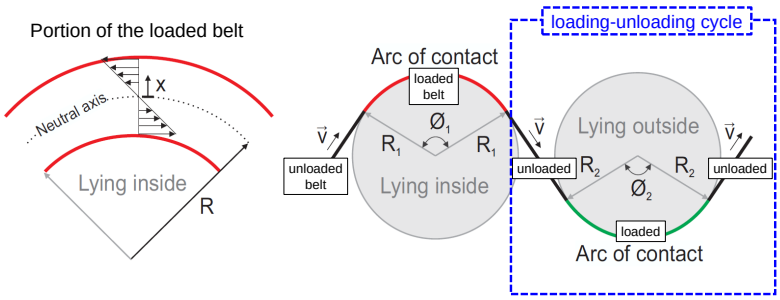

Figure 2.2 – Bending theoretical aspects when a belt is running on pulleys.

The bending strain value $\varepsilon_{a_{bend}}$ equivalent to that in Eq. 2.6 is calculated from the beam bending theory, and depends on the through-thickness distance from the neutral axis x and the curvature $1/R$:

$$\varepsilon_{a_{bend}} = \frac{x}{R} \tag{2.8}$$

For a rectangular belt section made of homogeneous isotropic material, e.g. flat belts, the neutral axis is at mid-thickness as schemed in Fig. 2.2. In poly-V belts, determining the value of x in Eq. 2.8 requires an accurate description of its cross section (Fig. 2.3).

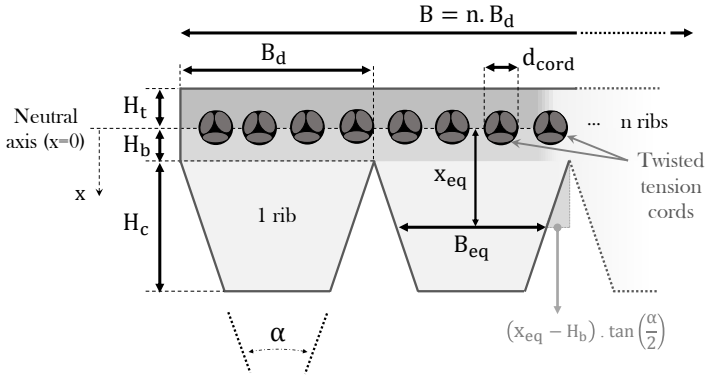

Figure 2.3 – Belt cross section: location of the neutral axis and key geometric parameters.

The neutral axis can be assimilated to the center of the tension cord layer (Appendix *A*3) so that the maximum bending strain value $\varepsilon_{a_{bend}^{max}}$ is given by Eq. 2.9.

$$\varepsilon_{a_{bend}^{max}} = \frac{H_b + H_c}{R} \tag{2.9}$$

Where H_b and H_c are the thicknesses (heights) of the belt middle and rib layers (Fig. 2.3).

Equation 2.6 suggests that the belt loss modulus E'' has to be evaluated for any given strain value ε_a. Since three layers of different elastomers compose the belt under study, the energy losses due to bending hysteresis can be decomposed as follows (Eq. 2.10):

$$\begin{aligned} W_{h_{bend}} &= \frac{1}{4} \cdot \int_0^{H_t} \pi \cdot E''_{Ht} \cdot (\varepsilon_{a_{bend}})^2 \cdot B \cdot dx \\ &+ \frac{1}{4} \cdot \int_0^{H_b} \pi \cdot E''_{Hb} \cdot (\varepsilon_{a_{bend}})^2 \cdot B \cdot dx \\ &+ \frac{1}{4} \cdot \int_{H_b}^{H_b+H_c} \pi \cdot E''_{Hc} \cdot (\varepsilon_{a_{bend}})^2 \cdot B_{eq} \cdot dx \end{aligned} \tag{2.10}$$

With

$$B_{eq} = B - 2 \cdot (x - H_b) \cdot \tan\left(\frac{\alpha}{2}\right) \cdot n \tag{2.11}$$

Where B is the belt width, H the thicknesses of the belt layer, α the rib wedge angle, n the number of ribs (Fig. 2.3) and $W_{h_{bend}}$ the bending energy loss per belt unit length.

In the poly-V belt ribs layer (H_c in Fig. 2.3), the equivalent belt width B_{eq} (Eq. 2.11) is also considered when calculating losses, because of the empty spaces between the ribs. Empty areas do not contribute to any hysteresis energy loss W_h.

Naturally, the integral terms in Eq. 2.10 must be calculated over the entire FEAD path, since each pulley i of radius R_i leads to a different bending strain value $\varepsilon_{a_{bend_i}}$ (Eq. 2.8).

2.3.2 Stretching losses

In poly-V belt transmissions, the belt made of polymers, generally EPDM-PET, stretches since it is subjected to varying tension as it runs on a pulley (Fig. 2.4). Accordingly, stretching hysteresis energy (power) losses only take place on pulleys transmitting power with $\Delta T = T_t - T_s \neq 0$ (Eq. 2.14).

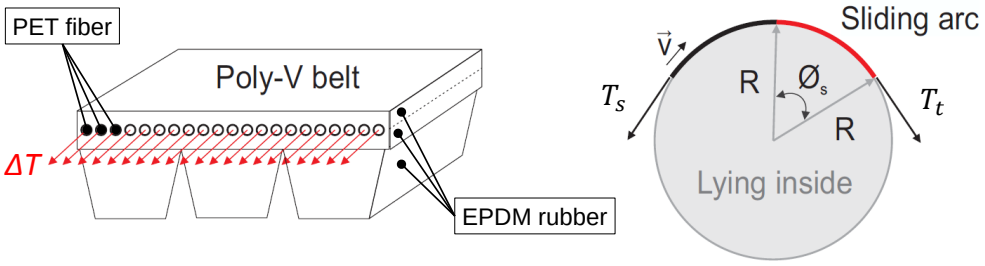

Figure 2.4 – Stretching theoretical aspect when a belt is running on pulleys.

The equation of the stretching hysteresis energy lost per belt unit length:

$$W_{h_{st}} = \frac{1}{4} \cdot \pi \cdot E''_{Belt} \cdot \varepsilon^2_{a_{st}} \cdot A \tag{2.12}$$

Where E''_{Belt} is the belt loss modulus which is from the entire belt tested in traction and compression via DMA, A the belt cross-sectional area and $\varepsilon_{a_{st}}$ the stretching-hysteresis strain which can be calculated from the Hooke's law:

$$\varepsilon_{a_{st}} = \frac{\Delta T}{c} = \frac{T_t - T_s}{\sum E'_k \cdot A_k} \tag{2.13}$$

Where ΔT is the effective pull transmitted between the pulleys via the free spans of the belt, and c the longitudinal stiffness. Indeed, ΔT corresponds to the difference between the belt span, T_t (tight) and T_s (slack), tensions around a pulley, c corresponds to the axial belt tensile modulus of each belt constituent k [14].

For a Voigt composite (Meaud [39]) such as the poly-V belt, k can be the top, the cords, the middle and the ribs layer leading to

$$\varepsilon_{a_{st}} = \frac{T_t - T_s}{(E'_{Ht} \cdot A_{Ht} + E'_{cord} \cdot A_{cord} + E'_{Hb} \cdot (A_{Hb} - A_{cord}/2) + E'_{Hc} \cdot (A_{Hc} - A_{cord}/2))} \tag{2.14}$$

Where E'_{Ht} and E'_{Hb} are appropriate storage moduli of the belt material for the top and middle layer, respectively. E'_{cord} is the storage modulus of the belt tension cords, E'_{Hc} the storage modulus of the belt material for the rib layer and A the belt cross-sectional area which is the sum of the belt cross-sectional areas of each layer, i.e. A_{Ht}, A_{Hb} and A_{Hc} (Eq. 2.17).

In the previous paragraph the term "appropriate" is used to designate the storage E'_H modulus, because here, we have to consider that the belt top and middle layers are thin and wide so plain strain conditions prevail rather than plain stress [14]. This implies that the classical storage modulus divided by $(1-\nu^2)$ is appropriate leading to Eq. 2.15.

$$E'_H = \frac{E'}{(1-\nu^2)} \tag{2.15}$$

In the same way, for the top and middle layer appropriate loss moduli E''_H:

$$E''_H = \frac{E''}{(1-\nu^2)} \tag{2.16}$$

Where E' and E'' are, respectively, the classical storage and loss moduli from the belt elastomer characterization (H_b or H_t layer samples) and ν the Poisson ratio.

Next, the belt cross-sectional areas used in Eq. 2.14 are given:

$$\begin{aligned} A_{Ht} &= B \cdot H_t \\ A_{cord} &\approx 2.8 \cdot n \cdot \frac{\pi \cdot (d_{cord})^2}{4} \\ A_{Hb} &= B \cdot H_b \\ A_{Hc} &= n \cdot \left[B_d - H_c \cdot \tan\left(\frac{\alpha}{2}\right) \right] \cdot H_c \\ A &= A_{Ht} + A_{Hb} + A_{Hc} \end{aligned} \tag{2.17}$$

Where B is the belt width, B_d the rib width, α the wedge angle, n the number of ribs, d_{cord} the diameter of a set of 3 twisted tension cords (Fig. 2.3) and H_t, H_b and H_c the thickness of the belt top, middle and ribs layer, respectively. Moreover, the cross-sectional area A_{cord} is approximated as $2.8 \cdot n$ multiplied by the area of a set of 3 twisted tension cords of diameter d_{cord}, because in practice there are around 2.8 twisted tension cords per rib. This can be observed in poly-V belts of profile PK (Fig. 1.8).

Finally, since in a FEAD as in Fig. 1.4 the poly-V belt is unloaded along the FEAD path due to resisting torques and loaded by the crankshaft, a stretching hysteresis loop occurs. Hence, the Eq. 2.12 must be applied to the crankshaft pulley.

2.3.3 Flank compression losses

Every time the poly-V belt passes by a pulley, its flanks are in contact with the pulley grooves. So, on the pulley due to the contact pressure P_c (Fig. 2.5, left), the belt-length $R \cdot \phi$ (Fig. 2.5, right) which was unloaded (no contact) along the belt span prior to the pulley, becomes loaded (compressed). After this, it will again be unloaded when entering the next belt-span. The compression state of the poly-V belt flanks is depicted in Fig.2.5.

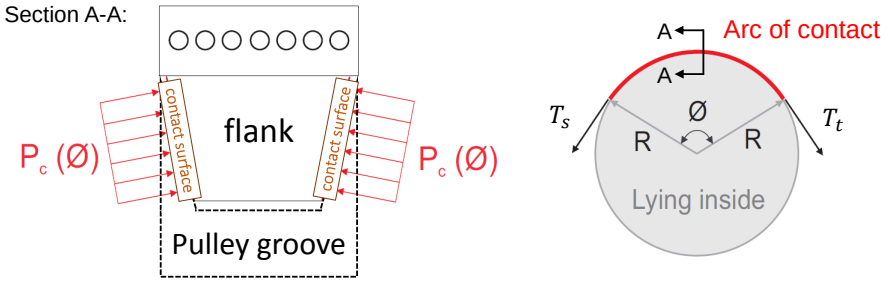

Figure 2.5 – Flank compression aspect along ϕ when a belt is running on pulleys.

The energy loss equation per belt unit length is given by Eq. 2.18.

$$W_{h_{fc}} = \frac{1}{4} \cdot \pi \cdot E''_{Hc} \cdot \varepsilon^2_{a_{fc}} \cdot n \cdot A_{1V} \tag{2.18}$$

Where E''_{Hc} is the loss modulus of the rib elastomeric material, n the number of ribs, A_{1V} the cross section area of one V (rib) (Eq. 2.19), and $\varepsilon_{a_{fc}}$ the flank compression strain value which can be calculated from Hooke's law (Eq. 2.20).

$$A_{1V} = \left[B_d - H_c \cdot \tan\left(\frac{\alpha}{2}\right)\right] \cdot H_c \tag{2.19}$$

$$\varepsilon_{a_{fc}} = \frac{P_z}{E'_{Hc}} \tag{2.20}$$

Where B_d, H_c and α are the geometric parameters as in Fig. 2.3, E'_{Hc} represents the storage modulus of the belt rib material (rubber), P_z is the horizontal component of the contact pressure P_c (Eq. 2.21).

$$P_z = P_c \cdot \cos\left(\frac{\alpha}{2}\right) \tag{2.21}$$

The flank compression corresponding forces are represented in Fig. 2.6.

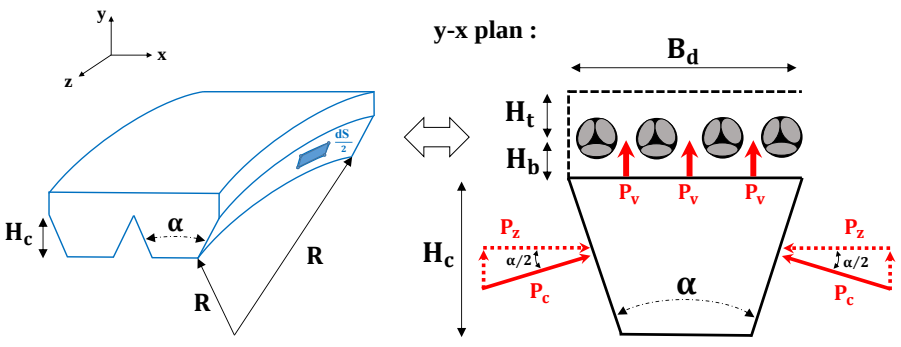

Figure 2.6 – V rib belt profile with P_z and P_c pressures.

The belt span tension profile on pulleys (Fig. 2.7) implies that the contact pressure P_c either is constant or depends on the arc of contact ϕ [14].

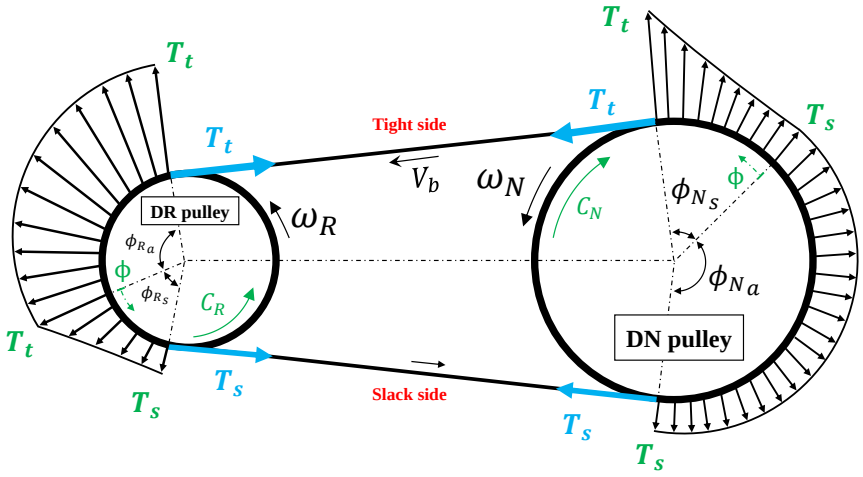

Figure 2.7 – Poly-V belt span tension profile.

On the driver (DR) pulley, in the sliding arc ϕ_{RS} (Fig. 2.7), the contact pressure $P_c(\phi)$ can be calculated using Eq. 2.22 (Appendix $A2$).

$$P_c(\phi) = \frac{(T_t - T_c) \cdot e^{-\mu_g \cdot \phi}}{2 \cdot n \cdot H_c \cdot R \cdot \tan\left(\frac{\alpha}{2}\right)} \tag{2.22}$$

Similarly, for a driven (DN) pulley, in the sliding arc ϕ_{NS} (Eq. 2.23) (Appendix $A2$).

$$P_c(\phi) = \frac{(T_s - T_c) \cdot e^{+\mu_g \cdot \phi}}{2 \cdot n \cdot H_c \cdot R \cdot \tan\left(\frac{\alpha}{2}\right)} \tag{2.23}$$

Where n, H_c, R, α are the geometrical parameters as in Fig. 2.3, ϕ the belt-pulley wrap angle as in Fig. 2.7 and the belt span tensions T_t, T_s, the $T_c = \rho_b V_b^2$ is the centrifugal action arising from the belt's inertia and μ_g the belt-pulley global friction coefficient.

2.3.4 Radial compression losses

Every time the poly-V belt passes by a pulley, also due to the pressure generated from the contact between the belt and the pulley, similarly to the flank compression cyclic loading, the belt middle and top layer are cyclically compressed. The radial compression of these layers is depicted in Fig. 2.8.

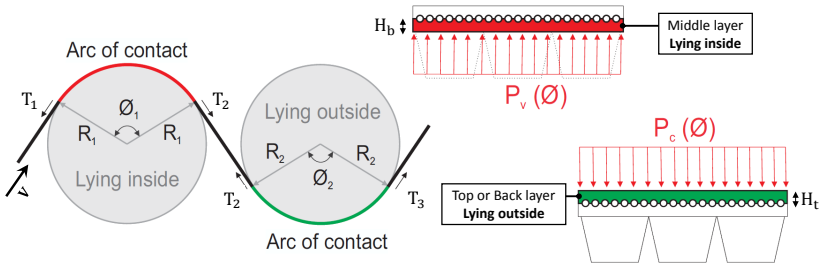

Figure 2.8 – Radial compression aspect when a belt is lying inside and outside pulleys.

In the case of radial compression hysteresis, there are two possibilities:

A **- Belt lying inside** (with its middle-layer under cyclic compression loading):

The energy loss equation per belt unit length is given by Eq. 2.24.

$$W_{h_{rc}} = \frac{1}{4} \cdot \pi \cdot E''_{Hb} \cdot \varepsilon^2_{a_{rc}} \cdot A_{Hb} \tag{2.24}$$

Where E''_{Hb} is the appropriate loss modulus for the belt middle material, A_{Hb} the belt middle-layer cross section area (Eq.2.25), and $\varepsilon_{a_{rc}}$ the radial compression strain (Eq.2.26).

$$A_{Hb} = B \cdot H_b \tag{2.25}$$

$$\varepsilon_{a_{rc}} = \frac{P_v}{E'_{Hb}} \tag{2.26}$$

Where B is the belt width and H_b the thickness of the belt middle layer (Fig.2.3), E'_{Hb} the appropriate storage modulus from the belt middle material and P_v a pressure generated by the pressure P_c (Eqs. 2.22 or 2.23). Indeed, P_v is the pressure responsible for cyclically compressing and decompressing the belt elastomer causing the loss of energy by radial compression hysteresis, and it is given by:

$$P_v = \frac{2 \cdot P_c \cdot H_c \cdot \tan\left(\frac{\alpha}{2}\right)}{B_d} \tag{2.27}$$

Where, H_c, B_d and α are the geometric parameters of the belt (Fig. 2.3) and P_c the contact pressure (Eq. 2.22 or 2.23).

B **- Belt lying outside** (with its top-layer under cyclic compression loading):

The energy loss equation per belt unit length is given by Eq. 2.28.

$$W_{h_{rc}} = \frac{1}{4} \cdot \pi \cdot E''_{Ht} \cdot \varepsilon^2_{a_{rc}} \cdot A_{Ht} \tag{2.28}$$

Where E''_{Ht} is the appropriate loss modulus for the belt top material, A_{Ht} the belt top-layer cross section area (Eq.2.29) and $\varepsilon_{a_{rc}}$ the radial compression strain value (Eq.2.28).

$$A_{Hb} = B \cdot H_t \tag{2.29}$$

$$\varepsilon_{a_{rc}} = \frac{P_v}{E'_{Ht}} \tag{2.30}$$

Where B is the belt width and H_t the thickness of the belt top layer (Fig.2.3), E'_{Ht} the appropriate storage modulus for the belt top material and P_v the belt-pulley contact pressure as in flat belts. Here, P_v is given by:

$$P_v = \frac{T - T_c}{R \cdot B} \tag{2.31}$$

Where T is the belt span tension, T_c the centrifugal action, R is the pulley pitch radius and B the belt width.

Remarks about flank and radial compression losses

The equations representing the contact pressure P_c (Eqs. 2.22 and 2.23) can be demonstrated considering an infinitesimal poly-V belt element and the sum of the contact, the centrifugal and the frictional forces in the belt sliding direction (Fig. 2.6). In addition, the differences between the equations 2.22 and 2.23 come from the boundary conditions related to driver and driven pulleys, respectively.

The constant pressures P_c acting in the adhesion arcs ϕ_a of both driven and driver pulleys are obtained when $\phi = 0$ in Eqs. 2.22 and 2.23, respectively. Also, Eqs. 2.22 and 2.23 are valid for ϕ varying from 0 to ϕ_s as shown in Fig. 2.7.

The equation 2.27 can be demonstrated considering the free body diagram and the sum of forces in the radial direction of the belt (Fig. 2.6).

Normally in FEADs, when the belt is lying outside, it is in contact with an idler or a tensioner pulley with no resisting torque. Therefore, no sliding arc exists and the belt tension T in Eq. 2.31 is constant and equal to T_t and T_s, since in the vicinity of an idler pulley the belt span tension ideally does not change.

In equations 2.18 and 2.24 (or 2.28) the energy loss by flank and radial compression $W_{h_{fc}}$ and $W_{h_{rc}}$ depend on the pulley wrap angle ϕ. Indeed, $W_{h_{fc}}$ and $W_{h_{rc}}$ depend on ϕ, because the loss modulus E'' depends on the frequency which the belt elastomer is stressed in compression (Eq. 2.5). This frequency is defined as the belt linear velocity V divided by the belt contact arc length $R \cdot \phi$. Also, to accurately predict the flank and radial hysteresis losses (i.e. consider along the belt-pulley arc-of-contact the correct strain, and therefore, to take into consideration the correct hysteresis loop as in Fig. 2.1) the strain $\varepsilon_{a_{fc}}$ and $\varepsilon_{a_{rc}}$ shall be calculated considering the maximum contact-pressure P_c. This pressure depends on the belt span tensions around the pulley, T_t and T_s. The maximum contact pressures P_c are obtained for driver and driven pulleys when $\phi = 0$ and $\phi = \phi_s$ in Eqs. 2.22 and 2.23, respectively.

Finally, Eqs. 2.18 and 2.24 (or 2.28) must be calculated over the entire belt transmission, since every time the belt passes by a pulley along the FEAD path, a loading and unloading cycle or a hysteresis loop occurs. Indeed, the belt is loaded from a null strain (no contact along the belt free span) to the compression strains 2.20 and 2.26 (or 2.30) on the pulleys and vice versa.

2.3.5 Shear losses

When the belt is running and subjected to resisting torques there is always a sheared belt layer [14] H_{sh} from the belt tension cords to the contact surface of the pulley (Fig. 2.9).

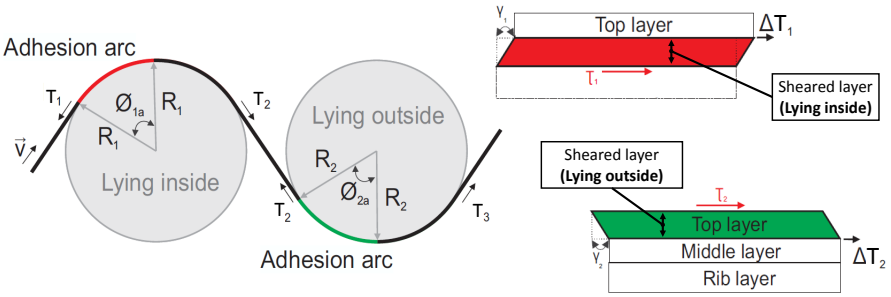

Figure 2.9 – Sheared belt layer theoretical aspect.

The sheared layer H_{sh} depends on the belt side in contact with the pulley. For the belt lying inside, H_{sh} in Fig. 2.10 can be calculated by Eq. 2.32.

$$H_{sh} = H_b + H_c^* \tag{2.32}$$

With

$$H_c^* = \frac{H_c^2 \cdot \tan\left(\frac{\alpha}{2}\right)}{B_d} \tag{2.33}$$

Where H_b, H_c, B_d, α are the geometrical parameters as in Fig. 2.3 and 2.10 and H_c^* the hypothetical sheared-layer thickness obtained by doing the equivalence between the areas $A1$ and $A2$ in Fig. 2.10.

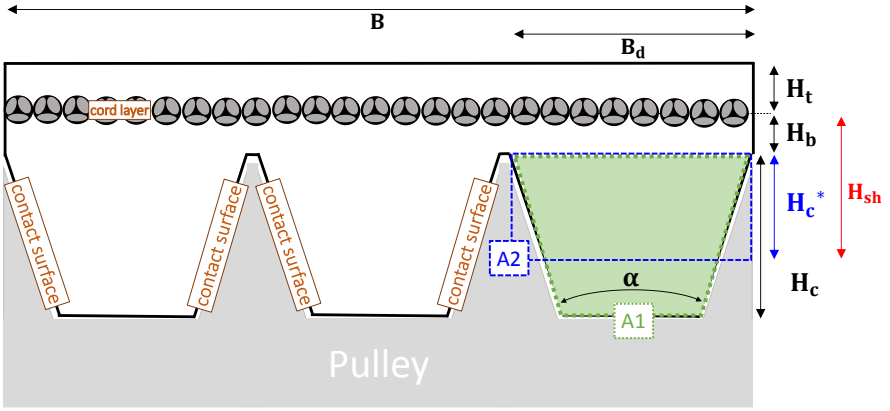

Figure 2.10 – Hypothetical poly-V belts sheared layer H_{sh}.

The (shear-hysteresis) energy loss equation per belt unit length is given by Eq. 2.34.

$$W_{h_{sh}} = \frac{1}{4} \cdot \pi \cdot G'' \cdot \gamma_{a_{sh}}^2 \cdot A_{sh} \tag{2.34}$$

Where A_{sh} is the cross-sectional area subjected to shear loading (Eq. 2.35) $\gamma_{a_{sh}}$ the shear angle (Eq. 2.38) and G'' the shear loss modulus of the belt rib and middle layers material, these are very often the same, and if the material is considered homogeneous and isotropic the relation 2.36 is valid.

$$A_{sh} = (H_b + H_c^*) \cdot B \tag{2.35}$$

$$G'' = \frac{E''}{2 \cdot (1 + \nu)} \tag{2.36}$$

Where H_b is the middle layer thickness, H_c^* the hypothetical rib sheared-layer thickness, B the belt width, ν the Poisson ratio and E'' the traction and compression loss modulus obtained via DMA.

To calculate the shear angle $\gamma_{a_{sh}}$ for equation 2.34, the Hooke's law can be applied, enabling the calculation of the shear stress τ_{sh} (Eq. 2.37).

$$\tau_{sh} = G' \cdot \gamma_{a_{sh}} \tag{2.37}$$

Where G' is the shear storage modulus and τ_{sh} the shear stress, which in FEADs, cyclically occurs and causes the loss of energy by hysteresis.

In parallel, if $\gamma_{a_{sh}}$ is considered to be small and constant the Eq. 2.38 can be obtained from Fig. 2.11.

$$\gamma_{a_{sh}} = \tan(\gamma_{a_{sh}}) = \frac{\varpi}{H_{sh}} \quad \rightarrow \quad \varpi = H_{sh} \cdot \gamma_{a_{sh}} \tag{2.38}$$

Where ϖ is the shear deflection, and according to Gerbert [14] this elongation of the cord have to take two cases into consideration (Fig. 2.12).

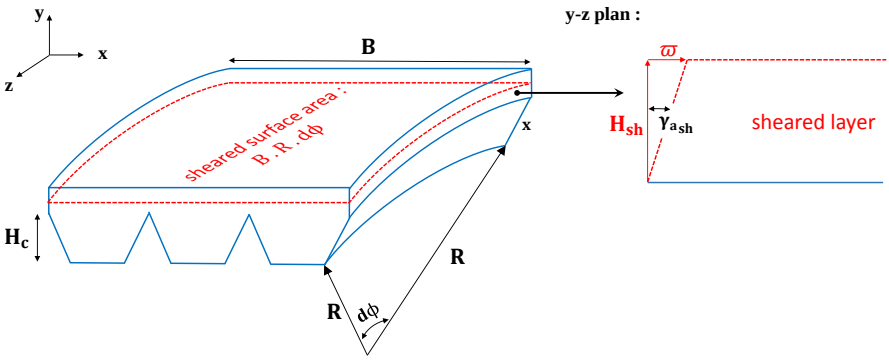

Figure 2.11 – Shear surface area and deflection of a small poly-V belt element.

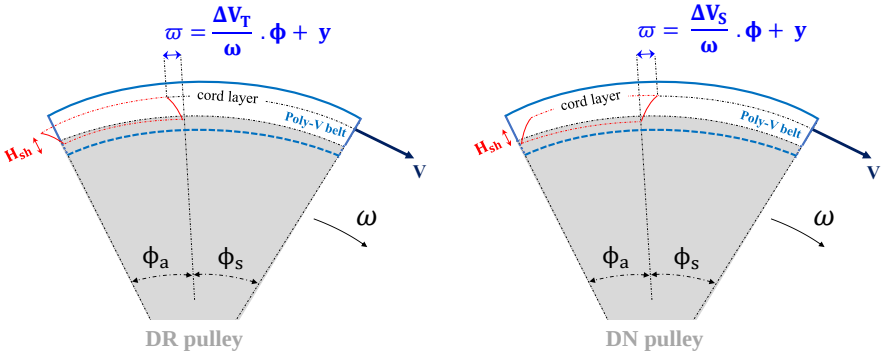

The pulley runs faster than the belt:

$$\Delta V_T = R.\omega - V$$

The belt runs faster than the pulley:

$$\Delta V_S = V - R.\omega$$

Figure 2.12 – Shear deflection at driver and driven pulleys.

The shear stress τ_{sh} can be found by back substitution into Eqs. 2.37, 2.38, and taking into account the shear deflection ϖ in Fig. 2.12 for driven pulleys (Eq. 2.39).

$$\tau_{sh} = G' \frac{\varpi}{H_{sh}} = \frac{G'}{H_{sh}} \cdot \left(\frac{\Delta V_S}{\omega} \cdot \phi + y \right) \tag{2.39}$$

Where ω is the pulley angular velocity, ϕ the wrap angle at the contact point considered, ΔV_S the relative velocity which moves the poly-V belt cord layer, and y the sum of increments $(\varepsilon - \varepsilon_s) \cdot R \cdot d\phi$ along ϕ represented by Eq.2.40.

$$y \;=\; \int_0^{\phi_a} (\varepsilon - \varepsilon_s) \cdot R \cdot d\phi \;=\; \int_0^{\phi_a} \frac{T(\phi) - T_s}{c} \cdot R \cdot d\phi \tag{2.40}$$

Where ε_s is the belt tensile strain at the belt-pulley seating point, T the belt span tension and c the strain stiffness along the belt as in stretching losses (Eq. 2.13).

Thus, the shear deflection τ_{sh} in Eq.2.39 for a driven pulley is expressed by Eq. 2.41.

$$\tau_{sh} \;=\; \frac{G'}{H_{sh}} \cdot \left(\frac{\Delta V_S}{\omega} \cdot \phi + \int_0^{\phi_a} \frac{T(\phi) - T_s}{c} \cdot R \cdot d\phi \right) \tag{2.41}$$

Similarly, for a driver pulley one gets:

$$\tau_{sh} \;=\; \frac{G'}{H_{sh}} \cdot \left(\frac{\Delta V_T}{\omega} \cdot \phi + \int_0^{\phi_a} \frac{T_t - T(\phi)}{c} \cdot R \cdot d\phi \right) \tag{2.42}$$

By introducing the following non-dimensional notation:

$$G_*^2 = \frac{G' \cdot B \cdot R^2}{H_{sh} \cdot c} \tag{2.43}$$

Considering an increase in tension dT over a small poly-V belt element $R \cdot d\phi$:

$$dT = \tau_{sh} \cdot B \cdot R \cdot d\phi \tag{2.44}$$

Where B is the belt width and τ_{sh} the shear stress. The terms 2.43 and 2.44 together with the shear deflection ϖ for driven pulleys:

$$\varpi = \frac{\Delta V_S}{\omega} \cdot \phi + y \tag{2.45}$$

Then, from equations 2.37, 2.38, 2.44, 2.45 and after differentiation to eliminate integral terms the following differential equation is valid for a driven pulley.

$$\frac{\mathrm{d}^2 T}{\mathrm{d}\phi^2} - G_*^2 \cdot T = G_*^2 \left(\frac{c \cdot \Delta V_S}{V} - T_s \right) \tag{2.46}$$

Where c is the strain stiffness, as before, and V the belt linear velocity.

Next, if the equation 2.46 is solved using appropriate Boundary Conditions (BCs), i.e., no shear at the beginning of the adhesive arc ϕ_a ($\gamma = \tau = \frac{\mathrm{d}T}{\mathrm{d}\phi} = 0$) and where the belt seats on the pulley, at $\phi = 0$, the belt span tension $T = T_s$.

Thus, the analytic solution of the equation 2.46 for a driven pulley is given by Eq.2.47.

$$T(\phi) = \frac{c \cdot \Delta V_S}{V} \cdot (\cosh(G_* \cdot \phi) - 1) + T_s \tag{2.47}$$

Similar analysis (equivalent Eq. 2.46 and BCs) can be made and the following equation demonstrated for a driver pulley is given by Eq. 2.48.

$$T(\phi) = -\frac{c \cdot \Delta V_T}{V} \cdot (\cosh(G_* \cdot \phi) - 1) + T_t \tag{2.48}$$

In addition, Tab. 2.1 with equations from the shear theory of Gerbert [14] can be useful to get the values of ΔV_S and ΔV_T for equations 2.47 and 2.48.

Finally, with $T(\phi)$ provided by 2.47 and 2.48 the Eqs. 2.41 and 2.42 can be supplied, then integrated, and by back substitution the energy lost by shear hysteresis can be calculated by Eq. 2.34.

Table 2.1 – Useful physical quantities from the shear theory of Gerbert [14].

	DriveN	**DriveR**
Tension ratio over the adhesion arc	$K_a = \frac{1}{1-\frac{\mu}{G_*}\cdot\frac{\cosh(G_*\cdot\phi_a)-1}{\sinh(G_*\cdot\phi_a)}}$	$K_a = 1 + \frac{\mu}{G_*}\cdot\frac{\cosh(G_*\cdot\phi_a)-1}{\sinh(G_*\cdot\phi_a)}$
Relative velocity at the beginning of adhesion arc	$\Delta V_{*A} = \frac{K_a-1}{\cosh(G_*\cdot\phi_a)-1}$	$\Delta V_{*A} = \frac{K_a-1}{K_a\cdot[\cosh(G_*\cdot\phi_a)-1]}$
Relative velocity which moves the cord layer	$\Delta V_S = \frac{T_s\cdot V}{c}\cdot\Delta V_{*A}$	$\Delta V_T = \frac{T_t\cdot V}{c}\cdot\Delta V_{*A}$

Remarks about shear losses

According to Gerbert [14], there is always a sheared layer H_{sh}, because the surface of the pulley and the belt tension member do not necessarily travel with the same velocity. As a result, in a belt transmission as in Fig. 1.4, shear stresses are at once generated by the crankshaft and gradually removed by the driven pulleys. This is a cyclic shear-stress-generation process since the engine is running and the belt is traveling the FEAD path. Along this path, from the crankshaft belt tight to slack span (anticlockwise direction), the belt is unloaded by the driven pulleys, then loaded by the crankshaft, which means that a hysteresis loop occurs. Thus, Eq. 2.34 must only be applied to the crankshaft pulley, where the loading and unloading cycle is completed.

The relation 2.36 between the shear and the loss can also be applied to calculate the storage shear modulus G' for Eq. 2.37.

In the case of the belt lying outside and subjected to a resisting torque the shear hysteresis model is similar to that we have just described, except the sheared layer H_{sh} (Eq. 2.32). In this case, H_{sh} is equal to H_t leading to $A_{sh} = H_t \cdot B$ in Eq. 2.35.

Summary of hysteresis phenomena

In Tabs. 2.2 and 2.3, the belt-hysteresis power loss phenomena are summarized.

Table 2.2 – Belt-hysteresis cyclic loading modes (location and nature).

Cyclic loading mode		**Where it occurs**		**Dynamic cyclic strain ε_a**	
	subscript	along the	length	model	nature
Bending	bend	arc of contact	$R\,\phi_i$	beam theory	bending
Stretching	st	FEAD path	L	Hooke's law	traction-comp
Flank comp	fc	arc of contact	$R\,\phi_i$	Hooke's law	traction-comp
Radial comp	rc	arc of contact	$R\,\phi_i$	Hooke's law	traction-comp
Shear	sh	FEAD path	L	Hooke's law	shear

Table 2.3 – Belt-hysteresis cyclic loading modes (frequency, model and dependency).

Cyclic loading mode		(un) Loading **frequency**	**Hysteresis energy loss W_h equations**	**Moduli dependency** as a function of
	subscript			
Bending	bend	$\Omega_{i_{bend}} = \frac{V}{R\,\phi_i}$	$W_{h_{bend}} = \int_0^H \pi\, E''\, (\varepsilon_{a_{bend}})^2\, B\, dx$	$F(\theta_{exp}, \Omega_{i_{bend}}, \varepsilon_{a_{bend}})$
Stretching	st	$\Omega_{i_{st}} = \frac{V}{L}$	$W_{h_{st}} = \pi\, E''\, \varepsilon_{a_{st}}{}^2\, A$	$F(\theta_{exp}, \Omega_{i_{st}}, \varepsilon_{a_{st}})$
Flank comp	fc	$\Omega_{i_{fc}} = \frac{V}{R\,\phi_i}$	$W_{h_{fc}} = \pi\, E''\, \varepsilon_{a_{fc}}{}^2\, n\, A_{1V}$	$F(\theta_{exp}, \Omega_{i_{fc}}, \varepsilon_{a_{fc}})$
Radial comp	rc	$\Omega_{i_{rc}} = \frac{V}{R\,\phi_i}$	$W_{h_{rc}} = \pi\, E''\, \varepsilon_{a_{rc}}{}^2\, A_{H_b\,(\text{or}\,H_t)}$	$F(\theta_{exp}, \Omega_{i_{rc}}, \varepsilon_{a_{rc}})$
Shear	sh	$\Omega_{i_{sh}} = \frac{V}{L}$	$W_{h_{sh}} = \pi\, G''\, \gamma_{a_{sh}}{}^2\, A_{sh}$	$F(\theta_{exp}, \Omega_{i_{sh}}, \gamma_{a_{sh}})$

Indeed, some insights into hysteresis phenomena are provided:

- The FEAD location along which the hysteresis losses occur;
- The frequency with which the hysteresis losses occur;
- The general energy-loss equation 2.3 applied to each phenomena;
- The energy-loss-equation loss modulus dependency for each phenomena;
- The models used to calculate the strain in the energy-loss equations;
- The nature of each poly-V belt cyclic loading mode.

In the above tables, the frequency equations represent the inverse of the time for which in a belt transmission as in Fig. 1.4, a belt element of length l or $R \cdot \phi_i$ and velocity V needs to complete a loading-unloading cycle corresponding to a hysteresis loop as in Fig. 2.1. These frequencies, which are used to predict the power loss, need to be in the frequency range within which the data on belt material properties are generally obtained via DMA. Moreover, the dependencies of the belt loss moduli on temperature (θ), frequency (Ω) and strain (ε) are highlighted to the corresponding hysteresis loading modes, since these moduli, and therefore, the losses of energy are strongly influenced by the temperature. Also, the loading frequency and dynamic strain influence on the moduli and on the losses of energy by hysteresis [14]. In practice, the temperature θ equals to the temperature in the engine room θ_{exp}. With respect to strains, the belt loss modulus' dependency on strain is neglected as in Appendix $A4$ (Payne effect). In the following sections, a method which uses the equivalency between temperature and loading frequency is also described to obtain the master curves [40].

2.3.6 Total belt hysteresis losses

Once all the energy losses per belt unit length equations W_h have been established, i.e. Eqs. 2.10, 2.12, 2.18, 2.24 (or 2.28) and 2.34, the hysteresis power loss due to bending, stretching, shear, flank and radial compression phenomena can be determined according to Eq. 2.49.

$$PL_{belt-hys} = W_h \cdot V \tag{2.49}$$

Where $PL_{belt-hys}$ is the belt-hysteresis power loss (Eq. 2.1) and V the belt linear velocity.

2.3.7 Results

Dynamic Mechanical Analysis

Correlation and Purpose

Dynamic Mechanical Analysis (DMA) is an experimental technique used to study and characterize materials. This technique is employed because it is most useful for studying the viscoelastic behavior of polymers. DMA is a technique where an equivalent strain is applied to the belt sample in a cyclic manner allowing one to determine the complex modulus E^* (Eq. 2.5). Moreover, the temperature of the sample or the frequency of loading are often varied, leading to variations in the complex modulus. The main purpose of DMA is to provide data on material properties to predict the belt hysteresis power losses as in Eq. 2.49. Indeed, in the modeling of the hysteresis losses, several equations depend directly or indirectly on the belt material properties: belt elastomers and cord (storage and loss) moduli. As these properties are rarely or not at all provided by belt manufacturers, the solution is to perform tests to provide basic data.

Method and Materials

The viscoelastic behavior of the belt constituents have been investigated. During tests, the independent variables that can be varied are the temperature, the loading frequency and the test strain. The dependent measured variable is the complex modulus of the tested material as in Eq. 2.5.

Indeed, the cause-and-effect relationship are studied, where:

- The engine operating conditions are chosen to be the independent variables (i.e. temperature, frequency, strain). The testing temperature equals to the temperature in the engine room, the loading frequency is compatible with Tab. 2.3 and the strain is compatible with Eqs. 2.8, 2.14, 2.20, 2.26 (or 2.30) and 2.38.
- The belt-hysteresis loss depends on the dependent variables (complex-modulus). The belt loss modulus acts directly on the hysteresis loss Eqs. 2.10, 2.12, 2.18, 2.24 (or 2.28) and 2.34 and the belt storage modulus influences on the cyclic loading modes strain (Hooke's law), except to bending-hysteresis.

The prediction of the belt hysteresis power loss, in the case of a FEAD, is possible thanks to the model developed in this thesis (modeling) and the Dynamic Mechanical Analysis, which permits obtaining the belt dissipative behavior (loss modulus) for a given operating condition: temperature, frequency (speed) and strain (loading).

The DMA analyzer used was a typical GABO (Appendix *A*6) with grips to hold the belt sample to perform traction/compression tests in a temperature controlled chamber.

In order to obtain the viscoelastic behavior of the poly-V belt and its constituent parts via DMA, three types of samples were prepared (Fig. 2.13):

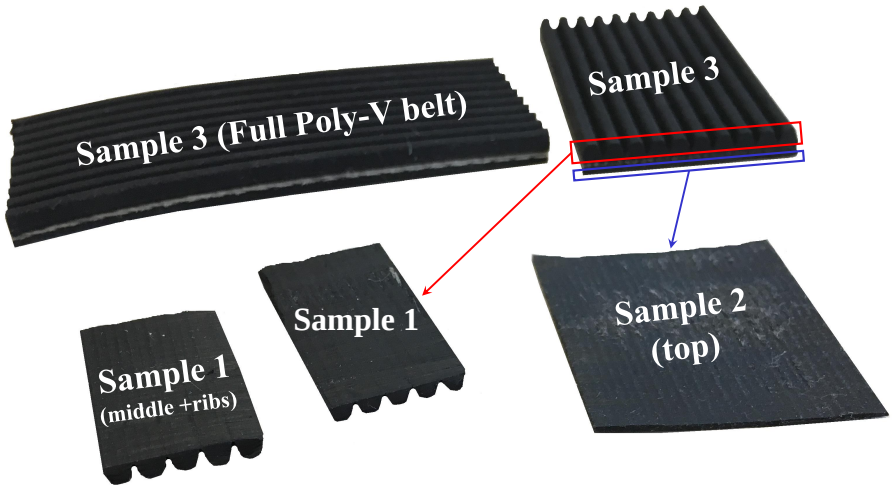

Figure 2.13 – Belt samples for the DMA tests.

- **Sample 1:** Rubber band from the belt middle and ribs layer;
- **Sample 2:** Rubber band from the belt top layer.
- **Sample 3:** Full poly-V belt (top, middle, ribs and tension cords);

In practice, the belt middle and rib layers are made of the same material (EPDM type 1), while the belt top layer is made from a different material (EPDM type 2). These samples, 1 and 2, are easy to obtain, since they are rubber bands directly extracted (cut-off) from the belt (Fig. 2.13). However, in the energy loss and strain equations of modeling, the belt-tension-cords properties E^*_{cord}, E'_{cord} and E''_{cord} are needed. Because of the difficulty to separate the cord member from the belt, the full poly-V belt (Sample 3) was prepared to be tested longitudinally via DMA. Next, a Voigt model from Meaud [39] is adopted to calculate the required data on belt tension-cords (Eq.2.50). Assuming that the poly-V belt can be considered as a Voigt composite (Fig.2.14)

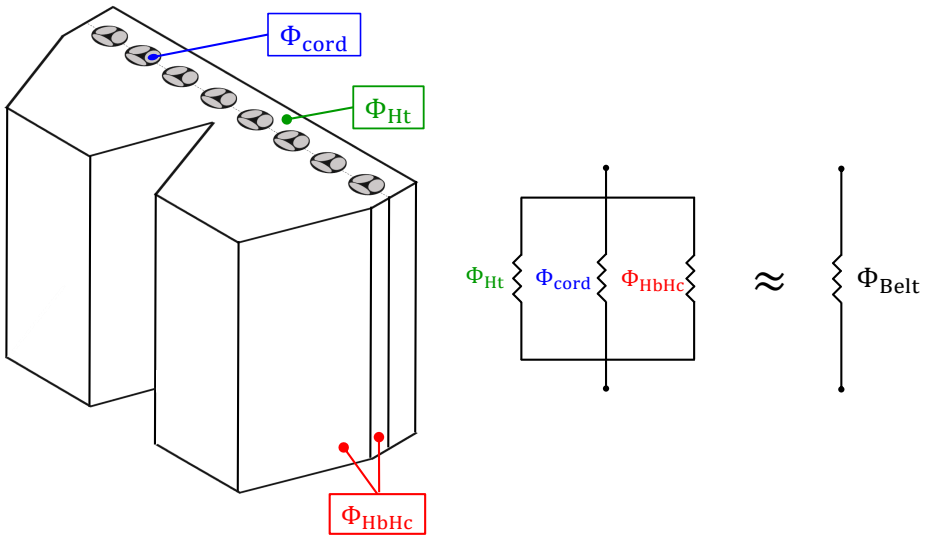

Figure 2.14 – Poly-V belt assimilated to a Voigt composite.

From Meaud [39] and Lakes [38], the complex modulus of the belt tension-cords E^*_{cord} in response to harmonic loading is given by Eq. 2.50.

$$E^*_{cord} = \frac{E^*_{Belt} - E^*_{Ht} \cdot \Phi_{Ht} - E^*_{Hc} \cdot \Phi_{HbHc}}{\Phi_{cord}} \tag{2.50}$$

Where E^*_{Ht} and E^*_{Hc} are the complex moduli of material from the belt top and rib layer, respectively; Φ_{Ht}, Φ_{cord} and Φ_{HbHc} are the volume fractions of materials from the belt top, cord and rib layers, respectively. Eq. 2.50 is also valid for the E'_{cord} and E''_{cord}.

For the poly-V belt in Fig. 2.14, the different Φ can be calculated as follows:

$$\begin{cases} \Phi_{Ht} &= A_{Ht}/A \\ \Phi_{cord} &= A_{cord}/A \\ \Phi_{HbHc} &= (A_{Hb} + A_{Hc})/A \end{cases} \tag{2.51}$$

Where A, A_{Ht}, A_{cord}, A_{Hb} and A_{Hc} are the cross-sectional area of the poly-V belt, top, cord, middle and ribs layer, respectively.

Note that in Eq. 2.51 to calculate the volume fractions, the cross-sectional areas were used instead of volumes. That is because the belt length L is simplified on both numerator and denominator of Eq. 2.51. Note also that Φ_{belt} is equal to the sum of Φ_{Ht}, Φ_{cord} and Φ_{HbHc}. Furthermore, $\Phi_{Belt} = 1$ which corresponds to the total volume of the Voigt composite (Fig. 2.14).

Methodology

Before describing the methodology of the DMA tests performed to provide data on belt material properties, the data acquisition conditions are detailed.

Data shall be acquired to correspond to the engine-range of operating conditions (speed, temperature). To this aim, belt-samples are tested here at

- **Constant strain amplitude**. Indeed, the constant value of strain can be assumed due to the hypothesis that the complex modulus of the elastomeric belt does not change much within the realistic range of strain theoretically experienced by the belt. So, the variation of the complex modulus as a function of strain is neglected.
- **Various temperatures**. Since experiments can hardly be performed for testing frequencies greater than 20 Hz, the equivalence between the temperature and the frequency (thermo-simplicity principle [40]) is used in this case to extrapolate the belt-material viscoelastic properties coinciding with the FEAD working conditions.
- **Discrete frequencies**: 0.2, 2, and 20 Hertz.

The applied methodology to obtain data from DMA is depicted in Fig.2.15. E.g. a loss modulus was measured for the DMA testing temperature ranging from 0 to 80 °C, and frequencies, equal to 0.2, 2 and 20 Hz. To apply the thermo-simplicity principle and extend the frequency domain as Butaud [40], Meyer [41] et al, e.g. from $0.2 \rightarrow 20$ Hz to $10^{-5} \rightarrow 10^5$ Hz (Fig.2.15), measurements at temperatures greater than the working temperature are needed. To this aim, the values of a (reference) temperature T_{ref} and strain are fixed. This temperature is set equal to the engine room temperature for which the power losses need to be evaluated. The strain ε_a for rubber sample testing is a mean and constant value representative of the poly-V belt cyclic loading modes.

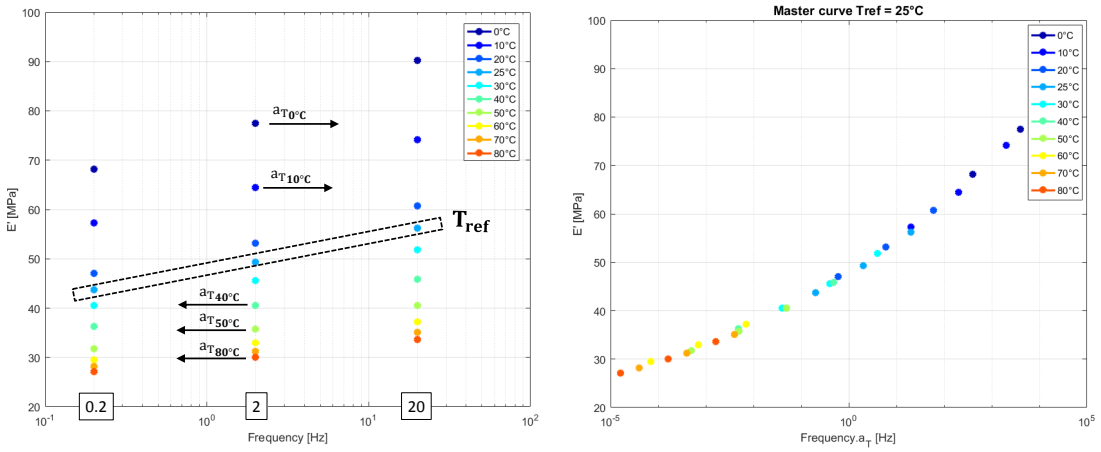

Figure 2.15 – DMA data example (left) and correspondent master curve (right).

Experimental results

The thermo-simplicity principle is used to predict the viscoelastic behavior of the material at T_{ref} over a broad range of frequencies by shifting the data obtained via DMA for each testing temperature (a_T, Fig.2.15). The master curve in Fig. 2.15 (right) was obtained. Next, the aforementioned process was repeated for the different samples and at two different work conditions : the engine operating either after ignition ($T_{ref} = 25°C$) or at steady-state ($T_{ref} = 60°C$). Finally, master curves were fitted (Fig. 2.16) and empirical equations describing the storage and loss moduli as a function of frequencies were obtained by DMA (Tab. 2.4, where Ω_i is defined Tab. 2.3).

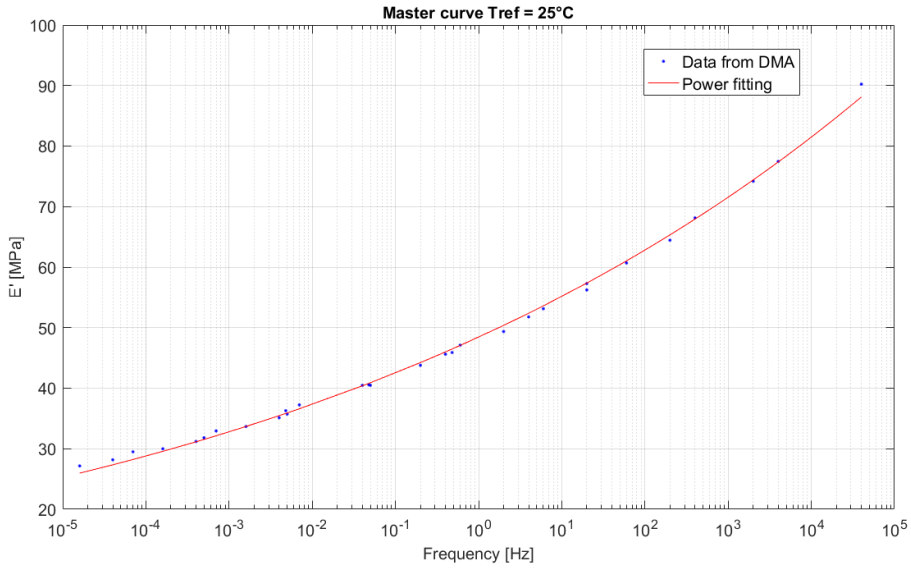

Figure 2.16 – Associated fit of the master curve in Fig. 2.15.

In addition, to calculate power losses, the master-curve equations from Tab. 2.4 can be used when the engine room temperature wanted is equal to T_{ref} and the magnitude of the FEAD strain (Eqs.2.8, 2.14, 2.20, 2.26 (or 2.30) and 2.38) are ideally situated around the testing strain (here $\varepsilon_a \approx 0.3$) with which the master curves were built.

Table 2.4 – Empirical equations describing the belt rubber moduli as $F(T_{ref}, \Omega_i, \varepsilon_a)$.

Sample	Range [Hz]	Modulus [MPa]	$T_{ref} = 25°C$	$T_{ref} = 60°C$
2	$10^{-2} \rightarrow 10^{4}$	$E'_{H_t} =$	$48.4 \cdot (\Omega_i)^{0.0565}$	$30.9 \cdot (\Omega_i)^{0.0565}$
2	$10^{-2} \rightarrow 10^{4}$	$E''_{H_t} =$	$6.1 \cdot (\Omega_i)^{0.0641} + 0.2$	$3.3 \cdot (\Omega_i)^{0.0684} + 0.6$
3	$10^{-2} \rightarrow 10^{4}$	$E'_{Belt} =$	$325.8 \cdot (\Omega_i)^{0.0516}$	$184.9 \cdot (\Omega_i)^{0.0496}$
3	$10^{-2} \rightarrow 10^{4}$	$E''_{Belt} =$	$31.4 \cdot (\Omega_i)^{0.0913} + 16.7$	$15.8 \cdot (\Omega_i)^{0.0753} + 11.3$
1	$10^{-2} \rightarrow 10^{4}$	$E'_{H_b} = E'_{H_c} =$	$59.5 \cdot (\Omega_i)^{0.0662}$	$31.2 \cdot (\Omega_i)^{0.0516}$
1	$10^{-2} \rightarrow 10^{4}$	$E''_{H_b} = E''_{H_c} =$	$4.6 \cdot (\Omega_i)^{0.1214} + 3.9$	$6.0 \cdot (\Omega_i)^{0.0352} - 2.0$

Case study

To exemplify the hysteresis power loss model presented herein, simulations were conducted on a generic FEAD (Fig. 2.17).

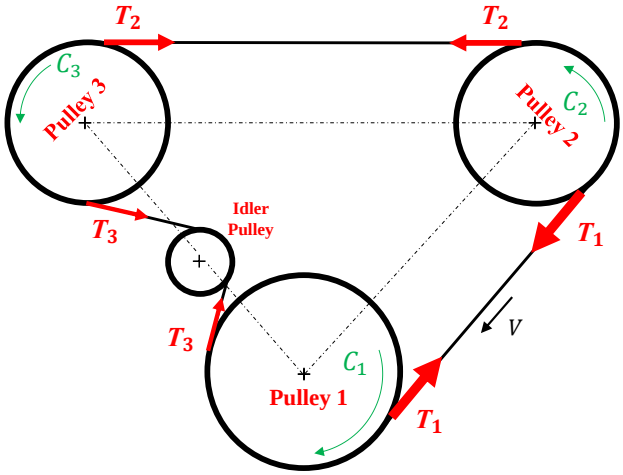

Figure 2.17 – Generic FEAD.

The pulley 1 is assimilated to the driving pulley, the two others $(2, 3)$ are accessory driven pulleys: alternator, compressor, water and steering pump, etc. Also, an idler pulley is added as it is often the case for FEADs, e.g. those presented in [2] and [7]. Parameters of the FEAD and belt in Fig. 2.17 are detailed in Tabs. 2.5 and 2.6.

Table 2.5 – FEAD geometric parameters and operating conditions.

No.	**Type**	μ	R **[mm]**	C **[N.m]**	x ; y **[mm]**
1	driver	1	100	83	0 ; 0
2	driven	1	60	50	100 ; 250
3	driven	1	60	50	−100 ; 250
4	driven	0.5	35	0	−70 ; 145

In Tab. 2.5 or 2.6, μ is the friction coefficient, R the pulley pitch radius, C the torque, x; y the center-coordinates of the pulley, L the belt-length, ρ_b belt-density, α wedge-angle, n number of ribs, ν Poisson ratio, B belt-width, B_d rib-width, H_t, H_b, H_c the thicknesses of a poly-V belt top, middle and ribs layer, respectively.

Table 2.6 – Poly-V belt geometric parameters and data.

Material	PET-EPDM
L	1301.5 mm
ρ_b	0.16 kg/m
α	40 degrees
n	10
ν	0.5

Profile	PK
H_t [mm]	0.9
H_b [mm]	1.6
H_c [mm]	2.4
B [mm]	35.6
B_d [mm]	3.56

Representativeness There are several interests of introducing an idler pulley, e.g. if the engine is considered to be running at constant idling speed with no engine speed fluctuation, the tensioner pulley might represent an automatic tensioning device as in [2] with no tensioner arm motion. Idler pulleys are also used to increase wrap-angles ϕ, decrease the belt setting tension T_0 and belt-span length to prevent transverse vibrations.

Dynamics In the hysteresis loss models, the belt span, T_t (tight) and T_s (slack), tensions are needed around each pulley of the FEAD in Fig.2.17. The belt span tensions can be obtained thanks to enhanced models (Hwang [2], Parker [7] et al.), or simply, the steady-state tensions in each belt span can be calculated according to Manin [30]:

$$\begin{cases} T_1 = T_0 + C_1/(2 \cdot R_1) \\ T_2 = T_1 - C_2/R_2 \\ T_3 = T_2 - C_3/R_3 \end{cases} \tag{2.52}$$

Where T_1, T_2, T_3 are the tension in each belt span, T_0 the setting tension, C_1, C_2, C_3 the torque on each pulley and R_1, R_2, R_3 the radius of each pulley.

Note that despite the apparent simplicity of Eqs. 2.52, the belt span tensions not only depend on the geometric parameters R and the tension T_0, but also depend on dynamic torques C of the accessory drives which are dependent on their torque curves (element feature). These kinds of curves usually vary as a function of the speed. The torques in Tab. 2.5 are valid at idling speed. In Fig.2.17, the angular speeds of the driven accessories ω_i will be approximated by Eq. 2.53.

$$\omega_i \approx \frac{R_1}{R_i} \cdot \omega_1 \tag{2.53}$$

Where R_1 and R_i are the pitch radius of the pulley 1 and pulley i^{th}, respectively. Also, the symbol $\approx$ was used in Eq. 2.53 to designate the accessory drives angular speeds, because of the belt-pulleys slip. Thus, the accessory drive angular speed ω_i is not exactly the amount calculated by the right side of Eq. 2.53, but this is a good approximation.

Conditions For the simulation case,

- Pulley 1 is considered to be running at idling speed ($\omega_1 = 600$ rpm);
- The setting tension T_0 is equal to 1400 Newtons;
- The working temperature is equal to either 25 or 60 Celsius.

Belt characteristics

Considering the belt described in Tab. 2.6 and Eqs. 2.51, the volume fractions used to calculate the properties on the belt tension cords are:

$$\begin{cases} \Phi_{Ht} &= 0.194 \\ \Phi_{cord} &= 0.184 \\ \Phi_{HbHc} &= 0.622 \end{cases} \tag{2.54}$$

Note that the considered poly-V belt is composed of 81.6% of EDPM-rubber and 18.4% PET-cords. The dissipation will not only be proportional to these fractions, but also to the property of each material and temperature. That is why, the temperature of 25 and 60 Celsius are considered corresponding to the engine after ignition and after some working time, respectively. In addition to Tab. 2.4 and thanks to Eq. 2.50, at these temperatures the properties of the poly-V belt tension-cords are calculated (Tab. 2.7).

Table 2.7 – Empirical equations describing the belt cords moduli in MPa with Ω in Hz.

	$T_{ref} = 25°C$	$T_{ref} = 60°C$
$E'_{cord} =$	$1770.7 \cdot (\Omega_i)^{0.0516} - 51.2 \cdot (\Omega_i)^{0.0565} - 201.04 \cdot (\Omega_i)^{0.0662}$	$1004.7 \cdot (\Omega_i)^{0.0496} - 32.7 \cdot (\Omega_i)^{0.0565} - 105.4 \cdot (\Omega_i)^{0.0516}$
$E''_{cord} =$	$170.9 \cdot (\Omega_i)^{0.0913} - 6.45 \cdot (\Omega_i)^{0.0641} - 15.4 \cdot (\Omega_i)^{0.1214} + 77.6$	$85.8 \cdot (\Omega_i)^{0.0753} - 3.49 \cdot (\Omega_i)^{0.0684} - 20.3 \cdot (\Omega_i)^{0.0352} + 67.8$

FEAD conditions

Throughout a typical engine-speed-range, for the simulation and to validate the use of the equations in Tabs. 2.4 and 2.7 which are valid for frequencies ranging from 10^{-2} to 10^4 Hertz, the loading frequencies of the hysteresis cyclic loading modes (Tab. 2.3) are calculated for the FEAD in Fig. 2.17 and represented in Fig.2.18.

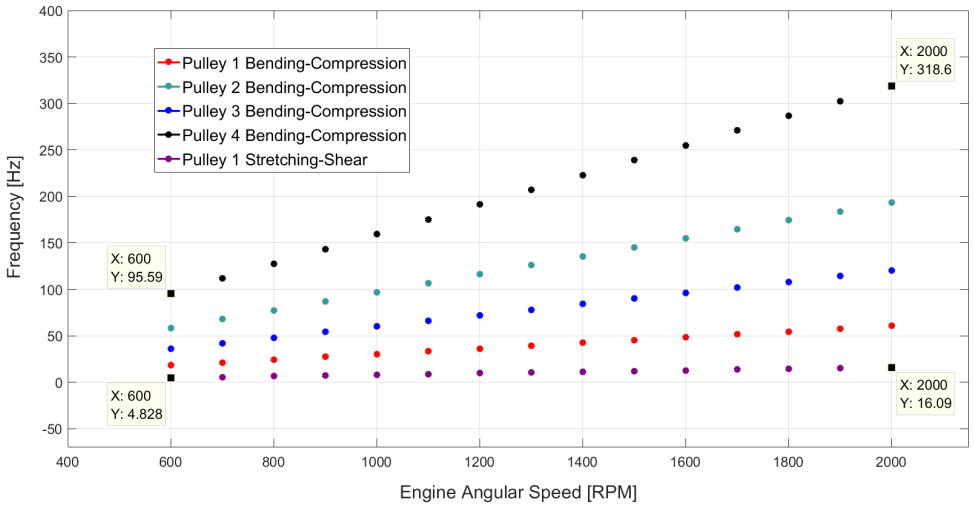

Figure 2.18 – Loading frequencies for the FEAD in Fig. 2.17.

The loading frequencies of a functioning FEAD must be situated in the belt-material DMA testing range from which the master curves were built. In this case, Fig. 2.17 shows that the loading frequency of the considered FEAD ranges from 4.8 to 318.6 Hz with the engine at idling speed. This interval is in the frequency-validity-range ($10^{-2} \rightarrow 10^{4}$ Hz) of the curves in Tabs. 2.4 and 2.7.

Moreover, Fig. 2.17 is only to give an idea of where an usual loading frequencies range is situated along a testing range for which the belt material is easily tested via DMA. Obviously, Fig. 2.18 is valid for the FEAD in Fig. 2.17 with the engine running at idle. If the engine is accelerated a similar range should be plotted for high loading frequencies.

For the FEAD in Fig. 2.17, a particular case of the Fig. 2.18 is considered (Tab. 2.8).

Table 2.8 – Loading mode frequencies (Hz) for the FEAD in Fig. 2.17.

	Bending	**Stretching**	**Flank comp**	**Radial comp**	**Shear**
Pulley 1	18.2	4.8	18.2	18.2	4.8
Pulley 2	58.1	0	58.1	58.1	0
Pulley 3	36.1	0	36.1	36.1	0
Idler	95.6	0	0	95.6	0

For example, flank compression does not occur on the idler pulley because there is no contact between the belt-ribs and the idler-pulley. So, in Tab. 2.8 the frequency corresponding to this cyclic loading mode is equal to zero, and it also means that the corresponding hysteresis loss is null. The other zeros are due to the characteristic of the cyclic loading modes: stretching and shear. Their hysteresis loops are completed on the crankshaft (pulley 1) and the frequency corresponds to the belt-traveling-frequency (i.e. one belt revolution). Note also that Tab. 2.8 is not only a particular case of Fig. 2.18 for the case study, but it is also a description of the FEAD "dissipative locations" corresponding to the cyclic loading modes.

Belt-pulley wrap ϕ, sliding ϕ_s and adhesion ϕ_a angles of the FEAD in Fig. 2.17 are also provided (Tab. 2.9). The wrap angles ϕ are from the FEAD geometry. The sliding ϕ_s and adhesion ϕ_a angles come from working conditions (Eq. 2.7). To that end, using Eq. 2.52 the belt span tensions can also be achieved (Eq. 2.55).

Table 2.9 – Wrap ϕ, sliding ϕ_s and adhesion ϕ_a angles (deg.) of the FEAD in Fig.2.17.

FEAD	ϕ	ϕ_s	ϕ_a
Pulley 1	197.9	145.2	52.8
Pulley 2	103.3	35.3	67.9
Pulley 3	166.4	109.8	56.5
Idler	107.6	0	107.6

$$\begin{cases} T_1 = 1816.7\ N \\ T_2 = 983.3\ N \\ T_3 = 145.0\ N \end{cases} \tag{2.55}$$

Belt-hysteresis power loss map

The fits in Tabs. 2.4 and 2.7 were combined with energy loss equations 2.10, 2.12, 2.18, 2.24 and 2.34 to predict the FEAD power loss coming from the poly-V belt cyclic loading modes by hysteresis (Fig. 2.19). The results are also rearranged and detailed (Tab. 2.11).

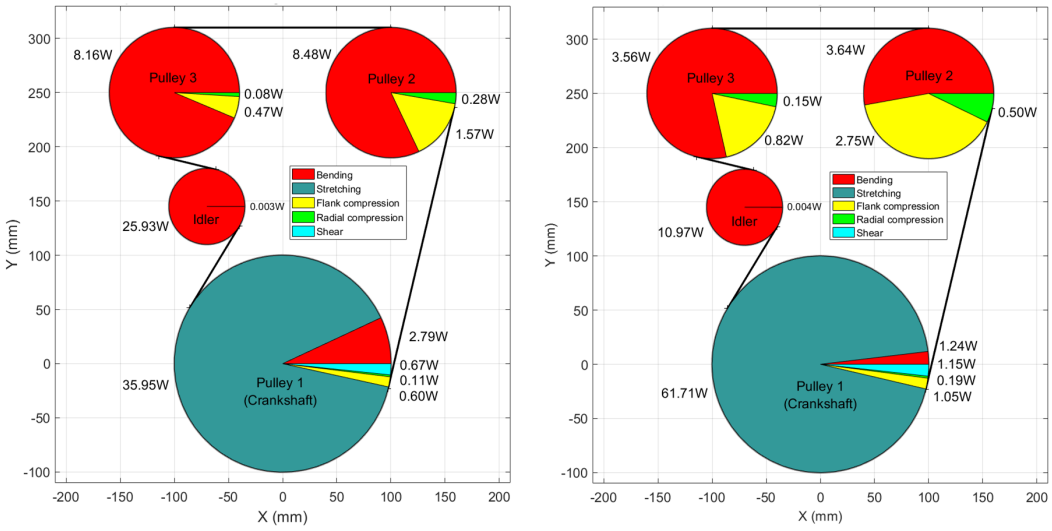

Figure 2.19 – Power Loss Maps of the generic FEAD in Fig.2.17 (left, 25°C) (right, 60°C).

Table 2.10 – Power losses in Watts (W) of the FEAD in Fig. 2.17.

	25°C	%	60°C	%
Pulley 1	40.1	47.2	65.4	40.4
Pulley 2	10.3	12.1	6.9	7.9
Pulley 3	8.7	10.2	4.5	5.1
Idler	25.9	30.5	10.9	12.4
Total	85.1	100	87.7	100

	25°C	%	60°C	%
Bending	45.4	53.3	19.4	22.1
Stretching	35.9	42.2	61.7	70.4
Flank comp	2.6	3.1	4.6	5.3
Radial comp	0.5	0.6	0.8	0.9
Shear	0.7	0.8	1.1	1.3

Table 2.11 provides a summary of the power losses in the FEAD (Fig. 2.17). These results are valid under the conditions defined in the case study section.

Thanks to the power loss map (Fig.2.19) of the Tab. 2.11, we notice that, at 25°C, for the bending losses (45.4 W) only 2.79 W are lost on the crankshaft (pulley 1). Also, the amount lost by bending is distributed among all pulleys, which is consistent, since the belt is always bent when passing by FEAD components: pulleys, idlers-pulleys, tensioner-pulleys, etc. Moreover, the loss of energy is inversely proportional to the curvature of the belt in the FEAD example (Fig.2.17): here around 30.5% (25.9 W) of bending is lost on pulley 4, as the pulley 4 has the smallest radius, then it imposes the biggest bending strain value $\varepsilon_{a_{bend}}$ (Eq. 2.8), which is directly proportional to the energy lost by (bending) hysteresis (Eq. 2.10).

One can see that around 1.65% (86.4 $\pm$ 1.3 W) of the power on input shaft (5236 W) is lost by belt hysteresis. This amount of energy lost can vary depending on the belt transmission and its characteristics. For example, considering the same belt elastomer, the FEAD geometry and engine work conditions, a thick belt would dissipate more energy than a thin belt, since a thick belt has more elastomer to be loaded and unloaded.

According to DMA experiments (Tab. 2.4) and data from Gerbert [14], it can be noticed that storage E' and loss E'' moduli decrease with temperature and increase with frequency. In Eq. 2.6, the loss modulus of the belt elastomer is directly proportional to the energy (power) loss. Thus, for temperatures higher than 25 Celsius, smaller amounts of energy lost would be expected and vice-versa, (e.g. Bending in Fig. 2.19). Note that, in this case, only the dissipative property of the belt material interferes in the energy loss. However, in the cyclic loading modes: stretching, shear and compression, which the Hooke's law is used to calculate the strain in Eq. 2.6, the loss is also inversely proportional to the square of the storage modulus of the belt elastomer. Thus, increasing temperature, and therefore, decreasing the complex modulus would on one hand decrease the power loss due to the loss modulus and on the other hand increase the power loss proportionally to the square of the storage modulus. These explain the decreasing of hysteresis losses for bending and increasing for others from $25°C$ to $60°C$ in Tab. 2.11.

2.3.8 Conclusions about belt-hysteresis losses

The power losses due to the belt bending, stretching, shear, flank and radial compression hysteresis have been investigated in this chapter. The research was done in the frame of the belt Front Engine Accessory Drive used in trucks.

Theoretical models have been developed and implemented to quantify an accurate amount of energy lost by hysteresis of the belt. However, there exists the possibility to go further through enhanced analyses (Appendix $A5$).

Up to now, it was highlighted that in a FEAD energy can be lost by belt bending, stretching, shear, flank and radial compression hysteresis.

In the present modeling the belt elastomers intrinsic properties were accounted for. More precisely, the belt elastomer viscoelastic properties were determined by DMA experiments. The Payne and Mullins effects (Appendix $A4$) as well as the dependency on frequency has been highlighted and took into consideration. Thus, a power loss map for a quasi-static application was obtained (Fig. 2.19).

The power loss map represents an easy and practical way to do a diagrammatic representation of power losses. It also permits determining the phenomenon (e.g. bending, stretching, shear, flank or radial compression), the location (pulley 1, 2, 3 or idler) and the quantity (amount in Watts) from which power is lost in a belt transmission (Fig. 2.17).

The bending, stretching, shear, flank and radial compression hysteresis are internal losses. The next sections of this chapter will consist in presenting external losses, e.g. the bearing losses, the pulley/belt slip losses, etc.

2.4 TENSIONER-HYSTERESIS LOSSES

The tensioner-hysteresis characterizes the power dissipated by friction during the tensioner-arm movement. The tensioner arm/pulley is a part of the automatic tensioning device whose function is to adjust the belt slack span tension value over a wide range of operating conditions (Fig. 2.20).

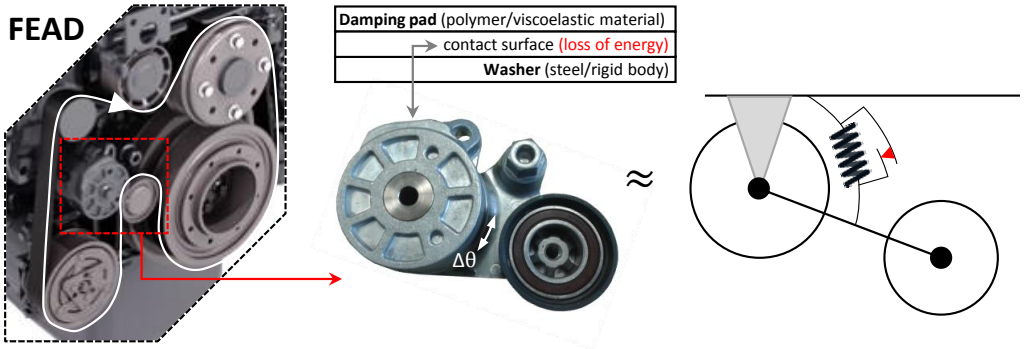

Figure 2.20 – Automatic tensioning device and its schematic diagram.

Tensioner pivot is realized by a plain bearing which induces friction and consequently energy loss. Indeed, when the tensioner-arm moves, it causes relative movements in the pivot assembly and thereby generates friction and thus damping (Fig. 2.21).

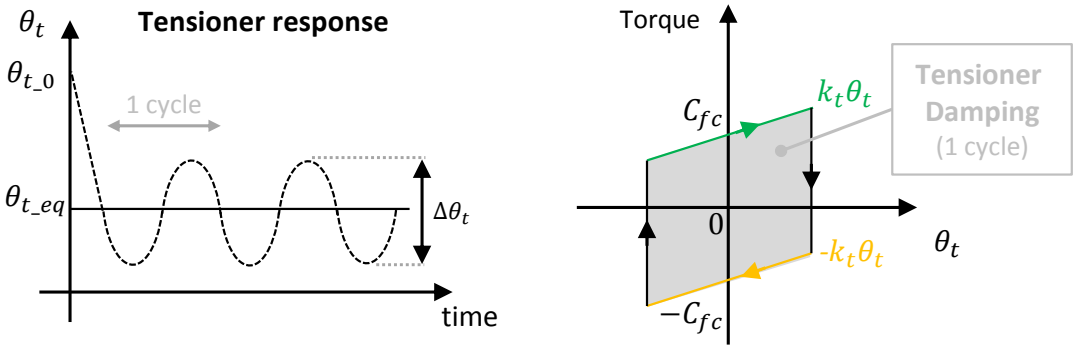

Figure 2.21 – Generic tensioner time response and hysteretic behavior.

According to Michon et al. [34] the dissipated energy due to the tensioner hysteretic behavior equals to the internal area of the hysteresis loop in Fig. 2.21. This amount of energy lost can be calculated by Eq. 2.56.

$$W_{tens-hys} = 2 \;\; C_{fc} \;\; \Delta\theta_t \tag{2.56}$$

Where $W_{tens-hys}$ is the dissipated energy in the tensioner pivot in (J), $\Delta\theta_t$ the amplitude of the tensioner rotation angle in (rad) and C_{fc} the tensioner frictional torque in (Nm). Thus, the tensioner hysteresis power losses $PL_{tens-hys}$ in (W) is obtained by Eq. 2.57.

$$PL_{tens-hys} = \frac{W_{tens-hys}}{2\pi} \; \Omega_t \tag{2.57}$$

Where Ω_t is the tensioner oscillation angular frequency in (rad/s). Also, the energy loss per period represented by Eq. 2.57 can be defined only if Ω_t is not nil. Moreover, the tensioner time response presented in Fig. 2.21 can be obtained by calculating the dynamic response as demonstrated by Hwang [2], Beikmann [5], Parker [7] et al.

2.5 BEARING POWER LOSSES

Bearings are used to enable rotational movement of the FEAD shafts, while reducing friction and handling stress. However, some power is dissipated inside the bearings. These power losses come from the rolling and sliding friction of balls or rollers against the rings of the bearing; lubricant drag and contact seals. A friction moment takes place in each bearing and it is partly dependent on the radial load supported which results from the belt/pulley resultant radial force. Several models (Schaeffler, Harris, etc.) such as the one developed by SKF [42] exist to compute the bearing power losses.

2.5.1 Model

As in [42], Eq. 2.58 gives the expression of the bearing power loss.

$$PL_b = \ M_b \ \ n_b \tag{2.58}$$

Where PL_b is the bearing power loss, n_b the rotational speed of the bearing and M_b the bearing total frictional moment (Eq. 2.59).

$$M_b = M_{rr} + M_{sl} + M_{seal} + M_{drag} \tag{2.59}$$

Where M_{rr} is the rolling frictional moment, M_{sl} the sliding frictional moment, M_{seal} the frictional moment of seals and M_{drag} the frictional moment due to drag in the bearing. The formulation used for M_b in Eq. 2.59 implies to collect several coefficients from the bearings manufacturer catalog [42]. It can be fastidious but leads to a more accurate estimation of the total friction moment M_b. Alternatively, a simpler formulation [23] can also be used. Equation 2.60 represents the total bearing power losses in a FEAD.

$$PL_{bear} = \sum_{i=1}^{ns} PL_{b\_i} = \sum_{i=1}^{ns} (PL_{b\_i\_F} + PL_{b\_i\_R}) \tag{2.60}$$

Where PL_{bear} is the FEAD total bearing power loss, PL_{b_i} the sum of power loss from the front $PL_{b\_i\_F}$ and rear $PL_{b\_i\_R}$ bearings of the i^{th} shaft and ns the number of shafts composing the FEAD. Moreover, Eq. 2.60 suggests that there are at least a pair of bearings per shaft (Fig. 2.22). In the case of tensioner and idler-pulleys, the same theory is applied with $L3 = 0$ in Fig. 2.22.

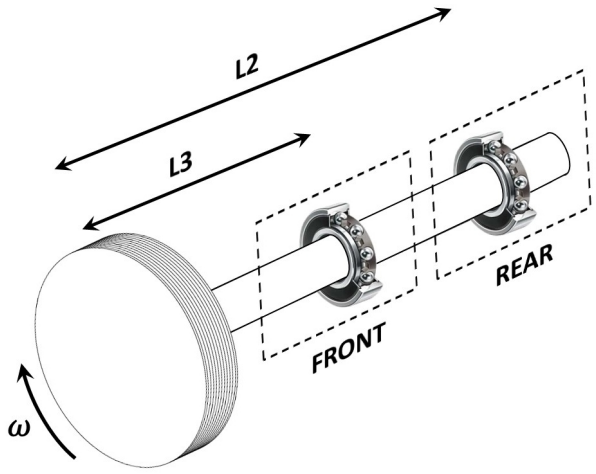

Figure 2.22 – Typical disposition of bearings supporting a shaft in a FEAD.

2.5.2 Bearing radial loads

The belt/pulley resultant radial force is a necessary parameter of the SKF model [42]. It depends on the system characteristics for which the bearing is operating.

The radial force acting on each pulley is mainly the resultant force of the belt-span tensions around the pulley under analysis. To calculate this force for each pulley/shaft regardless of their positions in the FEAD, some vector operations on the considered forces are necessary. Indeed, by using the belt-pulley seating-unseating points s, u (calculated geometrically) along the FEAD path, one can obtain the distance vectors $\vec{D}_{i-1}$ and $\vec{D}_i$ in the belt-span directions tangent to the ith pulley (Fig. 2.23).

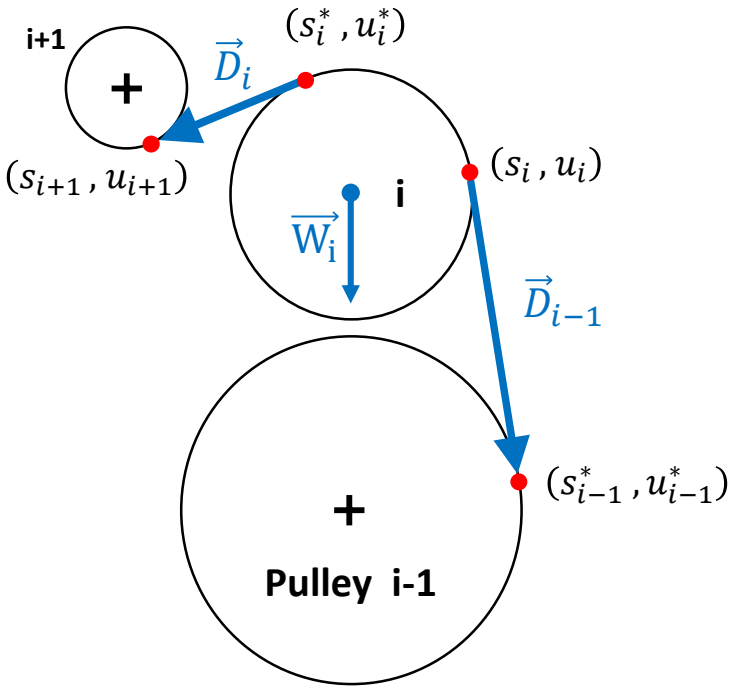

Figure 2.23 – Vector analysis on a FEAD generic pulley i.

The vectors $\vec{D}_{i-1}$ and $\vec{D}_i$ can be calculated as in Eq. 2.61.

$$\begin{cases} \vec{D}_{i-1} = (s_{i-1}^* - s_i \, , \, u_{i-1}^* - u_i) \\ \vec{D}_i = (s_{i+1} - s_i^* \, , \, u_{i+1} - u_i^*) \end{cases} \tag{2.61}$$

Assuming the FEAD as a vertical plane (Fig. 2.23), to take into consideration the total weight $\vec{W}_i$ of a generic shaft i in the resultant radial force calculation, the unit vector $\vec{G}$ with coordinates (0,-1) can be used to calculate the gravity vector $9.81\,\vec{G}$. Then, the weight $\vec{W}_i$ is equal to $9.81\,\vec{G}$ multiplied by the mass of all mechanical parts mounted on the shaft i. Moreover, the weight action is usually neglected since it is significantly smaller than the belt/pulley resultant force.

To compute the belt span tension vectors $\vec{T}_{i-1}$ and $\vec{T}_i$ the unit vectors $\vec{\mu}_{T_{i-1}}$ and $\vec{\mu}_{T_i}$ have to be calculated. This may be done by dividing the distance vectors $\vec{D}_{i-1}$ and $\vec{D}_i$ by their norms (Eq. 2.62).

$$\begin{cases} \vec{\mu}_{T_{i-1}} = \vec{\mu}_{D_{i-1}} = \frac{\vec{D}_{i-1}}{\|\vec{D}_{i-1}\|} \\ \vec{\mu}_{T_i} = \vec{\mu}_{D_i} = \frac{\vec{D}_i}{\|\vec{D}_i\|} \end{cases} \tag{2.62}$$

Next, the unit vectors $\vec{\mu}_{T_{i-1}}$ and $\vec{\mu}_{T_i}$ shall be multiplied by the scalars $\|T_{i-1}\|$ and $\|T_i\|$ which are the belt-span tensions obtained through an equilibrium analysis [2] (Eq. 2.63).

$$\begin{cases} \vec{T}_{i-1} = \left\|\vec{T}_{i-1}\right\| \ \vec{\mu}_{T_{i-1}} \\ \vec{T}_i = \left\|\vec{T}_i\right\| \ \vec{\mu}_{T_i} \end{cases} \tag{2.63}$$

Finally, to provide the belt/pulley resultant radial force F_{r_i}, which is the norm of $\vec{F}_{r\_i}$, needed for the SKF power loss model, a simple sum of vectors is performed (Eq. 2.64).

$$\vec{F}_{r\_i} = \vec{T}_{i-1} + \vec{T}_i + \vec{W}_i \tag{2.64}$$

Equation 2.64 is valid for bearings in the same plane of the pulleys (e.g. idler-pulleys) what, in practice, is not necessary the case of all bearings in a FEAD. Very often, there is a shaft supported by a couple of bearings as in Fig. 2.22. Consequently, the resultant radial force shall be calculated in each bearing. For example, let us consider the real case represented by the k^{th} shaft in Fig. 2.24. In this case the forces used to calculate the bearing power losses are $F_{r\_k\_f}$ and $F_{r\_k\_r}$ which are deduced from F_{r_k} using equilibrium equations of solid mechanics (Eq. 2.65). Moreover, note that in Fig. 2.24 since the pulley and the front-bearing are in the same plane, $L3$ is nil.

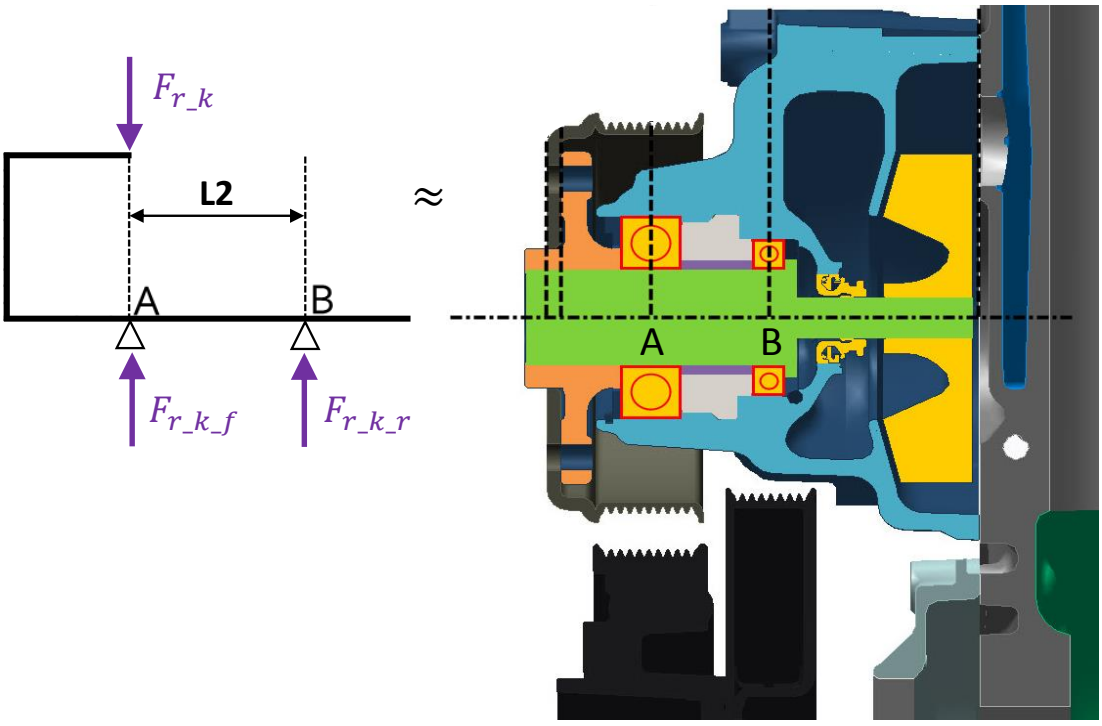

Figure 2.24 – Water pump and fan shaft with a bearing (B) out of the belt working plan.

$$\begin{cases} Fr\_k\_f = \left(\frac{L2}{L2-L3}\right) Fr\_k \\ Fr\_k\_r = \left(\frac{L3}{L2-L3}\right) Fr\_k \end{cases} \tag{2.65}$$

2.6 BELT-PULLEYS SLIP LOSSES

In contrast to belt internal losses (e.g. $PL_{belt-hys}$) and in the class of belt external or mechanical losses, the speed loss $\Delta\omega$, then power loss ΔP, is a characteristic of force conditioned (belt transmissions) systems [14]. This implies that the force transmission between the belt and pulley relies on contact load and friction (dissipation) for proper operation. Thus, since slip is associated with power loss leading to PL_{slip} according to Gerbert [14] it is possible to analyse the contact and sliding of the belt against the pulley. The analysis in this section is based on the modelling for two pulleys of the same size [43]. However, in this study, the slip theory from [43] and [14] has been extended for a general system (FEAD) with a generic number of pulleys.

The power transmitted between the belt and pulley may be written as in Eq. 2.66, where C is the torque transmitted by the pulley and ω its angular velocity. Next, the Eq. 2.66 can be differentiated as in Eq. 2.67. The quantities preceded by Δ might be considered as losses. Dividing Eq. 2.67 by 2.66 leads to the loss factors equation (2.68).

$$P = C\ \omega \tag{2.66}$$

$$\Delta P = \Delta C\ \omega + C\ \Delta\omega \tag{2.67}$$

$$\frac{\Delta P}{P} = \frac{\Delta C}{C} + \frac{\Delta\omega}{\omega} \ \rightarrow\ f_P = f_C + f_\omega \tag{2.68}$$

Where f_P, f_C, f_ω are the power, torque and angular speed loss (slip) factors, respectively. Moreover, from Eq. 2.68 the following relations can be established (Eq. 2.69).

$$f_P = \frac{\Delta P}{P} \quad f_C = \frac{\Delta C}{C} \quad f_\omega = \frac{\Delta\omega}{\omega} = s \tag{2.69}$$

This section is devoted to the study of the dimensionless quantity s in Eq. 2.69 ([21]), and therefore, the power loss PL_{slip} engendered by the belt-pulleys slip in a FEAD.

It is known that variation of tension in the belt longitudinal direction leads to variations in strain (Hooke's law) and velocity when the belt runs on pulleys. Moreover, pulleys are considered as rigid bodies, thus if a portion of the belt is considered moving around a pulley, the continuity of flow in the free belt spans is required (Eq. 2.70).

$$\rho_{bt}\ V_t = \rho_{bs}\ V_s = \rho_b\ V \tag{2.70}$$

Where ρ_b is the belt mass per unit length of unloaded belt, V the belt linear velocity and the subscripts t and s refer respectively to the tight and slack free belt span (Fig. 2.25). Also, considering an unloaded belt of length L, according to continuity of mass, the belt total mass $\rho_b\ L$ is conserved when the belt is subjected to elongations (Eq. 2.71).

$$\rho_{bt}\ L_t = \rho_{bs}\ L_s = \rho_b\ L \tag{2.71}$$

However, when the system is running, and therefore, the pulley is transmitting power, the belt is stretched of an amount of belt strain ε giving an additional length ΔL (εL). Thus, around a pulley the continuity of mass provides Eq. 2.72.

$$\rho_{bt}\ L\ (1+\varepsilon_t) = \rho_{bs}\ L\ (1+\varepsilon_s) = \rho_b\ L \tag{2.72}$$

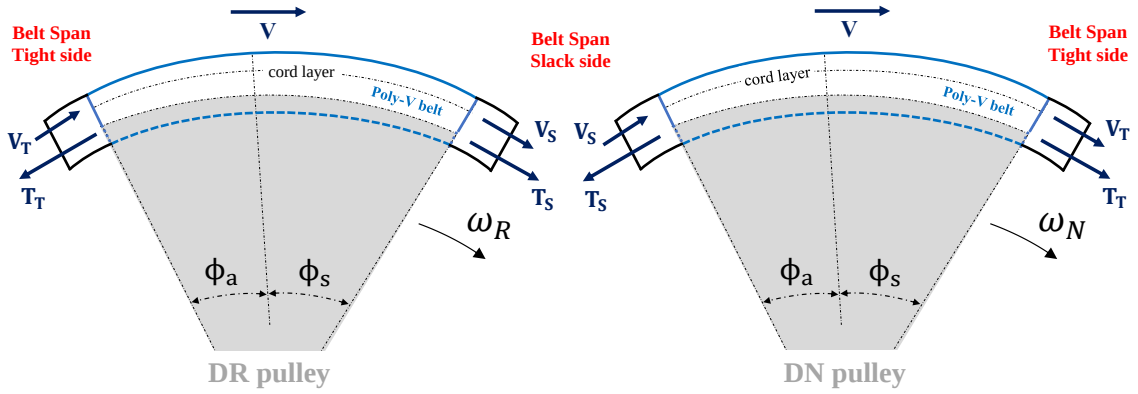

Figure 2.25 – Tight and slack tensions, slip and no-slip arcs of driver and driven pulleys.

Rearranging Eqs. (2.70 - 2.72) and eliminating the terms of mass ρ_{bt} and ρ_{bs} the tight and slack belt span velocities (V_t, V_s) can be obtained (Eq. 2.73).

$$\begin{cases} V_t = V \ (1+\varepsilon_t) \\ V_s = V \ (1+\varepsilon_s) \end{cases} \tag{2.73}$$

Where V is the belt linear velocity and ε the strain as in Eq. 2.74 (Hooke's law).

$$\varepsilon_j = \frac{T_j}{EA} \tag{2.74}$$

Where T_j is the j^{th} belt-span tension corresponding to the tight ($j = t$) or the slack ($j = s$) side and EA the tensile modulus (or strain stiffness along the belt).

Once the velocity of the belt is provided for both tight and slack sides (Eq. 2.73), one can analyse the velocity of the pulley, since the slip power loss is a consequence of the difference of velocities between the belt and the pulley. Thus, when the system is running, after radial compression the belt runs on the "true" radius r_{cp} [14] (Eq. 2.75).

$$r_{cp} = R - x_{cp} \tag{2.75}$$

Where R is the radius of the unloaded belt when it is wrapped around the pulley, which coincides with the pulley pitch radius R and x_{cp} the radial compression caused by the radial load T_j^*/R (Eq. 2.76).

$$x_{cp} = \frac{T_j^*}{R \ K} \tag{2.76}$$

Where T_j^* is the average belt-span (slack and tight) tensions around the pulley [44] and K the radial stiffness (Eq. 2.77).

$$K_h = \frac{E' \, B}{H_h} \tag{2.77}$$

Where E' is the belt storage modulus, B the belt width and H the belt thickness. Indeed, K in Eq. 2.77 depends on which belt-side is in contact with the pulley, i.e. if the belt is lying either inside ($h = b$) or outside ($h = t$) (Fig. 2.8).

To summarize, when the system is running, and therefore, the belt is loaded, the belt linear V_b and pulley V_p velocities might differ and can be written as in Eq. 2.78.

$$\begin{cases} V_b = V\ (1+\varepsilon) \\ V_p = (R - x_{cp})\,\omega \end{cases} \tag{2.78}$$

On driven (DN) pulleys, as the belt runs faster than the pulley ($V_b > V_p$), the sliding velocity V_{sl} responsible for the power losses by slip is defined as in Eq. 2.79.

$$V_{sl} = V_b - V_p \tag{2.79}$$

Equation 2.79 can be developed (Appendix $A7$) and rewritten as Eq. 2.80.

$$V_{sl} = V\,\frac{T - T_s}{EA} \tag{2.80}$$

Where V is the belt linear velocity, T the belt span tension and EA the tensile modulus.

Note that since in poly-V belt transmissions the pitch radius is much greater than the belt thickness ($R \gg H$), it was assumed that the dimensionless quantity C_* equals zero in the equation of V_{sl} (Appendix $A7$). Hence, Eq. 2.80 is valid for both driven and driver pulleys.

In addition to the sliding velocity V_{sl}, to quantify the power lost by slip PL_{slip} and based on the definition of power, we need now the frictional force dT over a small element $d\phi$ (Eq. 2.81). This force can be obtained by deriving the Euler's equation [37] as in [14].

$$dT = \mu\ T\ d\phi \tag{2.81}$$

Where μ is the belt-pulley friction coefficient and T the belt span tension.

The power loss by slip PL_{slip_i} on the i^{th} pulley-belt sliding zone (ϕ_s in Fig. 2.25) is the sum of elementary losses along the sliding arc as in Eq. 2.82.

$$PL_{slip\_i} \ = \int_0^{\phi_{s\_i}} (V_{sl\_i}\ \mu\ T)\ d\phi \ = \ \frac{V}{EA}\int_{T_{s\_i}}^{T_{t\_i}} (T - T_{s\_i})\ dT \tag{2.82}$$

Solving Eq. 2.82 for DN and DR pulleys one gets Eq. 2.83.

$$PL_{slip\_i} \ = P_i \left(\frac{T_{t\_i} - T_{s\_i}}{2\,EA}\right) = P_i\ s_i \tag{2.83}$$

Where P_i is the power transmitted and s_i the slip on a generic i^{th} pulley.

Finally, for a FEAD with np pulleys, the summation of the slip power losses on each pulley leads to Eq. 2.84.

$$PL_{slip} \ = \sum_{i=1}^{np} PL_{slip\_i} = \sum_{i=1}^{np} P_i \left(\frac{T_{t\_i} - T_{s\_i}}{2\,EA}\right) \tag{2.84}$$

It is worth noting that Eq. 2.84 is a part of Child's [45] slip-power-loss-equation (Eq.2.85).

$$PL_{slip} \ = \sum_{i=1}^{np} P_i \left[\left(\frac{T_t - T_s}{2\,EA}\right)_i + \left(\frac{\Delta V}{V}\right)_i + \left(\frac{\Delta C}{C}\right)_i \right] \tag{2.85}$$

Equation 2.85 thus clearly suggests additional slips due to speed loss ΔV and torque loss ΔC. However, Childs' experimental results [45] state that torque loss ΔC is independent of the belt tension and can be attributed to belt-bending hysteresis. Thus, in this analysis, since the belt-bending hysteresis is already taken into consideration in Eq. 2.1 inside $PL_{belt-hys}$, the slip contribution due to the torque loss ΔC should be neglected in Eq.2.85. Moreover, the speed loss ratio $\Delta V/V$ of the belt running on to a pulley can be determined as in Tab. 2.1 for driver and driven pulleys.

2.7 BELT VIBRATION LOSSES

In traction belt mechanics, there exist three types of vibrations for a moving belt: transverse (1), torsional (2) and longitudinal (3) vibrations as shown in Fig. 2.26.

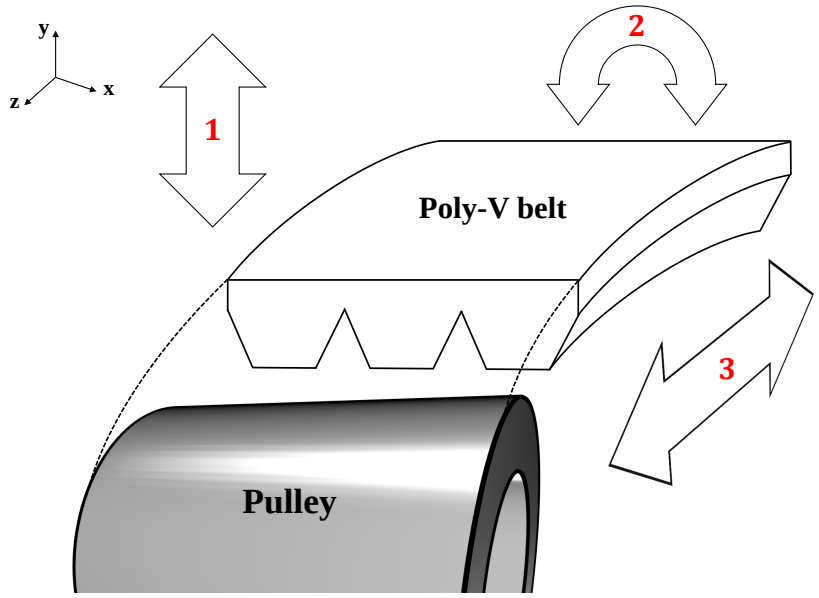

Figure 2.26 – Traction belt vibration types.

In FEADs, high level of belt transverse vibrations, and therefore, significant corresponding power losses, can be avoided by choosing an adequate belt-setting-tension and decreasing the belt-span length through the use of idler-pulleys. The main type of vibration causing power losses is the rotational vibration of the pulleys which is directly coupled with belt longitudinal vibrations (Fig. 2.26). This type of vibrations have been widely studied by many authors, e.g. Beikmann [5], Hwang [2], Parker [7] et al., since it is harmful to the system performance and durability.

In rotational modes, the pulleys rotate about their spin axes and the belt spans act as axial springs (Fig. 2.27). Rotational motions are induced by the engine acyclism, composed of a steady component (600 rpm) plus a dominant speed pulse of the modeled engine frequency 30 Hz with an amplitude of 16 rpm, as given for example by Eq. 2.86 which corresponds to a truck engine case (Fig. 1.4).

$$\omega_{CS}(t) = [\, 600 + 16\cos(2\,\pi\,30t)\,] \left(\frac{2\pi}{60}\right) \tag{2.86}$$

Equation 2.86 represents the angular speed fluctuations with a single cosine, however, a multi-harmonic engine acyclism can longitudinally excite the poly-V belt when the truck engine (Fig. 1.4) is not idling. It means that $\omega_{CS} > 600$ rpm in Eq. 2.86.

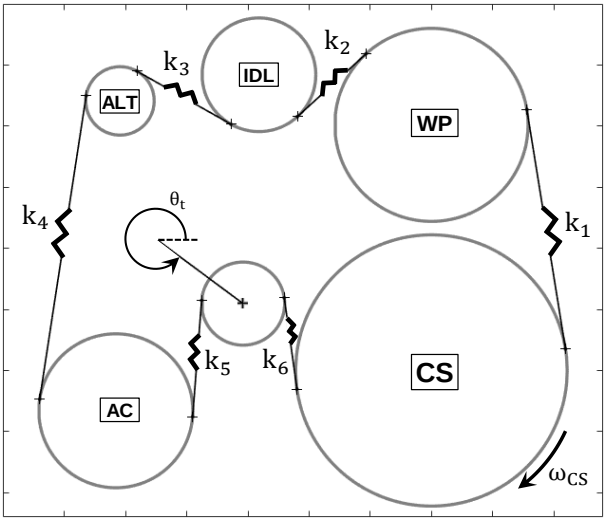

Figure 2.27 – Definition diagram for the serpentine belt drive system in Fig. 1.4.

Tension fluctuations resulting from the excitation in Eq. 2.86 are determined through numerical integration of the equations of motion, e.g. [2], [7] et al., or using modal superposition [5]. The tension fluctuations ΔT (e.g. Fig. 2.28) are the cause of additional belt stretching hysteresis power losses in the free j and wrapped i belt spans (Fig. 2.29).

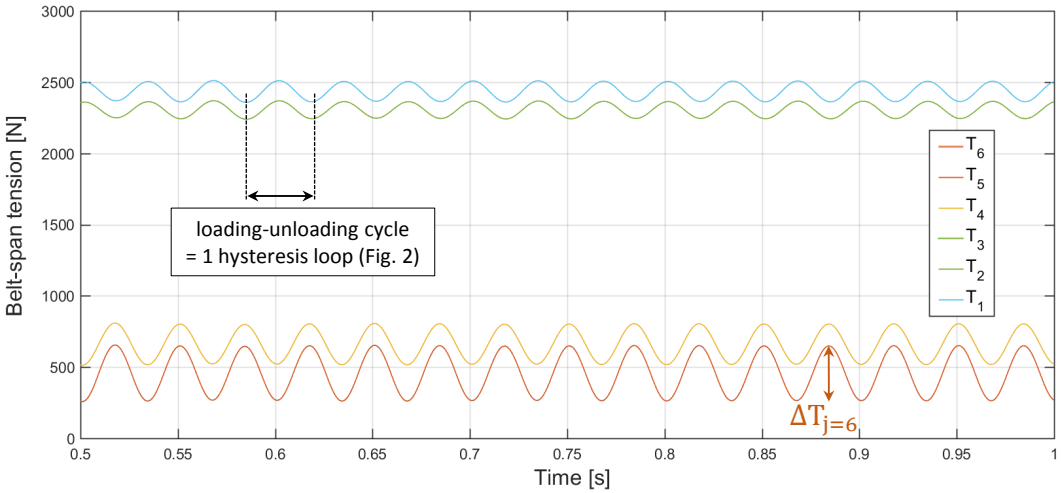

Figure 2.28 – Example of free belt-span dynamic tensions of Fig. 2.27.

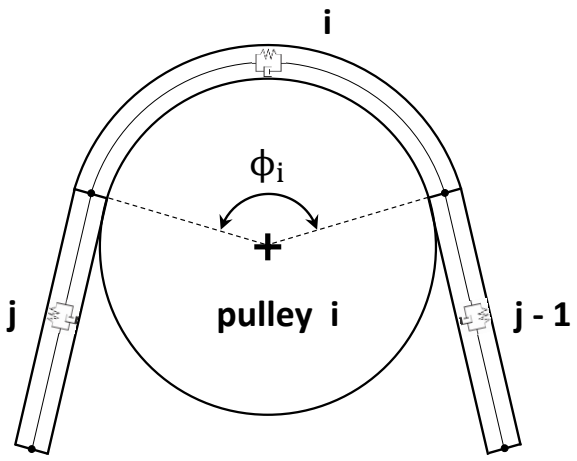

Figure 2.29 – Neighboring and wrapped belt-spans of a generic driven pulley i.

The belt stretching hysteresis power losses due to the difference between the equilibrium tensions [2] can be calculated through Eq. 2.49.
Similarly, the additional energy $W_{span\,j}$ and power $PL_{span\,j}$ losses by belt-hysteresis due to the variation of belt free span tensions, e.g. ΔT_j with $j = 1, 2, ...\,6$ for the FEAD in Fig. 2.28, can be calculated by Eqs. 2.87 and 2.88, respectively

$$W_{span\,j} = \pi \cdot E'' \cdot \Delta\varepsilon_j^2 \tag{2.87}$$

$$PL_{span\,j} = \lambda\ W_{span\,j}\ V \tag{2.88}$$

Where E'' is the loss modulus of the belt elastomer obtained via DMA, V the belt linear velocity, $\Delta\varepsilon_j$ the variation of strain to which the belt is subject during the belt travel along the free span j (Fig. 2.29) and λ a constant dependent on the belt-span length, the engine speed and the frequency of the tension fluctuations.
In Eq. 2.88, the quantity $(W_{span\,j}\,V)$ represents a complete loop of hysteresis (Fig. 2.1), however, if along a generic belt-span the corresponding harmonic tension (Fig.2.28) has time to complete two loading cycles then $\lambda = 2$ in Eq. 2.88. At the opposite, if the period of tension fluctuation is less than the time required to travel the belt span length, then $0 \leq \lambda \leq 1$. Moreover, according to Hooke's law, i.e. Eq. 2.74, the variations in belt-span tension, from the engine acyclism, leads to variation in strain and vice-versa (Eq. 2.89).

$$\Delta\varepsilon_j = \frac{\Delta T_j}{EA} \tag{2.89}$$

Where ΔT_j is the tension variation in a free belt-span j (or $j-1$ leading to ΔT_{j-1}) (Fig.2.29), EA the belt tensile modulus or strain stiffness along the belt.
For the wrapped belt-span i in Fig. 2.29 the energy $W_{span\,i}$ and the power $PL_{span\,i}$ losses as well as the variation in strain $\Delta\varepsilon_i$ are calculated exactly as Eqs. 2.87 - 2.89. However, here, as in [44] the variation in tension ΔT_i leading to $\Delta\varepsilon_i$ is taken to be an average, so that the ΔT_i acting on the wrapped belt span i in Fig. 2.29 is the sum of the neighboring belt-span tension variations ΔT_j and ΔT_{j-1} divided by 2 (Eq. 2.90).

$$\Delta T_i = \frac{\Delta T_j + \Delta T_{j-1}}{2} \tag{2.90}$$

The total power loss by belt vibration PL_{vib} can be calculated by Eq. 2.91.

$$PL_{\,vib}\ = \sum_{i=j=1}^{np} (PL_{span\,i} + PL_{span\,j}) \tag{2.91}$$

Alternatively, $PL_{\,vib}$ can also be written as a function of tension fluctuations ΔT_j (Eq.2.92) by introducing Eqs. 2.87-2.90 into Eq. 2.91). ΔT_j are obtained via a dynamic model [5].

$$PL_{\,vib}\ = \sum_{i=j=1}^{np} \frac{\pi\, E''}{(EA)^2} \left[\frac{5}{4}(\Delta T_j)^2 - \frac{1}{2}\,\Delta T_j\,\Delta T_{j-1} + \frac{1}{4}(\Delta T_{j-1})^2\right] V \tag{2.92}$$

Note that both ε_j and ε_i are cyclic since they depend on the cyclic belt-span tensions T_j and T_i leading to small belt-stretching hysteresis loops (Fig. 2.1). Moreover, these losses can be directly associated with the damping(dissipation) inside the belt spans in Fig. 2.29. Also, there are as many free belt-spans as there are wrapped belt-spans in a FEAD. For example, applying Eqs. 2.91 or 2.92 to the FEAD in Fig. 2.27, j and naturally i would range from 1 to 6. In addition, attention must also be paid to the first pulley during the analysis. In this case, the $j-1$ in Eqs. 2.91 or 2.92 shall be replaced by np, where np is the number of pulleys composing the FEAD.

2.8 NUMERICAL AND EXPERIMENTAL RESULTS

Simulation and experimental results are presented for the serpentine belt drive system defined in Tab. 2.11 and presented in Fig. 2.30, where the CrankShaft (CS) pulley is assimilated to the driving pulley, the two others AD1 and AD2 are accessory driven pulleys. The FEAD is considered to be running at 600 rpm and at 20°C.

Table 2.11 – Parameters of the experimental setup in Fig. 2.30.

	Pulley			Shaft				
	x_c (mm)	y_c (mm)	d (mm)	SKF ref. (Front & Rear)	L2(mm)	L3 (mm)	C (N. m)	
							S1	S2
CS	0	0	222	Tapered roller	130	94	11.6	57.2
AD1	0	201	158	Tapered roller	130	94	5.5	38.1
AD2	-405	0	158	Angular contact ball	160	104	0.5	0.5
Idler	-155	4	74	Deep groove ball	0	0	0	0

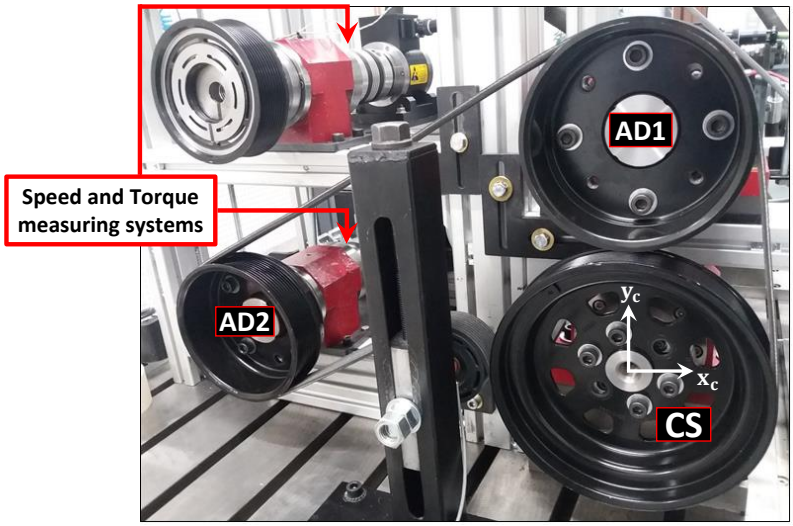

Figure 2.30 – Experimental setup with focus on the speed and torque measuring systems.

To evaluate PL_{FEAD} (Eq. 2.1) as a function of the power transmitted, a resisting torque on AD1 ranging from 5.5 to 45.3 N.m is applied on the shaft AD1 (Fig. 2.31). Consequently, in Fig. 2.30 as the CS is speed controlled, to maintain the speed (600 rpm) and offset the torque on AD1, a driving (on CS) and a resisting (on AD2) torques from 11.6 to 57.2 and 0.5 N.m are measured on the shafts CS and AD2 (Tab. 2.11), respectively.

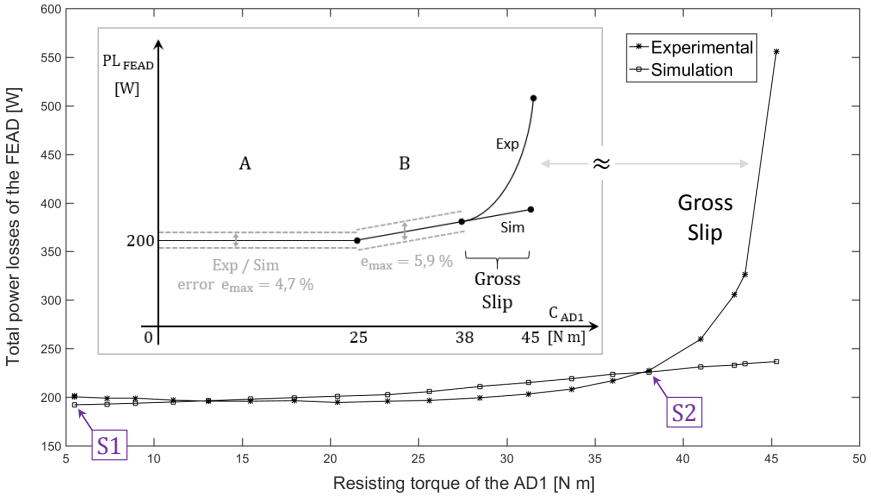

Figure 2.31 – Experimental and simulation results for the FEAD in Fig. 2.30.

Next, two case studies S1 (low torque) and S2 (high torque) are considered in Fig. 2.31. Changing from case S1 to S2, the objectives are: (1) to validate globally the power loss models in Eq. 2.1; (2) to highlight the effectiveness of the modelling of PL_{FEAD}.

The belt used here has the same characteristics of that in 2.6 except its length of 1715mm. Moreover, it is installed with a setting-tension $T_0 = 204$ N which is far below a common setting-tension representative of Truck FEAD applications ($T_0 = 600$ N) as in Fig. 1.4. However, a lower setting tension permits highlighting last results, e.g. PL_{slip}, not verified yet in this manuscript or in the previous analyses ([46] and [47]).

The FEAD power losses represented by Eq. 2.1 were both measured and simulated, with the model presented, see Tab. 2.12. Since the test bench in Fig. 2.30 is equipped with a speed and torque measuring system on each shaft, the power supplied by the crankshaft and the power consumed by the accessory drives are known. The difference between the power supplied and consumed is the power lost/measured in the FEAD (PLM, Tab. 2.12).

Table 2.12 – Summary of experimental and simulated power loss in Watts.

PL_{FEAD}	Low torques (S1)	High torques (S2)
Measured (PLM)	201.5	227.3
Simulated (PLS)	192.1	225.8
Error (PLM-PLS)/PLM	4.7 %	0.7 %

In Tab. 2.12, the simulated results are obtained from the power loss models of Eq. 2.1 with the exception of PL_{vib} and $PL_{tens-hys}$ for which only the power loss models are given here. Material properties from DMA characterization of the belt-elastomer and the belt-cords can be found in Tabs. 2.4 and 2.7.

Similarly the Power Loss Maps (PLMaps) in Fig. 2.19, however, now considering the $PL_{belt-hys}$, PL_{bear} and PL_{slip} phenomena (Eq. 2.1), the simulated power losses (PLS) corresponding to the case studies S1 and S2 in Fig. 2.31 are detailed in Tab. 2.13.

Table 2.13 – Distribution of the simulated power losses of Tab. 2.12.

Power losses in Watts on	Low torques (S1)			High torques (S2)		
	$PL_{belt-hys}$	PL_{bear}	PL_{slip}	$PL_{belt-hys}$	PL_{bear}	PL_{slip}
CS	1.9	29.8	0.1	2.2	37.1	4.2
AD1	3.9	36.5	0.1	4.0	58.0	4.3
AD2	3.7	8.3	~ 0	3.7	5.2	~ 0
Idler	18.5	89.2	0	18.5	88.5	0
FEAD	28	163.8	0.2	28.4	188.8	8.5

The losses in Tab. 2.13 are also detailed through PLMaps where the distribution of the power loss are represented with pie charts on each pulley (Figs. 2.32 and 2.33).

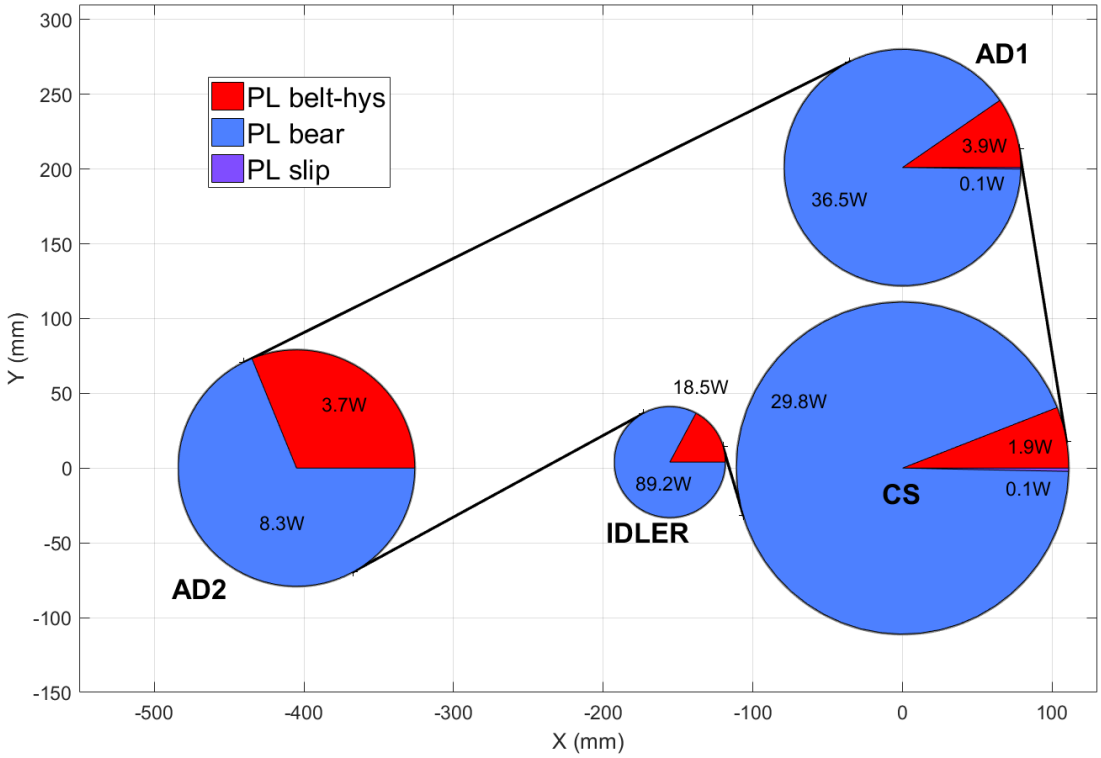

Figure 2.32 – Power loss map for low torques (S1).

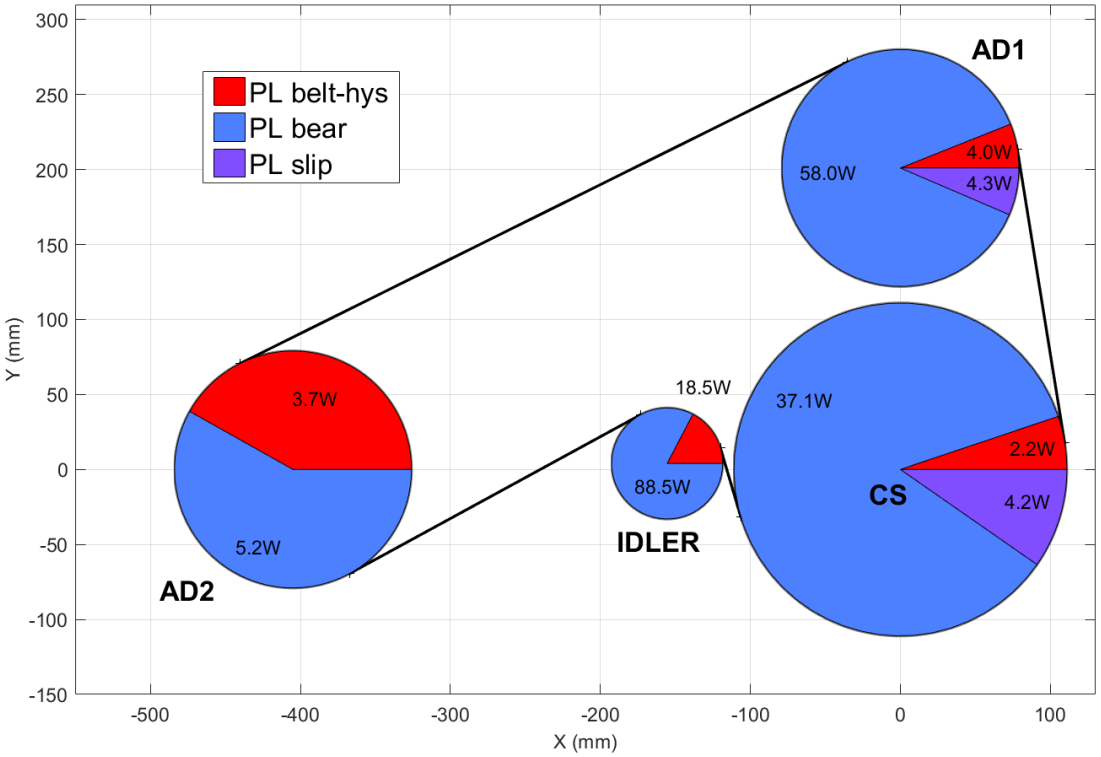

Figure 2.33 – Power loss map for high torques (S2).

2.9 SUMMARY AND CONCLUSIONS

The current chapter establishes a model for the power losses in a Front Engine Accessory Drive (FEAD). A new theory is presented and discussed, new mathematical models are developed and implemented to construct a representative FEAD power loss model. Finally, simulation results of a FEAD without torque fluctuations (engine acyclism) are compared to experimental results.

From case study S1 (Fig. 2.32) to situation S2 (Fig. 2.33) although torques have been increased (Tab. 2.11), and therefore, a greater power is transmitted, hence more power losses takes place in the FEAD as observed in experiments and simulations (Tab. 2.12). Indeed, when the FEAD accessory torques are increased, it results directly in a greater power loss due to PL_{slip} and indirectly PL_{bear} since the bearing total frictional moment which is dependent on the hubload [42], is changed. On the other hand, the $PL_{belt-hys}$ remains almost unchanged as the belt hysteresis depends mostly on the belt-bending and indirectly on the FEAD geometry which is identical in both cases S1 and S2. From S1 to S2, the bearings of the shafts CS and AD1 are more loaded and those of AD2 and idler less loaded, it was verified numerically and experimentally. Hence, for AD2 and idler, bearing power losses decrease compared to S1 (S2, Fig. 2.33). Moreover, from S1 to S2, the slip power losses have been increasing (and highlighted) on AD1 and CS providing a new power loss distribution of the FEAD considered in Fig. 2.30.

In Fig. 2.31 for both experimental and simulation results, 3 zones can be identified: (A) where the setting tension T_0 is enough to transmit power on all shafts. In this case, the FEAD total power losses PL_{FEAD} is constant and independent of the transmitted power; (B) where T_0 start becoming insufficient and the PL_{FEAD} increase linearly with the transmitted torque/power; (Gross Slip) where T_0 is not anymore sufficient to transmit the desired power and PL_{FEAD} increase exponentially. Moreover, gross slip only occurs experimentally and it is neither considered by the model in Eq. 2.1 nor partially by Childs [45] in his PL_{slip} model. It is because to predict analytically the power loss PL_{FEAD} in the gross slip zone is hard (due to complex tribological effects) and unnecessary since it never corresponds to the desired operation point of an engine (Fig. 1.4) working properly.

Finally, the relative error $(PLM - PLS)/PLM$ increases up to a maximum of 5.9% within the engine working conditions (zones A and B in Fig. 2.31) for both measured and simulated power losses, this is a reasonable error which permits validating the power loss models $PL_{belt-hys}$, PL_{bear} and PL_{slip} in Eq. 2.1. The discrepancy between measured and simulated power losses in Fig. 2.31 and Tab. 2.12 can be explained as possibly: (1) not all existing power loss phenomena have been taken into account; (2) the coefficients used to compute the frictional moments of the bearings might be under/miss estimated; (3) since the temperature in each bearing rolling contact surface is hard to be measured and it directly affects the estimation of bearing losses, the global bearing temperature of $20°C$ was measured and used in the bearing power loss model.

Chapter 3

FEAD POWER LOSSES OPTIMIZATION

Contents

This chapter is devoted to the presentation of the optimization methods applied to reduce the power losses occurring in a FEAD, since optimizing the power losses coming from this transmission help reducing the engine fuel consumption. To this aim, an optimization method based on a genetic algorithm has been developed; principles of real life (natural selection, cross-over and mutation) applied to computations have been used to minimize power losses. Genetic algorithms are commonly used in optimization because of their ability to handle complex engineering problems. For comparison purposes, the dynamic programming which is a technique based on the principle of sub-problematization has also been implemented. In this case, the optimization-problem consists in minimizing the power loss function representing the losses taking place in a front engine accessory belt drive. Results have shown that the total power losses can be reduced by tens of percent by adjusting both the positions of the engine accessories and the belt setting tension. Some experimental data confirm these numerical predictions.

3.1 METHODS

The FEAD optimization-problem can be formulated as multi-dependent-input-parameters with a single output: the total power loss (Eq. 2.1).

There exist several methods to solve this type of optimization problem (Tab. 3.1).

Table 3.1 – Example of algorithms to handle the FEAD optimization-problem.

Algorithms	Advantages
Brute Force (BF)	• Loop structure, simple to implement • Repeatability of the optimized solution
Dynamic Programming (DP)	• Repeatability of the optimized solution • Polynomial computation time
Genetic Algorithm (GA)	• Adding parameters in the optimization is straightforward • Polynomial computation time • Simple code structure

Algorithms	Drawbacks
BF	• Exponential computation time
DP	• Adding parameters slows the optimization process • Complex code structure
GA	• Choice of the GA's parameters is empirical • Non-repeatability (heuristic nature of the algorithm)

In Tab. 3.1, brute force consists in testing all different combinations of parameters, which is not a valuable method due to tremendous number of system combinations. However, the genetic algorithm and dynamic programming methods are valuable for the FEAD optimization problem mainly due to their adaptability to mechanical problems.

Dynamic programming (DP) is a method introduced in 1957 by Richard Bellman [48]. This method is well-known for its efficiency to find the optimal path from one point to another among a huge number of possibilities. The shortest-path algorithm is called Bellman-Ford. It was also discovered by Moore in 1957 through a maze [49].

Dynamic programming is a technique which permits decomposing a complex problem in various sub-problems and reducing the solution computation time from exponential to polynomial. Dynamic programming technique can be used alone or with other conventional methods. An example of FEAD power loss optimization using dynamic programming with brute force will be presented afterwards. Moreover, DP technique is effective in solving multi-step-decision process [50] [51], it is also able to deal with multi-parameter optimization problems and has been already adapted to engineering applications [52] [53].

Genetic Algorithms (GA) are nature inspired and designed to find the minimum of a function. Hans Bremermann [54] was a pioneer in the use of genetic inspired algorithms for optimization. One of the particularities of GAs is their heuristic nature: they include some randomness in the optimization process. This is not the case with brute force or dynamic programming (Tab. 3.1) which are deterministic.

Genetic algorithms are effective in solving multi-input-variables problems with multi-objectives as output. Where conventional algorithms cannot be implemented for dependent-input-parameters, GAs can handle this dependency thanks to the way they manipulate data. The adaptability and the polynomial computation time of the genetic algorithm are valuable for the FEAD optimization problem. The non-repeatability is not an issue because the algorithm converges to the global minimum of the FEAD total power loss function. When the algorithm is in the neighborhood of this minimum, the output parameters are similar up to certain decimal places. In practice, precision on the result must then be defined according to the measurement system accuracy in case of experimental validation.

Many applications of GAs exist in engineering, especially for the optimization problems. The fields of application are numerous and vary from crystal structure prediction [55] and health planning [56] to belt vibration reduction in the front end of engines [24].

3.2 OPTIMIZATION INPUT PARAMETERS

In this optimization study, the total power loss considered is represented by the belt-internal (belt-hysteresis) and the belt-external (bearings, slip) dissipative phenomena. The simulated and optimizable power loss PL_{FEAD} in the FEAD is defined by Eq. 2.1.

In 2.1, the parameters can be sorted in three categories:

- Geometric (G): pulleys-center positions, pulleys-diameters, belt-type, etc.
- Material (M): pulleys and belt constituting material (type, properties).
- Dynamic (D): crankshaft's rotation speed, torques, inertias, etc.

The power losses can be computed once provided these parameters, then through an optimization method, it is possible to find optimal parameters which permit dissipating the lowest amount of power in the FEAD. The main idea behind the optimization process is to find out the optimal input parameters G, M and D. To achieve this goal, optimization algorithms, e.g. DP and GA, will cleverly test several FEAD configurations (compute the power losses) - following certain rules - and find the parameters which, when used in the FEAD design, provide the lowest FEAD power losses during engine operation, hence minimizes the fuel consumption. That methodology can be applied to any belt transmission and not only to reduce FEAD power losses.

The power loss optimization algorithms take as input parameters the same parameters considered in the power loss models (Eq. 2.1): geometry, dynamics and materials data. The geometric parameters concern the geometry of the FEAD and its belt. In this study, the pulleys-center's positions will be optimized since they modify pulley wrap angles directly affecting the belt-hysteresis and bearing power losses (chapter 2).

The minimal setting tension $T_{0\,min}$ is the minimal tension to guarantee the power transmission [5], [2]. The setting tension T_0 will be considered in the optimization process because, in practice, it (e.g. idler brackets) is easy to be modified and modifying T_0 the belt-span tensions at equilibrium and the dynamics of the system are changed [5]. Also, by changing T_0 the dynamics of the belt transmission are also changed, e.g. bearings hub load are changed, consequently the corresponding FEAD power losses can be optimized.

The materials constituting the different layers of the belt can be chosen by the belt manufacturer and a posteriori by the engine designer. A similar reasoning can be applied for other FEAD mechanical parts: pulleys, tensioner-arm, etc. The temperature influences the behavior of the materials (dilatation, hysteresis, etc.) and the engine usually operates within a range from 20 to 100$°C$. The assumption was made to consider the material constituting the FEAD components at a constant and fixed temperature. Thus, the optimization is valid only under these conditions. However, the influence of temperature has already been studied and reported in [47].

Note that the parameters used to calculate the FEAD dynamics such as the belt setting tension affect the power loss calculations (chapter 2) and the setting tension T_0 is the tension in all belt-spans when the system is at rest (Fig. 3.1).

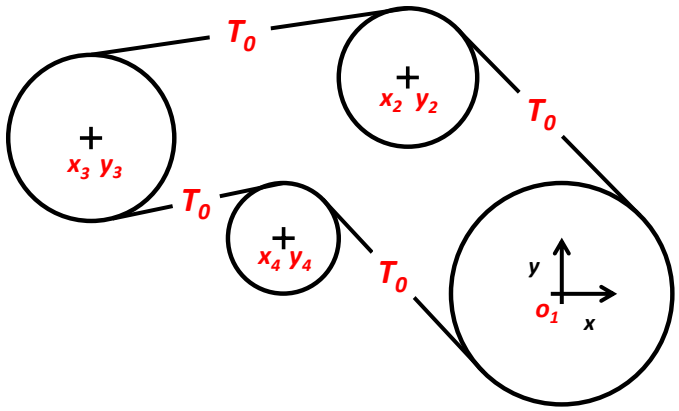

Figure 3.1 – Example of a FEAD with three pulleys and an idler at rest.

3.3 GENETIC ALGORITHM

Before applying the genetic algorithm to the FEAD power loss optimization problem, one can read [57] [58] which detail the principle of genetic algorithms. Using a genetic algorithm for a specific optimization problem requires knowing the input parameters and the function to be minimized (fitness function).

3.3.1 Fitness function

In this study, the expression of the fitness function F_f is the simulated power loss PL_{FEAD} (Eq. 2.1). It can be written as a function of X, Y, T_0 and Σ_ρ from chapter 2. Indeed, Σ_ρ is composed of the power loss model constants including the geometry (e.g. pulley-diameters) and the dynamics (e.g. accessory torques) of the FEAD not affected by the optimizable parameters X, Y, T_0 (Eq. 3.1).

$$F_f = PL_{FEAD}\,(\,X\,,\,Y\,,\,T_0\,,\,\Sigma_\rho\,) \tag{3.1}$$

With

$$X = \begin{bmatrix} x_1 \\ . \\ . \\ . \\ x_{np} \end{bmatrix} \quad Y = \begin{bmatrix} y_1 \\ . \\ . \\ . \\ y_{np} \end{bmatrix} \quad \Sigma_\rho = \begin{bmatrix} FEAD\ geometry \\ \\ FEAD\ dynamics \\ \\ FEAD\ materials \end{bmatrix}$$

Where X, Y are the pulley-center coordinates, T_0 is the belt setting tension, np the number of pulleys of the FEAD and Σ_ρ the constants terms used in the power losses calculation.

The optimization process consists in finding the X, Y and T_0 parameters such that the total power loss is minimal (Eq. 3.2).

$$PL_{FEAD}\,(\,X_{opt}\,,\,Y_{opt}\,,\,T_{0\ opt}\,,\,\Sigma_\rho\,) = min\,[PL_{FEAD}\,(\,X\,,\,Y\,,\,T_0\,,\,\Sigma_\rho\,)] \tag{3.2}$$

Where X_{opt}, Y_{opt}, $T_{0\ opt}$ are the optimized parameters which: (1) permit dissipating the lowest power in the FEAD; (2) should provide guidance to the FEAD designers.

3.3.2 Implementation

Computers have a limited (finite) calculation capacity. The optimization involves varying the optimizable parameters. Defining a range and a step for each parameter is then crucial to perform the optimization.

The pulleys-center coordinates should not be moved extensively far from their original position to avoid redesigning the entire engine. Conventionally, the pulley 1 (crankshaft) is chosen fixed, it is the origin (O1) of the coordinate system (Fig. 3.1). The other pulleys of $x_i - y_i$ coordinates ($i = 2, 3, 4$ in Fig. 3.1) can be moved to optimize the FEAD power losses. However, sometimes the pulleys can only be moved along specific directions due to geometrical constraints. Hence, a range and a step of discretization are set independently for each pulley i (Fig. 3.2).

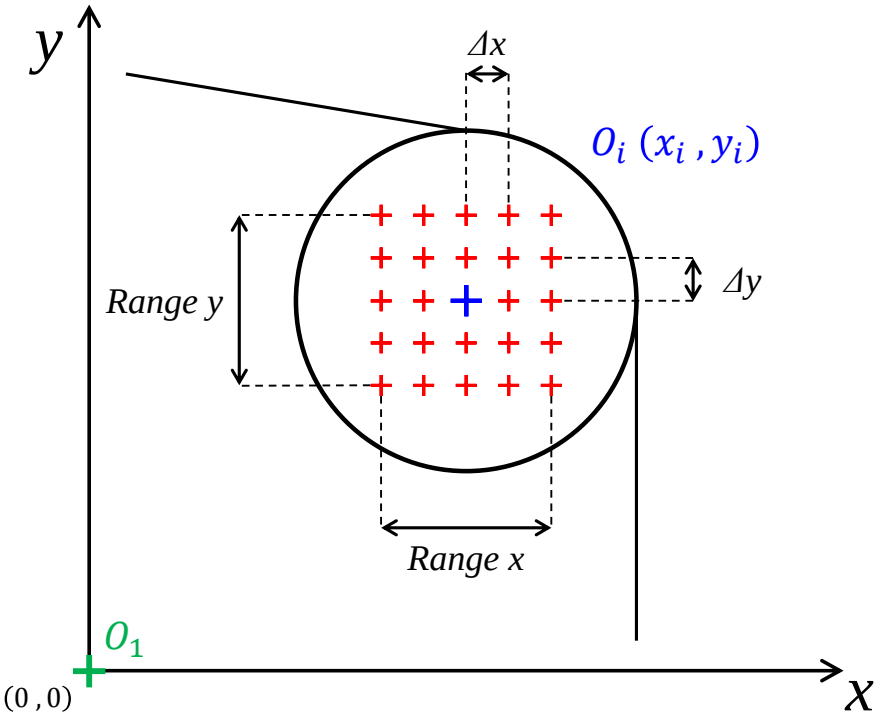

Figure 3.2 – Range and step (Δx, Δy) of discretization around the pulley-center location.

To guarantee the power transmission on every shaft of the FEAD, the belt setting tension T_0 has a theoretical minimal lower bound T_{0min}^* [30]. Thus, a higher lower bound $T_{0min} \geq T_{0min}^*$ is required to transmit power properly. In addition, an upper bound T_{0max} has to be set and should not be excessive to reduce belt life (Fig. 3.3).

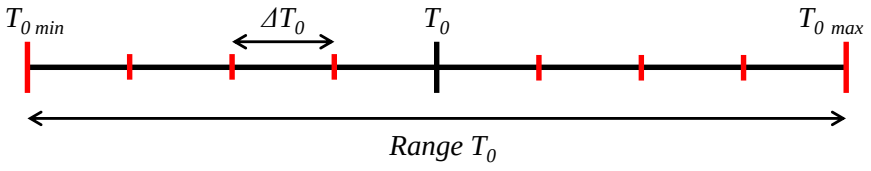

Figure 3.3 – Range and step (ΔT_0) of discretization around the setting tension T_0.

The FEAD power loss models from Eq. 2.1, and the genetic algorithm (Appendix *A*8) are implemented using MATLAB®. The genetic algorithm is designed to optimize a generic FEAD with any given number of pulleys. However, afterwards for the sake of simplicity and to exemplify the theory, we will consider the system with three pulleys and an idler shown in Fig. 3.1.

The optimizable parameters (X, Y, T_0) are stored in MATLAB® structures (Fig. 3.4).

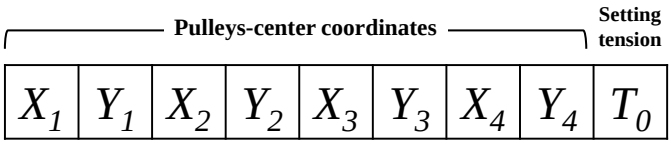

Figure 3.4 – Optimization-input-parameters structure of the FEAD_1.

Then, a structure named "Generation" composed of several FEADs (FEAD_1, ... , FEAD_{ng}) randomly generated by the genetic algorithm is created (Fig. 3.5).

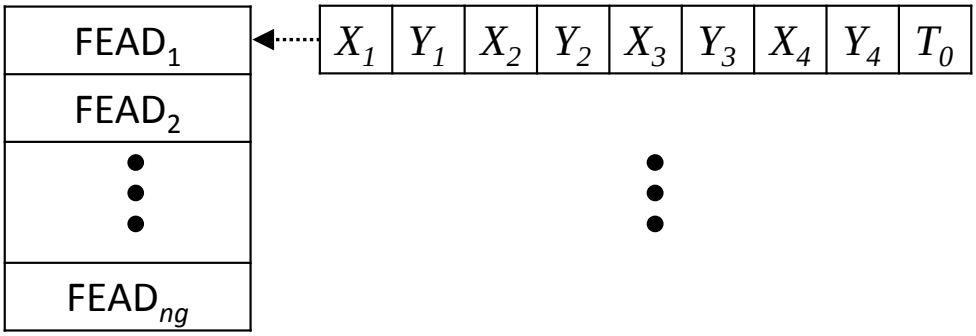

Figure 3.5 – Optimization Generation structure.

Moreover, in the Generation structure there are not only the optimizable parameters, but also data on the system geometry, the belt-material DMA data, calculation results including quasi-static, power losses as in chapter 2 and bearings information as required by [42].

The first generation of the genetic algorithm is created by loading the parameters from the FEAD to be optimized. The constant parameters (Σ_ρ in Eq. 3.1) are saved and will be used for the power loss calculations. The pulleys-center coordinates and the setting tension are randomly generated for each FEAD according to the range and step previously defined (Figs. 3.2 and 3.3). The generated population is then composed of several FEADs sharing the Σ_ρ but having different pulleys-center coordinates and setting tensions.

At each iteration, every FEAD of the population is evaluated through the total power loss function. The objective is to reach the lowest FEAD power loss amount. The stopping criterion should not be defined according to this value since it is not known before the optimization. Fixing the stopping criterion according to a finite number of generations remains a more appropriate choice. Hence, the stopping criterion is assumed to be the number of generations where the best FEAD (lowest power losses) remains without changing (decreasing / optimizing). Indeed when the best FEAD has not changed after a chosen number of generations, it is assumed that the optimization process has reached the optimal solution. The optimization time is dependent on the number of iterations.

3.3.3 Genetic functions

The genetic functions Selection, Crossover, Mutation are the key elements of the genetic algorithm (Appendix *A*8). They select, recombine and change the optimizable parameters of a generation by imitating the genes recombination occurring in nature (Fig. 3.6).

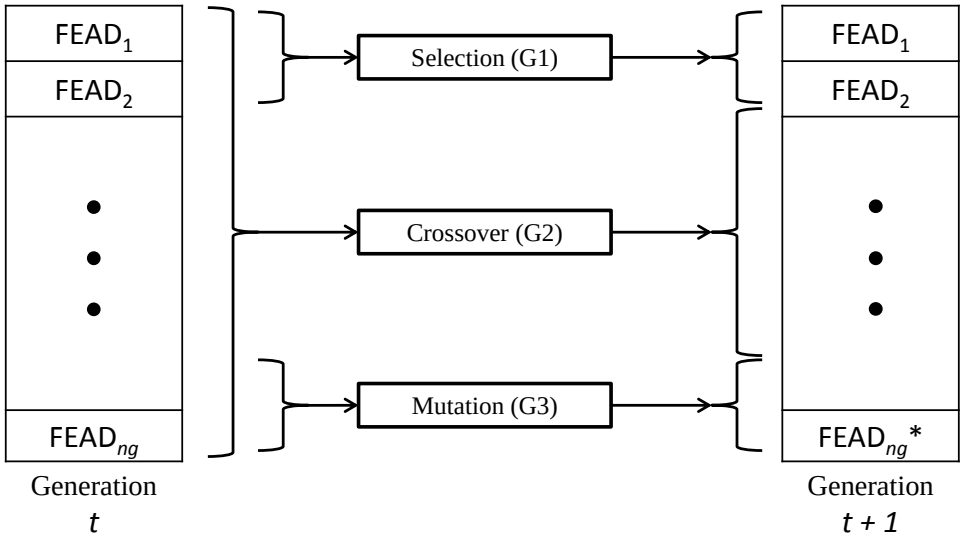

Figure 3.6 – Generic sequence of two consecutive generations (t and $t+1$) of FEADs.

As in real life the different individuals (FEADs) of a generation (t) will not experience the same alterations. Firstly, a generation is divided into different groups: selection, crossover, mutation. Secondly, these groups correspond to a percentage of the generation which will be selected, crossed or mutated (Fig. 3.6). Indeed, the first group (G1) is composed of the elites from the previous generation, the FEADs (e.g. $FEAD_1$ and $FEAD_2$) are transferred (selected) without any modifications; the second group (G2) is the result of the crossovers (recombination) of genetic material (optimizable parameters) between the FEADs from the previous generation t ; the third group (G3) is the result of the partial or complete change (mutation) of optimizable parameters between the FEADs from generation t. Details on these groups or genetic functions are presented hereafter.

The natural selection consists in transferring the best individuals from the previous (t) to the next ($t+1$) generation without altering their parameters (Fig. 3.6). Here, the best also called elites refer to the FEADs - percentage of the population - having the lowest FEAD total power loss, or as in nature, the best environmental adaptability [57].

Crossovers consist in creating a new FEAD (child), which parameters have fifty percent probability of being issued from one of the parents $FEAD_1$ and $FEAD_2$ in Fig. 3.7.

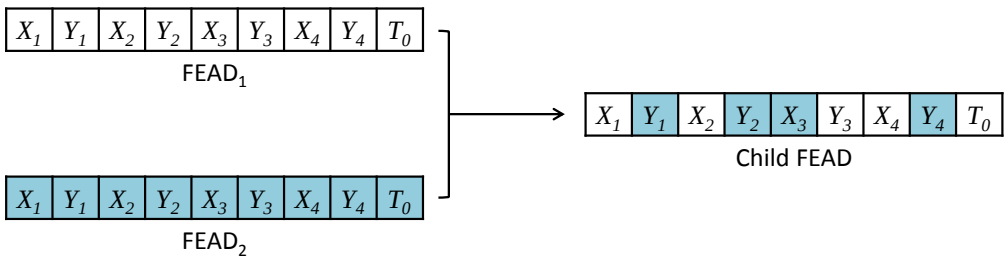

Figure 3.7 – Crossover of optimizable parameters of different FEADs.

In the literature, Umbarkar et al. [59], many methods exist for the crossovers. The choice has been made to cross the best (lowest PL) and worst (greatest PL) parameters in order to maximize the diversity of the population and ensure a fastest algorithm convergence to the optimal result. This was empirically observed. Moreover, it is also possible to randomly choose the individuals involved in crossovers [59] [60].

Mutation consists in regenerating randomly a fraction of the characteristics of the FEAD regarding the optimizable parameters, e.g. Y_1, X_3, T_0 in Fig. 3.8.

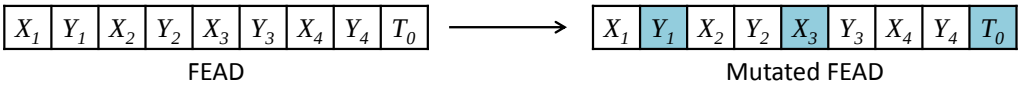

Figure 3.8 – Mutation of optimizable parameters of different FEADs.

It is worth noting that the random parameters Y_1, X_3, T_0 (Fig. 3.8) are generated within the ranges in Figs. 3.2 and 3.3, and they are not issued from the previous generations. Also, since there is no specific rule on the fraction of parameters to alter (mutate), the choice was made to regenerate a hundred percent of the parameters, again to provide diversity in the population of FEADs.

3.4 DYNAMIC PROGRAMMING

For comparison purpose, dynamic programming technique is also used to optimize the power losses taking place in the FEAD. As in genetic optimization, the optimizable parameters are X, Y, T_0.

Dynamic programming is also known as the technique of Bellman [48]. This technique is used here to provide the readers with another possible optimization method. The DP method is applicable for the FEAD case and can be directly compared with other methods (GA and BF in Tab. 3.1) and the experimental results provided afterwards.

3.4.1 Principle

The Dynamic Programming technique consists in decomposing a major and complex optimization problem in various sub-problems (Fig. 3.9) where Z are the individual criteria, S and U the state and decision variables, respectively.

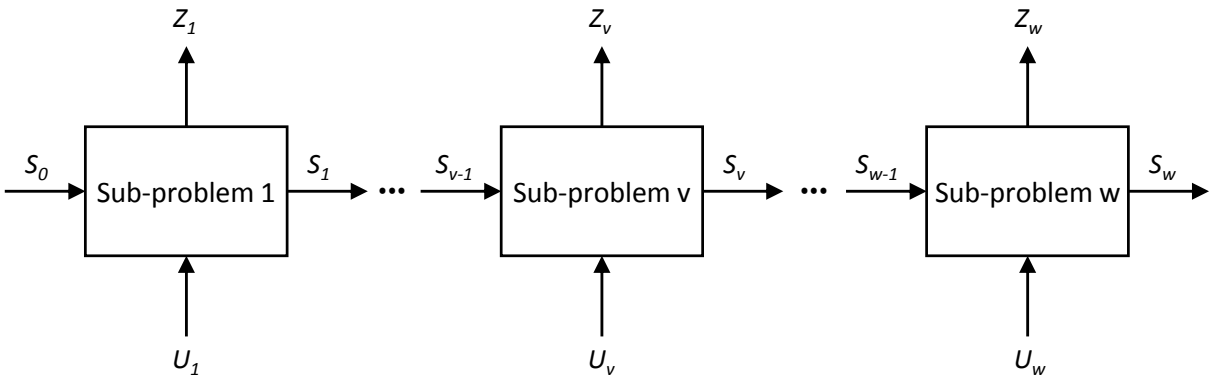

Figure 3.9 – Sub-problematization of a generic DP optimization problem.

This method is based on the principle of

- *Conditionality* which asserts that a sub-problematized problem as the one decomposed in Fig. 3.9 consisting of various decision variables can be decomposed into various embedded (sub) problems, each consisting of a single decision variable [50].
- *Optimality* which states that from any point on an optimal process the remaining process is optimal for the corresponding problem initiated at that point [61].

When using DP technique the optimization of a large problem is divided into the optimization of several smaller sub-problems [48] [50]. In addition, according to Bellman [48] optimizing the first sub-problem leads to the optimization of the second sub-problem and so on. This is due to the recursive relationship between them. Thus, the optimizations of the sub-problems leads to the optimization of the initial and large optimization problem, e.g. [51]. These optimizations can be performed either in forward or backward manners. Details on forward and backward optimizations are provided in [48].

3.4.2 FEAD application

The properties attributed to the variables Z, S and U from the generic case in Fig. 3.9 to optimize the FEAD using dynamic programming are: (1) the criteria Z correspond to the power losses (PL) from the sub-problems; (2) the state S and U are composed of the constant part (Σ_ρ) and the optimizable parameters (X, Y, T_0) (Eq. 3.1).

The dynamic programming method is applied on the FEAD represented in Fig. 3.10.

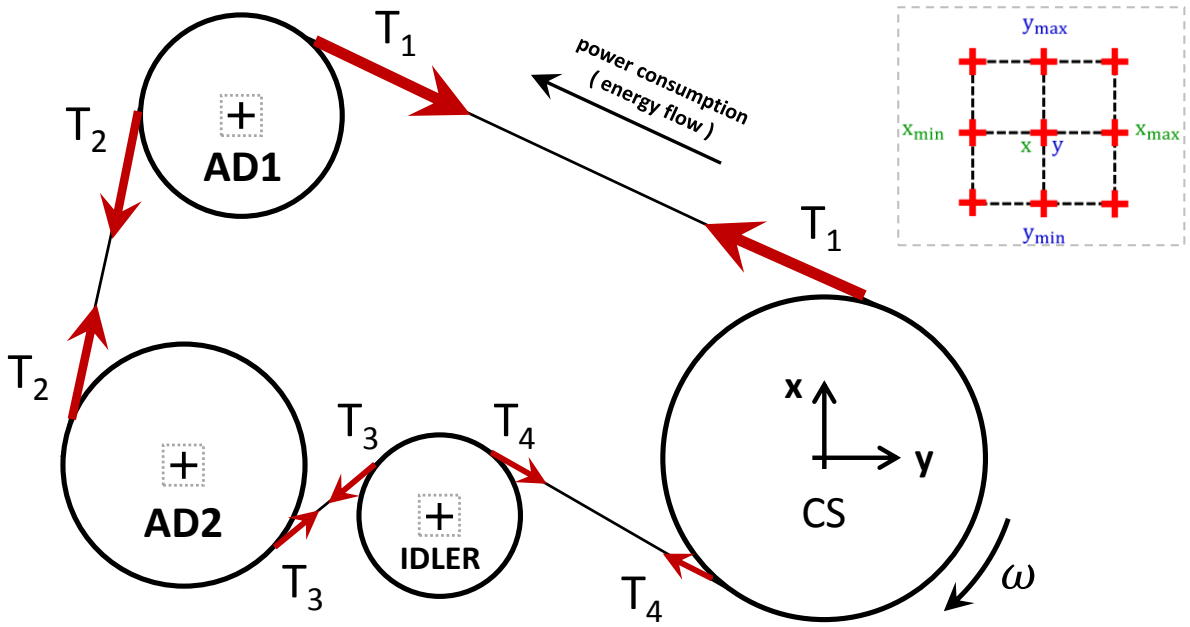

Figure 3.10 – FEAD with three pulleys and an idler in operation.

The belt transmission in Fig. 3.10 would suggest considering each pulley as a sub-problem. However, this is not in accordance with the sub-problematization in Fig. 3.9 because of the relationship between the pulleys. They are in fact connected dynamically through the belt-span tensions (Fig. 3.11).

Moreover, the belt spans tensions T_1, T_2 and T_3 in Fig. 3.10 can be obtained through an analysis at equilibrium as in [2].

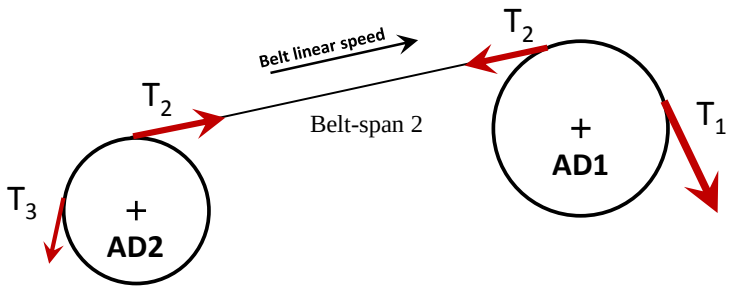

Figure 3.11 – Relation between two consecutive pulleys of a FEAD.

Sub-problematization Considering the pulley AD2, the FEAD power loss models, e.g. stretching and bearings (chapter 2), depend either directly on T_2 and T_3 or indirectly on T_1, T_2 and T_3 through an equilibrium analysis as in [2]. Thus, since a couple of moving pulleys contains the FEAD dependent information required for the power loss calculations, they are defined as the FEAD dynamic programming sub-problems. Moreover, the identified sub-problems of the FEAD example in Fig. 3.10 are presented in Fig. 3.12.

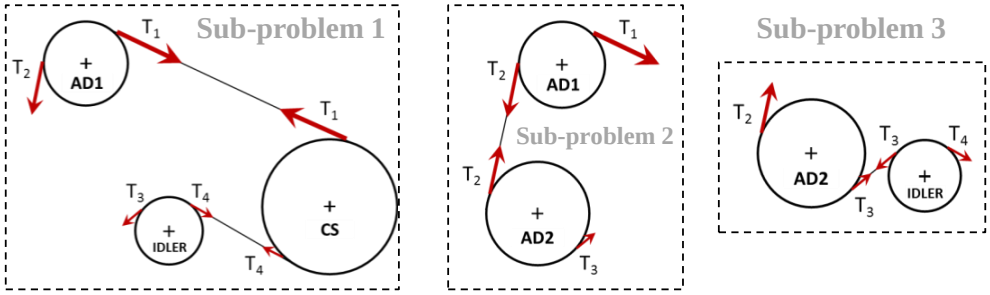

Figure 3.12 – Identified sub-problems of the FEAD in Fig. 3.10.

Note also that in Fig. 3.12 the sub-problem 1 is an exception to the definition because the crankshaft (CS) is the FEAD reference and it cannot be moved. Thus, the couple of moving pulleys are composed of the CS neighboring pulleys.

Optimization-steps In DP two possibilities of optimization are possible: either in backward which means optimizing the FEAD from the sub-problem 3 to 1 or in forward which means optimizing the FEAD from the sub-problem 1 to 3 (Fig 3.12). In this case, to coincide with the power consumption and energy flow in Fig. 3.10 the forward resolution was chosen to the multi-DP-optimization-steps FEAD decision model in Fig. 3.13.

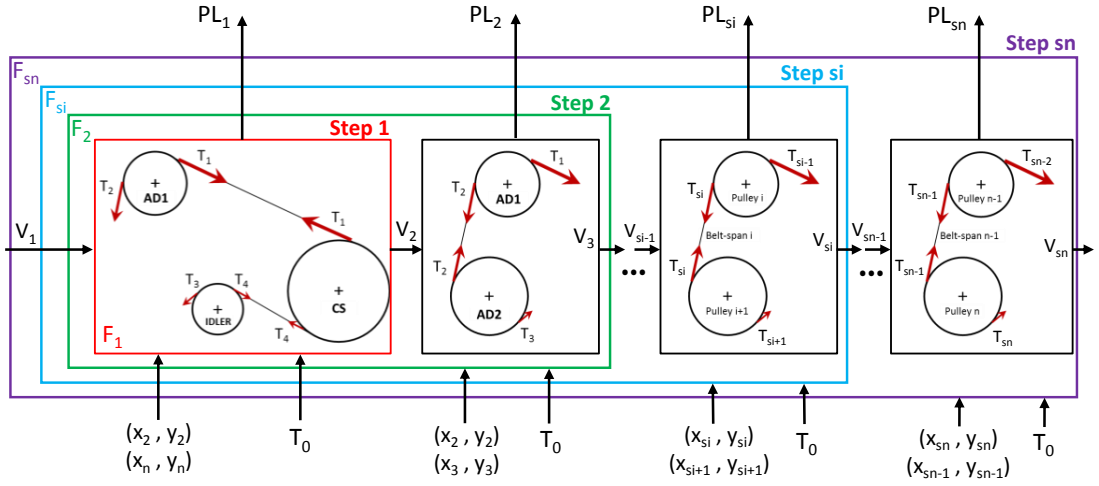

Figure 3.13 – Multi-DP-optimization-steps FEAD decision model.

Similarly to Fig. 3.9, the power loss (PL) is the criterion to be evaluated at each DP optimization step, V, X, Y, T_0 are the states and F ($\approx F_f$ of GA) is the function to be optimized or the group of sub-problems being optimized (Fig. 3.13).

Note that at the beginning of the DP optimization the state V_1 is constant since it is composed of the initial FEAD parameters X, Y, T_0 and Σ_ρ (Eq. 3.1). Then, $V_2, V_3, ...$ are variables since along the optimization, the state V is a combination between the previous-modified state and the optimized parameters corresponding to each optimization step.

For dynamic programming, with the Multi-DP-optimization-steps as in Fig. 3.13, the corresponding functions to be minimized can be written as in Eq. 3.3.

$$\begin{cases} F_1(V_1) = min\,[\,\sum_{ii=1}^{sn} PL_{ii}(\,x_2\,,\,y_2\,,\,x_n\,,\,y_n\,,\,T_0\,,\,\Sigma_\rho\,)\,] \\ \\ F_{si}(V_{si}) = min\,[\,\sum_{ii=1}^{sn} PL_{ii}(\,x_{si}\,,\,y_{si}\,,\,x_{si+1}\,,\,y_{si+1}\,,\,T_0\,,\,\Sigma_\rho\,)\,] \\ step \quad si = 2, 3, \,...\,(sn-1) \\ \\ F_{sn}(V_{sn}) = min\,[\,\sum_{ii=1}^{sn} PL_{ii}(\,x_{sn-1}\,,\,y_{sn-1}\,,\,x_{sn}\,,\,y_{sn}\,,\,T_0,\,\Sigma_\rho\,)\,] \end{cases} \tag{3.3}$$

Where the function F is a function/combination of the optimizable parameters X, Y, T_0 and the power loss model constants Σ_ρ. Also, Eq. 3.3's dependency is similar to Eq. 3.1.

The formulation of accumulation of optimized sub-problems in Eq. 3.3 leads to the optimization of the entire FEAD when the last step (sn^{th} step in Fig. 3.13) is performed.

Details on the implementation of the multi-DP-optimization-steps FEAD decision model (Fig. 3.13) are given in Appendix *A*9.

Note that similar to the optimization via GA, in this case, the optimizable parameters are generated within a range (Figs. 3.2 and 3.3) between maximum (x_{max} , y_{max}) and minimum (x_{min} , y_{min}) positions (Fig. 3.10). However, using DP the power losses (PL_i) are optimized following essential steps (Fig. 3.13). At the end, the output of the DP optimization model is a set of optimal parameters enabling to minimize the power losses in a FEAD due to the belt-hysteresis, belt-pulleys slip and bearings power loss (Eq. 2.1).

3.5 NUMERICAL AND EXPERIMENTAL RESULTS

Simulation and experimental results are presented for the serpentine drive system defined in Tab. 3.2 and presented in Fig. 3.14.

Table 3.2 – FEAD example. Initial data.

	Pulley			Shaft			
	x_c (mm)	y_c (mm)	d (mm)	SKF ref. (FRONT & REAR)	L2(mm)	L3(mm)	C (N. m)
CS	0	0	222	Tapered roller	130	94	11.7
AD1	-380	246.5	126	Angular contact ball	160	104	0
AD2	-414	0	158	Angular contact ball	160	104	5.8
Idler	-253	-40.5	90	Deep groove ball	0	0	0

Figure 3.14 – Experimental setup considered for FEAD optimization.

In Fig. 3.14, the CrankShaft (CS) is considered to be running at 600 rpm and at 20°C, where the driving torque of 11.7 N.m is applied. The resisting torque of 5.8 N.m is also applied on the shaft AD2. No torque is transmitted by pulley AD1 (Tab. 3.2).

The belt used here has the same characteristics of that in 2.6 except its length of 1715mm. Also, the belt is installed with a setting-tension $T_0 = 600$ N which is representative of industrial applications (Fig. 1.4).

Parameters setting Through the methods listed in Tab. 3.1 the power losses of the FEAD in Fig. 3.14 are minimized by varying the optimizable parameters within the ranges defined in Tab. 3.3, where x_2, x_3 and y_4 are the FEAD pulley-center locations defined by e.g. the engine designer, Δx and Δy the variation steps of the optimizable parameters for which the results were obtained. The ranges of variation in x and y are the dimensions which in practice (Fig. 1.4) are imposed by geometrical constraints of the neighbors' accessory drive (AD) systems. In Fig. 3.14, one could vary the ADs position of the dimensions in Tab. 3.3.

Table 3.3 – Setting of pulley-center location optimization parameters (mm).

	No.	Range x	Range y	Δx	Δy
CS	1	0	0	0	
AD1	2	$x_2 \pm 80$	0	5	
AD2	3	$x_3 \pm 16$	0	2	
Idler	4	0	$y_4 \pm 60$	2	

The theoretical minimal setting tension $T_{0min} = 57$ N for preventing pulley/belt gross slip is predicted by [30]. Thus, to properly transmit power and avoid belt-life reduction a reasonable range of the setting tension is chosen to be from 100 to 700 N. Moreover, to efficiently and quickly find the optimal solution, a precision of $\Delta T = 100$ N is used.

3.5.1 Simulations

Firstly, by using the power loss models in Eq. 2.1 one can simulate the corresponding power losses for the FEAD in Fig. 3.14. Then as in chapter 2, the losses in Watts can be represented in the form of a power loss map (Fig. 3.15).

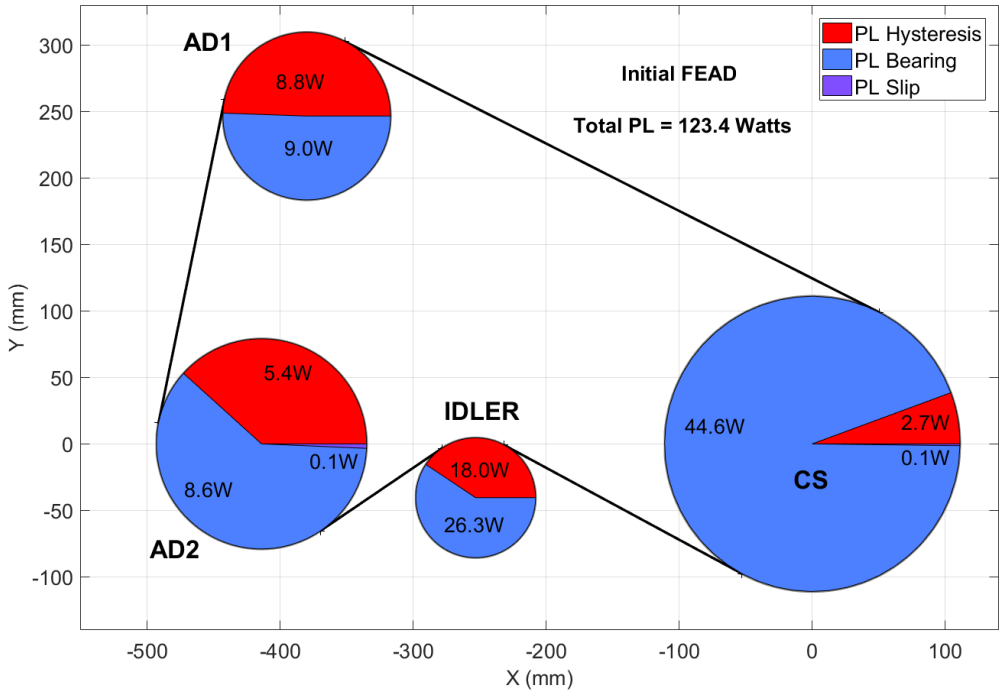

Figure 3.15 – Initial Power Loss Map (PLMap).

Secondly, to have a reference for the optimizations methods in Tab. 3.1 the minimal FEAD power losses are also obtained using brute force (Fig. 3.16).

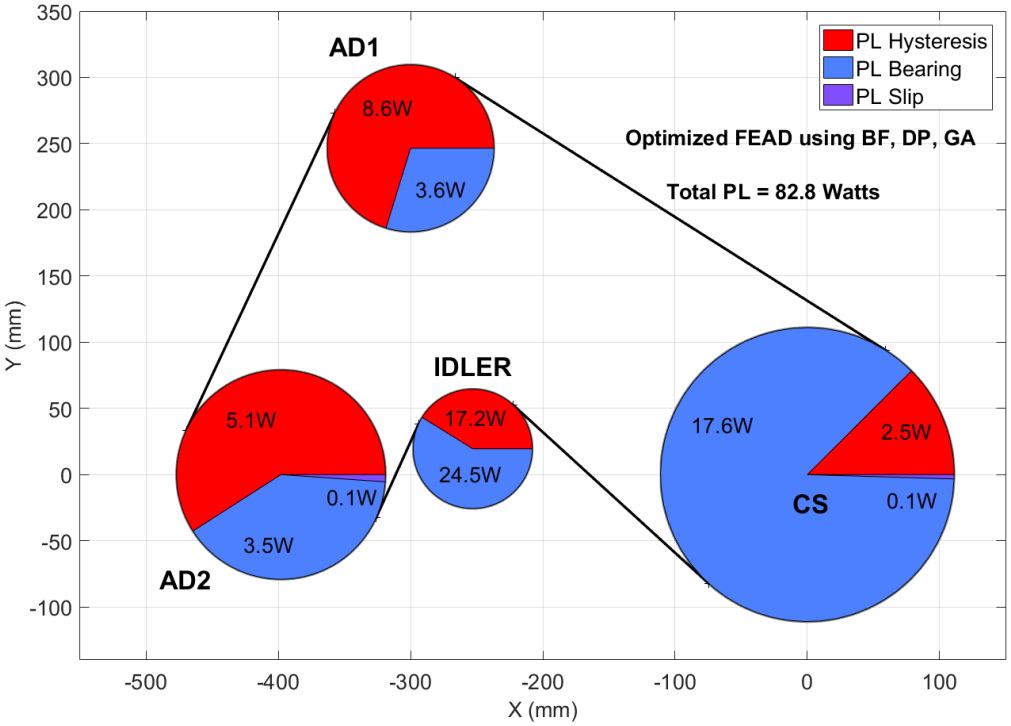

Figure 3.16 – Power loss map with X, Y, T_0 (100 N) optimized.

The optimal power loss map using the three different methods are the same (Fig. 3.16).

Moreover, the changes from the initial (Fig. 3.15) to the optimized FEAD in Fig. 3.16 can be observed by comparing Tab. 3.2 with Tab. 3.4.

Table 3.4 – Optimized geometry of the FEAD in Fig. 3.16.

	x_c (mm)	y_c (mm)
AD1	-300	246.5
AD2	-398	0
Idler	-253	19.5

In all cases, BF, DP and GA, the belt setting-tension has also been decreased to the lower bound $T_{0min} = 100$ N chosen in the previous section.

The results in Tab. 3.4 are the geometric parameters which give optimal wrap angles providing a good compromise between the parameters of the PL models in Eq. 2.1.

Similarly, for the setting tension and the range considered to be from 100 to 700 N the optimization algorithms converge to the lower bound setting tension because this is the tension which renders the lowest bearings hub-load, thus lowest friction moment meaning less power dissipated [42].

To obtain the optimal results (Fig. 3.16) the GA was set up according to Tab. 3.5 which represents the GA parameters empirically chosen to obtain the fastest convergence. Table 3.5 means that at each optimization-iteration, 64 individuals (i.e. FEADs) are generated, from which there are a percentage of elites, crossover and mutations. A stopping criterion is also set-up to stop the optimization after 32 iterations in the case of the FEAD power losses remain without decreasing/optimizing.

Table 3.5 – Genetic algorithm setting parameters for simulation.

Generated FEADs	Elites	Crossovers	Mutations	Stopping criterion
$ng = 64$	10 % of ng	60 % of ng	30 % of ng	32 iterations

To analyze the effectiveness of the optimizations, the initial and the optimized total power losses in Figs. 3.15 and 3.16 are summarized in Tab. 3.6.

Table 3.6 – Summary of simulated power loss in Watts.

	Initial PLMap	BF	GA	DP
Power loss simulated (PLS)	123.4	82.83	82.85	82.83

In Tab. 3.6, the optimized power loss using the genetic algorithm (GA) is not exact because of the heuristic nature of this optimization method, thus, an average value is chosen as the genetic algorithm was executed three times (Tab. 3.7).

Table 3.7 – Summary of GA simulated power loss (3 runs) in Watts.

	Run 1	Run 2	Run 3	Average
Power loss simulated (PLS)	82.83	82.85	82.87	82.85

Comparison of methods

There is no difference between the optimized FEAD geometries using brute force (BF), dynamic programming (DP) and genetic algorithm (GA) (Fig. 3.16), proofing these methods are equally effective to find the optimal solution (Tab. 3.6). However, although the layout of the FEADs using different methods are identical, the computational efforts (time) are not the same (Tab. 3.8). Moreover, a computer equipped with Microsoft Windows 7 operating system, 64 bits, 16GB RAM and 4 CPUs was used in simulations.

Table 3.8 – Comparison of methods to obtain the optimal solution under the same conditions.

Method :	BF	DP	GA
Time (s) :	3079	485	79

Table 3.8 clearly suggests using the genetic algorithm to optimize the FEAD power losses. However, the BF and DP methods present some advantages (Tab. 3.1) and might be used.

Concerning the optimization, from Fig. 3.15 to Fig. 3.16 the total FEAD power loss has substantially decreased and the pulleys-center location were optimized from Tab. 3.2 according to the displacements allowed in Tab. 3.3.

In Fig. 3.16 and Tab. 3.6, the total FEAD power loss is calculated as in Eq. 2.1 and the optimizable parameters are the FEAD geometry (X, Y) and setting tension T_0. However, these parameters could have been optimized separately to figure out the influence of each optimizable parameters. It will be done in the next paragraphs.

Setting tension optimization

In this case, the FEAD geometry (X ,Y) is fixed and equal to that defined in Tab. 3.2. The setting tension is chosen to be optimized in the range from 100 to 700 N (Fig. 3.17).

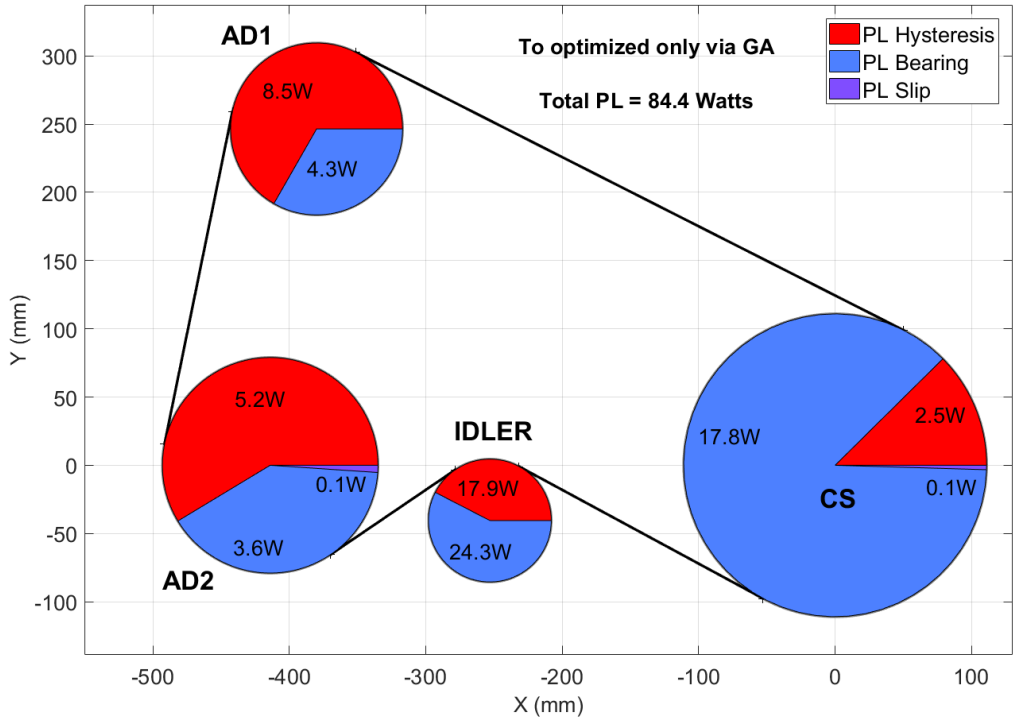

Figure 3.17 – Power loss map using GA with X, Y, fixed and T_0 (100 N) optimized.

From Fig. 3.15 although the geometry remains constant the power loss distribution has been changed and the total power loss has been optimized by around 30% (Fig. 3.17). Naturally, the belt setting-tension has been decreased to the lower bound $T_0 = 100$ N.

The results in Fig. 3.17 confirm that low setting tension leads to low power losses. Indeed, the bearing losses are directly proportional to the bearing radial loads that are related to the belt tension, consequently the lowest setting tension will produce the smallest power losses in the bearings that support the accessory shafts. Then, in this case, as decreasing the belt setting tension is relevant to minimize FEAD power losses, to dissipate less power, lower tensions should be used. As a matter of fact, in practice, to transmit high torques and not to have belt-pulleys gross slip the belt-setting tension is often overestimated.

FEAD geometry optimization

In the case of the geometry optimization, considering the setting tension as fixed and equal to that of the initial case $T_0 = 600$ N. The initial FEAD could be optimized by a few percentage (4.5% or 5.6 Watts) (Fig. 3.18).

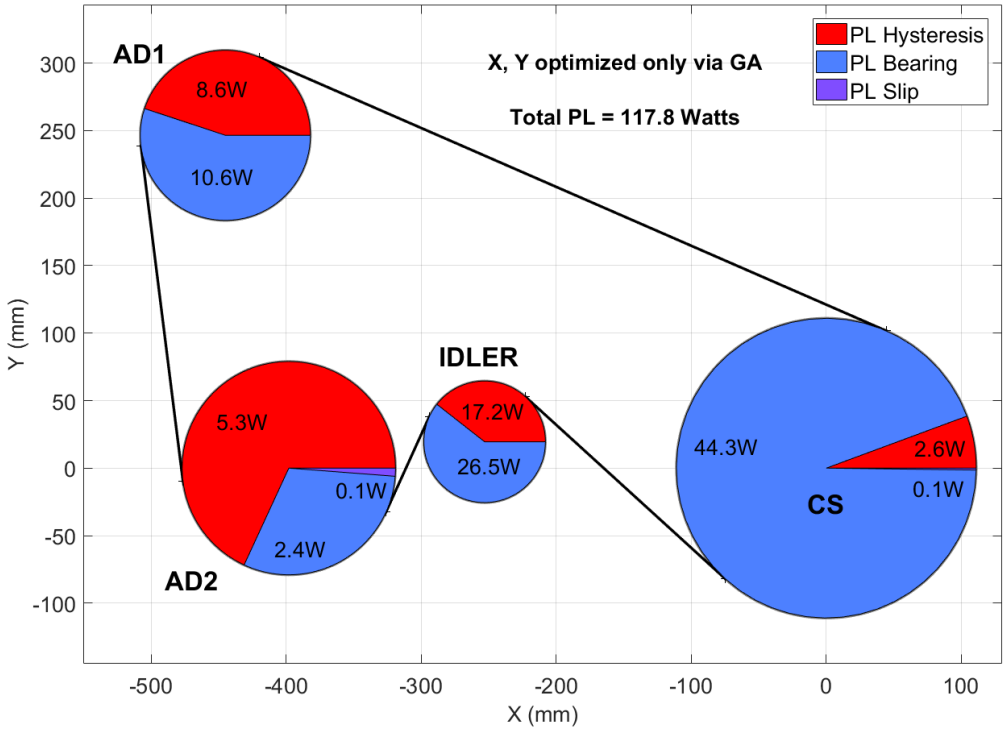

Figure 3.18 – Power loss map using GA with T_0 fixed at 600 N and X, Y optimized.

Table 3.9 – Optimized geometry of the FEAD in Fig. 3.18.

	x_c (mm)	y_c (mm)
AD1	-445	246.5
AD2	-398	0
Idler	-253	19.5

The geometry of the FEAD in Fig. 3.18 and Tab. 3.9 has substantially changed when compared to Fig. 3.15 and 3.16. Also, when compared to the initial case (Fig. 3.15) some power loss amounts have increased and others have decreased to find the geometric parameters that permit optimizing the total FEAD power losses (Eq. 2.1).

Fixed belt-length optimization

In the case where the belt length is considered as a constant and equal to the initial case (1715 mm), the FEAD power losses optimization is performed (Fig. 3.19) with the corresponding optimized pulleys-center positions (Tab. 3.10).

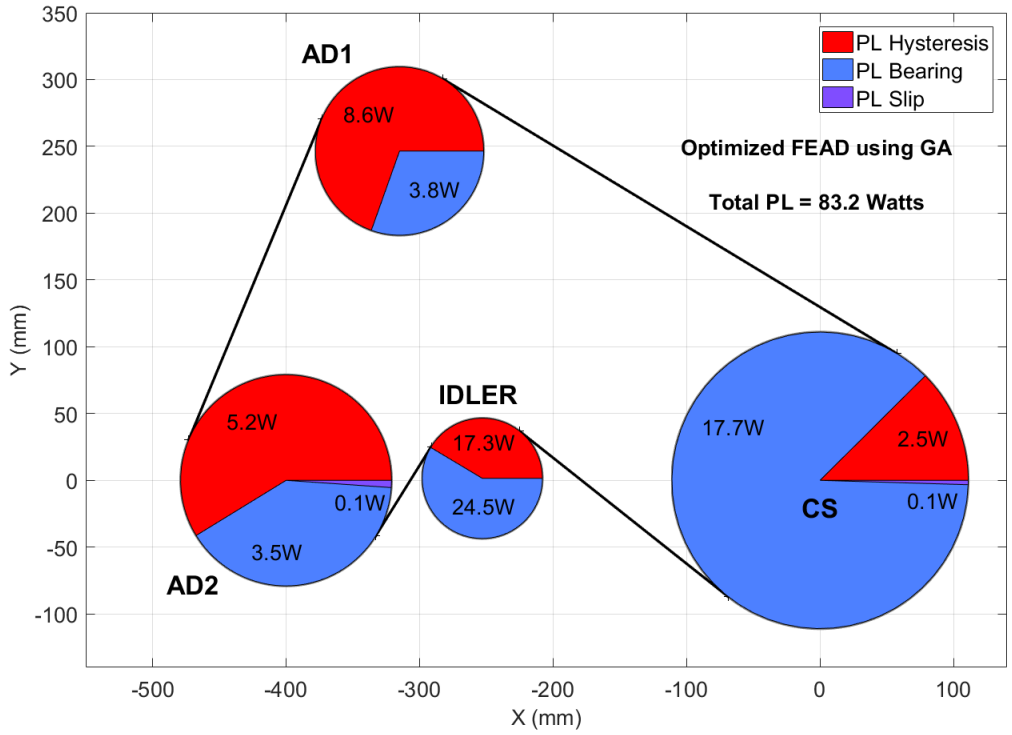

Figure 3.19 – Power loss map using GA with X, Y, T_0 optimized and belt-length fixed.

Table 3.10 – Optimized geometry of the FEAD in Fig. 3.19.

	x_c (mm)	y_c (mm)
AD1	-315	246.5
AD2	-400	0
Idler	-253	1.5

The FEAD layout in Fig. 3.19 is similar to the case where the belt length is not considered as a constant (Fig. 3.16). Indeed, the distributions of the power losses (slices of each pie chart) are the same of those in Fig. 3.16. The only thing that has changed is the magnitude of the power loss due to certain phenomena, e.g. compared to Fig. 3.16 the power losses (PL) Hysteresis on the idler has increased, since the FEAD could not be completely optimized because the constant belt length limits the pulleys degree of freedom.

In practice, to obtain the optimal parameters with the belt length equal to the initial belt-length, during the geometry optimization, the generated FEADs with the same belt length shall be selected. As the genetic-algorithm optimization is a convergent process, it converges towards the optimal solution, the selected FEADs with the same belt-length are energetically better than those from the initial generations.

Finally, the optimization considering the same belt length as a constraint (Fig. 3.19) is not as good as it is in Fig. 3.16. However, considering the same belt length can be an advantage if the FEAD designer does not want to change the FEAD main component, the belt.

3.5.2 Experiments

Experiments have been conducted to evaluate the FEAD power loss models in Eq. 2.1 and to validate the optimization procedure presented herein. The experimental setup is the FEAD with three pulleys and an idler in Fig. 3.14.

Since the test bench in Fig. 3.14 is equipped with a speed and torque measuring system on each shaft, the power supplied (PS) by the crankshaft (CS) and the power consumed (PC) by the accessory drives AD1 and AD2 are known. Thus, the difference between PS and PC is the power lost (PL) in the system (Tab. 3.11).

Table 3.11 – Summary of experimental (measured) results in Watts.

Power		**Initial FEAD layout** (X, Y from initial case and T_0 = 600 N)	**Optimized FEAD layout** (X, Y from same belt-length optimization and T_0 = 100 N)
Supplied by the CS	PS	646.4	601.4
Consumed by AD2	PC	507.1	512.1
Lost in the system	PL	139.3	89.4

Moreover, considering Tab. 3.11, the crankshaft CS in Fig. 3.14 is speed controlled to maintain the speed at 600 rpm. Consequently, the torque (power) supply is tailored (PS in Tab. 3.11), while the power consumed PC by the AD2 remains nearly unchanged: 1% of error due to the test bench electrical driving motor command. Indeed, the power consumed by the accessory drives AD2 remains unchanged because it only depends on its own resisting-torque curve which varies as a function of the speed. If the accessory-drive speed is constant, thus the power consumed PC is also a constant.

The most interesting result in Tab. 3.11 is the power lost in the system, which can be directly compared to that predicted by Eq. 2.1. However, the experimental power losses in Tab. 3.11 are larger than those predicted by Eq. 2.1. The validity of these results is analyzed hereafter.

Thus, in Tab. 3.12 the simulation and experimental results from Tabs. 3.6 and 3.11 are compared and it is worth noting that they are in the same order of magnitude.

Table 3.12 – Summary of simulated and experimental power loss in Watts.

	Initial FEAD	Optimized FEAD
Power loss measured (PLM)	139.3	89.4
Power loss simulated (PLS)	123.4	83.2
Difference PLM – PLS	15.9	6.2

The difference PLM – PLS can also be interpreted as a percentage of the power loss which were not identified/modeled yet. Alternatively, it may be due to the simplistic formulation of the model represented by Eq. 2.1. However, in Tab. 3.12, an interesting aspect is the decreasing of the PLM (measured) from the initial to the optimized case. Therefore, the optimization methods works, what should be done afterwards are: (1) to improve the FEAD PL models (Eq. 2.1); (2) to take into consideration in the generic optimization presented herein all PL phenomena in Eq. 2.1 including $PL_{tens-hys}$ and PL_{vib}; (3) to consider additional optimizable parameters to the FEAD PL optimization-problem.

3.6 SUMMARY AND CONCLUSIONS

Optimization algorithms have been implemented to optimize the power loss of FEADs. Relevant input parameters (pulleys-center location and belt setting tension) have been chosen for the optimization of the FEAD power losses (Eq. 2.1).

Although the design (X, Y) and operating (T_0) parameters are relevant and have been optimized, ideally, every parameter of the PL models in Eq. 2.1 should be optimized.

The optimization of a case study representative of industrial applications has shown that it is possible to optimize the FEAD power losses by at least 4.5% (5.6 W) (Fig. 3.18).

Simulations and experimental results have shown that the optimization algorithms were able to optimize the FEAD total power loss since the measured power losses are decreased from the initial to the optimized cases (Tabs. 3.11 and 3.12).

The genetic algorithm (GA) performs the FEAD power losses optimization faster, with less computational effort, than other methods (BF and DP) (Tab. 3.8).

In all cases (BF, DP and GA), the optimization or minimization of the FEAD power losses was performed from a global point of view, considering only the total power loss as criterion or function to be minimized (Eq. 2.1). However, the optimization process could have been more sophisticated to confirm, understand and improve the following checks: (1) the bearings power losses are mainly minimized by changing the belt setting tension; (2) the belt-hysteresis power losses are mainly optimized by adjusting the belt wrap angles of the pulleys; (3) the FEAD power losses due to belt-pulleys slip are not affected by the optimization since the setting tension T_0 is ranging over the slip limit tension. The third point might have been distinct under different FEAD operating conditions.

A supplementary fitness function could be considered in future works regarding, e.g. the belt transverse vibrations frequency. Indeed, if any excitation (engine torque fluctuation) is considered and the present setting tension T_0 optimization is performed, in this case, the optimized (low) T_0 leads to low critical frequencies increasing the risk of transverse vibrations occurrence.

In the case of industrial applications (Fig. 1.4), to minimize engines fuel consumption and properly design the FEADs not only parameters which respect the functional specifications (e.g. Tab. 3.2), but also parameters which reduce the power losses in the power transmission should be used (e.g. Tab. 3.4).

Chapter 4

EXPERIMENTAL VERIFICATION

Contents

This chapter presents the experiments which have served to validate the FEAD power losses. Firstly, elementary configurations of FEADs such as those presented in the chapters 2 and 3 were tested to validate the theory. Secondly, the FEADs EURO-6 and EDIT were considered to evaluate the total power loss dissipated in industrial applications by Volvo. The experiments were conducted at the Laboratory of Contact and Structural Mechanics (LaMCoS) at INSA Lyon in France.

4.1 TEST FIXTURE

The test fixture consists of a chassis mounted on a concrete slab (Fig. 4.1).

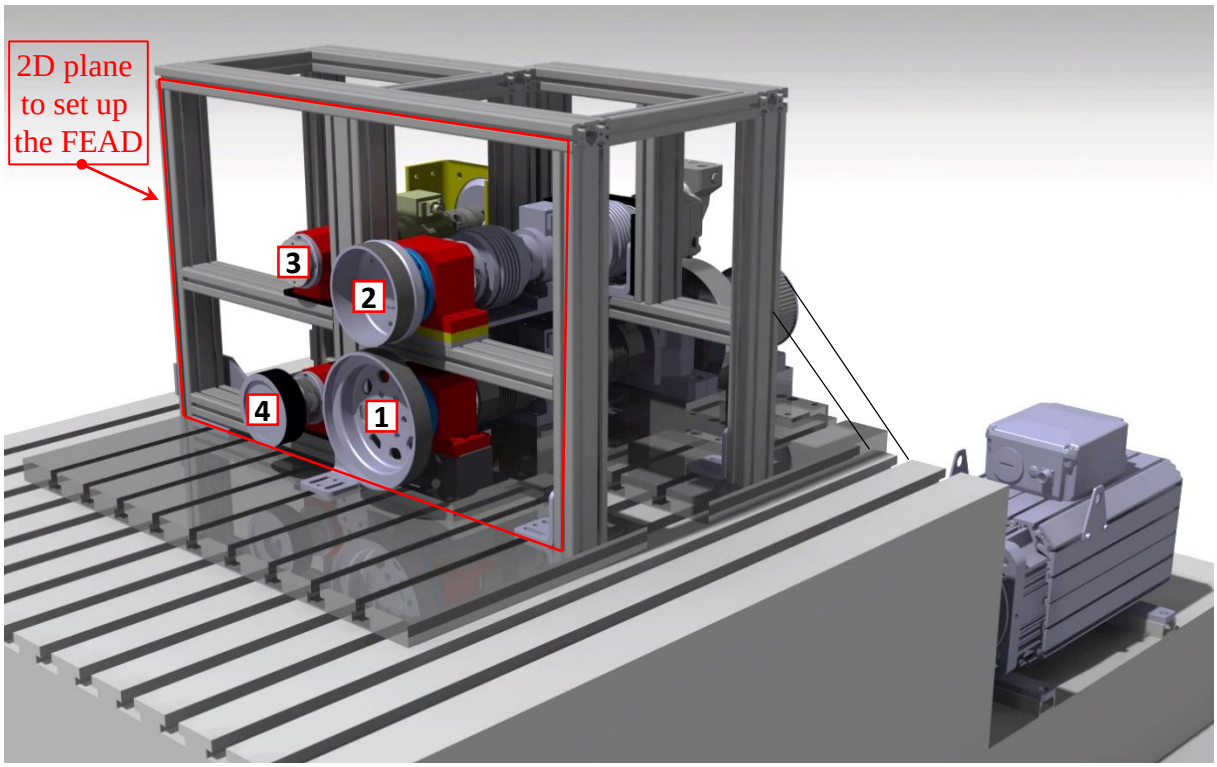

Figure 4.1 – CAD-based digital mock-up of the test bench.

To represent the accessory drives of a FEAD, on the shafts 1, 2, 3 and 4 of the test bench in Fig. 4.1 there are a 51.3 kW driver eletric motor, a hydraulic pump, an alternator and a 11 kW driven eletric motor, respectively. The hydraulic pump was chosen to guarantee, in case of need, high resisting torques as the one imposed by the water-pump and the fan in the FEADs of the engines of Renault Trucks.

As previously mentioned, the test bench in Fig. 4.1 is equipped with a speed and torque measuring system on each shaft, the power supplied (PS) by the crankshaft (shaft 1) and the power consumed (PC) by the accessory drives (shafts 2, 3, 4, ...) are known/measured. Thus, the difference between PS and PC is the power lost (PL) in the FEAD.

The diagram in Fig. 4.2 shows the measurement principle of the FEAD power losses (PL=PS−PC) of the test bench in Fig. 4.1. Indeed, PS and PC are not respectively only the power supplied and consumed but they are the power (torque times angular speed) measured by the speed and torque Measurement Systems MS1 and MS2 in Fig. 4.2.

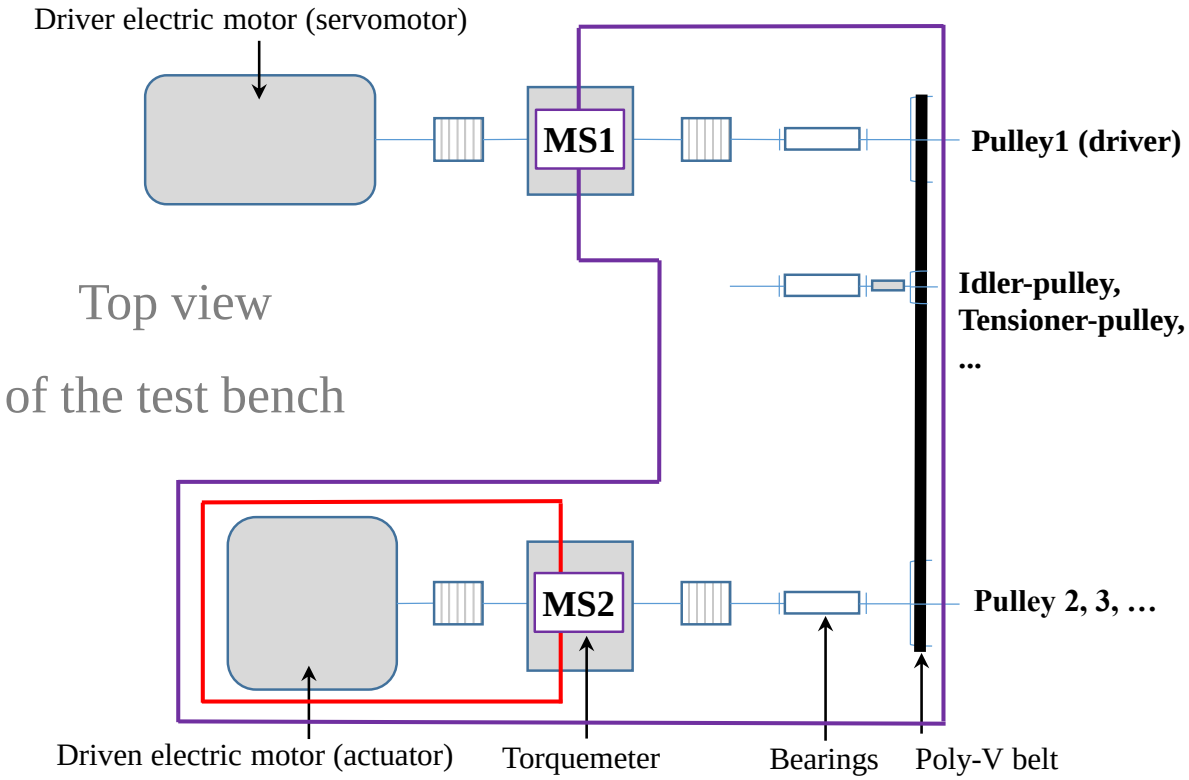

Figure 4.2 – Diagram of the general principle of measure of PL (PL_{FEAD}).

Each shaft of the test bench in Fig. 4.1 is essentially composed of a speed and torque measuring system, a resisting/driving accessory drive and flexible couplings (Fig. 4.3). All of these mechanical parts are supported by bearings which are close to the pulley driven by the poly-V belt.

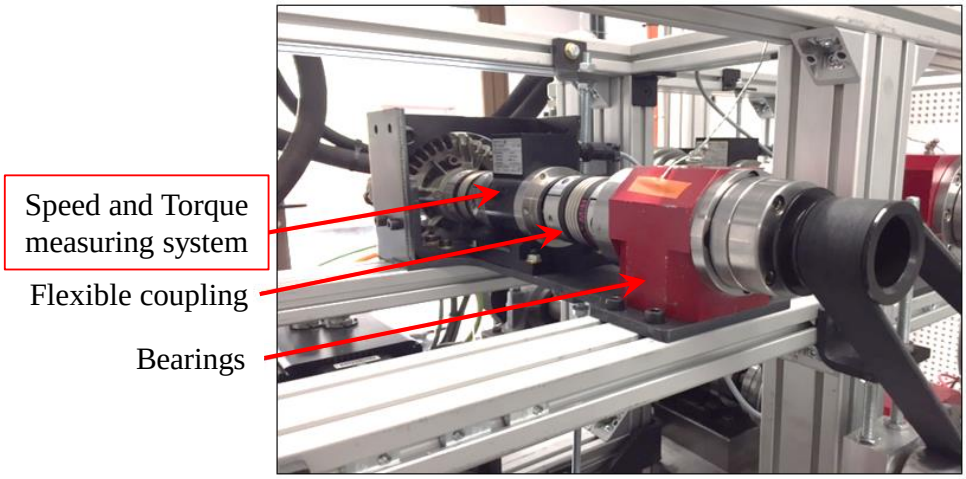

Figure 4.3 – Shaft example (No. 3) of the test bench in Fig. 4.1.

The test bench in Fig. 4.1 was designed to be able to test several configurations of FEADs. Indeed, the shafts can be moved to reproduce the FEADs of interest, i.e. the 2 pulleys, the 3 pulleys and 1 idler-pulley and the industrial applications such as EURO-6 and EDIT presented in the next sections.

4.2 DEVELOPMENT TESTS

The present section will give some examples of transmissions used to verify our modeling during the development phase.

Firstly, the simplest experimental setup is a 2-pulleys belt transmission (Fig. 4.4) used to verify fundamental phenomena such as the belt-bending-hysteresis.

Secondly, with an intermediate complexity the 3-pulleys and 1 idler-pulley FEADs in Figs. 4.6 and 4.7 were used to verify all FEAD power loss phenomena in Eq. 2.1 and establish reliable/useful theories (e.g. [62]) as in chapters 2 and 3.

Finally, the EURO-6 and EDIT layouts in Figs. 4.8 and 4.11 were considered to evaluate the power losses in industrial applications of FEADs designed by Renault Trucks.

No acyclism is considered in all case studies since it is not mechanically possible to be generated with the current version of the test bench.

4.2.1 2 pulleys system

The 2-pulleys belt transmission was tested considering 2 setups (A and B in Fig. 4.4).

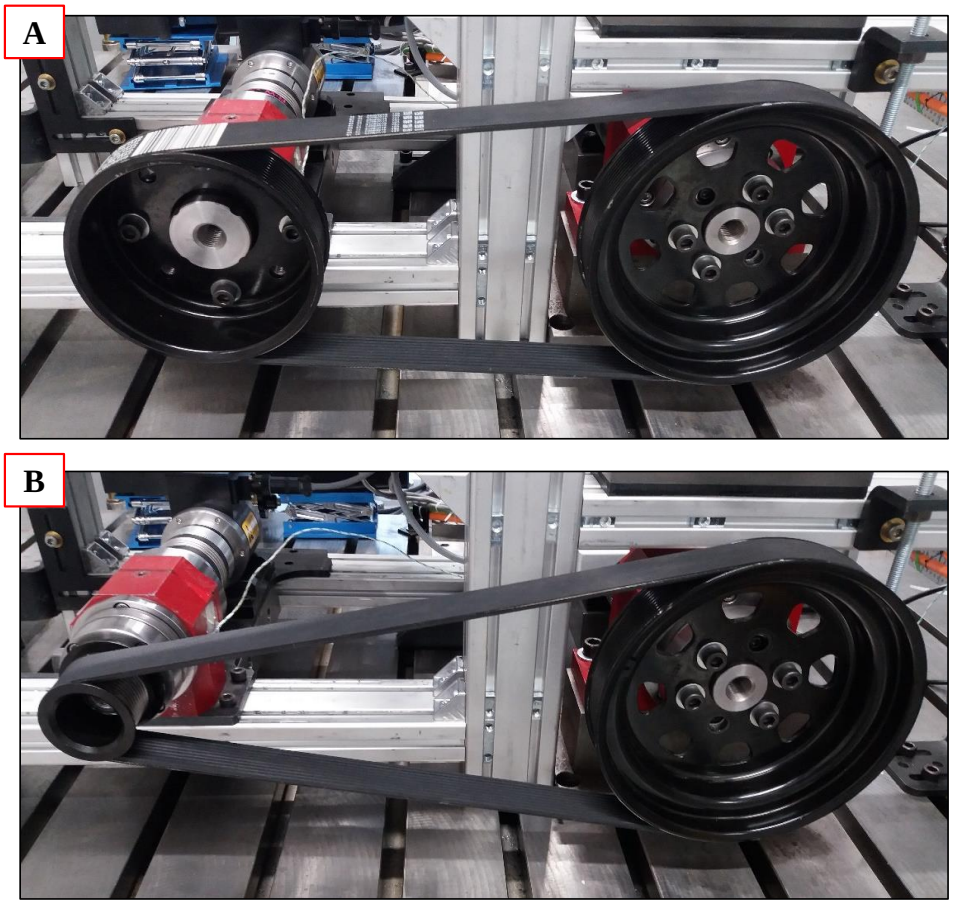

Figure 4.4 – 2 pulleys poly-V belt transmission, experimental setups.

In both setups A and B in Figs. 4.4 and 4.5:

- the same belt (Tab. 2.6) of length 1350 mm is used;
- the belt is installed with the setting tension $T_0 \approx 280$ N;
- no resisting torque is imposed on the driven (left) pulley;
- the CS, (right) pulley, is considered to be running at 600 rpm.

The results of the simulations of the setups in Fig. 4.4 are shown in Fig. 4.5.

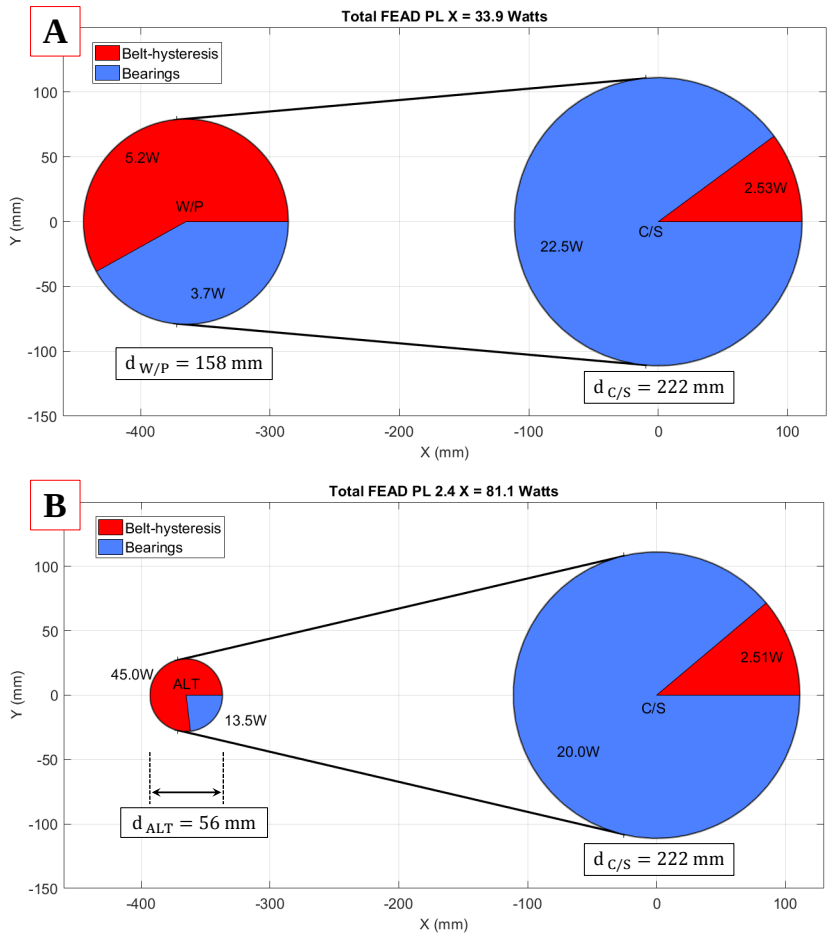

Figure 4.5 – 2 pulleys poly-V belt transmission, simulations of the FEADs in Fig. 4.4.

It is observed that the total power loss dissipated X ($\sim 34W$) is increased to 2.4X from the layout A to layout B (Fig. 4.5). In parallel, a close amount (2.1X) to that calculated numerically is also observed during the tests (Fig. 4.4). This comparison shows quite good agreement and permits validating partially the modeling in chapter 2.

It is worth noting that changing from layout A to B as in Fig. 4.4 permits mainly highlighting the belt bending-hysteresis dissipation mode. Indeed, with a smaller driven pulley (layout B) the belt is more bent than when considering the layout A. That is why the difference of around 45 Watts by belt-hysteresis on the driven pulley.

Moreover, from A to B in Fig. 4.5, the bearing power losses: (1) have slightly changed on the CS, firstly because the vectors orientation corresponding to the belt-span tensions have slightly changed, secondly because the CS runs at constant speed (600 rpm); (2) have significantly increased on the driven pulley, not only due to the change in the belt-spans vector direction, but also they have increased proportionally to the driven pulley rotation speed ratio increase of 158/56.

4.2.2 3 pulleys and 1 idler-pulley

Both Figs. 4.6 and 4.7 present an increase in complexity when they are compared to the 2-pulleys belt transmission system previously analyzed. In chapter 2 and 3 they are useful to validate the theory of power losses in FEADs and the associated optimization.

Figure 4.6 – FEAD case study used to validate the modeling of PL_{FEAD}.

Figure 4.7 – FEAD case study used to validate the optimization of PL_{FEAD}.

4.3 INDUSTRIAL CASE STUDIES

4.3.1 EURO-6

After performing the development tests which have permitted verifying with good agreement the power losses modeling and the associated optimization in chapter 2 and 3. Now, the FEAD of the standard engine EURO-6 (Fig. 1.4) is evaluated. It will be useful to have an idea of the loss of power in an industrial case, but also to serve as a reference for future FEAD designs such as EDIT presented in the next section.

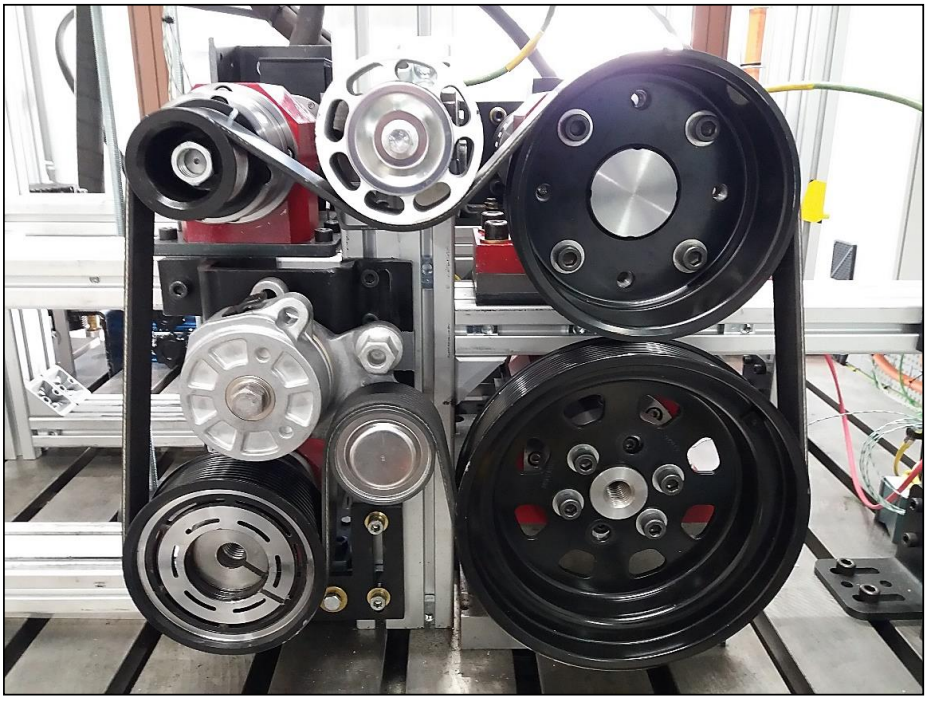

Figure 4.8 – EURO-6 experimental setup.

Let us consider the power loss simulations in Fig. 4.9, the belt is the same of that used in the development tests. It is also installed with a setting tension $T_0 = 456$ N. The engine (CS) is considered to be running at 600 rpm and the environmental temperature is $20°C$.

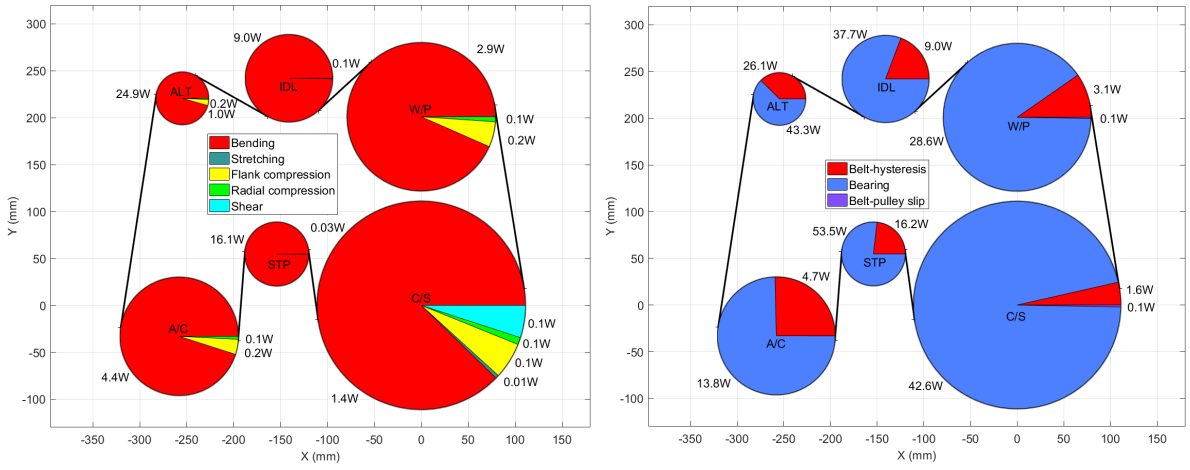

Figure 4.9 – EURO-6 power loss maps (CS at 601 rpm, $20°C$ and $T_0 = 456$ N).

Thus, belt-hysteresis and global (belt-hysteresis, bearings and slip) power loss maps as in chapter 2 are generated (Fig. 4.9). Next, the FEAD total power loss are obtained for several operating conditions (Tab. 4.1) and presented in Fig. 4.10 and Tab. 4.2.

Table 4.1 – EURO-6 torques in N.m for simulations and experiments (Fig. 4.10).

CS speed (rpm):	601	999	1497	Type
CS	15.0	18.4	22.7	Driving
WP	5.5	7.5	10.2	Resisting
ALT	0.2	0.3	0.3	Resisting
AC	0.6	0.6	0.7	Resisting

Indeed, as previously mentioned, the CS is speed controlled. Thus, to maintain the required CS speed the driving torque, which ranges from 15 to 22.7 N.m, is measured on the crankshaft (CS) as a function of its speed (Tab. 4.1). Similar analyses can be made on the others accessory drives WP, ALT and AC as a function of the CS speed.

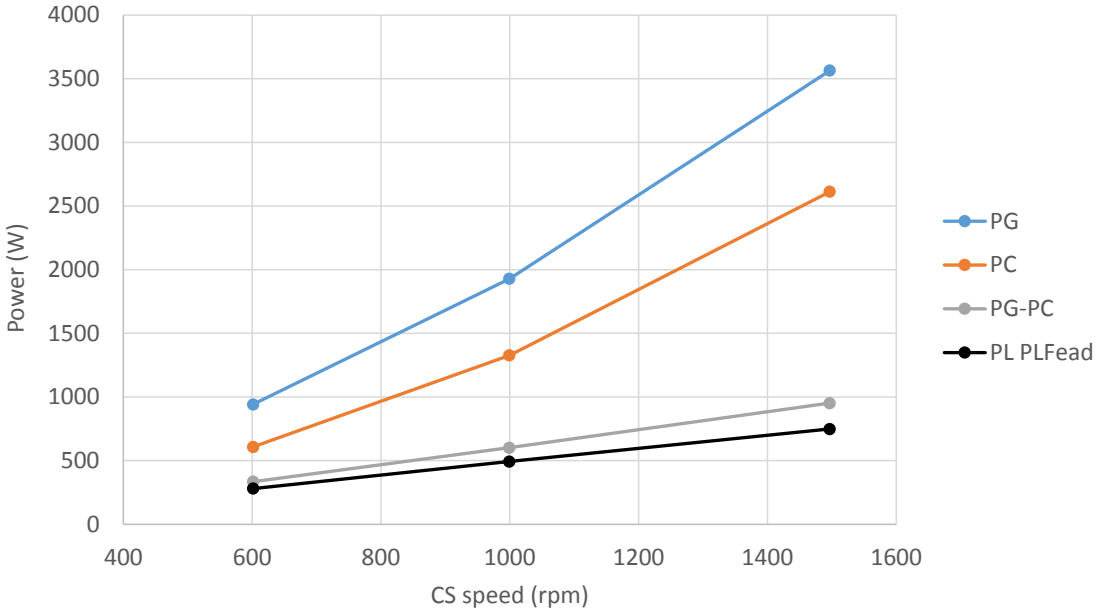

Figure 4.10 – Comparison of experimental and simulation results for EURO-6 ($20°C$, $T_0 = 456$N).

In Fig. 4.10, it can be noticed that the power generated (PG) by the driver pulley is obviously larger than the power consumed by the accessory drives (PC). The difference between them represents the power lost (PL) in the FEAD according to the principle in Fig. 4.2. So, a direct comparison between PG-PC and PL by PLFead* as in Tab. 4.2 permits partially confirming the developed theory.

Table 4.2 – Summary of the experimental and simulation results in Fig. 4.10.

		Power generated	Power consumed	Difference	PLFead	Relative error
To (N)	CS speed (rpm)	PG (W)	PC (W)	PG-PC (W)	PL (W)	%
456	601	942	607	335	280	16
456	999	1929	1327	602	493	18
456	1497	3564	2613	951	748	21

Although the relative error between measured (PG-PC) and simulated (PL PLFead) power losses is around 18% in Tab. 4.2, which is not enough to confirm the power loss modeling, their behaviors are similar: increasing from 601 to 1497 rpm and with a nearly constant difference between PG-PC and PL PLFead throughout the CS speed range.

*PLFead stands for Power Loss (PL) Front engine accessory drive (Fead). This is a simulation tool which was developed and implemented in parallel with the development of the (power loss and optimization) theories and will be presented in the next chapter.

4.3.2 EDIT

Simulations and experiments were also conducted on the prototype of EDIT (Fig. 4.11). As in Fig. 4.8, the pulleys are the same of those indicated by the functional specifications file (confidential) and the belt is also the same of that used in the development tests.

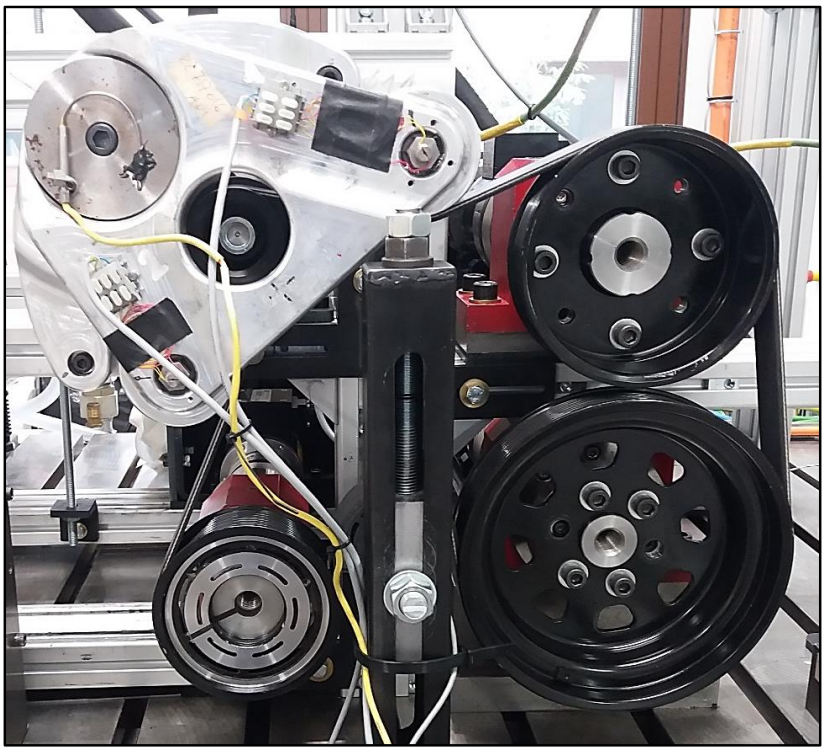

Figure 4.11 – EDIT experimental setup.

For the power loss simulations in Fig. 4.12, the belt is installed with a setting tension $T_0 = 530$ N, the CS is considered to be running at 600 rpm and the environmental temperature is $20°C$.

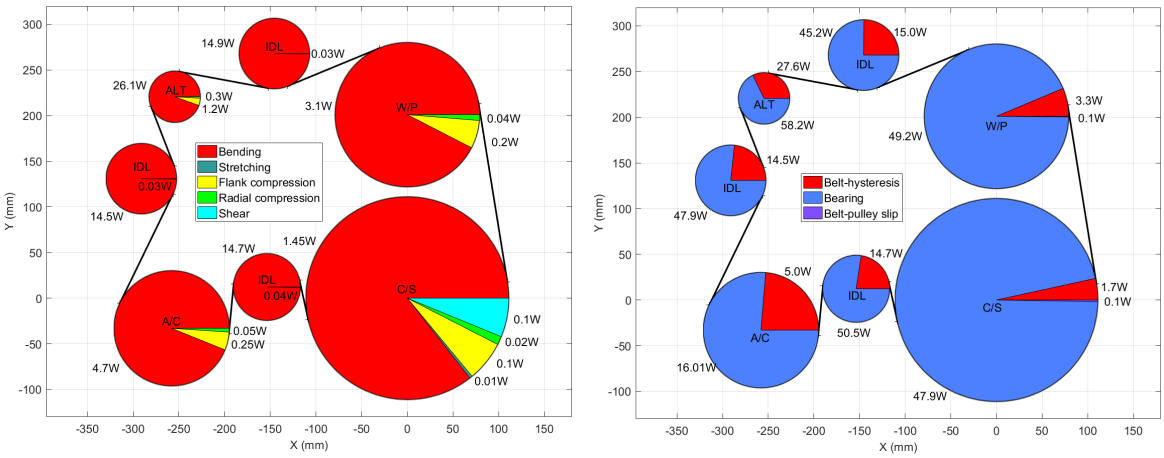

Figure 4.12 – EDIT power loss maps (CS at 601 rpm, $20°C$ and $T_0 = 530$ N).

By comparing Fig. 4.12 with Fig. 4.9 one can note that the distributions of power losses in both cases are globally similar, with the exception of a supplementary dissipative idler-pulley (IDL) between the accessory drives ALT and AC. Moreover, even if in the case of Fig. 4.12 the setting tension T_0 is higher than in Fig. 4.9, which increases the FEAD total power losses, EDIT layout dissipates more power than EURO-6 layout not only due to the supplementary idler-pulley but also due to the belt-bending-hysteresis.

In Figs. 4.13, 4.14 and 4.15 the FEAD power generated by the CS (PG), consumed by the accessory drives (PC), lost measured (PG-PC) and simulated by the simulation tool PLFead (PL) are presented as a function of CS speed for three belt setting tensions.

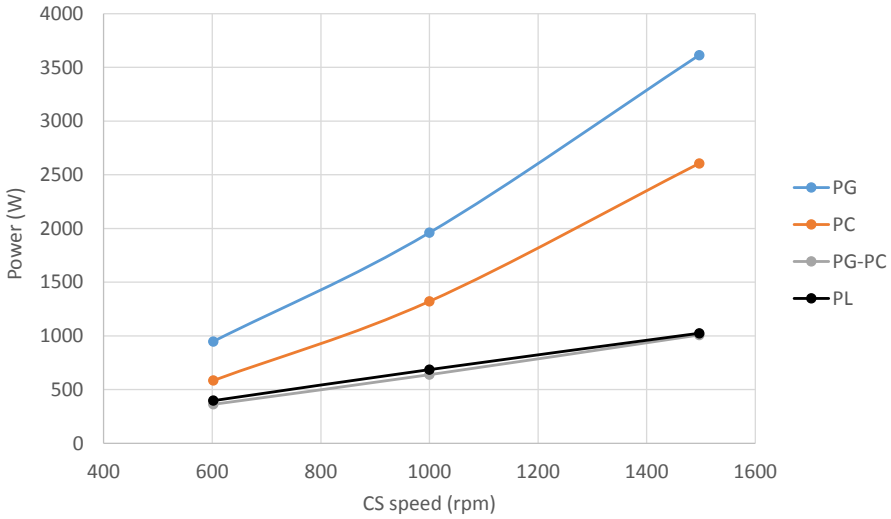

Figure 4.13 – Comparison of experimental and simulation results for EDIT ($20°C$, $T_0 = 530$N).

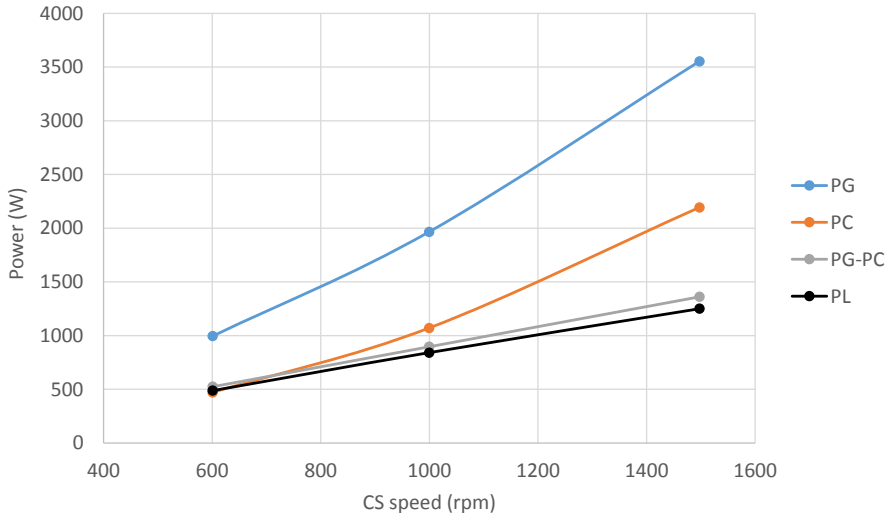

Figure 4.14 – Comparison of experimental and simulation results for EDIT ($20°C$, $T_0 = 980$N).

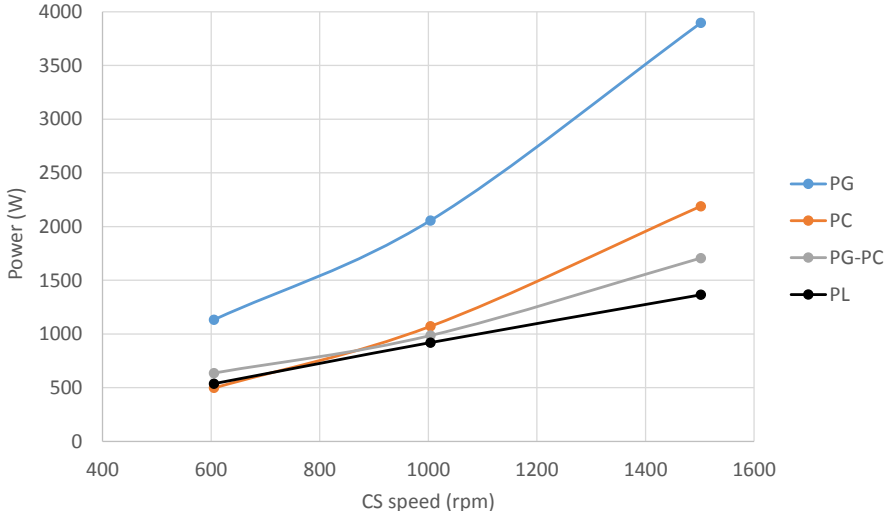

Figure 4.15 – Comparison of experimental and simulation results for EDIT ($20°C$, $T_0 = 1200$N).

The corresponding summary of power losses of Figs. 4.13, 4.14 and 4.15 are presented in Tabs. 4.3, 4.4 and 4.5.

Table 4.3 – Summary of the experimental and simulation results in Fig. 4.13.

		Power generated	Power consumed	Difference	PLFead	Relative error
To (N)	CS speed (rpm)	PG (W)	PC (W)	PG-PC (W)	PL (W)	%
530	602	948	584	363	397	9
530	1000	1960	1321	639	686	7
530	1497	3613	2605	1008	1024	2

Table 4.4 – Summary of the experimental and simulation results in Fig. 4.14.

		Power generated	Power consumed	Difference	PLFead	Relative error
To (N)	CS speed (rpm)	PG (W)	PC (W)	PG-PC (W)	PL (W)	%
980	601	995	471	524	488	7
980	1000	1966	1070	896	841	6
980	1498	3554	2193	1361	1250	8

Table 4.5 – Summary of the experimental and simulation results in Fig. 4.15.

		Power generated	Power consumed	Difference	PLFead	Relative error
To (N)	CS speed (rpm)	PG (W)	PC (W)	PG-PC (W)	PL (W)	%
1200	605	1133	497	635	537	15
1200	1004	2056	1071	985	920	7
1200	1502	3896	2190	1706	1365	20

Regarding the operating conditions of the EDIT setup, the torques measured when the CS is controlled to maintain the required speed of around 600, 1000 and 1500 rpm in Tabs. 4.3, 4.4 and 4.5, are close to those in Tab. 4.1. Indeed, it was observed that the driving and resisting torques do not change significantly ($< 10\%$, i.e. < 2 N.m) with neither the FEAD layout (EURO-6 or EDIT) nor the belt setting tension ($456 \leq T_0 \leq 1200$ N).

4.3.3 SUMMARY AND CONCLUSIONS

The belt transmissions verified using the test bench in Fig. 4.1 increase in complexity from a basic 2-pulleys system to industrial applications EURO-6 and EDIT. The 3 pulleys and 1 idler-pulley case study permits justifying more phenomena than the case with 2 pulleys and validating the power loss and optimization theories. After the development cases, the FEAD total power losses are verified for the industrial applications.

From a technical side, the power loss comparisons in this chapter show quite good agreement and permit validating the power loss models in Eq. 2.1. More specifically, note e.g. that in Figs. 4.13 and 4.14 the measured (PG-PC) and simulated (PL) power loss are close to each other. Sometimes the PL is higher than PG-PC showing that the models in Eq. 2.1 can, under certain operating conditions, overestimate the FEAD power losses (but remaining close to) taking place in practice (PG-PC). However, most of the cases (e.g. Tabs. 4.4 and 4.5), even in the case studies of the chapters 2 and 3, the measured (PG-PC) power losses are often greater than the simulated (PL) power losses. It may be due to the fact of not all existing FEAD power loss phenomena have been taken into consideration in the power loss models represented by Eq. 2.1 (e.g. seating and unseating power loss [14]). The results in the Tabs. 4.3, 4.4 and 4.5 confirm that a higher belt setting tension T_0 makes the FEAD dissipating more power loss. Similarly, higher CS speeds mean more power dissipation. Finally, when comparing the FEAD layouts it is shown that the EDIT layout (Fig. 4.12) dissipates more power that the EURO-6 layout (Fig. 4.9). It is, inter alia, because when operating as in Fig. 4.12 the belt is subjected to more loading-unloading cycles since the belt path along the EDIT layout is more sinuous than the belt path along the EURO-6 layout.

Chapter 5

SIMULATION TOOL

Contents

This chapter presents a simulation tool developed and implemented throughout the thesis. Indeed, similarly the research papers which provides scientists with new tools and theories, the present simulation tool provides the engineers of Volvo Trucks with an advanced theory: (1) developed (chapters 2 and 3); (2) validated (chapter 4); and (3) implemented in a friendly simulation environment using MATLAB®.

5.1 PLFead

PLFead (Fig. 5.1) is the name of the simulation tool which stands for Power Losses (PL) Front engine accessory drive (Fead). Indeed, through PLFead it is possible to model a FEAD (create a poly-V belt, position pulleys, etc.), to calculate its geometry, dynamics and, a posteriori, to predict and minimize the FEAD total power losses by optimizing its design parameters (transmission layout) and operating conditions (belt setting tension).

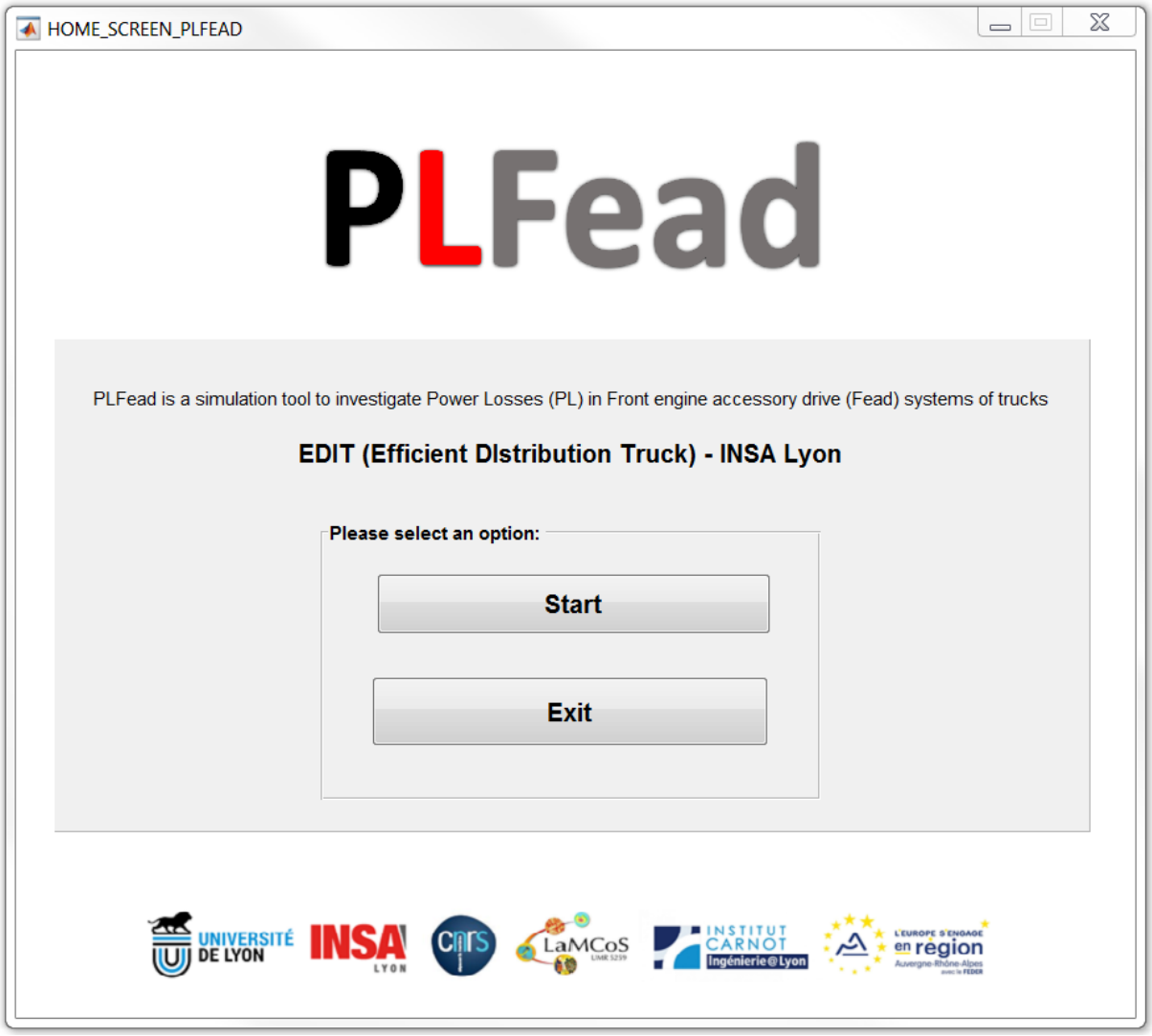

Figure 5.1 – Home screen of PLFead.

The current version of PLFead includes the belt-hysteresis, the belt-pulley slip and the bearings power loss models. Only validated models have been implemented in this tool. Future versions should include the tensioner-hysteresis and belt-vibrations power losses, i.e. the FEAD power losses resulting from the engine torque fluctuations.

5.2 STRUCTURE

5.2.1 Modules

PLFead is divided into three parts:

- Pre-processor
- Solver
- Post-processor

In PLFead, the concept of MATLAB® structures were used. Indeed, the PLFead's user can start a simulation or a project called e.g. EDIT which has a FEAD (i.e. a structure) composed of several other structures corresponding power loss dissipating elements (belt, bearings, tensioners, etc.) and characteristics.

In PLFead, a project or a job corresponds to an analysis of power losses coming from a well-defined belt transmission (geometry, work conditions: kinematics, dynamics, etc.). While executing PLFead routines or after each PLFead step, data files are created (.dat) and associated with the current project. Also, equivalent MATLAB® formatted data files (.mat) are created and available for simulation. These files contain all necessary information for the next PLFead steps.

The pre-processor permits modeling the belt, the pulleys and the ensemble (FEAD), i.e. choosing then assigning material properties to the belt layers, and generating the simulation model in the files (.dat, .lis, .mat). Some files exist only to visualize results and choices until the current point, others to be used in the PLFead Solver.

The solver gets information from the pre-processor, so setting parameters need to be previously informed, mainly those directly involved in the FEAD power losses. However, the main goal at this part of PLFead is to solve all needed equations for calculating power losses in a FEAD.

The post-processor permits, after setting the work context and solving the power loss equations, displaying results (power loss maps), post-processing operations, etc.

The possibility of running PLFead without passing by interface was also implemented. It means that through an external (.dat) file, it is possible to run PLFead, predict and optimize the FEAD, and finally, plot the corresponding power loss maps when required.

The next sections present some examples of the flowcharts of PLFead.

5.2.2 Flowcharts

The flowcharts in Figs. 5.2 and 5.3 present the different components of the Pre-processor and Solver of the simulation tool (PLFead), namely the input files of each routine, sub-routines and resulting files.

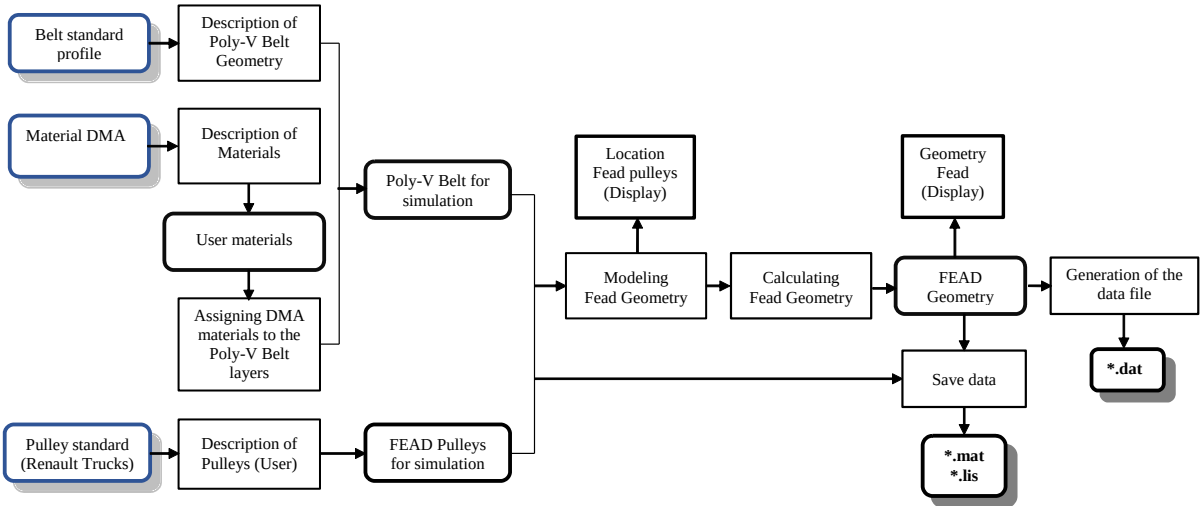

Figure 5.2 – Flowchart of the PLFead pre-processor.

In Fig. 5.2, the blue rounded rectangles represent the external data from experiments, catalog of belts or standard pulleys list of the EDIT project. The black rounded rectangles are data chosen by the user, sometimes standard data modified, or results of the solver. The rectangles represent other functionalities and the small * are output data files.

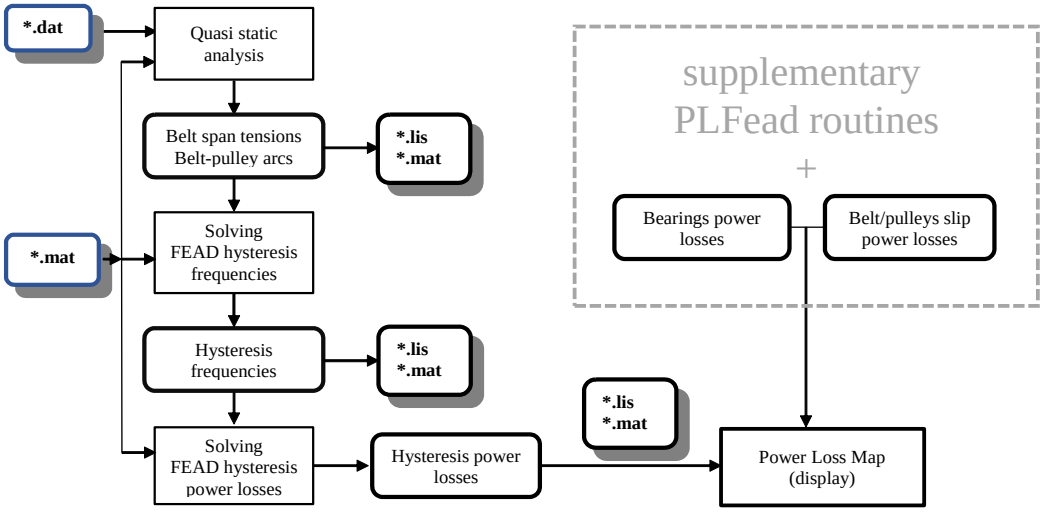

Figure 5.3 – Flowchart of the PLFead solver.

In Fig. 5.3, the blue rounded rectangles above represent the data from the pre-processor of PLFead. For example, the input data file (.mat, .dat) containing the FEAD geometric parameters calculated in the "FEAD Geometry" routine. Moreover, they are input data files to solve for example the energy loss equations. The black rounded rectangles above are resulting data or additional information provided by the user. The rectangles represent other different functionalities of PLFead. The small * are output data files.

5.3 INTERFACES

The next example of interfaces present an easy way to apply the developed theory step-by-step from modeling the FEAD to the optimization of its power losses.

5.3.1 Geometry

First of all, the geometry of belt transmission must be described, i.e. its components such as the belt, the pulleys and the layout. The modeling of the FEAD is possible through the main interface in Fig. 5.4. It appears after pushing the start button in Fig. 5.1.

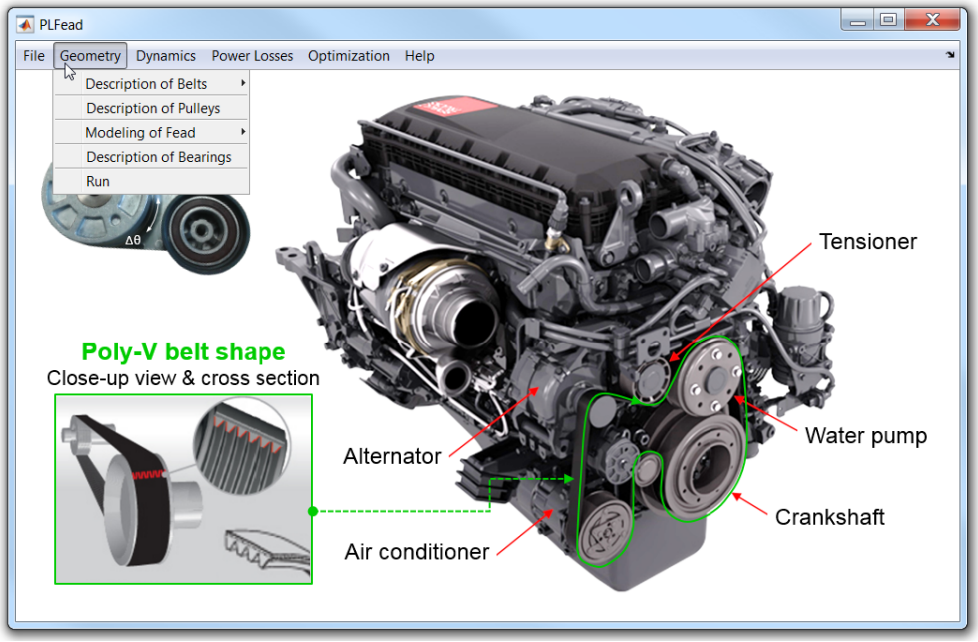

Figure 5.4 – PLFead menus, Geometry.

In PLFead, the belt can also be chosen from a menu of options (Fig. 5.5).

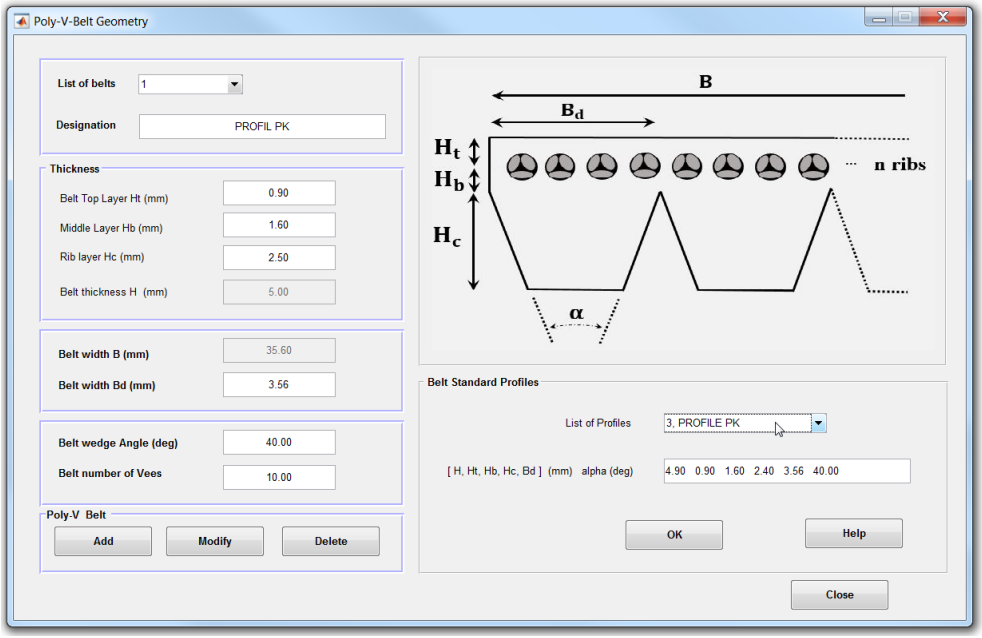

Figure 5.5 – Poly-V belt geometry interface.

Similarly, the pulleys can be chosen from a database, which for a while contains only standard pulleys used in the development tests and industrial case studies in chapter 4. However, the simulation tool can be upgraded with other models of pulleys.

Once all components (belt, pulleys, layout) are declared the geometry of the FEAD is calculated using the formulas in Fig. 5.6.

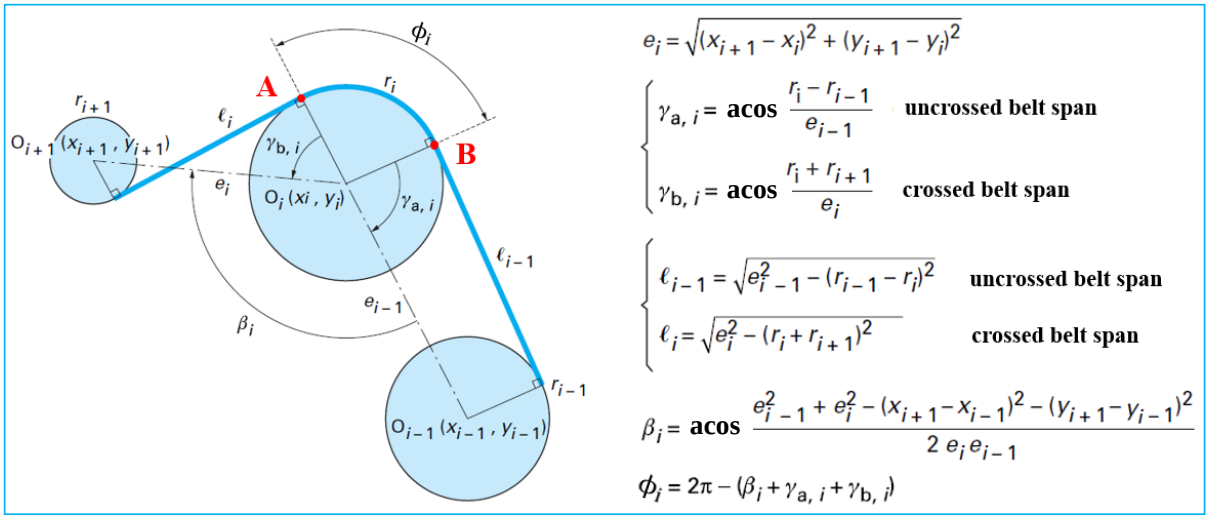

Figure 5.6 – Implemented formulas from [30] for calculating the FEAD geometry.

It is worth noting that Fig. 5.6 is a generic reasoning which is performed for all sets of 3 pulleys composing the FEAD, then the geometric parameters are stored in matrices and plotted as the FEAD example in Fig. 5.7.

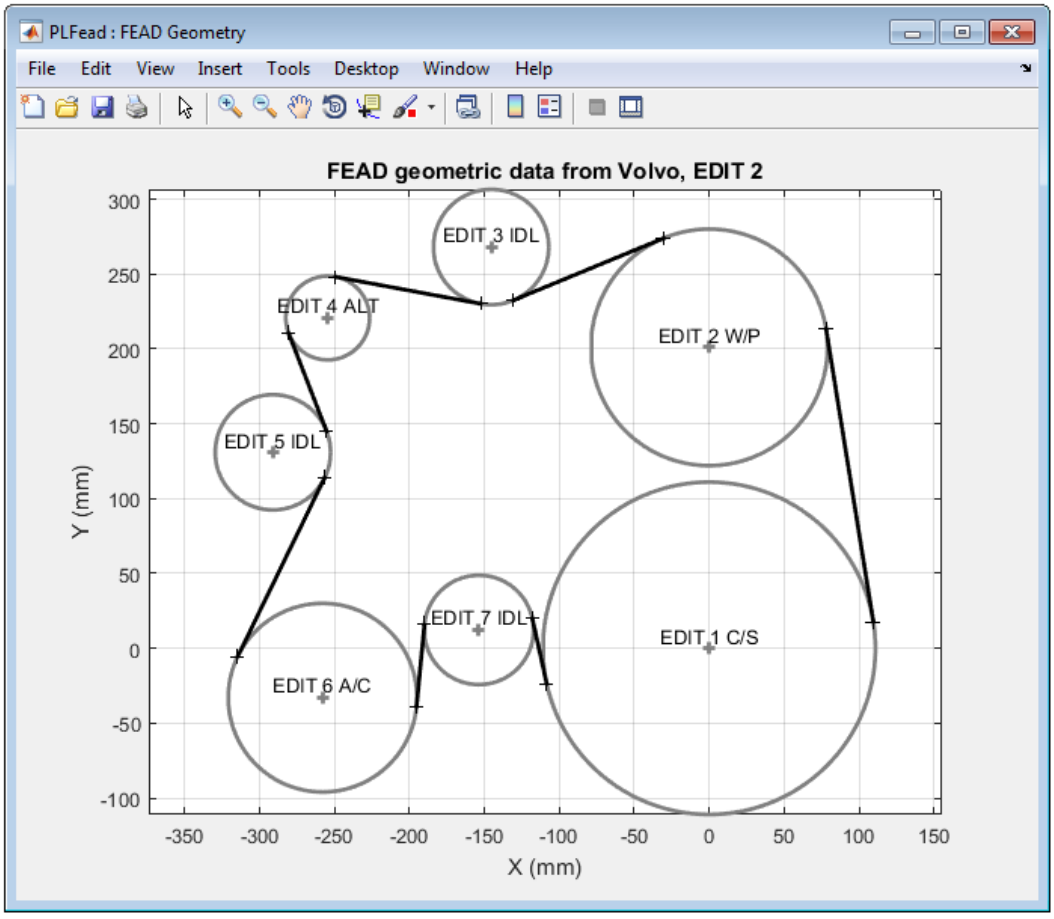

Figure 5.7 – FEAD example after calculating its geometry.

5.3.2 Material

Still in the pre-processor, the viscoelastic properties of the poly-V belt material, which is characterized via DMA as in chapter 2, are also introduced into the database of PLFead and available to be used afterwards in the power loss simulations (Fig. 5.8).

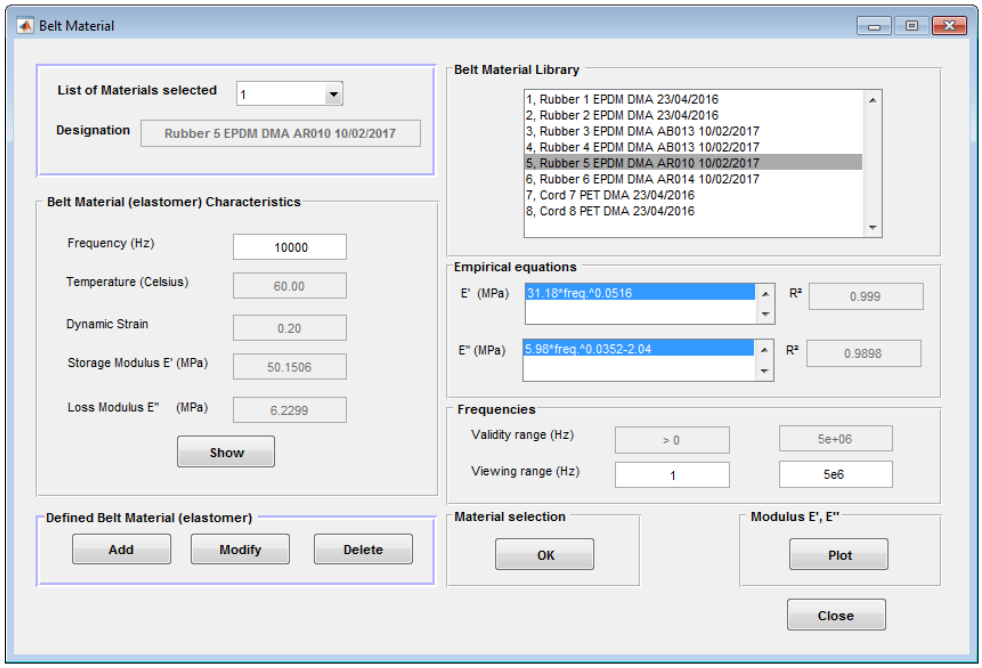

Figure 5.8 – Description of Material DMA, displaying material properties.

The belt properties are available in the form of empirical equations (Tabs. 2.3 and 2.7) and can be consulted (Fig. 5.8) and assigned to the various layers of the belt (Fig. 5.9).

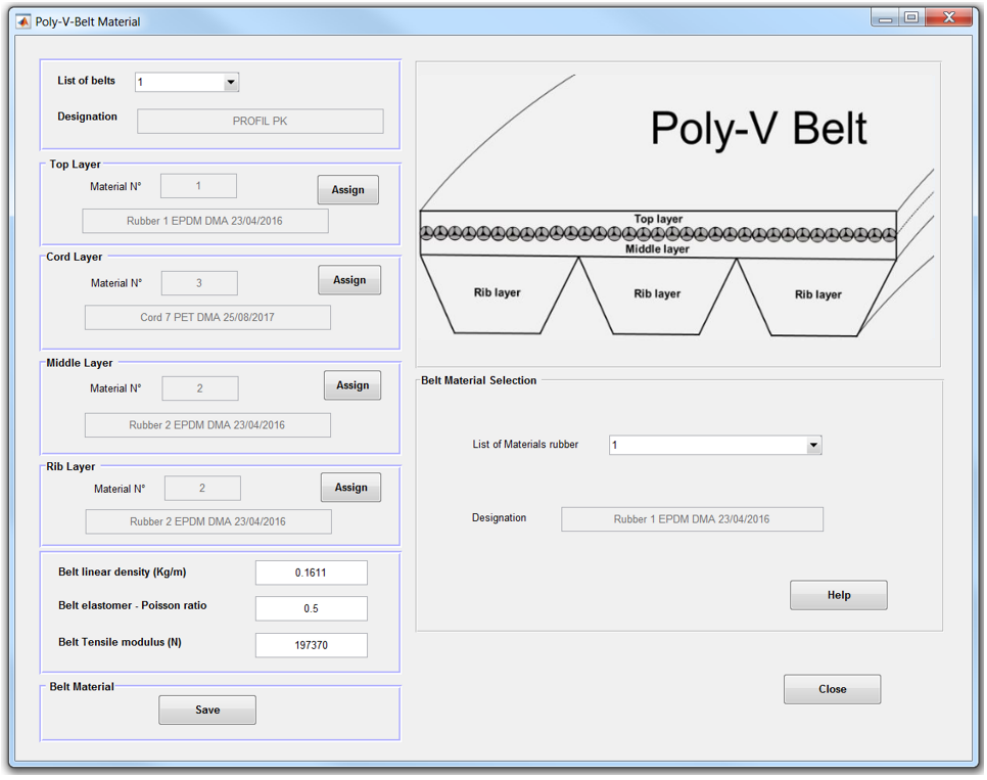

Figure 5.9 – Assignment of poly-V belt materials.

5.3.3 Dynamics

After modeling the FEAD by declaring the belt material/dimensions, the position and characteristics of the pulleys to be used in the power loss simulations. A hybrid discrete-continuous model [63] for the belt dynamics could have been considered since it permits knowing the behavior of the serpentine belt-drive through the dynamic responses. Thus, e.g. if the engine torque fluctuations (acyclism) are considered, the dynamic responses can be calculated as well as the magnitude of the tensioner oscillation necessary to the tensioner-hysteresis power loss model in Eq. 2.57.

Differently of the FEAD power losses modeling (chapter 2) which considers possibly all relevant models (Eq. 2.1), in PLFead only the validated belt-hysteresis, belt-pulley and bearings power losses models were implemented. Therefore, to provide them with basic dynamic information, an equilibrium analysis [2] is satisfactory.

Through the PLFead interface in Fig. 5.10, it is possible to perform an equilibrium or a quasi-static analysis.

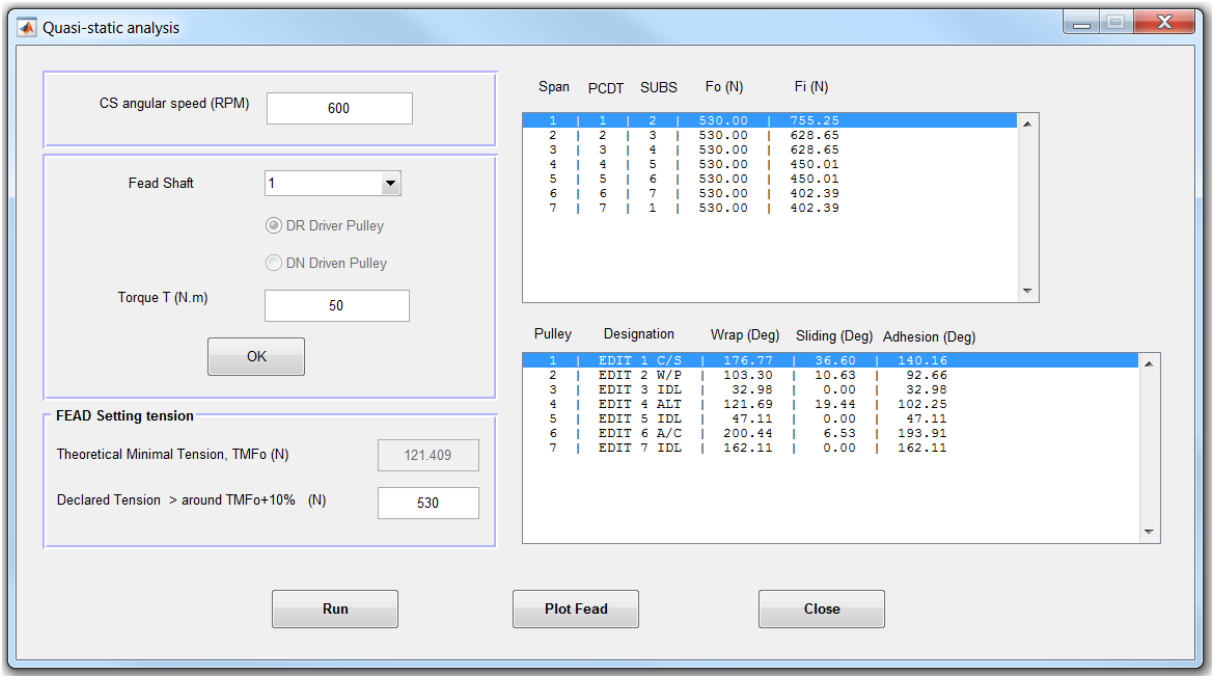

Figure 5.10 – PLFead interface to perform a equilibrium analysis.

Indeed, through a quasi-static analysis the tensioner arm motion is neglected. It is due to the fact that no engine torque fluctuations can currently be generated by the test bench in Fig. 4.1, therefore, this version of PLFead does not contain dependent (validated) belt-vibrations power loss models such as the tensioner-hysteresis and others.

5.3.4 Power losses

From the interface in Fig. 5.4, the power loss simulation can be launched as in Fig. 5.11.

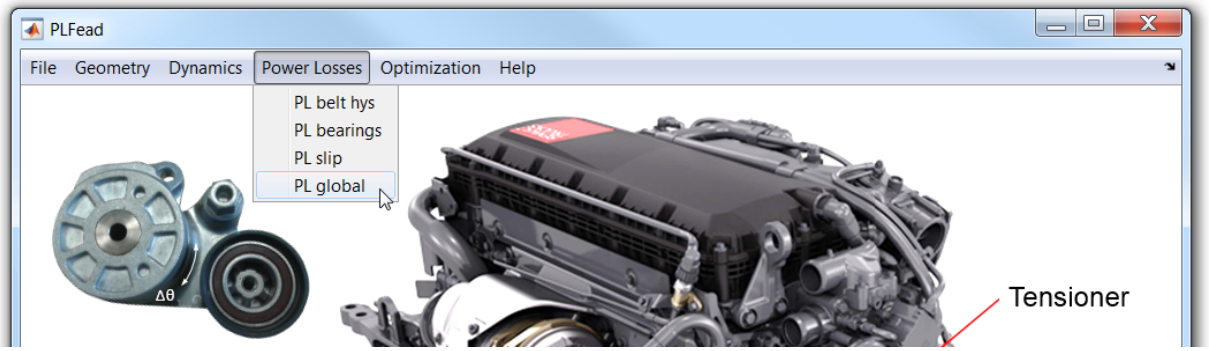

Figure 5.11 – Power loss menus of PLFead.

Up to now, due to the reasons previously invoked, as not all power loss phenomena could be implemented, the "PL global" in Fig. 5.12 does not represent all the models as in Eq. 2.1 but only the belt-hysteresis ("PL belt hys"), the bearings ("PL bearings"), the belt-pulley slip ("PL slip") FEAD power losses.

Once the simulations have been run (Fig. 5.11), a full description of the FEAD power losses distribution is provided by PLFead (Fig. 5.12).

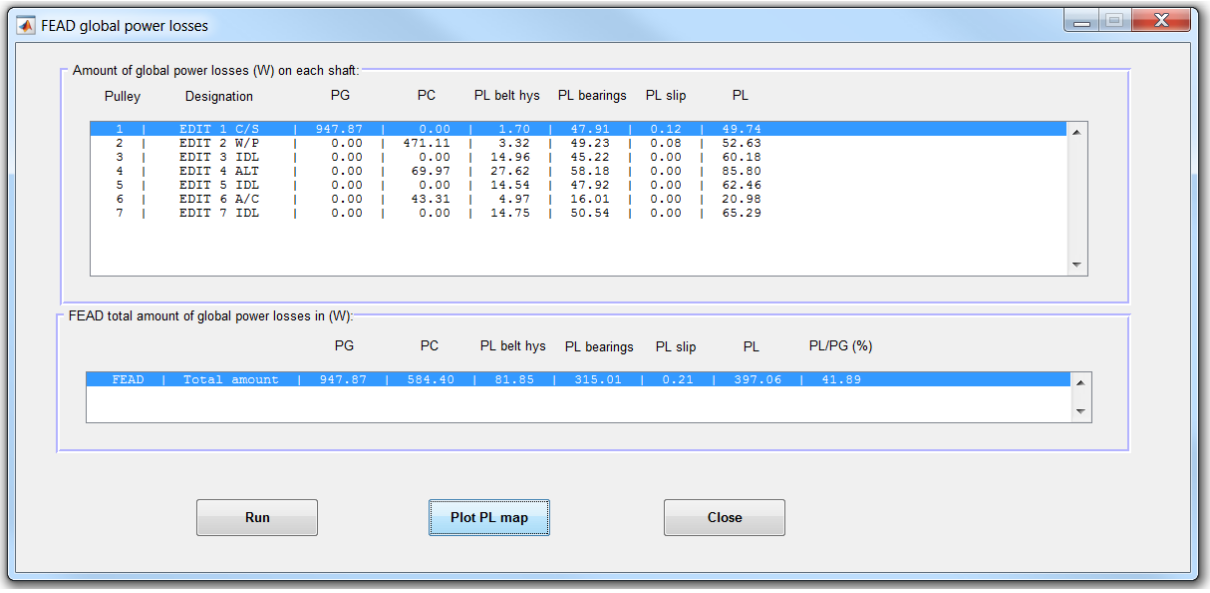

Figure 5.12 – PLFead menu representing the FEAD power losses.

The corresponding power loss map ("Plot PL map"), as presented previously (chapters 2, 3 and 4), can also be displayed on screen for the belt-hysteresis, the bearings, the slip or the sum of all of them, i.e. the global or the total FEAD power losses.

5.3.5 Optimization

The global PLMap provided by "Plot PL map" (Fig. 5.12) is available in Fig. 5.13 as an "Initial PL map" and in the computer's memory to be optimized using the optimization methods: Genetic Algorithm (GA) or Dynamic programming (DP).

From the interface in Fig. 5.4, by triggering the optimization (Fig. 5.13), all necessary parameters for the optimization process (chapter 3) can be set up.

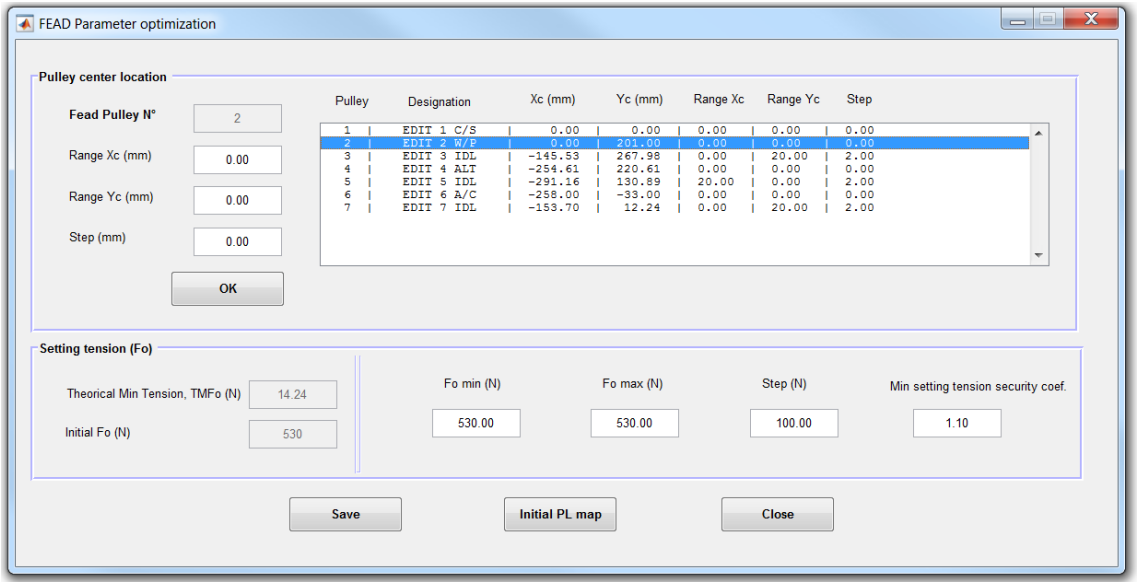

Figure 5.13 – PLFead interface, setting parameters for optimization using GA or DP.

Moreover, by triggering Optimization and e.g. the Genetic Algorithm tabs in Fig. 5.4, another specific interface to set up all GA optimization parameters appears (Fig. 5.14).

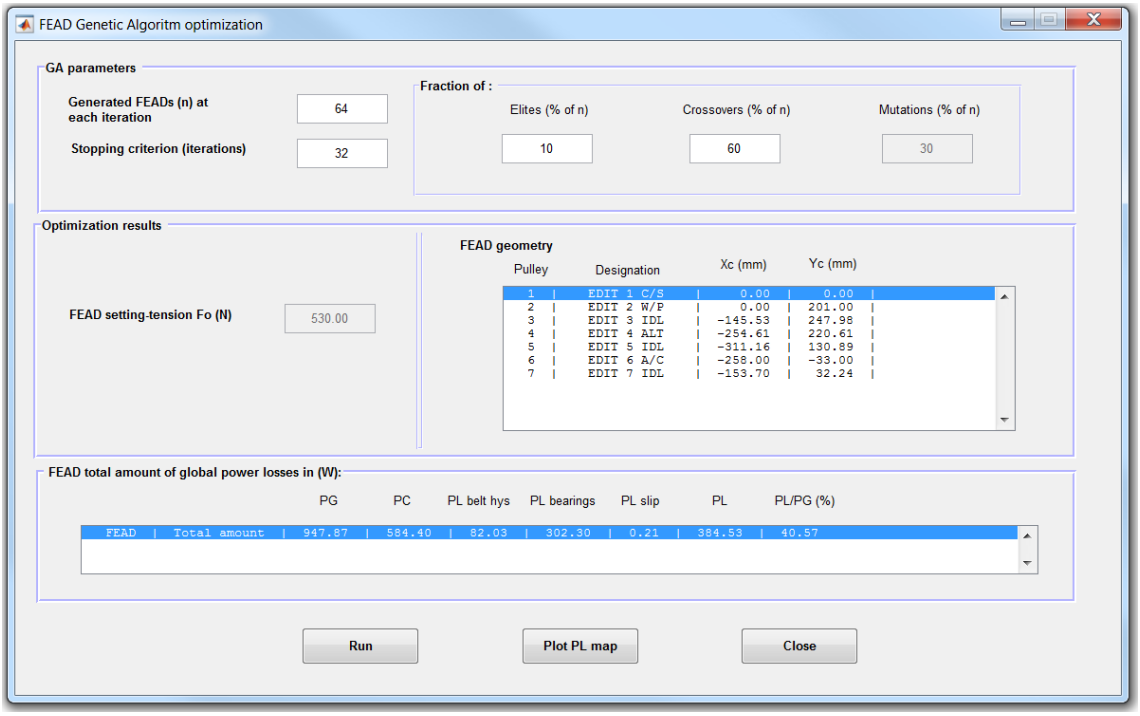

Figure 5.14 – Genetic Algorithm (GA) PLFead optimization interface.

The last step is to "Run" the models, and therefore, to analyze and compare the results before (Initial PL map) and after (Plot PL map in Fig. 5.14) the optimization.

5.4 SUMMARY AND CONCLUSIONS

PLFead is a simulation software/tool based on the process of modeling real phenomena with a set of mathematical formulas representing the power losses occurring in FEADs.

PLFead currently contains all the theory developed and validated throughout this thesis.

Firstly, PLFead was created to test new theories of power losses, in addition to imitating processes to understand how they behave under different, initial and operating, conditions of the system under analysis.

Secondly, PLFead was improved step by step in accordance with the development of the models and algorithms, as from the beginning the aim was to create an effective tool and provide its users with all the necessary (data, models, conditions) to perform useful power loss and optimization analyses.

Finally, PLFead was created mainly for facilitating the calculation and optimization of the power losses taking place in the Front Engine Accessory Drives of vehicles such as cars and trucks. Thanks to PLFead it is possible to: (1) start a power loss simulation only from an ordinary components' database and scientific models previously implemented; (2) set the FEAD (belt, pulley) and working conditions; (3) perform one or various simulations; (4) obtain relevant results of power losses and associated optimizations which would help designers to develop more environmental friendly poly-V belt transmissions.

Chapter 6

EXPERIMENTAL CHARACTERIZATION AND SIDE RESEARCH

Contents

6.1 BELT STIFFNESS AND DAMPING

To obtain the stiffness and damping of the belt in Tab. 2.6, which is a composite and visco (damping) elastic (spring) material as seen in chapter 2, the mechanical behavior of a belt-span is assimilated to a damped mass-spring system as in Fig. 6.1.

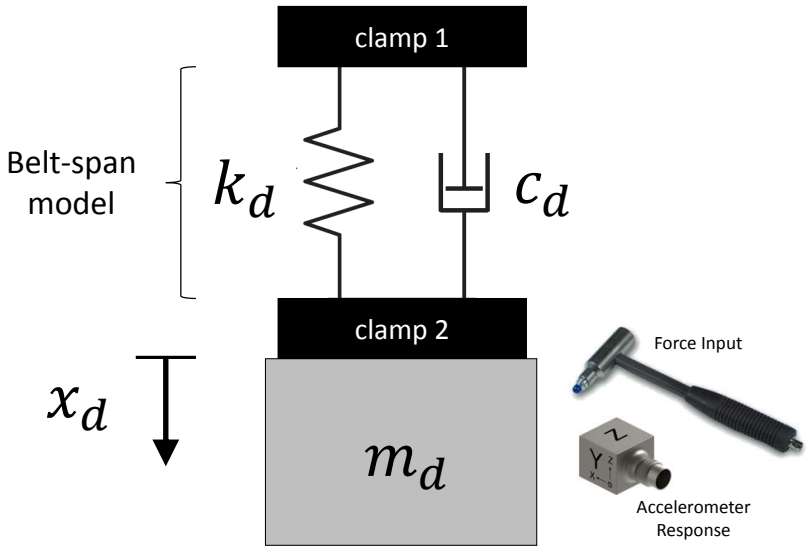

Figure 6.1 – Damped mass-spring system.

In practice, the system in Fig. 6.1 is represented by a poly-V belt sample (from Volvo) of length l_d which is stretched by a mass m_d (Fig. 6.2). Also, to measure the vibrations when the system is excited, an accelerometer is attached to the mass.

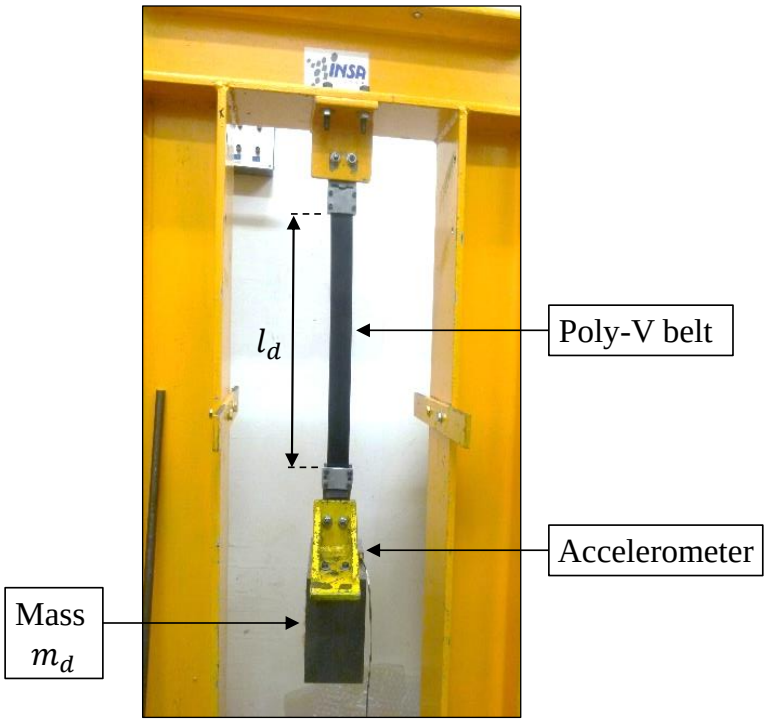

Figure 6.2 – Damped mass-spring system, experimental setup.

The equation of motion of the system in Fig. 6.1 is represented by Eq. 6.1.

$$m_d \ \ddot{x_d}(t) \ + \ c_d \ \dot{x_d}(t) \ + \ k_d \ x_d(t) = F_{ext}(t) \tag{6.1}$$

Where

- m_d is the mass of the system;
- c_d is the viscous-dampening capacity of the system;
- k_d is the stiffness of the system.

Assuming that the solution of the Eq. 6.1 with no external force ($F_{ext} = 0$) is in the form of $x_d(t) = X_d \, e^{rj \ t}$, which is a harmonic motion with rj a complex number.

If $c_d < c_c = 2\sqrt{k_d \cdot m_d}$. The damping ratio α_d can be calculated (Eq. (6.2)).

$$\alpha_d = \frac{c_d}{c_c} = \frac{c_d}{2\sqrt{k_d \cdot m_d}} \tag{6.2}$$

In the case of free vibration, the solution of the Eq. 6.2 is thus equal to Eq. 6.3.

$$x_d(t) = X_d \ e^{-\left(\frac{c_d}{2\,m_d}\right)t} \cdot e^{j\sqrt{\frac{k_d}{m_d} - \left(\frac{c_d}{2\,m_d}\right)^2}} \tag{6.3}$$

The natural frequency f_n of the free system is equal to Eq. 6.4.

$$f_n = \frac{\sqrt{\frac{k_d}{m_d} - (\frac{c_d}{2\,m_d})^2}}{2\,\pi} = \frac{\omega_n}{2\,\pi} = \frac{\omega_0\sqrt{1-\alpha_d^2}}{2\,\pi} \tag{6.4}$$

Where

- ω_n is the radian frequency of the damped system;
- $\omega_0 = \sqrt{\frac{k_d}{m_d}}$ is the radian frequency of the undamped system;
- α_d is the damping factor.

The damping factor α_d can be obtained from the logarithmic decrement δ_d in Eq. 6.5.

$$\delta_d = \frac{1}{n_{vib}} \quad \ln\left[\frac{x_d(t)}{x_d(t + n_{vib}\,t)}\right] \tag{6.5}$$

Where $x_d(t)$ is the amplitude at time t and $x_d(t + n_{vib}\,t)$ is the amplitude of the peak n_{vib} periods away, where n_{vib} is any integer number of successive, positive peaks. In addition, the log decrement δ_d can be founded by means of an impact test on the mass in Fig. 6.2. An example of the response of this damped system is represented in Fig. (6.3).

The damping ratio α_d is then found from the logarithmic decrement δ_d [64] (Eq. 6.6).

$$\alpha_d = \frac{\delta_d}{\sqrt{\delta_d^2 + 4\,\pi^2}} \tag{6.6}$$

Subsequently, the stiffness k_d can be determined by Eq. 6.7.

$$k_d = \left(\frac{4\,\pi^2\,m_d}{1-\alpha_d^2}\right) \ f_n^2 \tag{6.7}$$

Also, the stiffness along the belt or tensile modulus EA can be obtained multiplying k_d by the span length l_d according to the Eq. 6.8.

$$EA = k_d \cdot l_d \tag{6.8}$$

Where EA is the tensile modulus, k_d the belt-span stiffness and l_d the belt-span length.

Experimental tests were made for $m_d = 18.9$ kg and $l_d = 0.34$ m of the system in Fig. 6.2 and for several impact tests the time response were similar to the response in Fig. 6.3.

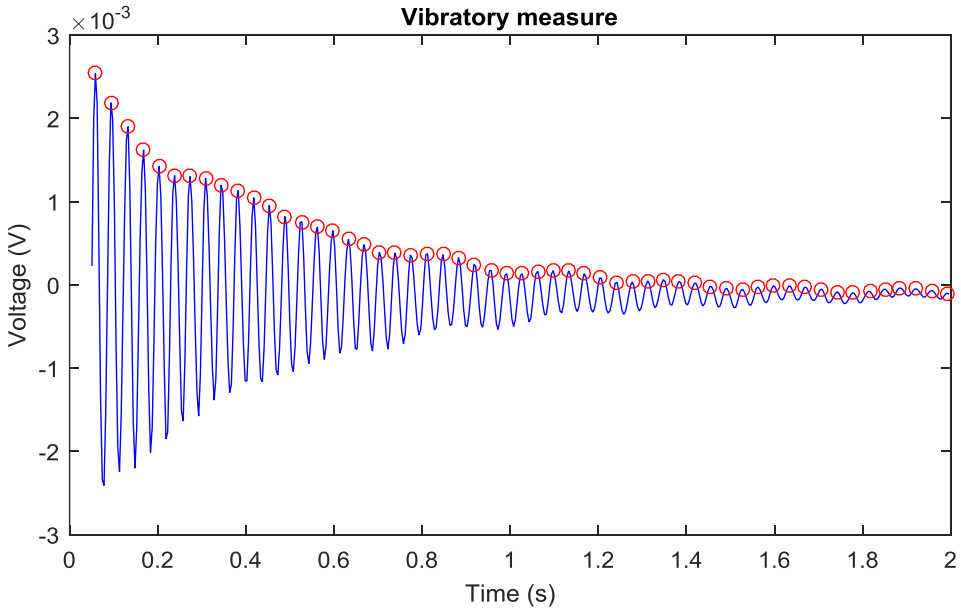

Figure 6.3 – Impact test response of the system in Fig. 6.2.

The results for 3 runs of impact tests are presented in Tab. 6.1.

Table 6.1 – Results for 3 runs of impact tests on the system in Fig. 6.2.

	Run 1	Run 2	Run 3	Average	Units
α_d	0.0152	0.0156	0.0119	0.0142	
f_n	28.06	28.06	27.55	27.89	[Hz]
k_d	587439	587469	566591	580500	[N/m]
c_d	101.1	103.7	77.6	94.2	[N.s/m]
EA	199729	199740	192641	197370	[N]

In this work, $EA = 197370$ N is assumed to be representative of the tensile modulus of the poly-V belts currently used in the FEADs of Volvo Trucks and is used in simulations.

6.2 PULLEY-BELT FRICTION COEFFICIENT

The belt-pulley wrap angle ϕ is divided in two angles: the adhesive ϕ_a and the sliding angle ϕ_s [14]. In the adhesive arc Coulomb friction contact is considered. Simultaneously, in the sliding arc kinematic friction conditions take place at low speed due to the relative motion (sliding) between the pulley and the belt. These are the assumptions made for the identification of the friction coefficient μ to supply the required information of the FEAD power loss models (e.g. Eq. 2.23).

Thus, to identify the friction coefficient between the poly-V belt and the pulley two experimental setups are proposed. Firstly, the friction coefficient between the belt and the pulley is measured under an initial belt tensions and a relative velocity between the belt and the pulley to reflect actual operating conditions [20]. Secondly, the local friction coefficient is considered to serve as a reference for the (global) friction coefficient obtained by the first method since the local friction coefficient is supposed to represent the local properties of the contact between two materials: the rubber (belt) and the steel (pulley).

6.2.1 1st method: global friction coefficient

In this case, a resisting torque is imposed to the pulley's shaft by the difference of tensions between the tight (T_t) and slack (T_s) sides in Fig. 6.4.

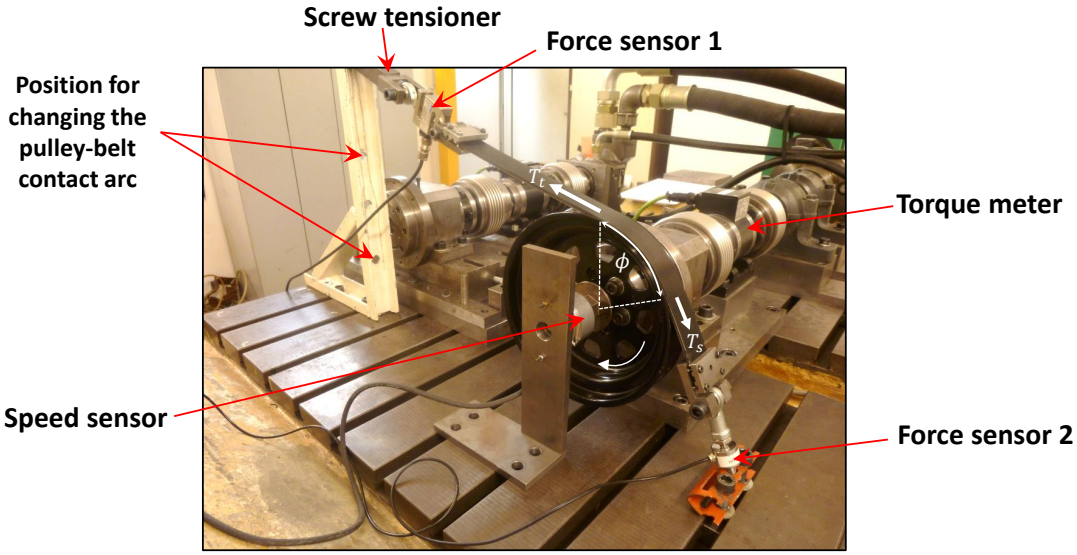

Figure 6.4 – Experimental set-up for measuring the global friction coefficient.

The objective is to measure a friction coefficient, just at the moment, when the torque is enough to cause sliding. This coefficient depend on several parameters: the material, the roughness, the temperature, the sliding speed, etc.

This method consists basically of applying, through the screw tensioner in Fig. 6.4, a difference of tension $(T_t - T_s)$ on the belt-span tight side. The belt-span sample is therefore stretched since it has one side fixed and the other side tensioned by the screw tensioner. In short, ϕ (Fig. 6.4) is adjusted, T_0 is set up, the pulley is slowly rotated and the driving torque as well as T_t and T_s are measured. Indeed, on both belt-spans (Fig. 6.4) force sensors are installed to measure the tensions T_t and T_s, and therefore, the resisting torque imposed to the pulley running under gross slip conditions. Moreover, the pulley-belt contact pressure is proportional to the difference of tension $(T_t - T_s)$.

After setting the static tension T_0, the pulley is rotated to obtain a uniform torque adapted to the operating conditions of the belt and the pulley. The resulting friction coefficients are a static (before sliding) and a kinematic coefficients (when the belt slips on the pulley (Fig. 6.5) which should be used according to FEAD operating conditions.

The coefficients in Fig. 6.5 (right) are global, since the testing methodology as in [20] does not take into account the v-ribbed belt and pulley geometries (grooves).

The global friction coefficient between the poly-V belt and the pulley can be calculated by the Euler's Eq. 6.9 [37] with the centrifugal action $T_c = 0$ since the belt is fixed.

$$\mu_g = \frac{1}{\phi} \cdot \ln \frac{T_t}{T_s} \tag{6.9}$$

Where T_t, T_s and ϕ are, respectively, the belt-span tensions and the wrap-angle (Fig. 6.4).

In Eq. 6.9, the pulley wedge angle α does not interfere in the μ_g calculation, i.e. μ_g is obtained exclusively from the belt-span tensions T_t, T_s measured by the force sensors and the belt wrap angle ϕ, measured directly on the pulley in Fig. 6.4.

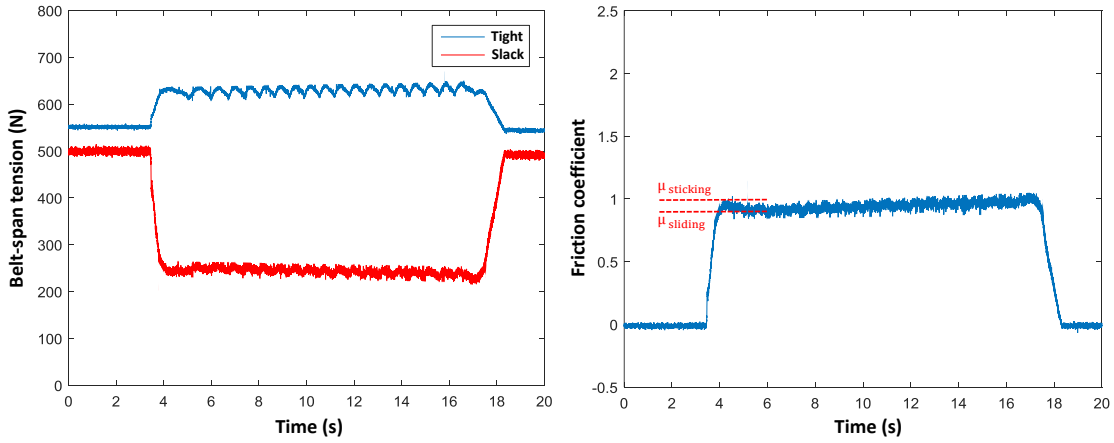

Figure 6.5 – Example of results, similar to those in [20], obtained experimentally.

To serve as a reference for the belt-pulley friction coefficient used in simulations, another method has been evaluated and typical values of friction coefficient of the belt used here in simulations are given at the end of the next section.

6.2.2 2nd method: local friction coefficient

The second method uses a specific machine which tests linearly a poly-V belt sample. This approach permits considering the ribs layer of the poly-V belt. The friction coefficient measured is local since the poly-V belt groove is locally taken into consideration and the coefficient is measured from a tribological point of view. Actually, the testing procedure is similar to that used by Amijima [65] ; a piece of belt is pressed by a normal load P_x against a flat grooved plate with (known) wedge angle α. In this case, the v-ribbed contact surface of the pulley geometry (region of the grooves) is considered, even if the latter is a linear v-ribbed profile (Fig. 6.6). The poly-V belt is pulled by a traction force. The maximal value of this force is noted T_{max}. Then, the relationship between T_{max} and the applied normal load P_x gives the frictional coefficients μ_g and μ_l in Eq. 6.10.

$$\frac{T_{max}}{P_x} = \mu_g = \frac{\mu_l}{\sin \frac{\alpha}{2}} \tag{6.10}$$

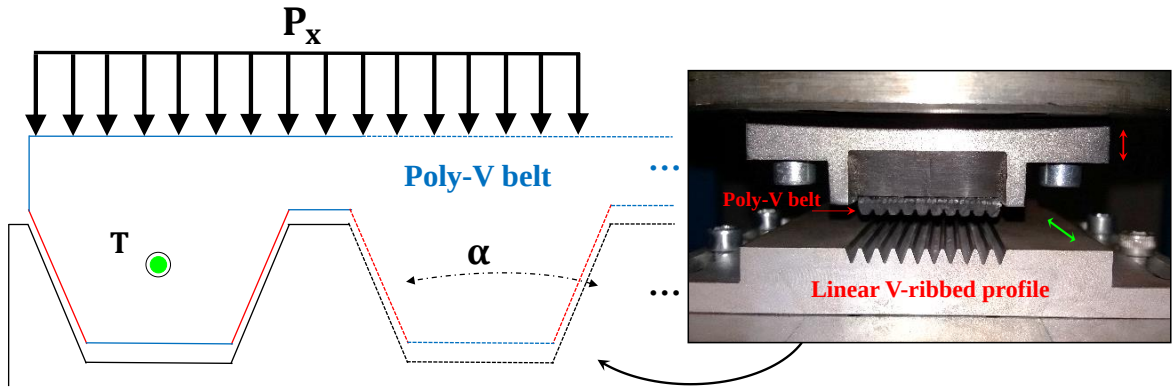

Figure 6.6 – Schematic diagram showing the local friction coefficient testing principle.

Another way to present the result in Eq. 6.10 is during experimental testing to plot T_{max} versus P_x, normally this ratio is a linear relationship, where the inclination is simply μ_g. Sometimes, this global coefficient is mistaken with the virtual coefficient of friction, which has the same role for flat belts, but here the global coefficient and its relation with the local coefficient is the $\sin\frac{\alpha}{2}$ representing the poly-V belt geometry (Eq. 6.10).

In practice, to obtain the friction coefficient, the test bench (tribowave) designed recently during the thesis of Tonazzi [66] is used (Fig. 6.7).

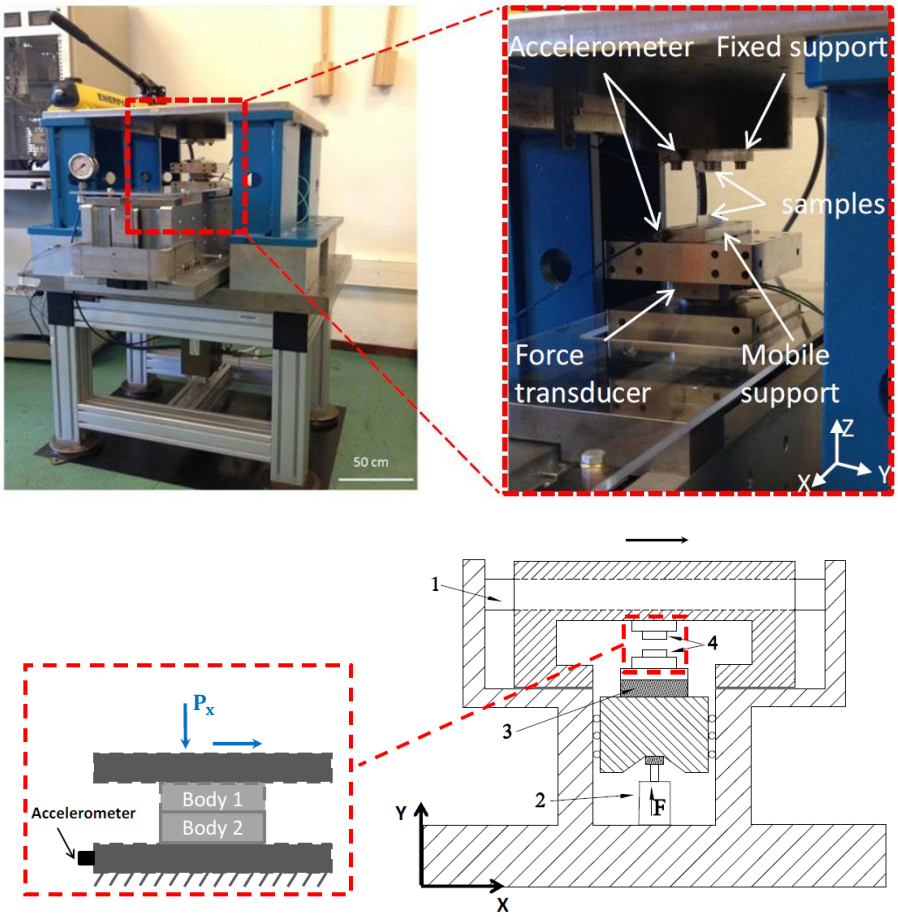

A general scheme of the experimental set-up PEDEBA:
1- Hydraulic cylinder, 2- Hydraulic piston, 3-Force transducer, 4-Specimens.

Figure 6.7 – Experimental apparatus for measuring the local friction coefficient [66].

As described by Eq. 6.10 the global μ_g and the local μ_l friction coefficients are obtained from the ratio T_{max}/P_x measured taking into consideration the linear movement between two samples (or bodies as in Fig. 6.7). The first sample is a piece of poly-V belt. The second sample is a linear v-ribbed profile as in Fig. 6.6 representing the pulley. This was manufactured exclusively to perform the present friction tests.

To guarantee representative operating conditions, as these to which the belt and pulleys of FEADs are subjected, and have the same test pulley-belt contact surface conditions, the temperature and profile roughness with the same coating of the pulleys of Volvo trucks were carefully set up. Moreover, not only the surface roughness, but also other parameters of the pulleys and the poly-V belt used in simulations and experiments were considered in a testing campaign performed during the thesis. Indeed, the force, the belt/pulley relative speed, the temperature representing the engine room temperature, the pulley and belt roughness have been taken into consideration.

The axial traction force is proportional to the belt/pulley contact pressure and depends on the belt/pulley contact surface (properties) and sliding speed. For the experiments, representative conditions of the belt/pulley contact were considered (Tab. 6.2). Indeed, the sliding velocities were calculated using the theory developed in Appendix $A7$.

Moreover, the surface roughness Ra of $0.3\,\mu m$ and $0.8\,\mu m$ for the pulleys and Ra $= 5.6\,\mu m$ for the poly-V belt were observed (Fig. 6.8). Two temperatures were considered to be representative of the engine-room temperature when the engine has just started ($20°C$) and after some working hours ($80°C$, Tab. 6.2).

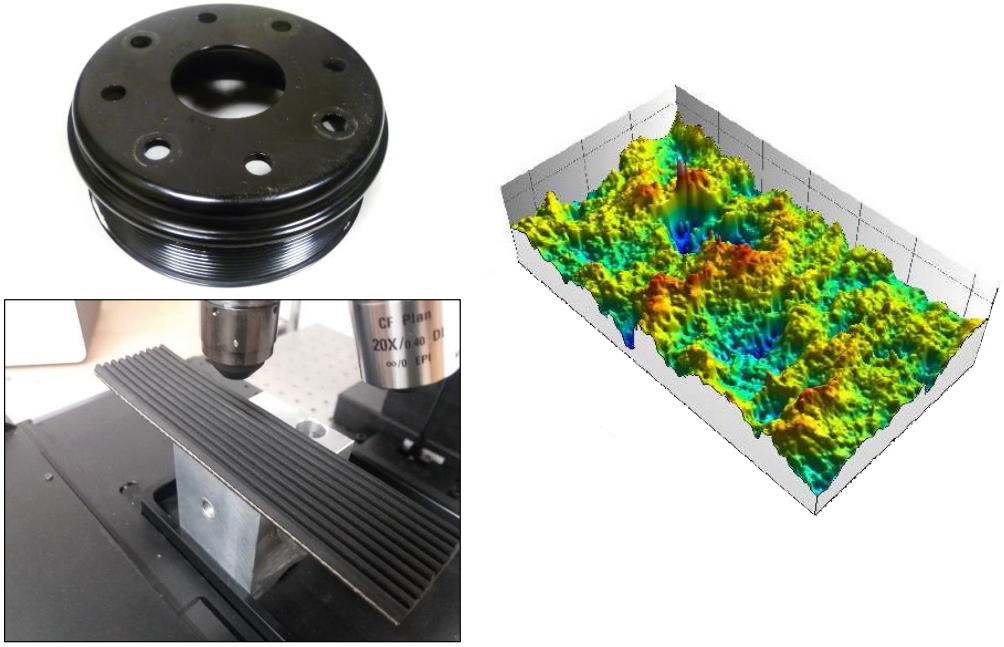

Figure 6.8 – Example of poly-V belt and pulleys, surface roughness analyses.

Finally, experimental results of the local friction coefficient between the poly-V belt with Ra $= 5.6\,\mu m$ and the for two types of pulleys with Ra $= 0.3\,\mu m$ and $0.8\,\mu m$ are presented in Tab. 6.2 for several operating conditions.

Table 6.2 – Summary of experimental local friction coefficient results.

					Pulleys roughness R_a = 0.3 µm	Pulleys roughness R_a = 0.8 µm
Initial Normal load	Sliding normal load	Axial traction force	Sliding velocity	Temperature	Local friction coefficient	Local friction coefficient
1000 N ≈ 0.5 MPa	950 N	437 N	1 mm/s	20 °C	0.46	0.66
1500 N ≈ 0.7 MPa	1350 N	594 N	1 mm/s	20 °C	0.44	0.68
2000 N ≈ 1 MPa	1950 N	839 N	1 mm/s	20 °C	0.43	0.75
400 N ≈ 0.2 MPa	350 N	154 N	0.5 mm/s	20 °C	0.44	0.62
2100 N ≈ 1 MPa	1935 N	813 N	0.5 mm/s	20 °C	0.42	0.64
4200 N ≈ 2 MPa	3850 N	1540 N	0.5 mm/s	20 °C	0.40	0.64
400 N ≈ 0.2 MPa	375 N	154 N	0.1 mm/s	20 °C	0.41	0.61
2100 N ≈ 1 MPa	1900 N	741 N	0.1 mm/s	20 °C	0.39	0.59
4200 N ≈ 2 MPa	3850 N	1425 N	0.1 mm/s	20 °C	0.37	0.59
400 N ≈ 0.2 MPa	320 N	147 N	0.01 mm/s	20 °C	0.46	0.56
2100 N ≈ 1 MPa	1800 N	720 N	0.01 mm/s	20 °C	0.40	0.52
4200 N ≈ 2 MPa	3700 N	1332 N	0.01 mm/s	20 °C	0.36	0.52
400 N ≈ 0.2 MPa	350 N	140 N	0.1 mm/s	80 °C	0.40	0.45
2100 N ≈ 1 MPa	1850 N	611 N	0.1 mm/s	80 °C	0.33	0.44
4200 N ≈ 2 MPa	3625 N	1196 N	0.1 mm/s	80 °C	0.33	0.46
2000 N ≈ 1 MPa	1825 N	657 N	1 mm/s	80 °C	0.36	
2000 N ≈ 1 MPa	1850 N	611 N	0.1 mm/s	80 °C	0.33	
2000 N ≈ 1 MPa	1800 N	468 N	0.01 mm/s	80 °C	0.26	

In summary, the global and local coefficients do not depend on the belt-pulley contact pressure, they decrease when the surface roughness and temperature are increased and increase with the belt-pulley sliding velocity.

In this thesis, depending on operating conditions, $\mu_g \, \epsilon \, [0.88 \;\; 1.75]$ for the inside of the belt and $\mu_l \, \epsilon \, [0.3 \; 0.6]$ for the backside of the poly-V belt contacts are chosen and represent measurements for the poly-V belt used in Volvo Truck FEADs.

The values of the presented local μ_l and global μ_g friction coefficients are close to those in [2], where for the backside of the belt $\mu_l = [0.4 \;\; 0.8]$ and for the inside of the belt $\mu_g = [0.4 \;\; 1.4]$ on a older and on a new dry belt, respectively.

6.3 TENSIONER CHARACTERIZATION

As seen in chapter 2, to predict the tensioner-hysteresis losses some parameters are needed such as the amplitude of the tensioner rotation angle and the tensioner oscillation angular frequency, these are obtained from a dynamic analysis (Fig. 2.21) of the FEAD assuming engine torque fluctuations as excitation. In this section, we want to characterize the frictional torques (Eq. 2.56) of the tensioners used in the EURO-6 and EDIT engines.

6.3.1 Experimental setup

To analyze the dissipative behavior of the tensioners, the apparatus in Fig. 6.9 was set up. Indeed, a rotation is imposed to the tensioner by means of the shaker while the frictional torque is measured by the (force and displacement) sensors in Fig. 6.9.

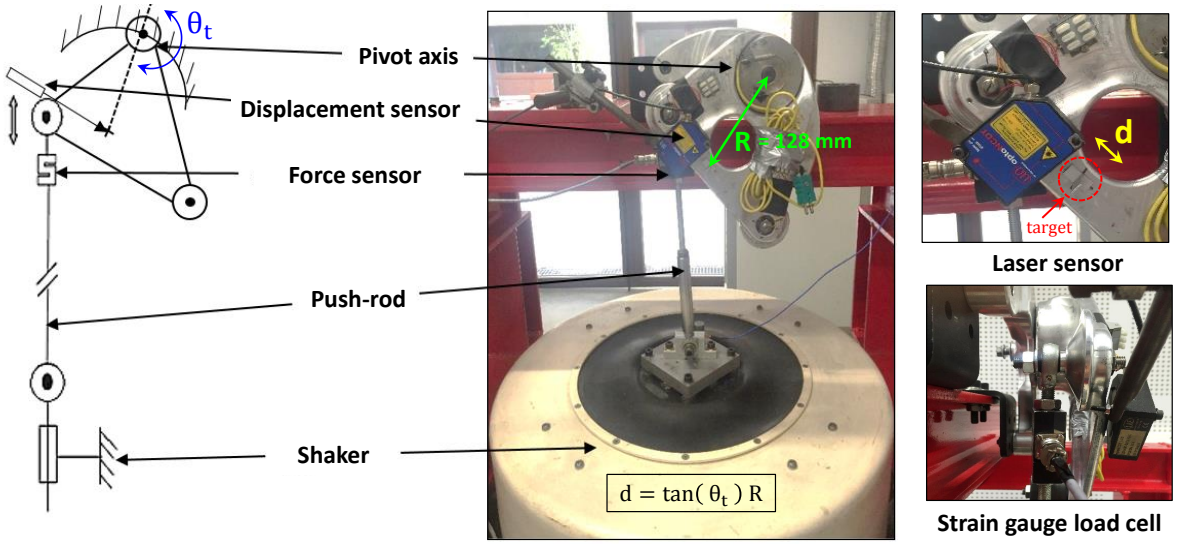

Figure 6.9 – Experimental setup used to characterize the tensioner.

As an example, differently from the tensioner in Fig. 2.20 used in EURO-6 engines, the dual tensioner in Fig. 6.9 is a new type of tensioner designed by Dayco to be used in the micro hybrid Volvo truck (EDIT) as a self-tensioner system. Unlike the EURO-6 tensioner, the dual tensioner has two idler-pulleys, an arc-shaped bracket and a pivot without spring.

One of the two sensors used in the test bench in Fig. 6.9 (right) is a strain gauge sensor, it is connected directly with a push-rod to an axis of the tensioner pulley. The connection device is a spherical junction which means that there is no extra torque in the connection. The other one is a laser displacement sensor which is fixed to the frame of the test bench with a magnetic base. A target is glued (small aluminum corner plate) to the tensioner arm to catch the laser signal, hence the rotation about the tensioner pivot is measured.

Thus, test data are composed by the force and the displacement used to excite the tensioner with the shaker in Fig. 6.9. According to the tensioner geometry and by applying trigonometric relations, the tensioner rotation angle and frictional torque at the tensioner pivot can be obtained. In the next section, experimental tensioner hysteresis curves, i.e. the plot of the rotation angle versus the frictional torque results, are given for EURO-6 and EDIT tensioners. It permits characterizing their dissipative behavior, and therefore, predicting the corresponding tensioner-hysteresis losses as detailed in chapter 2.

6.3.2 Tensioners dissipative behavior

Hysteresis curves are presented in Fig. 6.10 for the dual tensioner used in the EDIT oscillating at several frequencies and subjected to the same linear amplitude d = 1 mm, where d is as in Fig. 6.9. For other amplitudes, i.e. 2 mm and 3 mm, see Appendix *A*10.

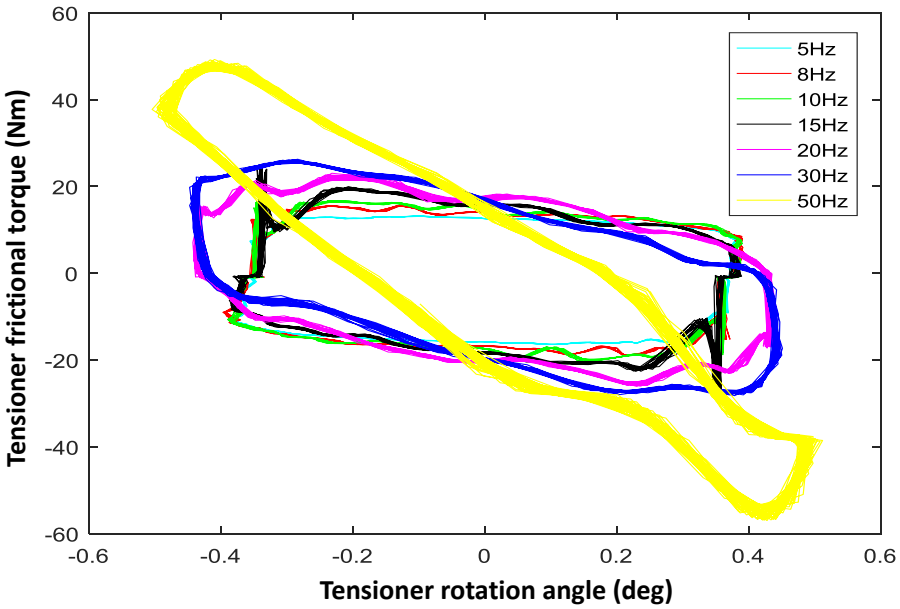

Figure 6.10 – EDIT tensioner hysteresis curves with the shaker linear amplitude of 1mm.

From these curves, one can clearly identify that with the same amplitude, the variation range of the tensioner rotation angle angle is the same. The slope of each curve becomes more and more negative due to damping pad material (viscoelastic/dissipative property) and unstable with increasing frequency because of inertial effects. Also, the value of the frictional torque C_{fc} is almost the same except in the case of high frequencies.

Hysteresis curves were also obtained for several tensioner rotation angles and excitation frequencies (Figs. 6.11, 6.12 and Appendix *A*10).

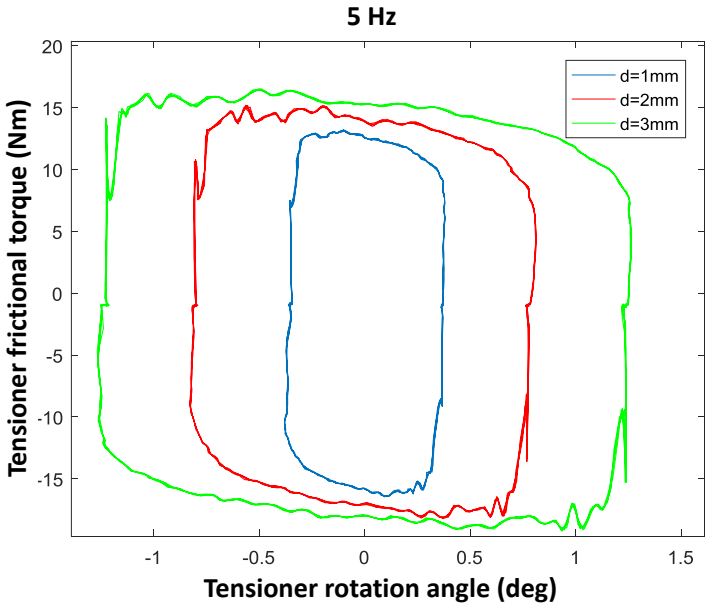

Figure 6.11 – EDIT tensioner hysteresis curves for an excitation frequency of 5 Hz.

Figure 6.11 indicates that with the same frequency, the increase of the shaker linear amplitude, i.e. the tensioner rotation angle, will increase the dissipation of energy which is proportional to the internal surface of the hysteresis curve [34]. Moreover, the value of the tensioner frictional torque increases locally when the amplitude slightly increases due to the acceleration effect. Also, peaks appear at the corner of the curves. The reason could be either from the clearence at the joint between the tensioner pulley screw and force sensor or from the push-rod inversion of movement. Finally, in Fig. 6.11 the tensioner frictional torques are nearly the same or slightly increases when the amplitude (d) imposed by the shaker increases [67]. However, when the frequency is high, e.g. 30Hz in Fig. 6.12, the dissipation is smaller due to more complex, probably inertial, effects.

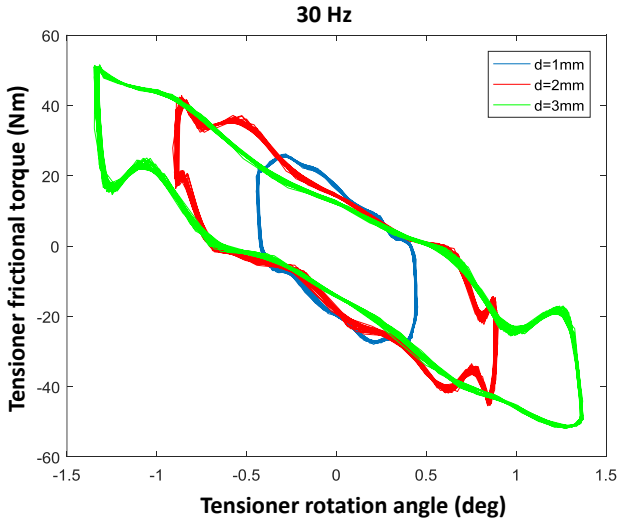

Figure 6.12 – EDIT tensioner hysteresis curves for an excitation frequency of 30 Hz.

One might believe that the dissipation (frictional torque) in the tensioner would increase with the increase of the tightening torque (Fig. 6.13) because one would think the bigger the tightening torque is, more heat (friction) will be generated. However, in reality, the tensioner frictional torque is independent of the tightening torque. That is what is observed in the Fig. 6.13 and those in Appendix $A10$, the variation of the tested tightening torque does not change practically the internal area of the hysteresis curves. In other words, the hysteresis, and therefore, the dissipation in the tensioner-pivot is not impacted by the dual-tensioner tightening-torque setting.

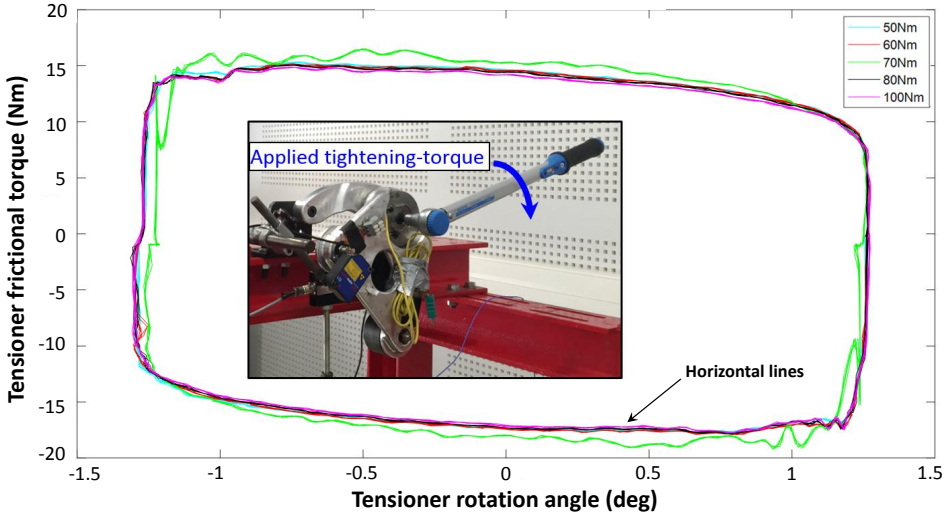

Figure 6.13 – EDIT tensioner hysteresis curves for 5 tightening torques, 3mm and 50Hz.

6.3.3 Conclusions about tensioners characterization

The EURO-6 tensioner was characterized experimentally during the internship of LI [68], the main outputs result of this work are presented in Appendix $A11$ - it is worth noting that the hysteresis curves of the EURO-6 Tensioner are very similar to those presented for the EDIT tensioner in the previous section and Appendix $A10$. This may be due to the differences between the tensioners (i.e. size and design). Indeed, the current version of the tensioner used in the Efficient Distribution Truck (EDIT) has no counter-spring. So the hysteresis curves obtained through the characterization of the EDIT tensioner are theoretically horizontal lines (no stiffness) as in Fig. 6.13.

The theory about the tensioner-hysteresis power losses in chapter 2 is applicable to both EDIT and Euro-6 tensioners. To this aim, the value of the tensioner frictional torque C_{fc} in Eq. 2.56 equals to the distance from zero to the upper or the bottom lines of the hysteresis curve (Fig. 2.21). In theory, this parameter is a constant value and it is specific to each tensioner. Measurements as shown in the previous section or in [68] show that it can change a little with testing conditions: the testing frequency, the amplitude and the temperature. It means that external effects can interfere in testing measurements. That is why, in practice, an average of the tensioner frictional torque from experimental hysteresis curves should be taken to be representative of the tensioner's oscillation.

As shown in the previous section and in [68], one can conclude that tensioner structural characteristics (counter-spring, inertia) and work conditions (excitation frequency) have an impact on the power losses estimation. The frequency which the tensioner oscillates is directly proportional to the magnitude of the engine (acyclism) torque fluctuations. So, if the engine acyclism is sufficiently small to obtain the tensioner oscillations, then in this case, the tensioner-hysteresis power losses can even be neglected.

In the case of non-negligible engine torque fluctuations, and thus tensioner oscillations the tensioner frictional torque C_{fc} shall be extracted from tensioner-hysteresis curves obtained from a tensioner characterization as in the previous section for calculating the tensioner-hysteresis power losses (Eq. 2.57). It is worth noting that Eqs. 2.56 and 2.57 need the amplitude of the tensioner rotation angle and the oscillation angular frequency. These parameters are classically obtained through the dynamic responses of the serpentine belt drive system containing the tensioner under analysis.

6.4 TORSIONAL VIBRATION DAMPER

To go further, during the thesis the Torsional Vibration Damper (TVD) was also analyzed. In the following, a brief summary of how the TVD is characterized is given. Next, some insights on the implementation of elastomeric constitutive law of the TVD rubber-ring and the consequences on TVD dynamics are explained. The reason of the existence of this section is justified by the fact that it uses the master curves theory in chapter 2 to explain the changes (impact of viscoelasticity, i.e. loss, dissipation) in the TVD dynamics. Moreover, this section could inspire further research about TVD hysteresis power losses similar to those modeled and optimized in chapters 2 and 3.

6.4.1 General characterization

A TVD is generally composed by two or three metal parts with a rubber-ring between them, corresponding respectively to the single and dual mass rubber TVD (Fig. 6.14). The stiffness and damping of the TVD must be determined for the simulation models.

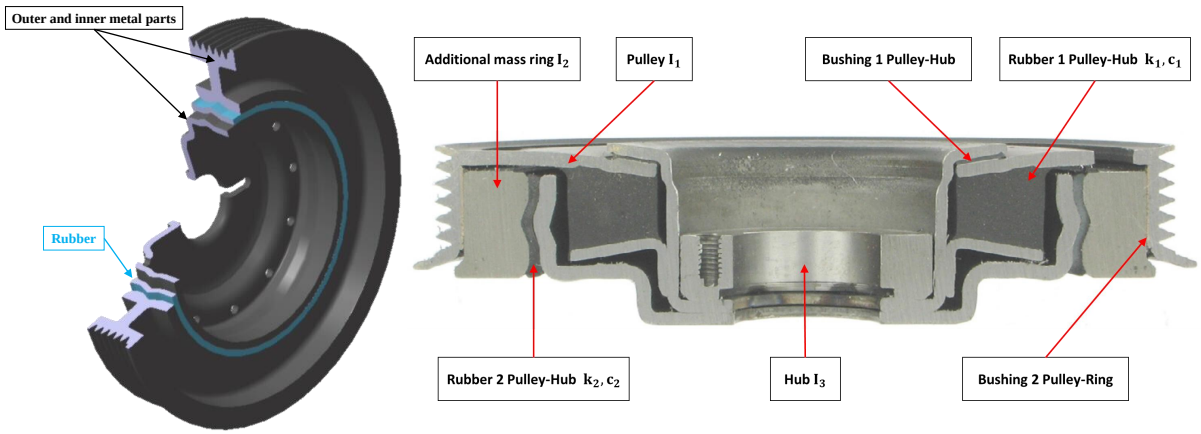

Figure 6.14 – Single (left) and Dual (right) mass rubber TVD crankshaft pulley.

For the determination of the stiffness and damping coefficients of the rubber ring used in TVDs, an experimental characterization method is presented by Manin et al in [33]. Also, the methodology proposed in [33] is illustrated through an example. The torsional stiffness of the rubber ring K_{cst}, which can be modeled by a spring in parallel with a torsional damper connecting two inertias, as in [69] K_{cst} can be estimated by Eq. 6.11.

$$K_{cst} = \frac{2\,\pi\,R_{rr}^3\,L_{rr}\,G'}{e_{rr}} \tag{6.11}$$

Where R_{rr} is the external radius of the rubber ring, L_{rr} the ring width, G' the shear modulus of the rubber ring and e_{rr} the ring thickness. As in experimental testing in [33], where Manin et al [70] explain that the damping ratio ξ can be determined from the bandwidth for an attenuation of 3 dB (Eq.6.12). The frequency f_n is provided by Eq.6.13.

$$\xi = \frac{\Delta f(-3dB)}{2 \cdot f_n} \tag{6.12}$$

$$f_n = \frac{1}{2 \cdot \pi} \cdot \sqrt{\frac{(K_{cst})_n}{I_n}} \tag{6.13}$$

The natural frequency f_n and the corresponding ξ come from the Frequency Response Function (FRF) of the system with the metal parts and rubber-ring included [33].

6.4.2 Implementation of elastomeric constitutive law

Actually, the TVD is an essential component of power transmission systems such as the Front Engine Accessory Drives (FEAD). The FEAD of a vehicle is a system composed of individual accessories such as the compressor, the alternator, the water and steering pumps, etc. These accessories are coupled to pulleys driven in rotation by a poly-V belt, itself driven by the crankshaft pulley. This driving pulley is commonly used as a torsional vibration damper for the crankshaft since rotational vibrations are harmful to the system performance [63] and may cause fatigue failure of structural components.

Indeed, the viscoelasticity of the rubber used in vibration dampers such as the TVD has rarely been explored. Recently, Bhatti [71] indirectly compared viscoelastic dampers with Magnetorheological dampers. Also, the TVD behavior was speedily investigated by Jauregui [72] through a case study of a complicated model. A particularity of these studies is that they consider rheological models such as Maxwell [71], Kelvin [72] [73], etc. Yet, such rheological models significantly increase the complexity of the differential equations which are usually solved using complex schemes. Other authors analyzed the dynamic characteristics of the stiffness and the damping from an experimental point of view. See Wakabayashi [74] and Kinoshita [75] who studied the TVD experimentally. However, in [74] the results were fitted to a specific engine case. Recently, Manin et al. [33] proposed a methodology to easily characterize the pulley torsional vibration damper.

In the case of trucks, including the EDIT, the TVD is composed of an inner ring (hub) mounted on the crankshaft extremity, an intermediate viscoelastic rubber ring and an outer ring used as a poly-V pulley (Fig. 6.15). Generally, in simulation and for sake of simplification, the TVD dynamic properties – stiffness and damping – are chosen to be constant [63], although these properties depend on the operating temperature, the shear strain amplitude and the frequency to which the TVD is subjected because of its intermediate ring which is made of a viscoelastic material [38].

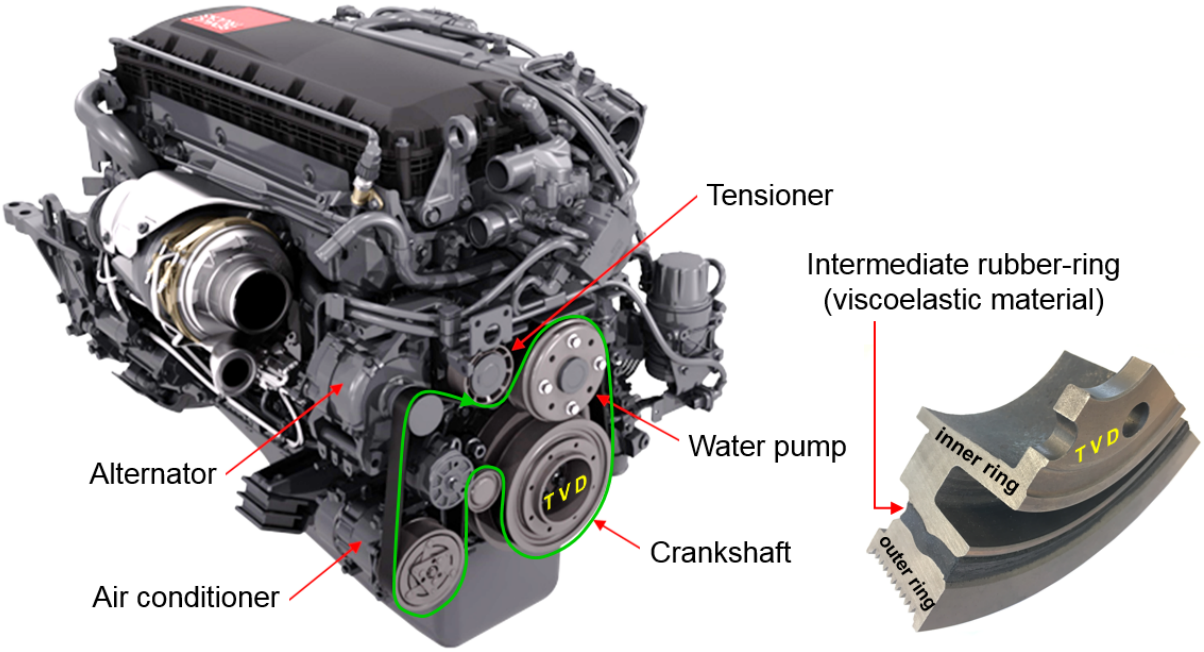

Figure 6.15 – Serpentine belt drive system of a truck with its TVD pulley.

The objectives of this work are

1. to propose a methodology based on the TVD-elastomer master curves to predict the temperature/frequency viscoelastic response of the TVD;
2. to simply and directly consider the viscoelastic properties of the constituting rubber-ring in the damper's equation of motion;
3. to highlight the influence of taking into consideration the viscoelastic properties of the elastomer when computing the TVD dynamic response;
4. to evaluate the coefficients of the equation of motion, stiffness and damping, as a function of the engine operating conditions.

In turn, this work aims at accurately calculating the viscoelastic TVD response which is of key importance in order to provide a realistic and accurate representation of the system dynamics, which is in accordance with Jauregui's works [72] and associated conclusions.

6.4.3 Classic model

The torsional vibration damper in Fig. 6.15 can be modeled by a one degree-of-freedom (DOF) mass-spring-damper system as in [69], it is also similar to the base excitation one (DOF) harmonically excited system in [76], however, in this case, the single DOF is the rotation around z-axis (Fig. 6.16).

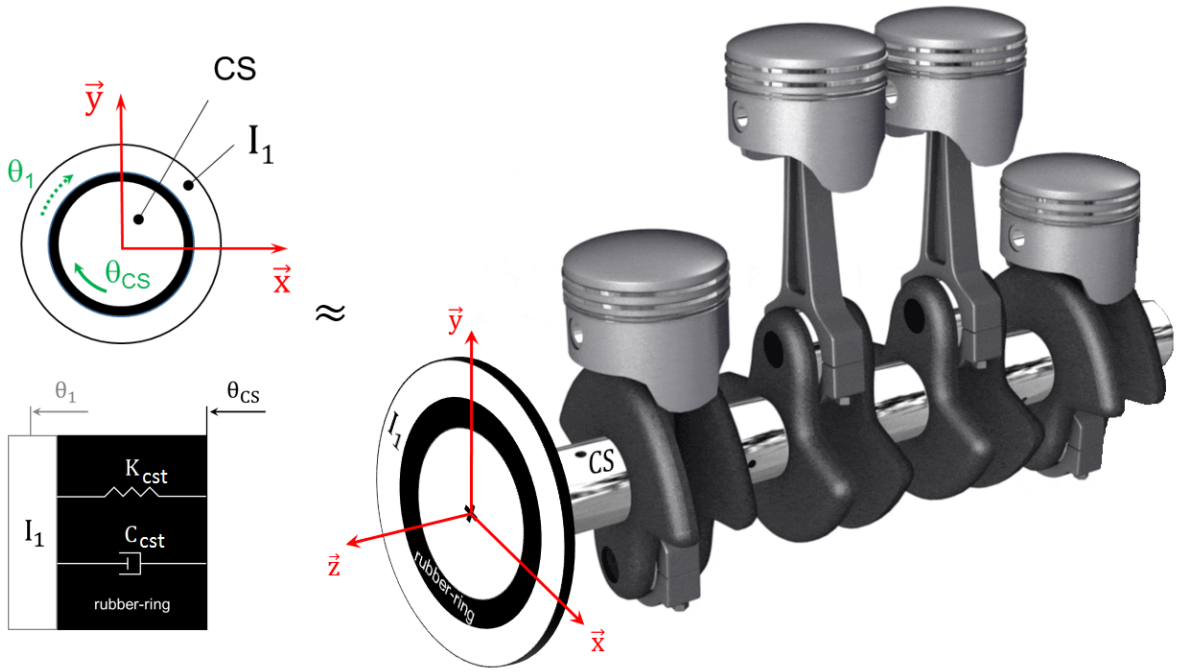

Figure 6.16 – Tensioner vibration damper and its schematic diagrams.

Supposing the engine at idling, the driving torque fluctuation usually contains two main harmonics (ω_{acy} , $2\,\omega_{acy}$). However, in this study, only the prevailing harmonic generally represented as $\theta_{CS} = \theta_{amp}\,\sin(\omega_{acy}\,t)$ is considered. The difference between the torque experienced by the TVD outer-ring and the driving torque imposed by the crankshaft results in an angular lag of θ_1 with respect to the excitation θ_{CS}, and is due to the viscoelastic properties of the TVD intermediate rubber-ring (Fig. 6.16).

In order to evaluate the impact of considering the intermediate rubber-ring viscoelastic properties influenced by temperature and frequency and leading to varying TVD stiffness K_{cst} and damping C_{cst} coefficients, let us consider the equation of motion in Eq. 6.14 for the system shown in Fig. 6.16.

$$I_1\,\ddot{\theta}_1 + C_{cst}\,\dot{\theta}_1 + K_{cst}\,\theta_1 = C_{cst}\;\theta_{amp}\;\omega_{acy}\,\cos(\omega_{acy}\,t) + K_{cst}\;\theta_{amp}\,\sin(\omega_{acy}\,t) \tag{6.14}$$

Where I_1 is the outer-ring inertia, K_{cst} the stiffness and C_{cst} the damping of the rubber-ring. The angle θ_1 is the DOF considered, θ_{amp} and ω_{acy} are, respectively, the amplitude and the excitation radian frequency of the fluctuations (acyclism) in angular displacement.

The steady-state response of θ_1 have an amplitude and phase as in Eq. 6.15 ([76]). This is the Frequency Response Function (FRF) of one DOF base excitation system with the frequency ratio r_{rr}, natural frequency ω_n and damping ratio ξ as in Eq. 6.16.

$$FRF\begin{cases}\frac{\theta_1}{\theta_{CS}} = \frac{\sqrt{1+(2\,\xi\,r_{rr})^2}}{\sqrt{(1-r_{rr}^2)^2+(2\,\xi\,r_{rr})^2}} \\ \\ \varphi_{\theta_1} = \tan^{-1}\left[\frac{2\,\xi\,r_{rr}^3}{1-r_{rr}^2+(2\,\xi\,r_{rr})^2}\right]\end{cases} \tag{6.15}$$

Where

$$r = \frac{\omega_{acy}}{\omega_n} \qquad \omega_n = \sqrt{\frac{K_{cst}}{I_1}} \qquad \xi = \frac{C_{cst}}{2\sqrt{K_{cst}\,I_1}} \tag{6.16}$$

Equations 6.15 and 6.16 were chosen because they are part of a classical formulation in the frequency-domain and the frequency domain is the one in which the TVD elastomer is characterized via DMA.

6.4.4 TVD rubber-ring viscoelastic properties

The TVD intermediate ring is made of rubber which can be described as a viscoelastic material. For this type of material, an intermediate between purely elastic and purely viscous materials [38] a complex modulus E^* is usually defined. Thus, the Eq. 2.5 can also be defined to represent the viscoelastic properties of the TVD rubber-ring. The real part of E^* (storage modulus E') relates to the elastic behavior of the ring, and defines the capacity of its material to store energy. The imaginary part of E^* (loss modulus E'') relates to the material's viscous behavior, and defines the energy dissipative ability of the rubber-ring to dampen the crankshaft torque fluctuations. As in Eq. 2.5, for the rubber of the poly-V belts, the complex modulus E^* is obtained via DMA characterization and varies as a function of the temperature θ_{exp}, the loading frequency f_{exp} and the dynamic strain ε_{exp} experienced by the rubber-ring.

The TVD intermediate ring material data shall be acquired to coincide with the engine-range of operating conditions (speed, temperature). To this aim, the rubber-ring was tested at conditions, i.e. a dynamic strain, various temperatures and discrete frequencies as in Fig. 6.17, representative of industrial applications (Fig. 6.15). The thermo-simplicity principle can also be used as in chapter 2 to predict the viscoelastic behavior of the rubber-ring at the temperature in the engine room (T_{ref}) over a broad range of frequencies by shifting the data obtained via DMA for several temperatures (Fig. 6.17). As a result, a master curve is obtained (Fig. 6.17, right). It will be further fitted (Tab. 6.3) in order to be used in the TVD viscoelastic model as explained in the next paragraphs.

6.4.5 Viscoelastic model

When the viscoelastic properties of the TVD rubber-ring are considered, the equation of motion 6.14 becomes Eq. 6.17 with variable stiffness K_{var} and damping C_{var} since they depend on the temperature, the frequency and the dynamic strain as the rubber-ring complex modulus E^* described in the previous section.

$$I_1\ddot{\theta_1} + C_{var}\,\dot{\theta_1} + K_{var}\,\theta_1 = C_{var}\ \theta_{amp}\ \omega_{acy}\,\cos(\omega_{acy}\,t) + K_{var}\ \theta_{amp}\,\sin(\omega_{acy}\,t) \tag{6.17}$$

Actually, K_{var} and C_{var} are deduced from E^* (E', E''). Let us examine the dependency of these terms on E^* and point out the way to determine them.

The torsional stiffness K_{cst} of a rubber-ring in Fig. 6.16 can be estimated by Eq. 6.11, where the G' is the shear modulus of the rubber-ring which is assumed here to be a homogeneous and isotropic material. Thus, Eq. 6.18 is valid to calculate G' from E' obtained via DMA with the Poisson ratio of the rubber $\nu \approx 0.5$. Moreover, K_{cst} becomes K_{var} when the viscoelastic properties of the rubber-ring are taken into consideration.

$$G' = \frac{E'}{2\,(1+\nu)} \ \rightarrow\ K_{var} = \frac{\pi\,R_{rr}^3\,L_{rr}}{e_{rr}\,(1+\nu)}\ \cdot\ E'(\theta_{exp}, f_{exp}, \varepsilon_{exp}) \tag{6.18}$$

It is worth noting that as E' in Eq. 2.5, K_{var} varies as a function of the temperature θ_{exp}, the loading frequency f_{exp} and the dynamic strain ε_{exp} experienced by the rubber-ring.

In parallel, the damping C_{cst} in Fig. 6.16 can be calculated using the third term of Eq. 6.16 where the only unknown is the damping ratio ξ (Eq. 6.19)

$$C_{cst} = 2\,\sqrt{K_{cst}\,I_1}\,\xi \tag{6.19}$$

However, according to [70] and [77] the structural loss factor η is equal to twice the damping ratio ξ, i.e. $\eta = 2\xi$ (at resonance [78]) and $\eta = E''/E'$ for viscoelastic materials (rubber-ring) leading to Eq. 6.20.

$$C_{var} = \sqrt{K_{var}\,I_1}\ \cdot\ \frac{E''(\theta_{exp}, f_{exp}, \varepsilon_{exp})}{E'(\theta_{exp}, f_{exp}, \varepsilon_{exp})} \tag{6.20}$$

Similarly, C_{var} depends on the temperature θ_{exp}, the frequency f_{exp} and the strain ε_{exp} experienced by the TVD rubber-ring.

In the next paragraphs, the differences between Eqs. 6.14 and 6.17 are evaluated thanks to the TVD response (FRFs) for several operating conditions (temperature and frequency). The differences between the constant (K_{cst}, C_{cst}) and the varying (K_{var}, C_{var}) stiffness and damping of the torsional vibration damper are also discussed.

6.4.6 Results

Results are presented for the TVD with inertia and geometric parameters in Tab. 6.3. This is the crankshaft TVD used in the FEAD of the six-cylinders engine in Fig. 6.15.

Table 6.3 – Inertia and geometric parameters of the TVD considered.

I_1 (Kg mm^2)	R_{rr} (mm)	L_{rr} (mm)	e_{rr} (mm)
31344.2	90	35	7

6.4.7 Dynamic Mechanical Analysis

In Eqs. 6.18 and 6.20 the storage and loss E', E'', and therefore, the complex E^* moduli can be obtained via DMA measurements of the TVD rubber-ring. Indeed, as explained in chapter 2, DMA is an experimental technique which consists in applying a cyclic and controlled strain (here $\varepsilon_{exp} = 0.2\%$), to a sample at different frequencies (0.2, 2, 20Hz) and testing temperatures, from -10 to $120°C$, as in Fig. 6.17 (left). Then, master curves are built to predict the mechanical behavior of the TVD rubber-ring under the engine operating conditions as in Fig. 6.17 (right), a given master curve corresponds to a given reference (engine room) temperature. In the case of the TVD rubber-ring, master curves were obtained and fitted (Tab. 6.4) for the engine room temperature of 20, 40, ... , $100°C$.

Further details about the DMA apparatus, principle, and the companion master curve reconstruction methodology can be found in chapter 2.

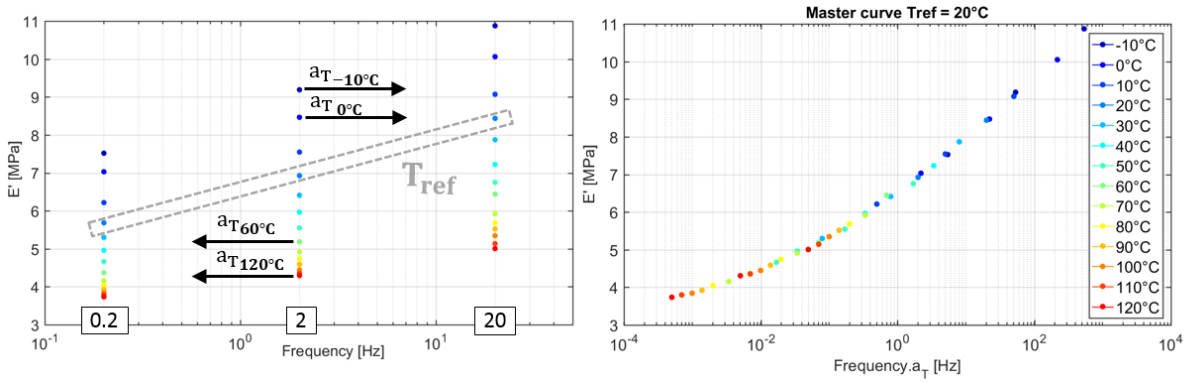

Figure 6.17 – TVD rubber-ring DMA data (left) and correspondent master curve (right).

Table 6.4 – Empirical equations describing the TVD rubber-ring moduli as F(θ_{exp}, f_{exp}, 0.002).

T_{ref} (°C)	Storage modulus E$'$(MPa)	Loss modulus E$''$ (MPa)
20	$6.55\ f_{req}^{\ 0.0814}$	$5.79\ f_{req}^{\ 0.0156} - 4.81$
40	$5.68\ f_{req}^{\ 0.0815}$	$5.41\ f_{req}^{\ 0.0163} - 4.58$
60	$5.02\ f_{req}^{\ 0.0820}$	$6.17\ f_{req}^{\ 0.0141} - 5.47$
80	$4.49\ f_{req}^{\ 0.0808}$	$6.07\ f_{req}^{\ 0.0139} - 5.49$
100	$4.27\ f_{req}^{\ 0.0835}$	$6.34\ f_{req}^{\ 0.0137} - 5.81$

6.4.8 Numerical results

The Tab. 6.5 gives data on stiffness and damping of the TVD in Tab. 6.3. Both constant values K_{cst} and C_{cst} are used to simulate the FRF resulting in the resonance frequency of 216 Hz and damping ratio of 0.075 (Tab. 6.5).

Table 6.5 – TVD characteristics at $60°C$ used to trace the constant FRF in Figs. 6.18 and 6.19.

K_{cst} (N m/rad)	C_{cst} (N m s/rad)	Resonance (Hz)	Damping ratio ξ
58000	6.4	216.5	0.075

The TVD geometric parameters from Tab. 6.3 with its rubber-ring material properties (stiffness, damping) calculated from DMA characterization (Eqs. 6.18 and 6.20) are then used in Eqs. 6.15 and 6.16 for several operating conditions of the torsional vibration damper producing the Figs. 6.18, 6.19, 6.20 and 6.21.

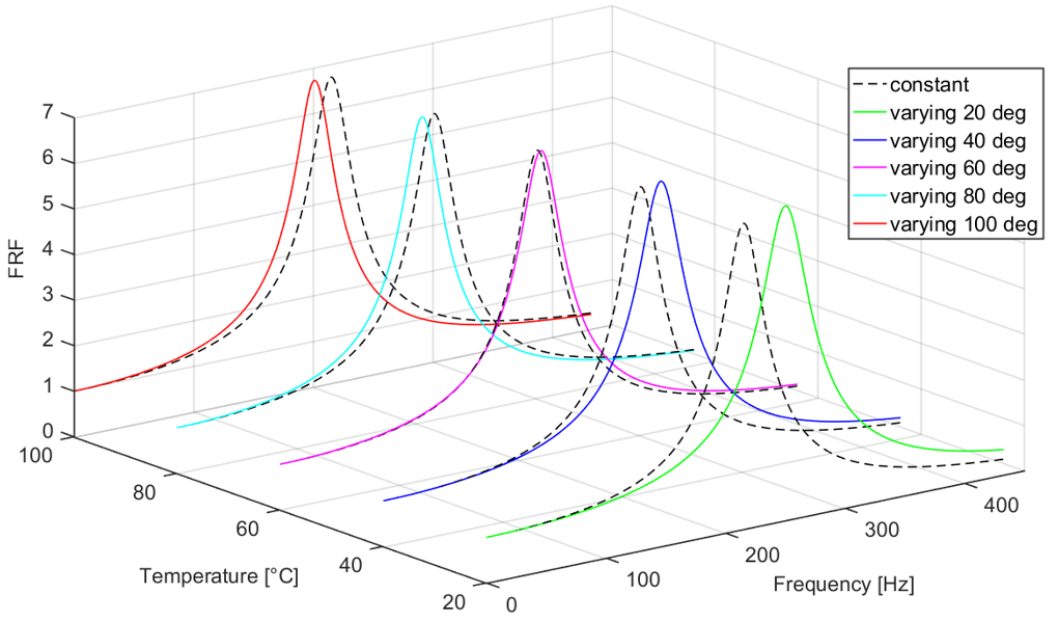

Figure 6.18 – TVD amplitude, frequency response for several temperatures.

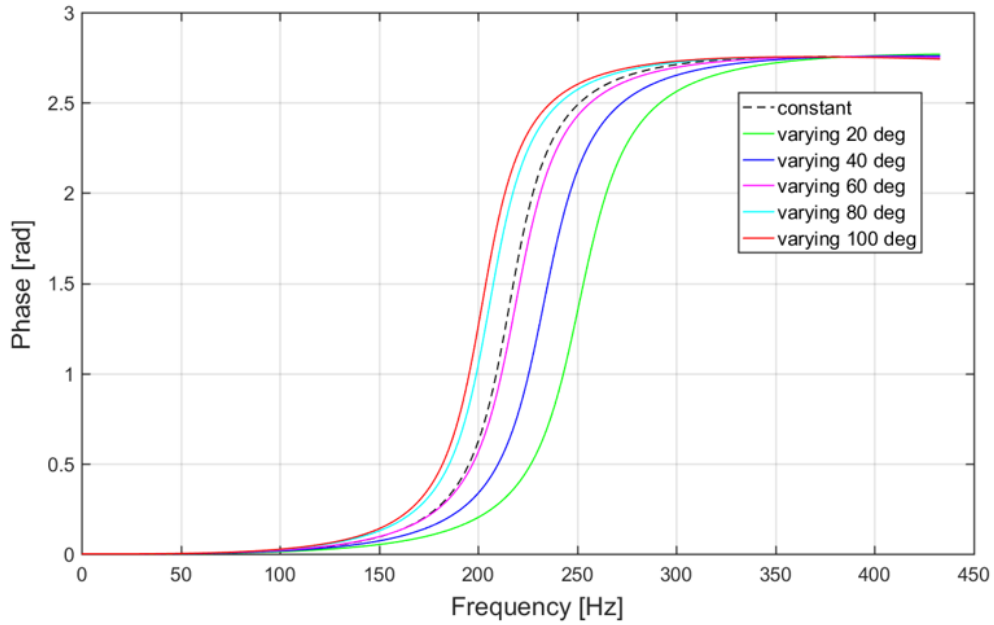

Figure 6.19 – TVD phase, frequency response for several temperatures.

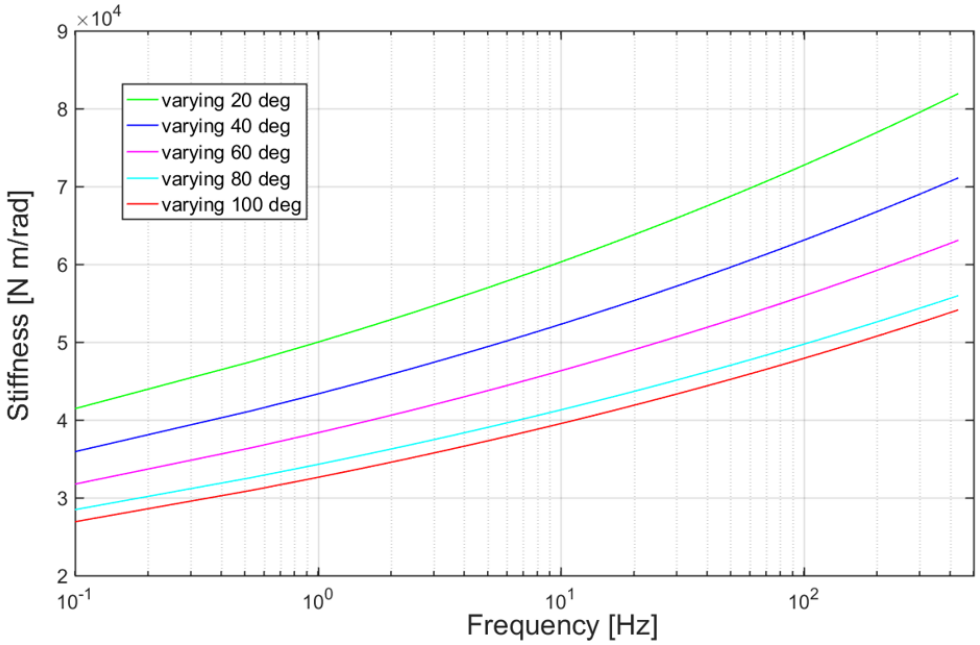

Figure 6.20 – TVD rubber-ring stiffness K_{var} for several temperatures.

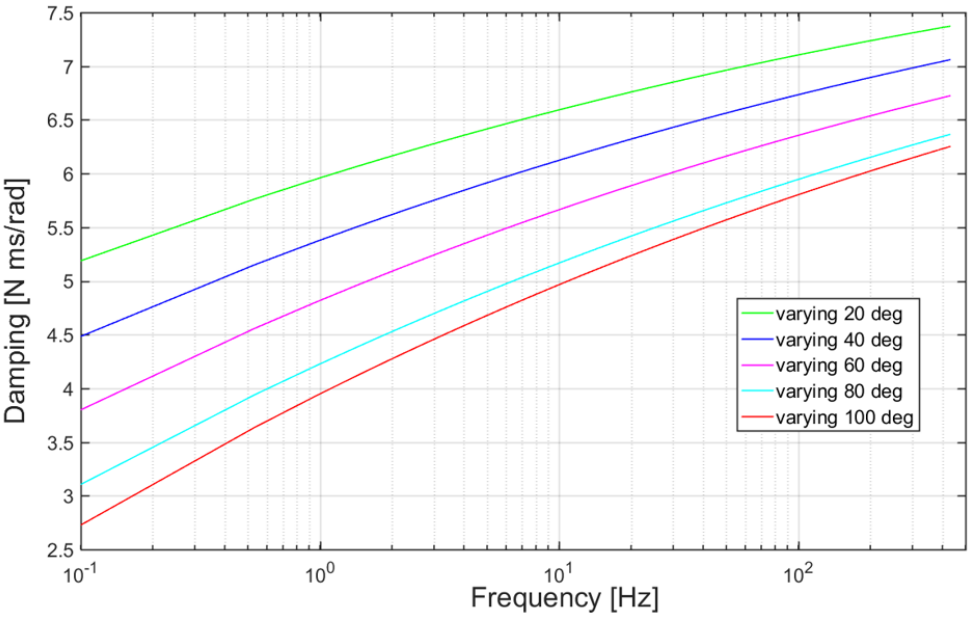

Figure 6.21 – TVD rubber-ring damping C_{var} for several temperatures.

The range of the testing temperature is chosen to be representative of the TVD working conditions, even in severe conditions of use, and the range of the excitation frequency is chosen to be equal in size to two times the TVD resonance frequency. Even if, in practice, the resonance frequency corresponds to an operation point to be avoided, in this work, it permits analyzing clearly the change (viscoelasticity effects) in the frequency responses of the TVD thanks to the symmetry of the FRFs and shifting in relation to each other.

The difference between the results obtained with constant and varying coefficients for several temperatures and the frequency domain equal to two times the TVD resonance frequency are also presented in Figs. 6.22 and 6.23.

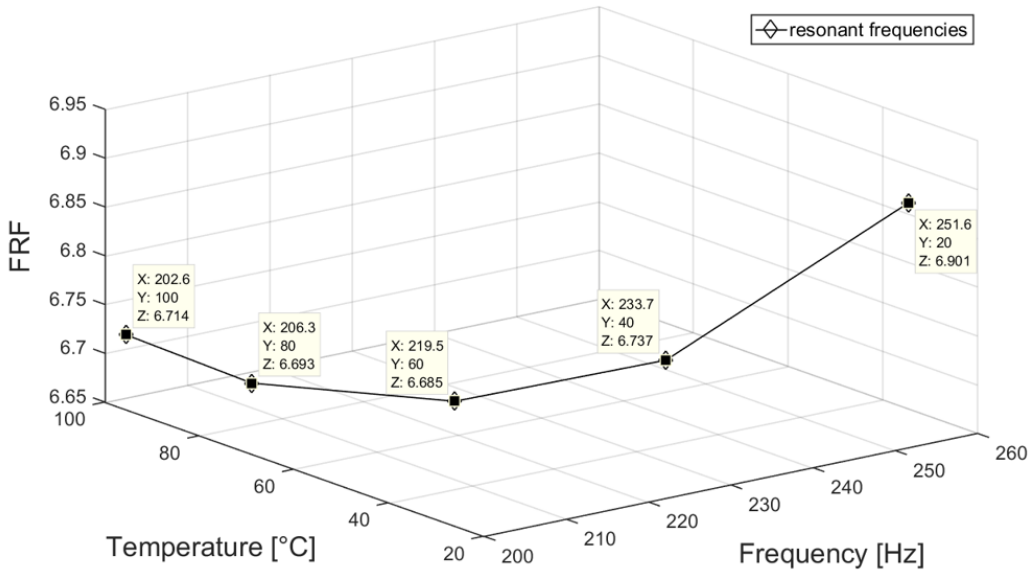

Figure 6.22 – FRFs maximum peaks provided by K_{var} and C_{var}.

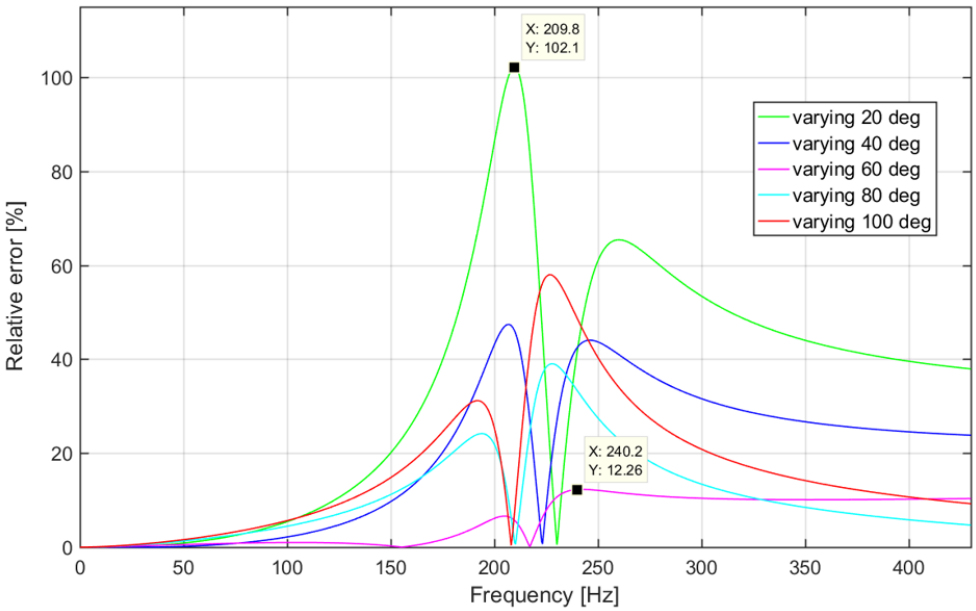

Figure 6.23 – FRFs (relative) error made when K_{cst} and C_{cst} are used instead of K_{var} and C_{var}.

These results are summarized, discussed and verified experimentally in the next sections.

6.4.9 Experimental verification

After generating numerical results for a case study (Tab. 6.3) of the TVD in Fig. 6.15, we wanted to verify experimentally the effectiveness of the TVD modeling as a single DOF system (Fig. 6.16) since verifying the effectiveness of the modeling means validating experimentally simulation results which point out an interesting behavior (FRFs) of the TVD when its viscoelastic properties are considered. Thus, through the experimental setup in Fig. 6.24 the TVD could be tested under specific operating conditions. Indeed, the range of temperature is chosen to be representative of the TVD working conditions and the range of the excitation frequency is chosen to be equal in size to two times the TVD resonance frequency as before.

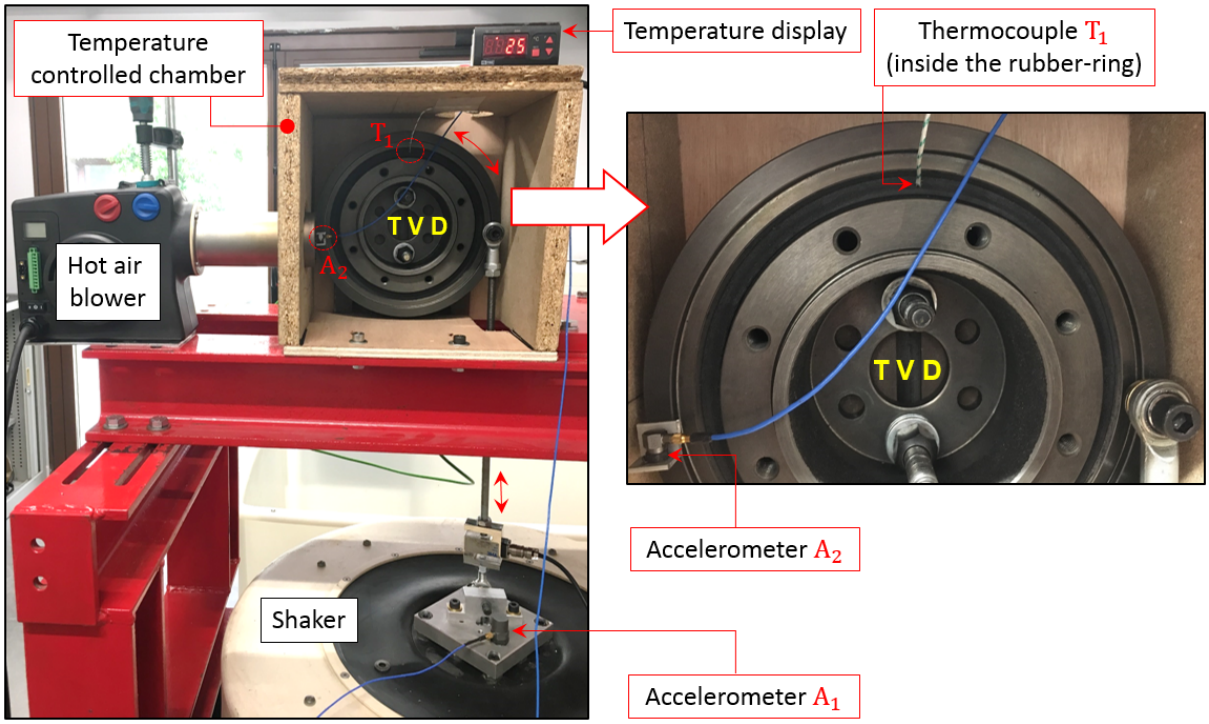

Figure 6.24 – Experimental setup used to test the TVD under specific operating conditions.

In Fig. 6.24, the hub of the TVD is fixed and through a push-rod system the outer-ring of the TVD is harmonically excited by a shaker. A hot air blower and a temperature controlled chamber (closed during the tests) are also used to increase the temperature from environment to high temperature. This testing temperature is measured by the thermocouple T_1 inside the TVD rubber-ring and the FRFs in Figs. 6.25 and 6.26 are obtained from the ratio between the accelerometers A_1 and A_2 in Fig. 6.24.

As a result of the experiments, the stiffness and damping obtained experimentally through the -3dB method (Eq. 6.12) and Eq. 6.19 show good agreement ($\leq 11\%$ of error) with those obtained via Eqs. 6.18 and 6.20 for the temperature of $60°C$ (Tab.6.6).

Table 6.6 – Comparison between TVD stiffness and damping, simulated and measured at $60°C$.

	Stiffness [Nm/rad]	Damping [N ms/rad]	Resonance [Hz]	Damping ratio
Simulations	58000	6.4	216.5	0.075
Experiments	60526	5.8	221.2	0.067
Rel. error [%]	4.4	9.2	2.2	11.0

As previously mentioned, the frequency responses in Figs. 6.25 and 6.26 were obtained experimentally. They confirm some interesting points observed in simulations, e.g. when the TVD working temperature is increased the resonance frequency is decreased, i.e. the FRFs are shifted to the left when the TVD is subjected to high temperatures (Tab. 6.7).

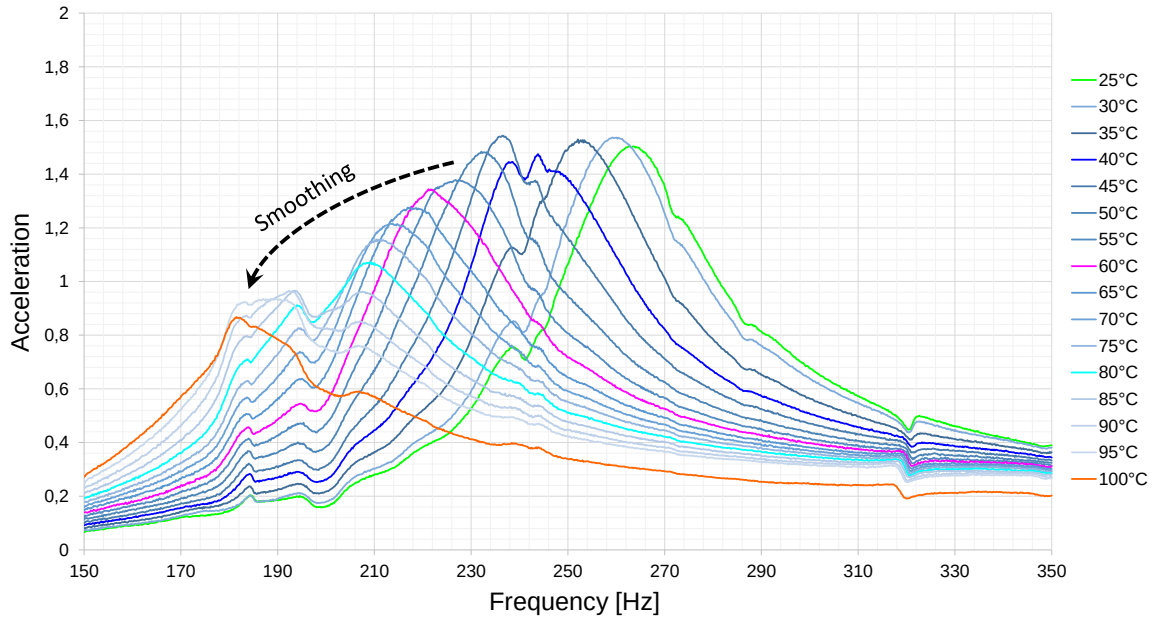

Figure 6.25 – Experimental FRF (amplitude) of the TVD for several temperatures.

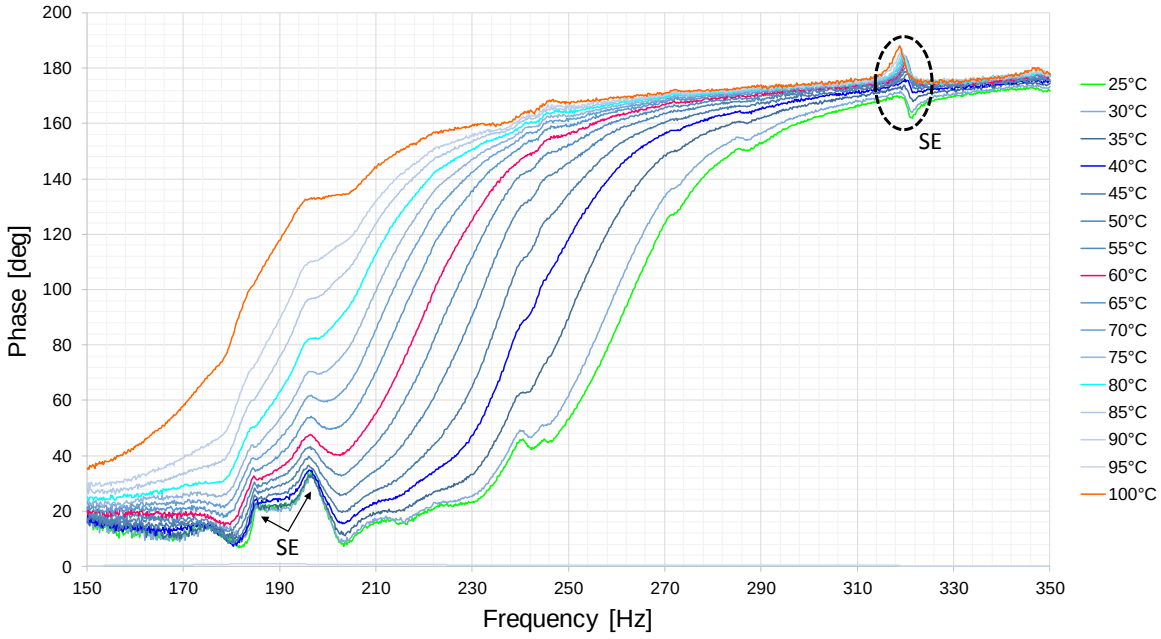

Figure 6.26 – Experimental FRF (phase) of the TVD for several temperatures.

Table 6.7 – Comparison of resonance peaks from simulations and experiments.

Temperature [°C]	Amplification [g]	Peak experiments [Hz]	Peak simulations [Hz]	Relative error [%]
20	0	274.2	251.6	8.2
40	1.5	243.8	233.7	4.2
60	1.3	221.2	219.5	0.8
80	1.1	209.2	206.3	1.4
100	0.6	206.9	202.6	2.1

6.5 SUMMARY AND CONCLUSIONS

Constant stiffness K_{cst} and damping C_{cst} are considered in Tab. 6.5. Sometimes, these average values are used to represent the TVD operating at steady conditions, e.g. $\theta_{exp} = 60°C$, $\varepsilon_{exp} = 0.2\%$ and f_{exp} coinciding with the engine acyclism ($\sim$ 30Hz), and throughout the engine operation point. In practice, K_{cst} and C_{cst} are often used in straightforward models (e.g. Eq. 6.14), whereas they are used here to highlight the variation of the TVD response (Eq. 6.15) as a function of the temperature and frequency. Moreover, the response of the TVD is analyzed as a function of its operating conditions (temperature, frequency) because it is assumed here the viscoelastic complex moduli and, consequently, the TVD rubber-ring properties K_{var} and C_{var} dependent exclusively on the temperature and frequency (no Payne effect, Appendix $A4$), thus for the constant strain $\varepsilon_{exp} = 0.2\%$, different operating conditions lead to the responses as in Figs. 6.18 and 6.19.

The differences between the FRFs in the Figs. 6.18 and 6.19 are proportional to the rubber-ring stiffness and damping variations in the Figs. 6.20 and 6.21 since the FRFs are generated from K_{var} and C_{var} using Eqs. 6.15 and 6.16. Thus, both the FRFs and the rubber-ring properties from DMA vary proportionally with the TVD operating conditions (temperature, frequency) and the empirical equations in Tab. 6.4.

In Fig. 6.18 when the TVD working temperature is changed, e.g. from $\theta_{exp} = 60°C$ to $80°C$, the maximum amplitude (peak) value of its FRF slightly changes (Fig. 6.22), i.e. it changes by a few percent with a maximum of 3.3% at $\theta_{exp} = 20°C$ when compared to the constant case in Tab. 6.5 ($\theta_{exp} = 60°C$).

Assuming K_{cst} and C_{cst} (constant FRF in Fig. 6.18) for the same temperature ($\theta_{exp} = 60°C$) seems to be good approximations of the realistic K_{var} and C_{var} (FRF at $60°C$ in Fig. 6.18) with a maximum relative error of around 12.3% (Fig. 6.23). However, throughout the engine operating point with f_{exp} ranging from 0Hz (engine at rest) to 2 times the TVD resonance frequency ($\sim$ 430Hz) in Fig. 6.23, the relative error increases substantially when the temperature is changed. For example, comparing the FRF at $20°C$ obtained at $\theta_{exp} = 20°C$ (K_{var} and C_{var} as in Eqs. 6.18 and 6.20) and FRF at $60°C$ (K_{cst} and C_{cst} as in Tab. 6.5) at $\theta_{exp} = 60°C$ the relative error, i.e. $(FRF_{20°C} - FRF_{Constant})/FRF_{20°C}$, between these TVD responses can reach around 100%, more precisely, 102.1% (Fig. 6.23).

Another interesting point when considering the viscoelasticity of the TVD rubber-ring is the different resonance frequencies in Tab.6.7 accordingly with its operating conditions, i.e. the strain, the temperature and the frequency to which the rubber-ring is subjected. When the temperature is increased the TVD resonance peak is shifted to the left. This is because the stiffness K_{cst} in Eq. 6.11 depends on G' which depends on E' (Eq. 6.18), and therefore, on the rubber-ring complex modulus (temperature, frequency and strain), thus the TVD resonant frequency calculated by the second term of Eq. 6.16 also depends on the TVD operating conditions.

Overall, the comparison between simulations and experiments shows good agreement with small relative error (Tab. 6.7). However, when the temperature is increased the FRFs are more dampened (smoothing) and there are some side-effects (SE), respectively, due to the complex viscoelastic material behavior and due to the fact of not being able to impose a pure torsional mechanical excitation to the TVD. In the latter case, it means there also are the response of other modes (directions) in the FRFs supposed to be 1-DOF.

Chapter 7

SUMMARY, CONCLUSIONS, AND FUTURE WORK

Contents

This chapter summarizes the research presented in the previous chapters, and suggests future work in the area of modeling and optimization of power losses in Front Engine Accessory Drives of vehicles.

7.1 SUMMARY AND CONCLUSIONS

The model, derived in chapter 2, describes the location and the origin of the power lost by a functioning FEAD. The resulting equation (Eq. 2.1) forms the basis for the power loss predictions and serves as the criterion for the optimization methods.

The power loss models are detailed along the chapter 2, where five cyclic modes of loading and unloading the poly-V belt when it is transmitting power in a FEAD are stated. These cyclic modes are the bending, stretching, shear, flank and radial compression hysteresis.

Among all the poly-V belt cyclic loading modes, only the bending depends exclusively on the belt transmission geometry and the viscoelastic properties of the poly-V belt material. The other modes are coupled, for example, the radial compression of the middle layer of the poly-V belt depends on the compression of the poly-V belt flanks, i.e. forces resulting from the belt/pulley contact pressure penetrate the flanks of the poly-V belt to cyclically compress the material of the belt middle layer all along the arc of contact.

An experimental procedure using the principle of Dynamic Mechanical Analysis and the master curve reconstruction methodology provides the basis for hybrid simulations which combine theoretical and experimental data to obtain the power losses.

To provide a representative FEAD power loss model, in addition to the belt-hysteresis other phenomena have been modeled in chapter 2. Indeed, the slip between the poly-V belt and the pulleys is fully described and compared to the literature. Models by SKF describing the power loss inside the bearings are adapted to the case of FEADs. Finally, tensioner and belt vibrations hysteresis power losses are fully modeled to be considered in the case where the system is subjected to engine (acyclism) torque fluctuations.

The genetic algorithm and dynamic programming methods, applied in chapter 3, form the basis for the optimization analyses and their results should provide guidance to FEAD designers in the future.

The optimization methods (GA and DP) were compared to the Brute Force (BF) method, which reaches the exact and optimal solution by testing all possibilities of changing the optimizable parameters to reduce the power losses, and the results obtained by this comparison are encouraging with respect to the algorithms performance and the optimization.

Experiments verify several key points of the power loss analyses. For example, the power losses taking place in the FEADs are not independent phenomena, but coupled to each other. Indeed, at the beginning of the testing campaign and through the development tests on the 2 pulleys system it was already clear that to validate only one power loss phenomenon, e.g. bending, which only depends on the belt transmission geometry and belt properties, is impossible since the belt needs to be installed, so a minimum contact pressure that causes flank and radial compression exists. However, the decreasing in the sum of all (total) FEAD power losses predicted by theory is verified experimentally in chapter 3 and the simulated total power losses presents good agreement with the experimental verification for several FEADs in chapter 4.

The analyses predicting (chapters 2 and 5) and optimizing (chapter 3) the total FEAD power losses agree quite well with experimental measurements (chapter 4).

As briefly discussed in chapter 5, the implemented simulation tool (PLFead) allows the user to simulate the power losses of several FEADs at the same time, to quickly change the parameters of a belt transmission and relaunch the simulation to quantify new power losses. PLFead also permits generating a huge number of belt transmissions and applying optimization techniques to obtain the FEAD which dissipates the minimal power losses.

PLFead is a tool composed of validated power loss models and, inter alia, algorithms which permit to obtain optimal results in terms of geometry and belt setting tension leading to the dissipation of a minimal amount of power losses.

Required parameters for simulations are determined in chapter 6 using classic procedures inspired in the literature. The obtained parameters, e.g. tensile modulus, are consistent with those obtained by other authors. However, in this case, the belt stiffness, damping and friction coefficient and so on, are available for trucks and should serve as reference for future studies. In the same way, the hysteresis curves obtained for the tensioners will be useful to generate simulation and experimental results when needed. It means that when engine torque fluctuations will be generated and taken into consideration experimentally and numerically as a part of the total FEAD power losses.

The torsional vibration damper used in FEADs of Volvo trucks is analyzed at the end of the chapter 6, its behavior is simulated assuming constant and varying (viscoelastic) rubber-ring properties, then compared to experiments. The changes in the damper's responses are calculated numerically through 3D FRFs for several operating conditions (temperature, frequency). Finally, these simulations of the damper's responses present good agreement with equivalent results obtained experimentally under the same operating conditions of simulations.

7.2 FUTURE WORK

The analytical, simulation and experimental results suggest future work, to improve the predictions and optimization of the power losses, and provide a better understanding of the power loss phenomena taking place in a FEAD.

1. Generate engine torque fluctuations experimentally. This would produce useful experimental results which can be used for comparisons with simulations results, generated by e.g. the belt vibration power loss model in chapter 2, for a case study.

2. Find new and better methods to isolate and identify experimentally each power loss type (bearings, slip, hysteresis). Indeed, all these losses are interdependent and difficult to isolate.

3. Include other significant parameters, than the pulleys-center location and the belt setting tension, in the optimization of the FEADs. This would contribute to improve the optimization by acting on the model(s) and/or the parameter(s) highly relevant to the optimization of the power losses.

4. Include other models in the power loss prediction and optimization. For example, in this thesis, it was demonstrated that the TVD rubber-ring has a viscoelastic behavior. Thus, similar to the poly-V belt, the TVD also dissipates power when it is sheared and unsheared cyclically as result of the engine torque fluctuations.

Chapitre 8

FRENCH SUMMARY (Résumé étendu)

Contents

Chapitre 1. Introduction

1.1. Motivation et EDIT

Ces dernières années, des efforts importants ont été entrepris afin de développer des transmissions de véhicules énergiquement plus efficaces. Ces efforts sont une conséquence directe des nouvelles normes d'émission polluantes plus strictes, encourageant les constructeurs de véhicules à réduire les pertes de puissance de leurs moteurs. Ainsi, ces moteurs deviennent donc plus efficaces et moins polluants.

Cette thèse est motivée par des problématiques environnementales de réduction de pertes d'énergie, par des interrogations de la part des constructeurs de véhicules sur l'amélioration de la performance de leur moteurs et par ma volonté de faire progresser la science et la technologie.

Cette thèse a été achevée dans le cadre du projet EDIT (i.e. Efficient Distribution Truck). En effet, Renault Trucks et six partenaires travaillent sur ce projet qui rassemble des technologies innovantes liées à l'aérodynamisme, à l'hybridation du moteur, aux pneumatiques et à la communication véhicule-infrastructures dans le but de réduire la consommation de 13% par rapport à un véhicule EURO-6. Le véhicule prototype utilisé est le Renault Trucks D Wide Euro 6 (Fig. 8.1) équipé d'une caisse frigorifique. Le projet EDIT est labellisé par le pôle de compétitivité LUTB Transport et Système de Mobilité et a été sélectionné dans le cadre du 19ème appel à projet FUI Régions.

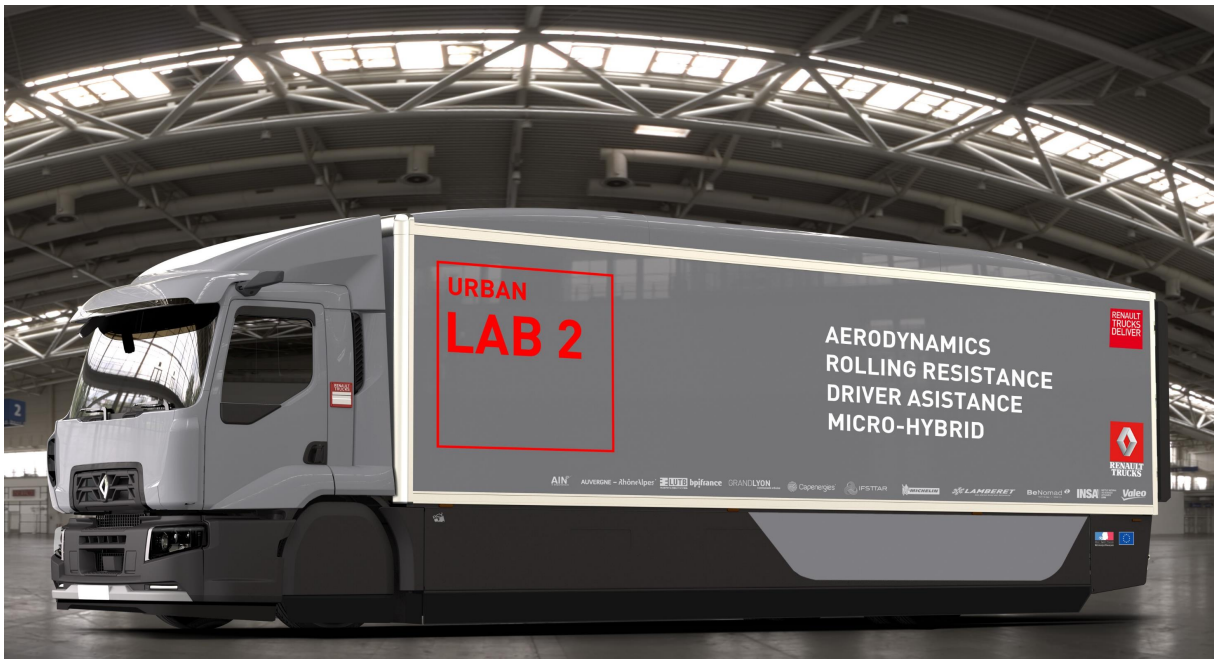

FIGURE 8.1 – Camion Renault Range D Wide (Urban Lab 2).

L'objectif du projet EDIT est de proposer des innovations applicables à l'horizon 2020. Elles concernent principalement quatre domaines : l'aérodynamisme, le "Stop and Start" et micro-hybride, la connectivité et les pneumatiques. Concernant le deuxième domaine, Renault Trucks collabore avec l'INSA de Lyon sur la réduction des pertes de puissance de la face avant moteur, dans le but d'optimiser le rendement du système micro-hybride.

1.2. Face avant moteur et ses accessoires

Les transmissions par courroie striées ou poly-V (Fig. 1.3), aussi appelées serpentines, sont utilisées très largement dans l'industrie automobile ainsi que dans d'autres domaines industriels pour la transmission mécanique de puissance.

La courroie poly-V est très flexible et légère (faible masse linéique), ce qui permet la conception de transmissions entraînant plusieurs accessoires avec des parcours de courroie sinueux et des rayons d'enroulement faibles (Fig. 1.2). Les courroies poly-V présentent plusieurs avantages (Fig. 1.7) par rapport à d'autres modèles (plates, trapézoïdales) ; par exemple, au lieu d'utiliser plusieurs courroies trapézoïdales ou une courroie plate très large pour transmettre une puissance donnée, une seule courroie poly-V moins large suffit pour transmettre cette même puissance. Une courroie poly-V peut avoir plusieurs dimensions et profils (Fig. 1.6) et sa largeur (nombre de stries) est choisie en fonction de la puissance transmise. Les matériaux constituant la courroie sont généralement des polymères, en d'autres termes des matériaux viscoélastiques. Ces matériaux sont disposés de façon à avoir un module d'élasticité très élevé dans le sens longitudinal de la courroie. Le modèle d'une courroie poly-V idéalisé à partir d'observations au microscope est présenté Fig. 1.8.

Dans les moteurs de véhicules, une courroie poly-V sert à transmettre la puissance fournie par le moteur à combustion interne aux différents accessoires (alternateur ou alterno-démarreur, pompes, compresseur, etc) (Fig. 1.4). Cette transmission par courroie poly-V constitue principalement ce qu'on appelle la façade accessoire du moteur (FEAD).

Une face avant de moteur est composée de plusieurs accessoires et d'une courroie qui les entraîne. Des galets tendeurs sont aussi fréquemment et stratégiquement utilisés pour éviter une collision entre la courroie et la structure environnante (Fig. 1.14) et pour accroître la capacité de transmission de puissance en augmentant les arcs d'enroulement des poulies. D'autres tendeurs, mécanique ou hydraulique, sont également utilisés afin de permettre d'une part l'installation de la courroie, soumise à l'arrêt à une tension dite d'installation ou de pose T_0 (Fig. 1.20), et d'autre part le maintien d'une tension constante dans les brins adjacents. Par contre, il y a de la dissipation d'énergie sous forme de chaleur, aussi bien dans la courroie poly-V qu'au niveau de ses surfaces de contact, et de ses accessoires (tendeurs, roulements) ; ceci peut être dû à l'hystérésis ou au frottement sec de Coulomb, par exemple.

Pour les calculs des pertes de puissance dans une façade accessoire de moteur (FEAD), des notions de la dynamique d'un système hybride constitué d'éléments discrets (les poulies) et continu (la courroie) sont nécessaires. Concernant les calculs des pertes de puissance de base, comme par exemple l'hystérésis de la courroie, une analyse dynamique en régime quasi-statique peut répondre aux besoins des modèles de pertes de puissance ; cette analyse détermine les brins mous T_s et les brins tendus T_t d'une transmission (cf. Fig. 1.19). De plus, dès qu'il existe une différence de tension entre les brins adjacents à une poulie, il apparaît deux arcs de contact [14], un arc de glissement ϕ_s et un arc d'adhésion ϕ_a (Fig. 1.21). La somme des arcs de glissement et adhésion est égale à l'arc d'enroulement ϕ, qui à son tour est un résultat du calcul de paramètres géométriques de la façade (Fig. 1.18).

Les objectifs de cette thèse sont donc notamment de modéliser les pertes de puissance d'une face avant moteur, puis de les optimiser, de valider expérimentalement les modèles de pertes de puissance et les implémenter dans un outil logiciel ; de caractériser les composantes de façade (e.g. courroie, tendeurs), et de communiquer les résultats obtenus.

Chapitre 2. Modélisation

2.1. Pertes de puissance par hystérésis

L'énergie dissipée par une FEAD en fonctionnement a plusieurs origines :

$$PL_{FEAD} = PL_{hys} + PL_{bear} + PL_{slip} + PL_{vib} \tag{8.1}$$

1. Hystérésis de la courroie et du tendeur PL_{hys}
2. Frottements dans les roulements PL_{bear}
3. Glissements entre la courroie poly-V et les poulies PL_{slip}
4. Vibrations longitudinales dans les brins de courroie PL_{vib}

Les pertes de puissance (énergie) ci-dessus correspondent souvent à la surface interne de courbes d'hystérésis similaires à celle de la Fig. 8.2.

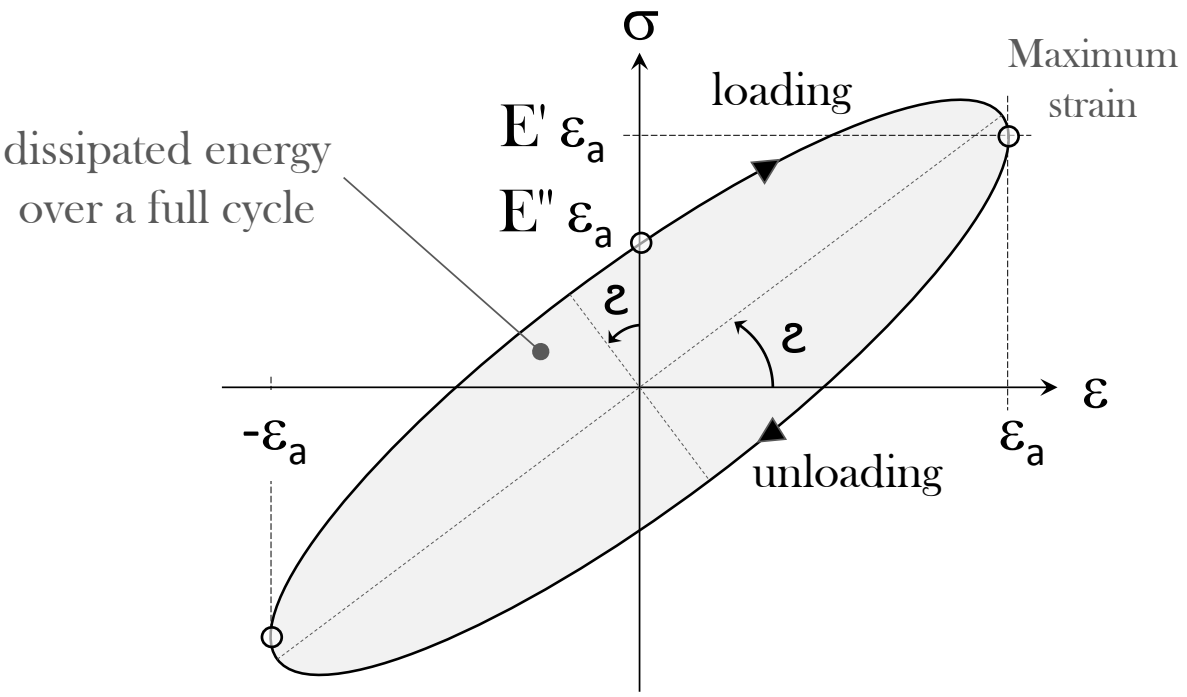

FIGURE 8.2 – Courbe contrainte-déformation pour un matériau viscoélastique.

Cette courbe correspond au comportement dissipatif des matériaux viscoélastiques de la courroie poly-V quand ils sont linéairement (petites déformations) et cycliquement (charges alternatives) sollicités au long du parcours de la courroie d'une face avant moteur. Des courbes d'hystérésis (comportement hystérétique) similaires existent également pour les tendeurs (cf. Annexes $A10$ et $A11$).

Les modèles de pertes de puissance sont résumés au cours de la prochaine section.

2.2. Modèles de pertes de puissance par hystérésis

Au long de son parcours et pendant la transmission de puissance, une courroie poly-V subit des charges cycliques dont l'aspect physique et la région concernée sont présentés en résumé à la Fig. 8.3.

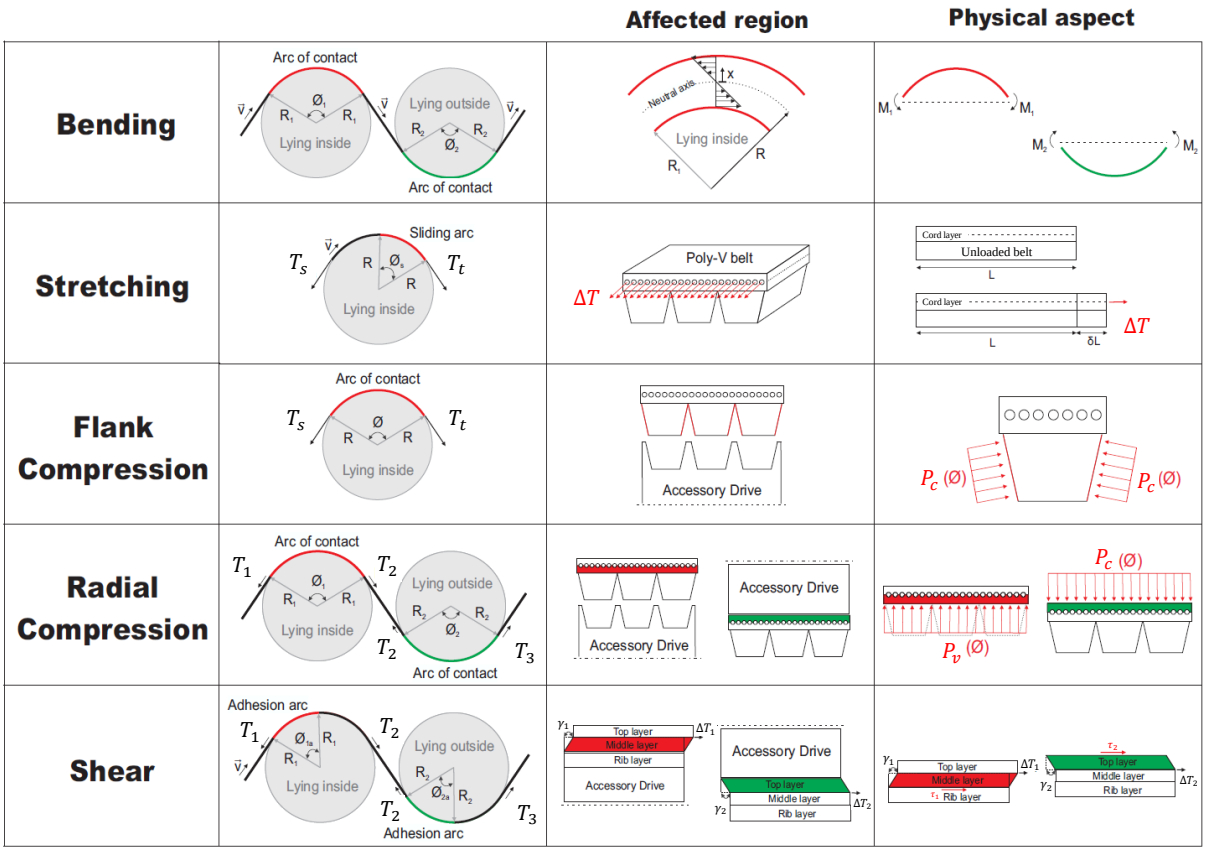

FIGURE 8.3 – Résumé des phénomènes des pertes de puissance par hystérésis de la courroie.

L'objectif des modélisations des phénomènes (Fig. 8.3) dans le chapitre 2 est de trouver un modèle mathématique qui décrit l'énergie dissipée par unité de longueur de la courroie W_h, puis de trouver la puissance correspondante dissipée en multipliant cette énergie par la vitesse linéaire de la courroie V (Eq. 8.2).

$$PL_{belt-hys} = W_h \cdot V \tag{8.2}$$

Une fois que les modèles mathématiques sont décrits, on peut constater que dans les équations relatives à l'énergie W_h, il y a des modules de perte E'' et de stockage E'.

Les modules E' et E'' représentent deux propriétés des matériaux composant la courroie poly-V (EPDM et PET), et notamment leur capacité à respectivement stocker de l'énergie (puis de la restituer au système) et dissiper de l'énergie (amortir le système).

Comme les modules E' et E'' ne sont pas des données fournies par les fabricants de courroies, les matériaux des différentes couches de la courroie poly-V ont été découpés (Fig. 8.4), puis testés en utilisant l'analyse mécanique dynamique (DMA) dans le but d'obtenir les équations empiriques qui décrivent le comportement de ces matériaux. On peut alors calculer les modules de stockage E' et de perte E'' en fonction de la température, de la déformation et de la fréquence des charges cycliques.

2.3. Résultats

2.3.1. Analyse Mécanique Dynamique

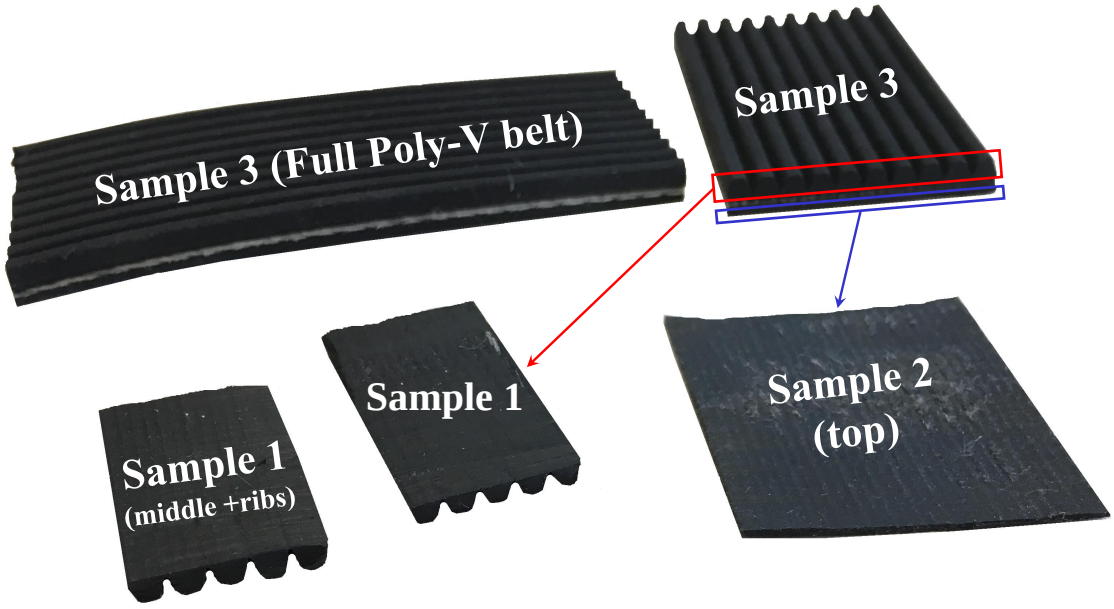

FIGURE 8.4 – Echantillons de courroie pour les Analyses Mécanique Dynamique (AMD).

Les analyses mécaniques dynamiques ne peuvent être effectuées que pour certaines valeurs de fréquence. Dans les analyses de cette thèse, les valeurs de 0.2, 2 et 20 Hertz ont été choisies (Fig. 8.5). Une courbe maîtresse des modules, utilisant l'équivalence temps/température (i.e. fréquence/température), est construite afin d'être ajustée et intégrée dans les modèles des pertes de puissance à la place des modules E' et E''.

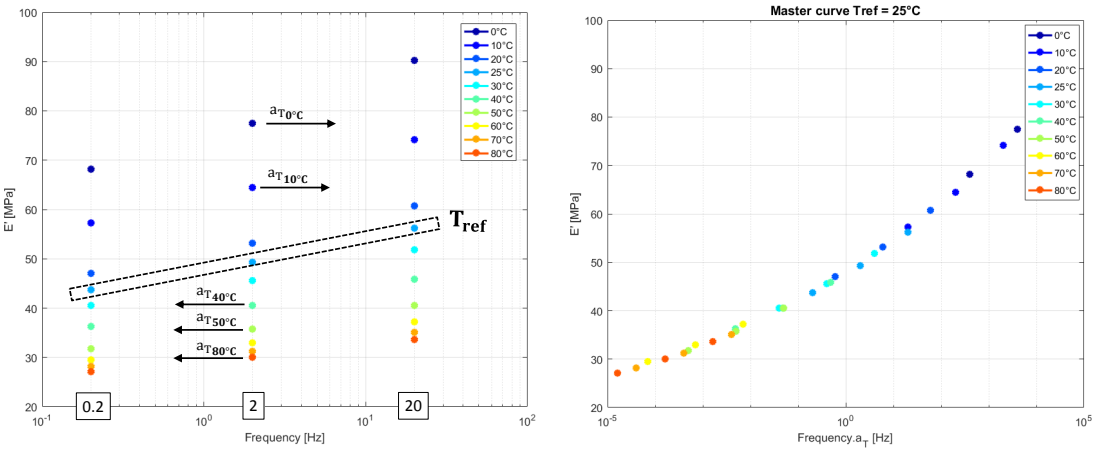

FIGURE 8.5 – Données issues des essais AMD (à gauche) et courbe maîtresse associée (à droite).

Dans les figures ci-dessus, les propriétés des matériaux de la courroie poly-V ne varient qu'en fonction de la température et de la fréquence. Cette spécificité est due à l'effet Payne ; en effet on assume que les modules E' et E'' ne dépendent pas de la déformation, car ils ne changent quasiment pas en fonction des déformations cycliques subies par les matériaux de la courroie pendant le fonctionnement d'un moteur (cf. Annexe $A4$).

2.3.2. Cartographie des pertes de puissance

Plusieurs études de cas ont été considérées durant cette thèse, chacunes ayant un objectif spécifique. Par exemple, les cartographies des pertes de puissance représentées Fig. 8.6 ont le but de mettre en évidence l'effet de la température sur les pertes par hystérésis de la courroie.

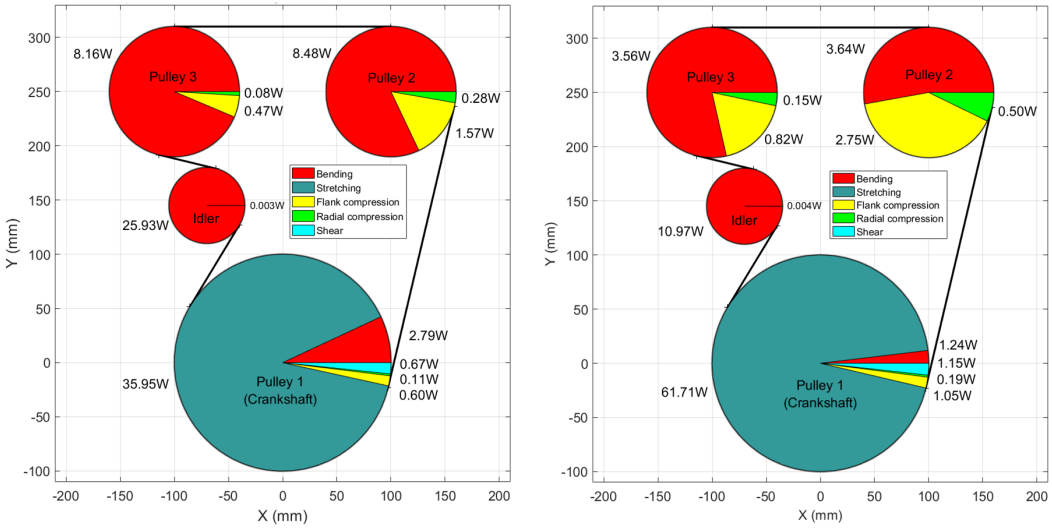

FIGURE 8.6 – Pertes de puissance de la façade à la Fig. 2.17 (à gauche, $25°C$) (à droite, $60°C$).

D'autres cartographies de pertes de puissance globale ont aussi été analysées (Fig. 8.7).

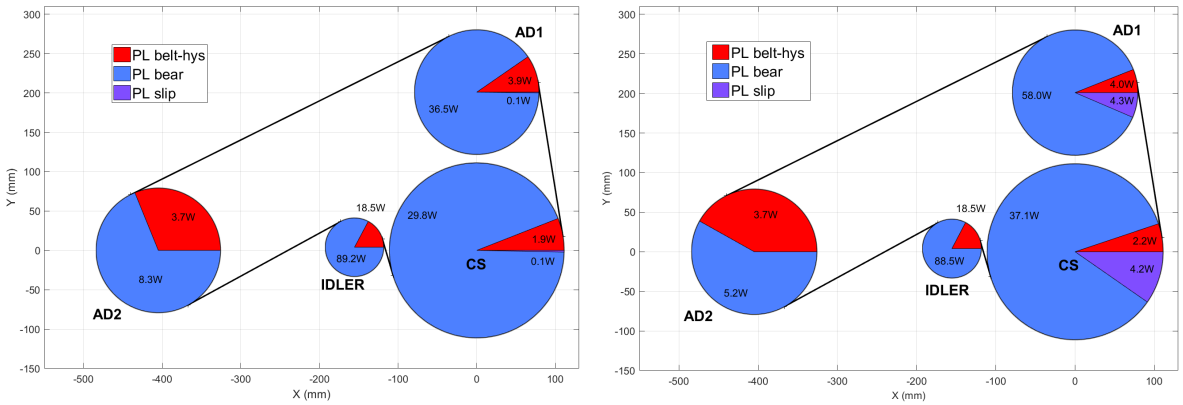

FIGURE 8.7 – Pertes de puissance pour de faibles (à gauche) et forts (à droite) couples résistants.

Dans ce cas, la somme des pertes par flexion, étirement, cisaillement, compression radiale et compression des flancs de la courroie (Fig. 8.6), devient PL belt-hys (Fig. 8.7).

Des modèles de pertes de puissance dans les roulements et de pertes de puissance dues au glissement courroie/poulies ont été, respectivement implémentés et développés. Ceux-ci représentent les pertes de puissance PL bear et PL slip (Fig. 8.7).

Des représentations schématiques telles que celles de la Fig. 8.7 ont servi pour représenter les pertes de puissance à plusieurs régimes de fonctionnement de façades (vitesse du vilebrequin, couples résistant, etc), mais aussi pour optimiser les pertes de puissance.

2.3.3. Vérification expérimentale

Afin de valider les pertes de puissance, en d'autres termes, vérifier que les pertes de puissance prédites par les modélisations correspondent à ce que l'on mesure dans la réalité, le montage expérimental de la Fig. 8.8 a été mis en place.

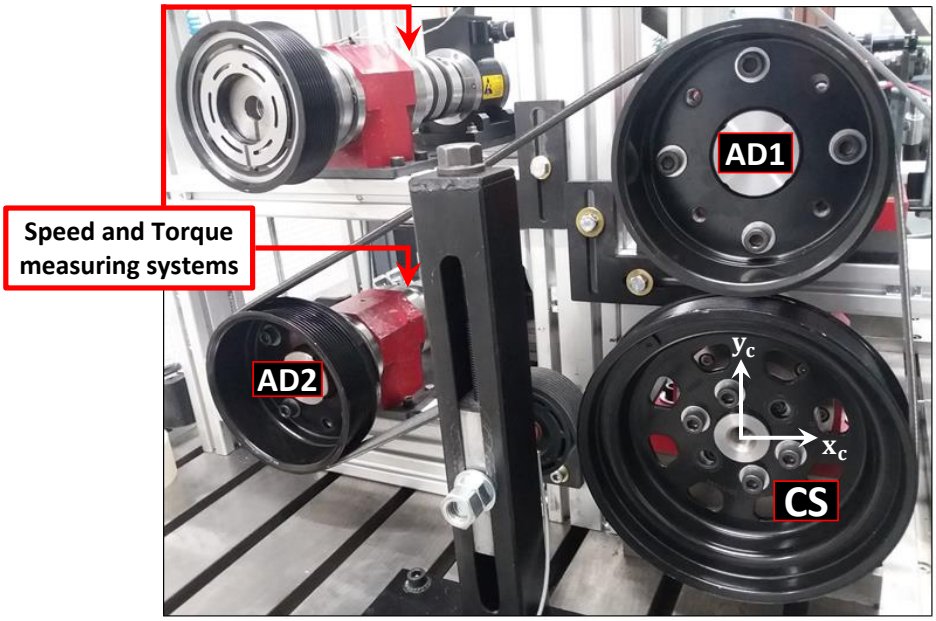

FIGURE 8.8 – Montage expérimental avec le détail du système de mesure de vitesse et de couple.

Plusieurs régimes de fonctionnement de la façade sur le banc d'essais ci-dessus ont été testés (Fig. 8.9), notamment différents couples résistants imposés par la poulie AD1. Puis la perte de puissance PL_{FEAD} a été évaluée expérimentalement et au travers de simulations.

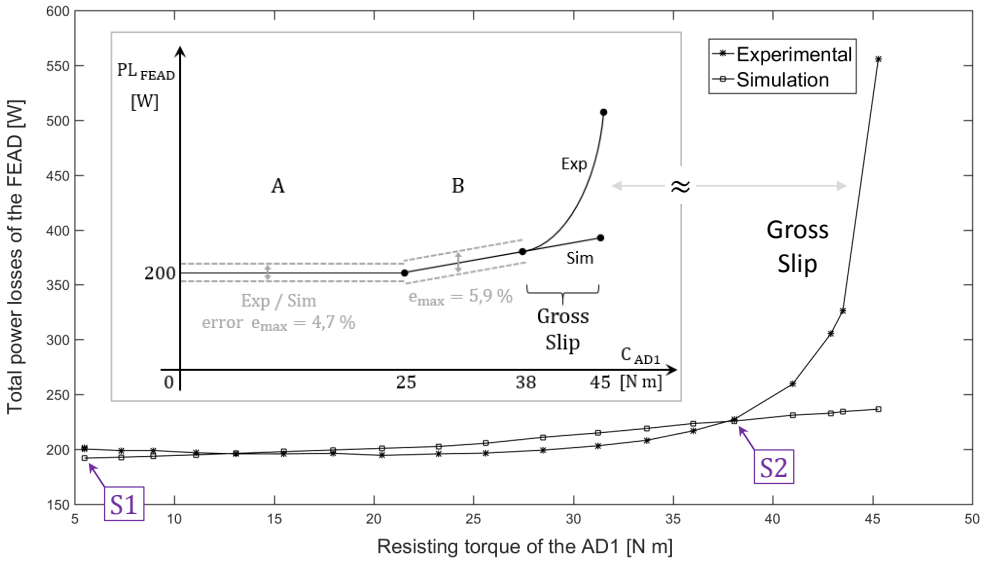

FIGURE 8.9 – Résultats d'expériences et de simulations pour la façade de la Fig. 8.8.

Les résultats de simulations correspondent bien à ceux issus des expériences avec des erreurs relatives faibles (< 6%) (Fig. 8.9), à l'exception d'une zone (gross slip / glissement généralisé) dans laquelle la façade est sensée ne pas fonctionner puisqu'il n'y a pas de transmission de puissance.

Chapitre 3. Optimisation

Dans ce chapitre, deux méthodes (l'algorithme génétique et la programmation dynamique) sont appliquées au problème d'optimisation des faces avant moteur dans le but d'optimiser les pertes de puissances modélisées lors du chapitre précédent. Les paramètres pris en compte dans les optimisations des pertes de puissance sont la géométrie (centre des poulies X, Y) et les conditions de fonctionnement (tension de pose T_0) des faces avant moteur.

Le problème d'optimisation est formulé de la façon suivante : PL_{FEAD} est la perte de puissance totale dissipée par la façade (à optimiser), X, Y et T_0 sont les paramètres optimisables, et F_f est la fonction fitness dont le minimum est ciblé à chaque optimisation.

$$F_f = PL_{FEAD}\,(\,X\,,\,Y\,,\,T_0\,,\,\Sigma_\rho\,) \tag{8.3}$$

avec

$$X = \begin{bmatrix} x_1 \\ . \\ . \\ . \\ x_{np} \end{bmatrix} \quad Y = \begin{bmatrix} y_1 \\ . \\ . \\ . \\ y_{np} \end{bmatrix} \quad \Sigma_\rho = \begin{bmatrix} FEAD\ geometry \\ \\ FEAD\ dynamics \\ \\ FEAD\ materials \end{bmatrix}$$

Le processus d'optimisation consiste à chercher les paramètres optimisés qui minimisent la perte de puissance totale (Eq. 8.4).

$$PL_{FEAD}\,(\,X_{opt}\,,\,Y_{opt}\,,\,T_{0\ opt}\,,\,\Sigma_\rho\,) = min\,[PL_{FEAD}\,(\,X\,,\,Y\,,\,T_0\,,\,\Sigma_\rho\,)] \tag{8.4}$$

Où X_{opt}, Y_{opt}, $T_{0\ opt}$ sont les paramètres optimisés qui :

1. rendent les faces avant moteur énergiquement plus efficaces
2. devraient fournir des orientations aux concepteurs de façades accessoires.

Numériquement, les paramètres optimisables sont considérés dans les intervalles et suivant les pas de discrétisation représentés sur les Figs. 8.10 et 8.11.

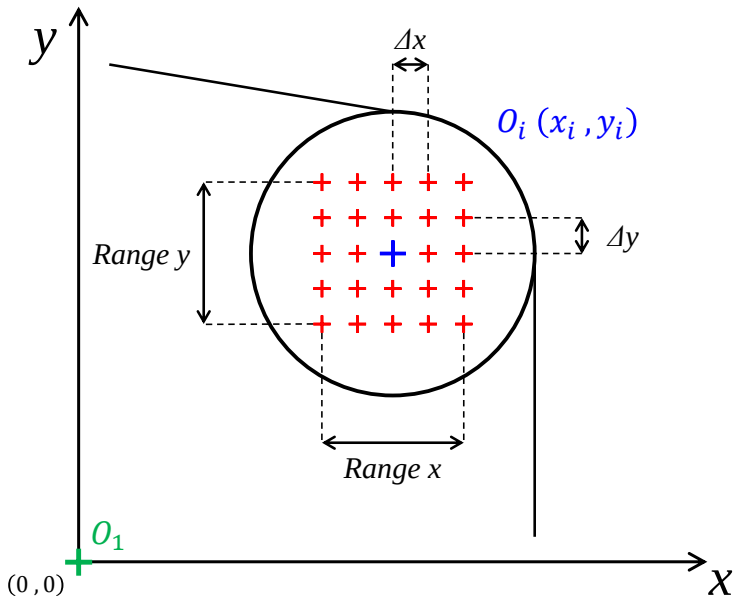

FIGURE 8.10 – L'intervalle et le pas (Δx, Δy) de discrétisation autour du centre des poulies.

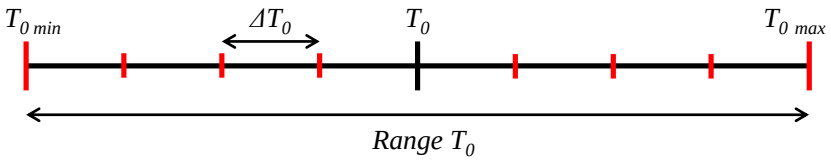

FIGURE 8.11 – L'intervalle et le pas (ΔT_0) de discrétisation autour de la tension de pose T_0.

Les intervalles de discrétisation doivent idéalement représenter dans la réalité des changements de paramètres raisonnablement atteignables de la façade dans le but de l'optimiser tout en garantissant la transmission de puissance et la longévité de ses composants.

Le pas d'optimisation est effectivement un paramètre qui doit être choisi selon le degré de précision de l'optimisation. En effet, par exemple, si la fonction à optimiser (Eq. 8.4) est très sensible à la plus petite des variations d'un paramètre optimisable quelconque, dans ce cas, le pas de discrétisation (Figs. 8.10 ou 8.11) doit être petit pour repérer un point minimum de la fonction à optimiser, s'il en existe, entre deux changements consécutifs du paramètre optimisable en question.

3.1. Algorithme génétique

Pour optimiser une façade, l'algorithme génétique génère aléatoirement plusieurs (ng) FEADs constituant une génération (Fig. 8.12). Plusieurs générations sont ensuite générées et entre deux générations consécutives les fonctions génétiques sont appliquées.

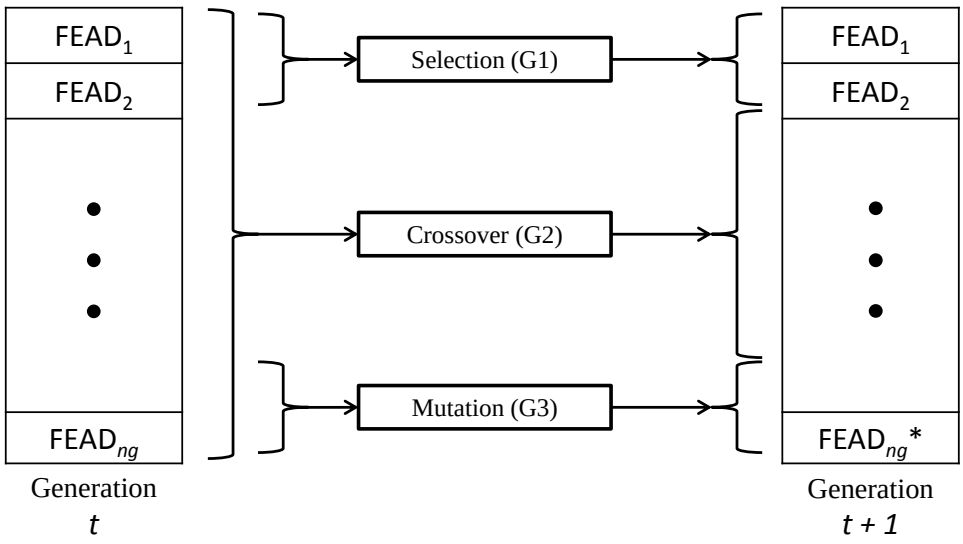

FIGURE 8.12 – Séquence générique de deux générations consécutives (t et $t + 1$) de façades.

Les fonctions génétiques sont des opérations effectuées sur l'ensemble des façades et entre les générations (Fig. 8.12) dans le but de minimiser la fonction qui décrit les pertes de puissance (Eq. 8.1). La mutation change aléatoirement les caractéristiques des façades. Le croisement (ou crossover) est responsable de l'échange de caractéristiques entre façades énergétiquement efficaces et inefficaces. La sélection choisit les façades les plus énergétiquement efficaces, et les conserve durant l'optimisation.

3.2. Programmation dynamique

En parallèle, une des autres méthodes utilisées pour l'optimisation des pertes des puissances dans les façades accessoires est la programmation dynamique. Cette méthode consiste à diviser le problème d'optimisation global (façade) en sous-problèmes, puis à les optimiser plus facilement en utilisant les étapes d'un modèle (Fig. 8.13).

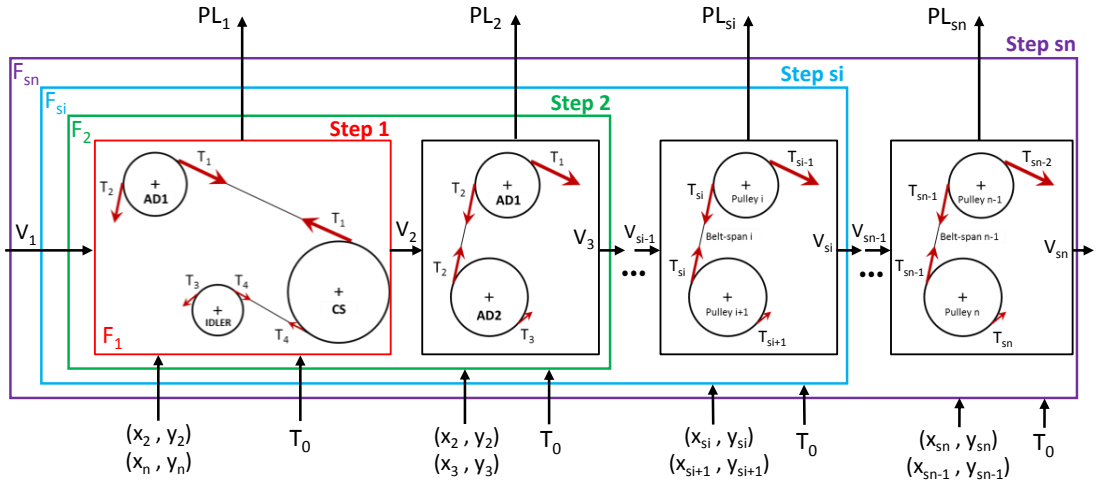

FIGURE 8.13 – Modèle de décision avec les multiples étapes de programmation dynamique.

Une fois les pertes de puissance modélisées (chapitre 2), optimisées (Figs. 3.15 et 3.16) et comparées en utilisant différentes méthodes d'optimisation (Tab. 3.8), le banc d'essais configuré (Fig. 8.14) a été utilisé afin de vérifier la pertinence des solutions d'optimisation proposées et de valider les résultats (Tab. 3.12).

FIGURE 8.14 – Montage expérimental avec le détail du système de mesure de vitesse et de couple.

Chapitre 4. Vérification expérimentale

Ce chapitre décrit plus en détail les expérimentations, i.e. le banc d'essais, le principe de mesure des pertes de puissance, les essais de développement et les études de cas industriels (EURO-6 et EDIT).

Le banc d'essais (Fig. 8.15) est composé de quatre axes principaux, dont deux peuvent imposer soit des couples moteur soit des couples résistants. La position des axes, et donc des centres de poulies montées à leur extrémité, peut être modifiée. De plus, différents diamètres de poulies peuvent être utilisés, aussi bien que différentes configurations de tendeurs et de galet enrouleurs.

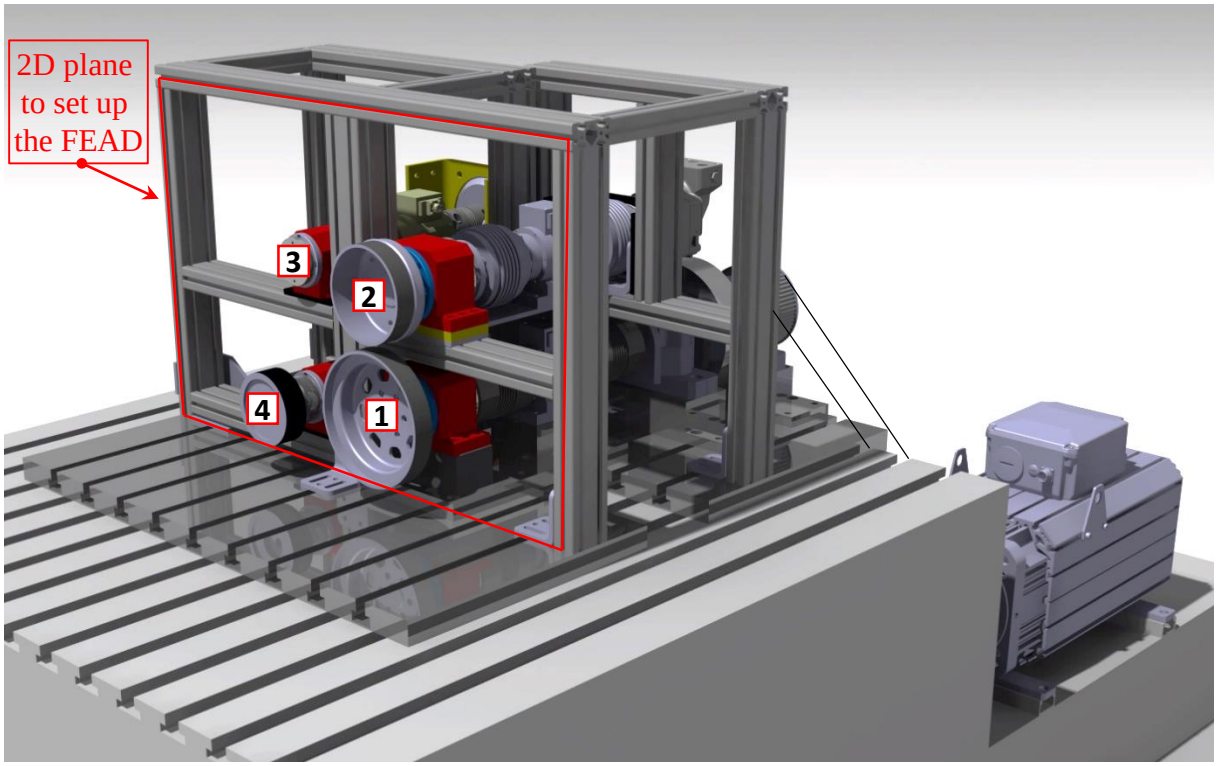

FIGURE 8.15 – Maquette numérique du banc d'essais.

Un moteur électrique de 51.3 kW de puissance entraîne l'axe 1 (Fig. 8.15). Une pompe hydraulique est accouplée à l'axe 2 afin d'imposer un fort couple résistant représentatif d'une pompe à eau et d'un grand ventilateur d'une façade de camion. En outre, sur l'axe 3 un alternateur a été installé et sur l'axe 4 un autre moteur électrique, plus petit que celui monté sur l'axe 1, représente un système de climatisation.

Le principe de mesure des pertes de puissance (PL=PS−PC) du banc d'essais (Fig. 8.15) est représenté Fig. 8.16. Les puissances fournies PS et consommées PC sont mesurées par les systèmes (couplemètre avec tachymètre intégré) MS1 et MS2 (Fig. 8.16) ; la puissance dissipée dans la façade accessoire est égale à la puissance mesurée par le système MS1 moins la puissance mesurée par le système MS2. Cette puissance est une puissance globale, c'est-à-dire qu'il est impossible actuellement d'isoler chaque phénomène de dissipation et de mesurer la perte de puissance correspondante. La stratégie choisie est donc de mesurer la perte de puissance globale sur le banc d'essais, puis de la comparer avec les résultats de simulations, et enfin d'évaluer la comparaison entre la somme des pertes de puissance simulées et la perte de puissance globale mesurée : si cette différence présente un erreur relative acceptable, les modélisations sont satisfaisantes.

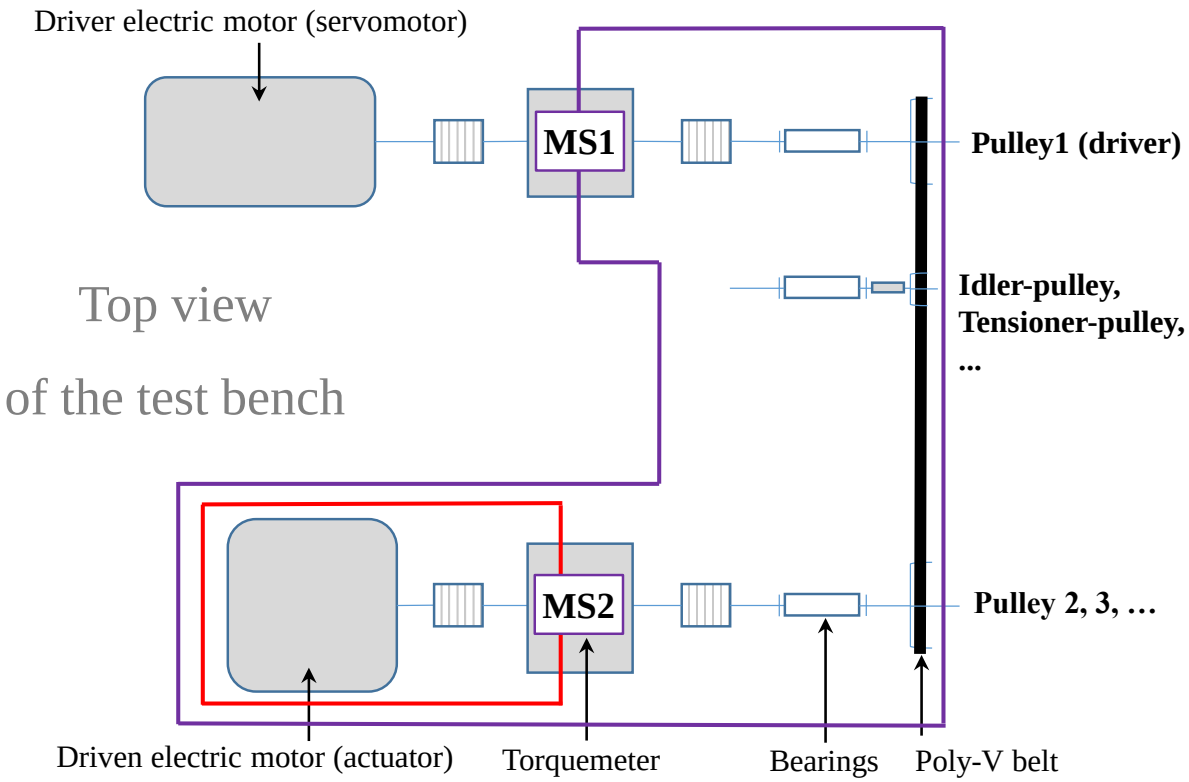

FIGURE 8.16 – Schéma de principe de mesure des pertes de puissance (PL_{FEAD}).

Lors des modélisations, des essais de développement, tels que ceux des façades représentées Fig. 8.17, ont été nécessaires afin de comprendre la participation et la dissipation de phénomènes élémentaires qui contribuent aux pertes de puissance.

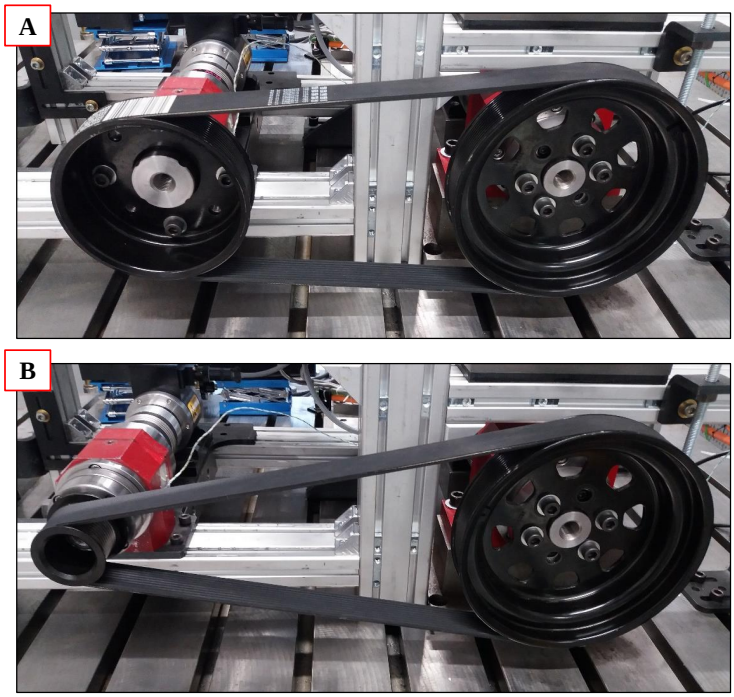

FIGURE 8.17 – Montage expérimental d'un système constitué de deux poulies.

Ces façades ont été analysées expérimentalement et numériquement (Fig. 8.18). Ensuite, les façades industrielles EURO-6 (Fig. 8.19) et EDIT (Fig. 8.21) ont été évaluées.

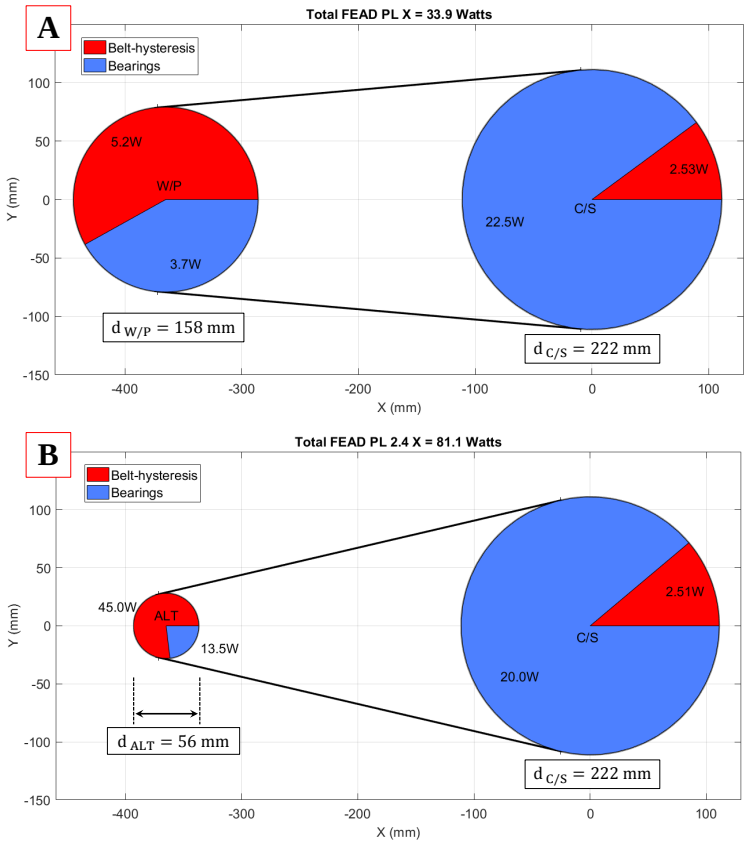

FIGURE 8.18 – Système constitué de deux poulies, simulations des façades à la Fig. 4.4.

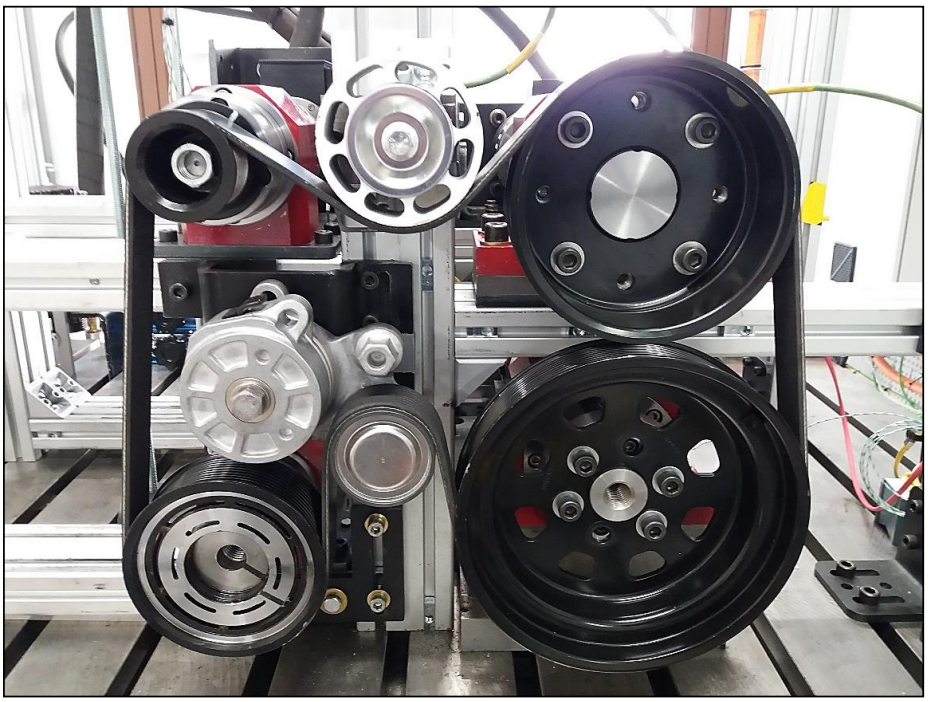

FIGURE 8.19 – Montage expérimental de la façade EURO-6.

Concernant la façade de référence EURO-6, les résultats d'essais et de simulations sont cohérents ; l'équation PG $\geq$ PC + PL PLFead est respectée, les pertes de puissance augmentent avec la vitesse du système, et la perte de puissance mesurée (PG-PC) est supérieure à la somme des pertes modélisées et simulées (PL PLFead). Cette différence signifie que toutes les pertes de puissance dans la façade n'ont peut-être pas été modélisées, ni prises en compte dans les simulations et donc dans la comparaison (Fig. 8.20).

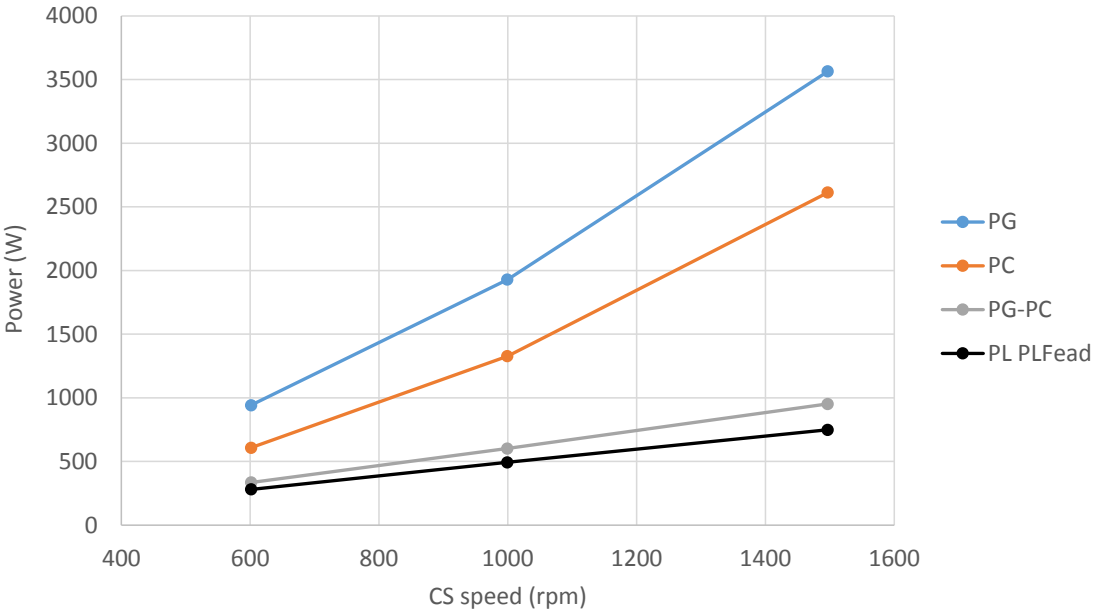

FIGURE 8.20 – Comparaison des résultats d'essais et de simulations pour EURO-6 ($T_0 = 456$N).

Le montage expérimental de la façade EDIT (Fig. 8.21) a été considéré afin d'évaluer les pertes de puissance de ce prototype de façade.

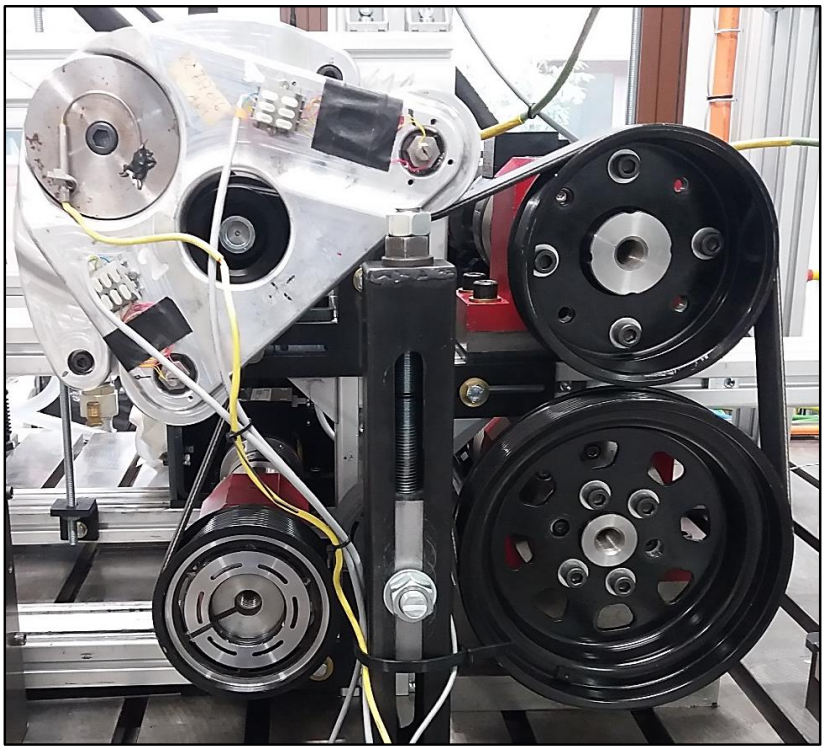

FIGURE 8.21 – Montage expérimental de la façade EDIT.

Selon les essais EDIT, il est possible de démontrer que pour les mêmes conditions de fonctionnement (i.e. vitesse du vilebrequin, tension d'installation de la courroie, etc.), la façade EDIT est énergétiquement moins efficace que la façade EURO-6. Cela est dû au fait qu'au long du parcours de la courroie dans le cas EDIT, celle-ci est soumise à de plus fortes contraintes cycliques (par exemple des flexions et des contre-flexions). Les pertes sont donc plus importantes. Par contre, l'erreur relative est plus satisfaisante dans le cas d'EDIT (Tabs. 4.3, 4.4 et 4.5), surtout pour des faibles tensions d'installation ($\leq$ 980N) de la courroie poly-V.

Le cas limite de tension de pose $T_0 = 980$N est présenté Fig. 8.22. Pour les tensions $T_0 \leq 980$N, les pertes de puissance dans la façade sont inférieures, et les modélisations correspondent bien aux essais avec une erreur inférieure ou égale à 9% (Tabs. 4.3 et 4.4).

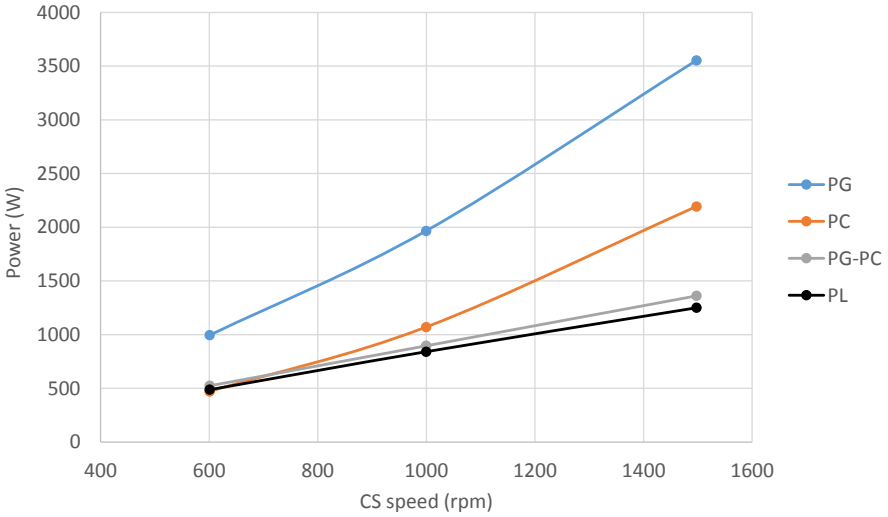

FIGURE 8.22 – Comparaison des résultats d'essais et de simulations pour EDIT ($T_0 = 980$N).

De ce fait, si l'objectif est de calculer les pertes de puissance dans la façade avec une faible erreur (chapitre 2) et potentiellement de les optimiser avec les méthodes du chapitre 3, la tension de pose qui devrait être retenue pour EDIT serait $T_0 < 980$N. Idéalement, ce serait la tension de pose minimum T_{0min} (Fig. 1.20) la plus adaptée car celle-ci permet de transmettre la puissance nécessaire et de dissiper le minimum de puissance.

Chapitre 5. Outil de simulation

Ce chapitre est consacré à la présentation de l'outil logiciel PLFead (Fig. 8.23). PLFead a été développé afin de proposer aux utilisateurs un outil pratique et efficace pour la simulation des pertes de puissance dans les façades accessoires et pour les calculs associés aux propriétés des matériaux de la courroie poly-V, à la géométrie, à la dynamique et pour l'optimisation de la façade.

PLFead a été organisé en trois parties : pré-processeur, solveur et post-processeur :

A l'aide des interfaces du pré-processeur de PLFead l'utilisateur peut modéliser la façade, par exemple choisir les poulies, les matériaux de la courroie et les positions des poulies (layout), et obtenir le nécessaire (e.g. angle d'enroulement des poulies) pour le calcul des pertes de puissance. Le solveur se sert ensuite des résultats du pré-processeur pour résoudre toutes les équations qui décrivent les pertes de puissance. Le post-processeur affiche les résultats des calculs effectués par les algorithmes du pré-processeur et du solveur. Ces résultats de calcul de pertes de puissance sont présentés sous forme de tableaux et de cartographies.

Une fois passée l'interface d'accueil du logiciel PLFead (Fig. 8.23), l'ensemble des calculs et sous calculs sont lancés à partir de l'interface principale (Fig. 8.24).

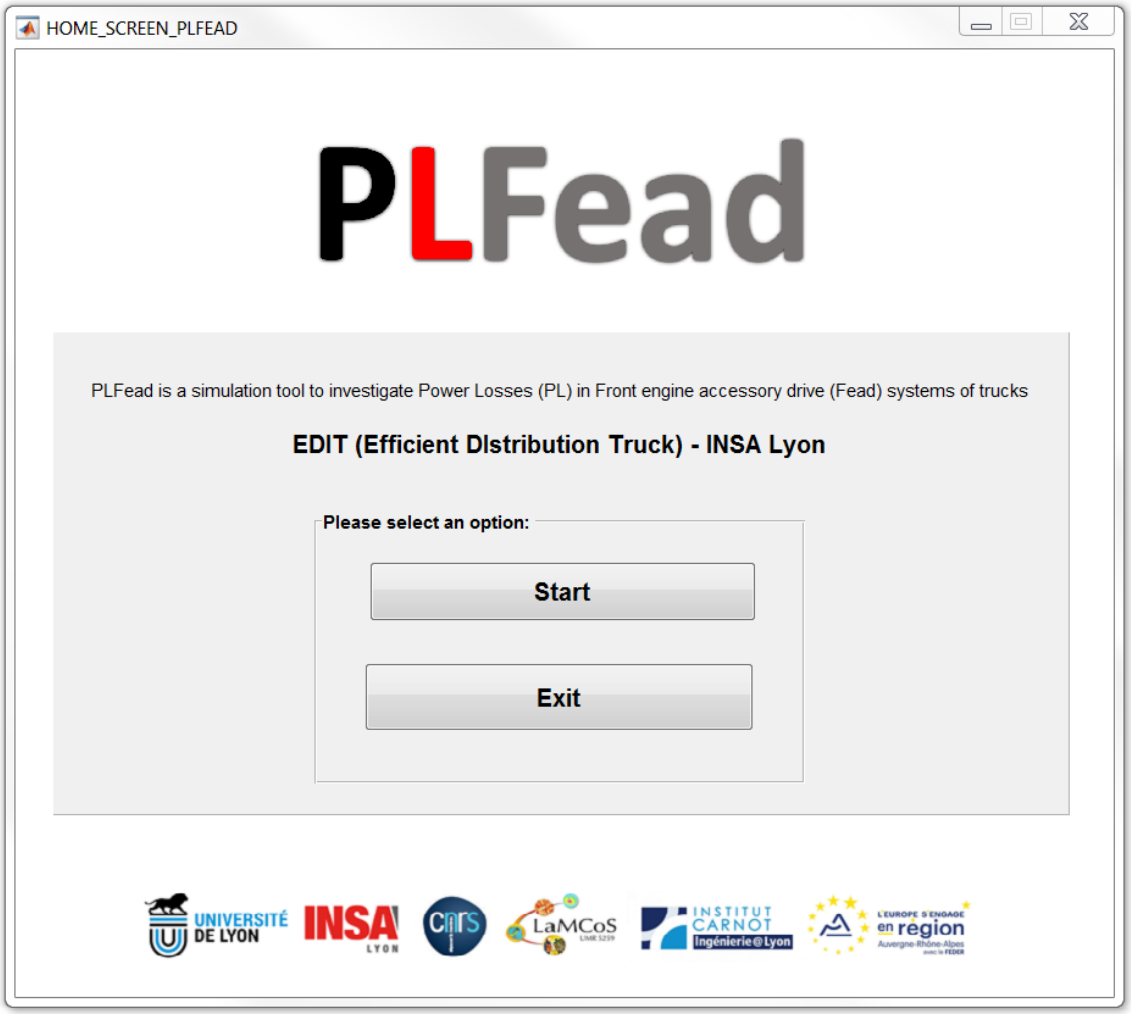

FIGURE 8.23 – Home screen de l'outil logiciel PLFead.

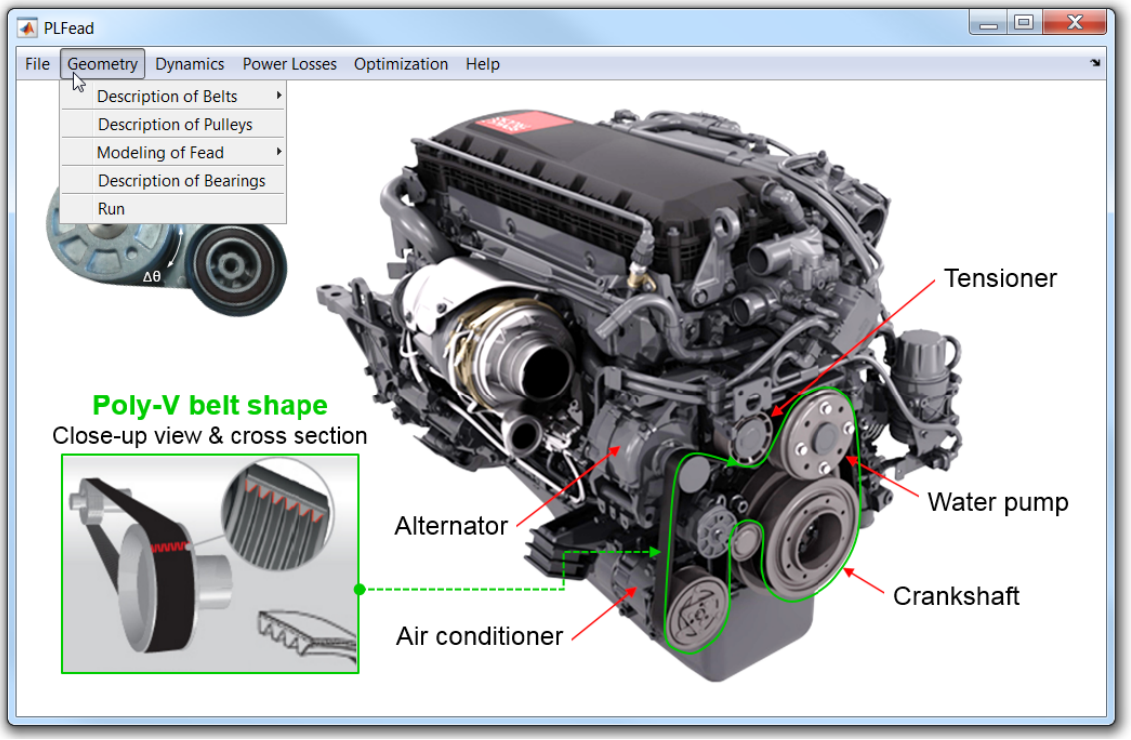

FIGURE 8.24 – Menus de PLFead.

Parmi d'autres fonctionnalités du logiciel PLFead, on peut retrouver dans la "Description of belts" (Fig. 8.24), la "Poly-V Belt Geometry" (Fig. 8.25) ou le "Poly-V Belt Material" (Fig. 8.26).

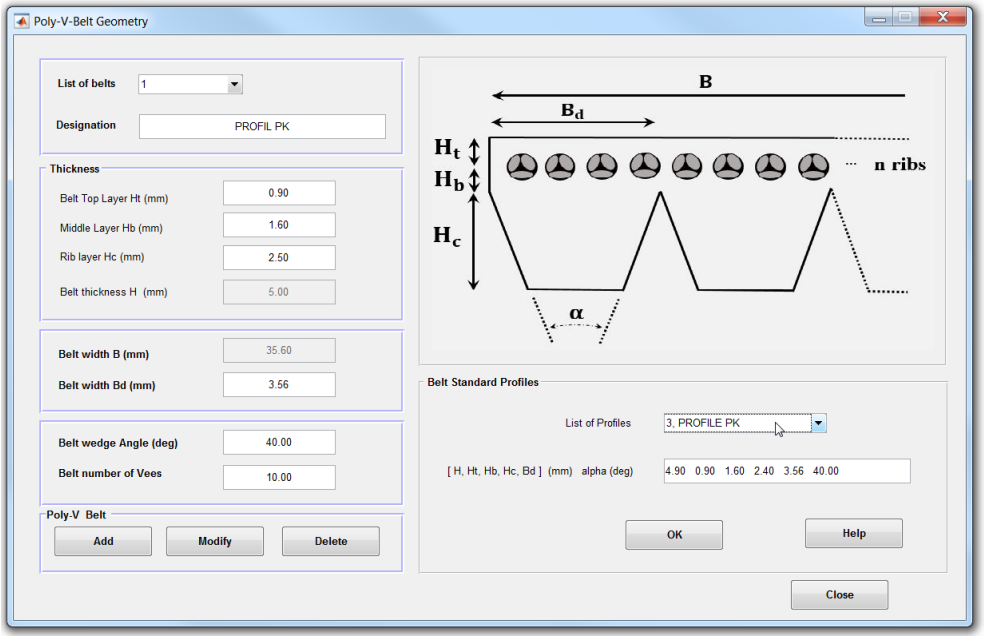

FIGURE 8.25 – Interface concernant la géométrie de la courroie poly-V.

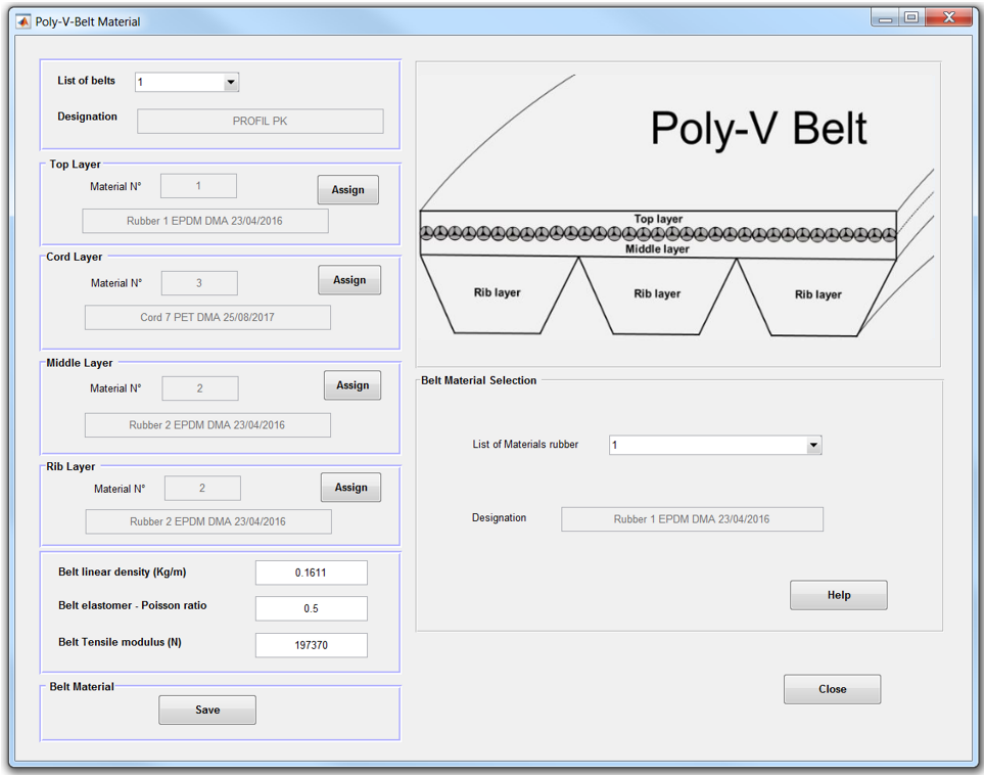

FIGURE 8.26 – Affectation des matériaux de la courroie poly-V.

Ces interfaces permettent d'ajuster la taille de la courroie simulée selon les différents profils standard disponibles, puis d'affecter les propriétés des matériaux, principalement des polymères (par exemple le caoutchouc EPDM), caractérisés via DMA.

Une fois toutes les informations nécessaires aux calculs des pertes de puissance fournies, et les calculs exécutés par le solveur, des interfaces du post-processeur de PLFead, telles que celles présentées Figs. 8.27 et 8.28, apparaissent.

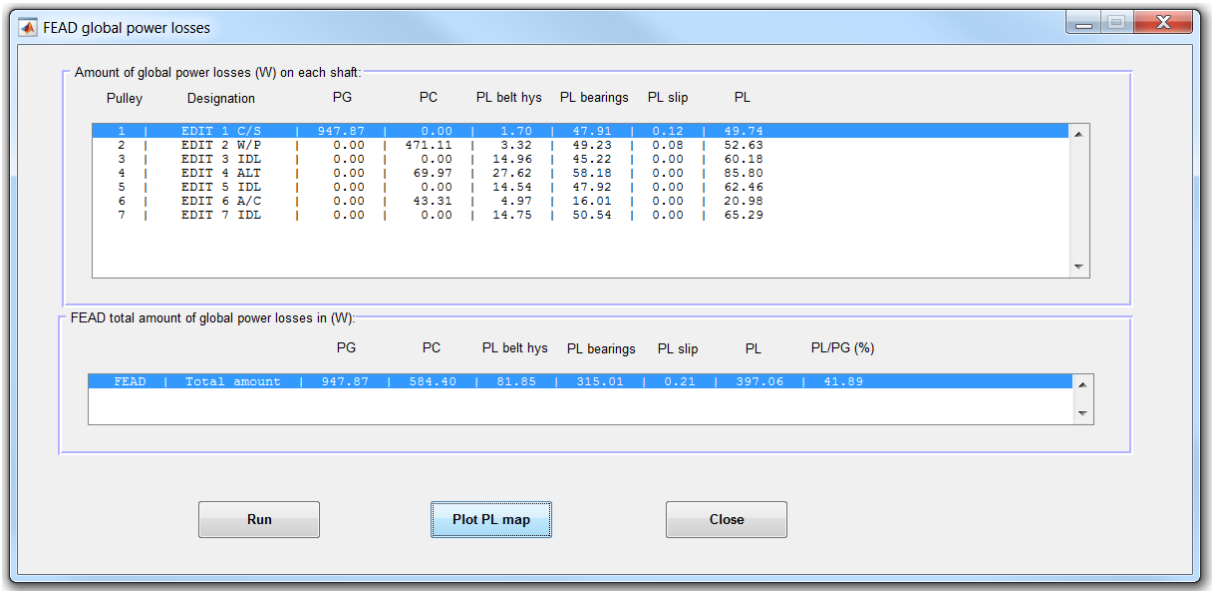

FIGURE 8.27 – Menus de PLFead représentant les pertes de puissance d'une façade accessoire.

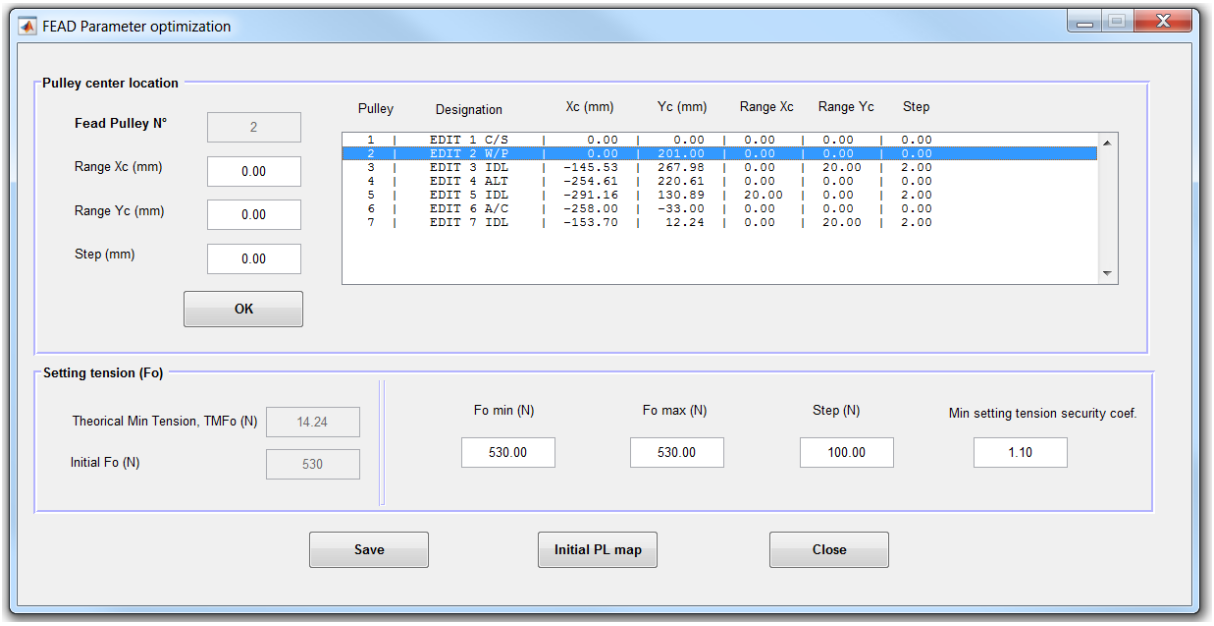

FIGURE 8.28 – Interface de PLFead pour le réglage de paramètres d'optimisation (GA et DP).

Grâce aux interfaces des Figs. 8.27 et 8.28, l'utilisateur peut notamment : (1) avoir plus de détails sur la distribution des pertes de puissance, ainsi que sur la géométrie de la façade ; (2) régler des paramètres supplémentaires (range, step) pour que l'algorithme (génétique ou de programmation dynamique) effectue l'optimisation des pertes de puissance.

D'autres représentations graphiques, telles que les cartographies (par exemple PLMaps Fig. 8.6), sont automatiquement créées dès que nécessaire par PLFead et permettent à l'utilisateur de se rendre compte aisément de la distribution des pertes de puissance.

Chapitre 6. Caractérisations et recherche additionnelle

Pour le calcul des pertes de puissance, plusieurs paramètres sont nécessaires, notamment des paramètres de la courroie poly-V, des paramètres du contact courroie/poulies et des paramètres de dissipation (couple de frottement) des tendeurs. Toutefois, ces paramètres ne sont pas (ou partiellement) fournis par les fabricants de composants (courroies, poulies, tendeurs) de façades. La solution a donc été d'identifier : (1) le module d'élasticité en traction de la courroie ; (2) le coefficient de frottement entre les poulies et la courroie ; (3) le couple de frottement agissant sur le pivot de deux différents tendeurs soumis à plusieurs conditions de fonctionnement (par exemple, la fréquence et l'amplitude angulaire d'oscillation du tendeur).

De manière analogue à la viscoélasticité du caoutchouc de la courroie, dans ce chapitre, la viscoélasticité de l'anneau en caoutchouc de la poulie damper (TVD) a été prise en compte dans les équations du mouvement du TVD, grâce à la méthodologie de construction de courbes maîtresses. Ce travail supplémentaire a été motivé par le fait que cela pourra prochainement susciter l'envie d'aller plus loin dans les modélisations de la dynamique et des dissipations d'énergie, ainsi que dans la prise en compte des effets de la viscoélasticité du caoutchouc dans les composants de façade.

6.1. Identification des paramètres matériau de la courroie

Plusieurs tests d'impact (essais de choc) ont été effectués sur la masse m_d (Fig. 8.29).

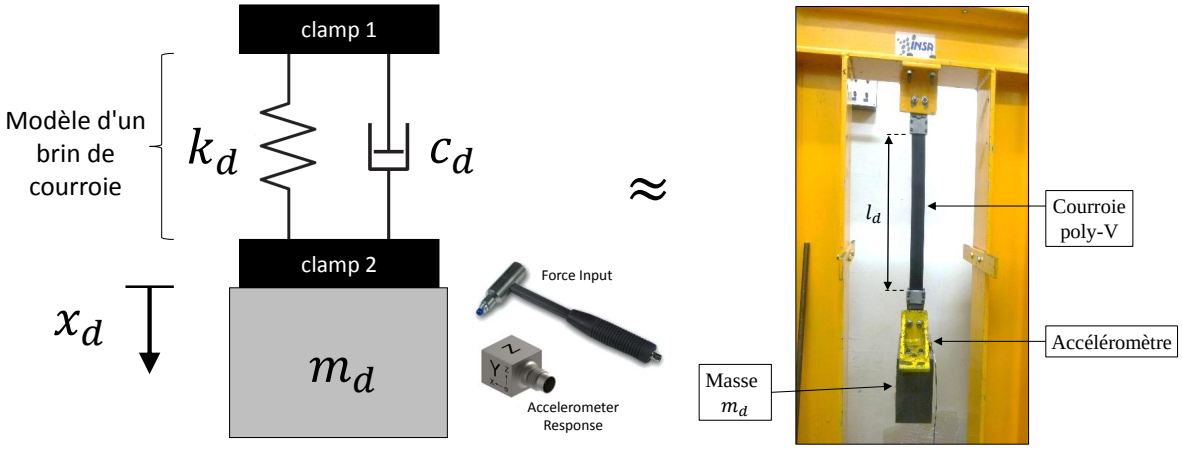

FIGURE 8.29 – Système masse-ressort amorti.

Des courbes similaires à celle de la Fig. 6.3 ont été acquises pour la définition des paramètres utiles aux calculs des pertes de puissance (Tab. 6.1). Ces paramètres ont été obtenus en utilisant le décrément logarithmique δ_d (Eqs. 6.6, 6.7 et 6.8) de la mesure des vibrations amorties générées par le choc.

6.2. Coefficient de frottement global

D'autres paramètres utiles pour les calculs des pertes de puissance sont les coefficients de frottement entre la poulie et la courroie. Cette section du manuscrit est consacrée à l'explication des méthodes utilisées. La première méthode (Fig. 8.30) coïncide avec la méthode initialement proposée par Cepon et al [20] qui utilise du gross slip (glissement sur tout l'arc de contact $R\,\phi$ entre la poulie et la courroie poly-V).

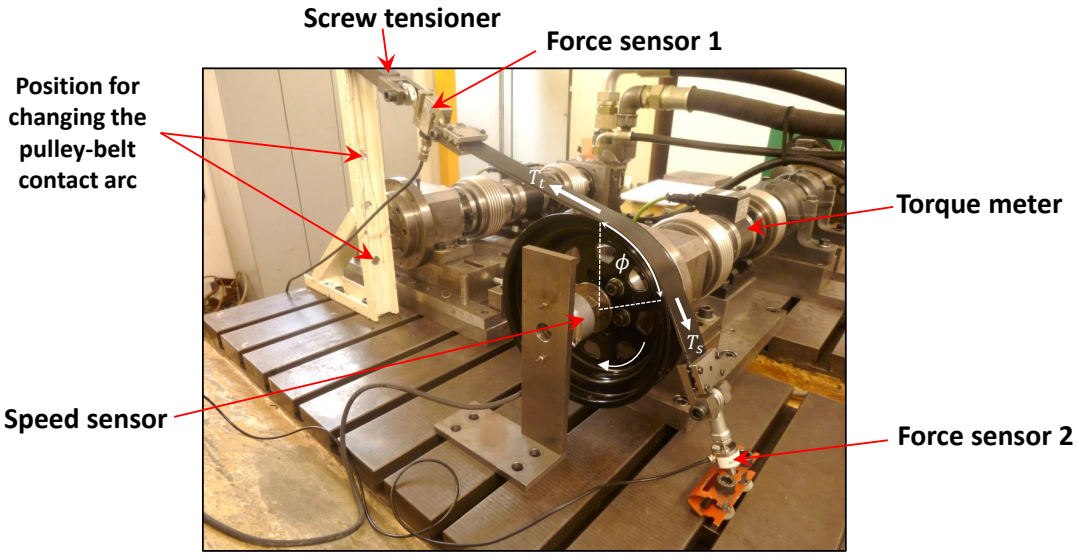

FIGURE 8.30 – Montage expérimental pour la mesure du coefficient de frottement global.

Un exemple de résultat obtenu lors des essais du type gross slip est présenté Fig. 8.31.

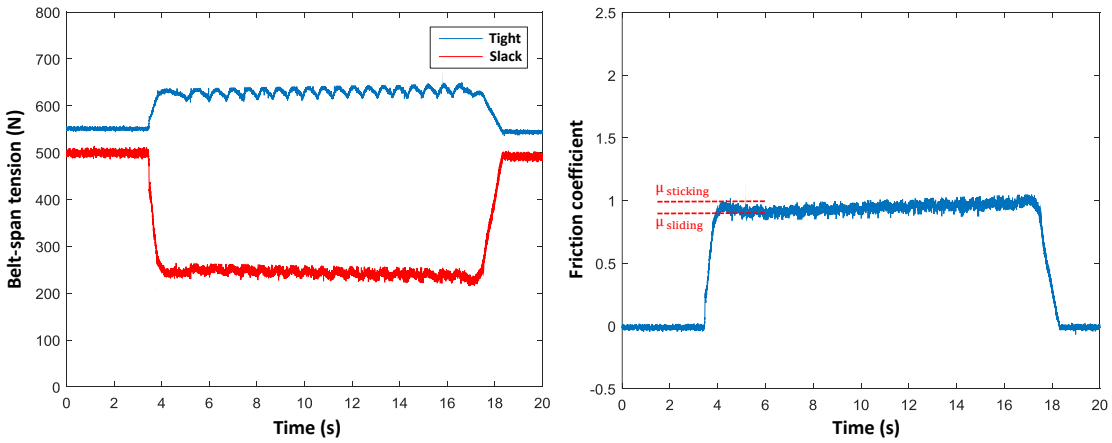

FIGURE 8.31 – Exemple de résultats, similaires à ceux dans [20], obtenus expérimentalement.

Cette méthode a l'avantage d'obtenir le coefficient de frottement dans les conditions réelles d'utilisation de la poulie et de la courroie poly-V. On observe même des effets réels du frottement par à-coups (stick-slip) (Fig. 8.31).

La valeur du coefficient de frottement global $\mu_g \in [0.88 \;\; 1.75]$ reste approximativement égale à ce qu'il est possible de trouver dans les articles scientifiques (e.g. Hwang et al [2]).

6.3. Coefficient de frottement local

Le coefficient de frottement local μ_l, relié au coefficient global μ_g par l' Eq. 6.10, représente également une mesure du frottement entre les surfaces de la poulie et de la courroie qui sont en contact. Par contre, dans ce cas, le coefficient est obtenu plus du point de vue de la tribologie (Fig. 8.32).

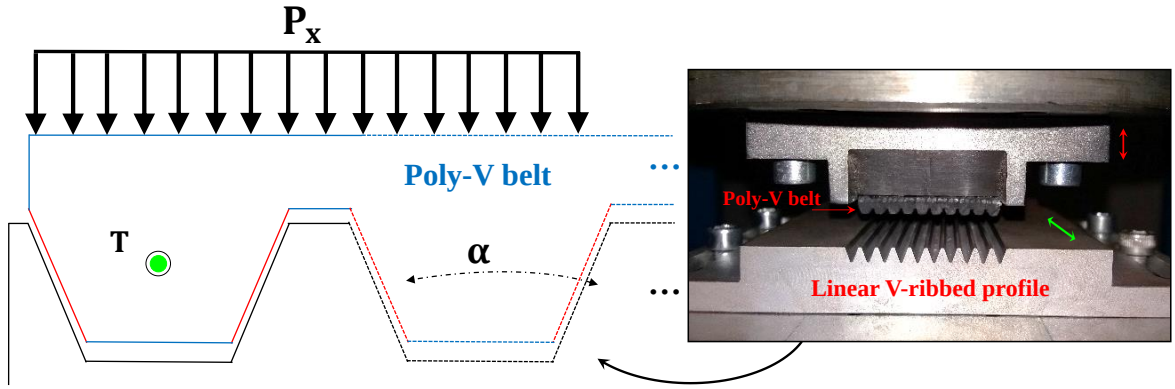

FIGURE 8.32 – Schéma de principe des essais pour la mesure du coefficient de frottement local.

Deux supports ont été conçus (Fig. 8.32) afin d'utiliser le banc d'essais tribologiques tribowave (Fig. 6.7) avec la géométrie de la courroie (angle α des stries) pour la mesure du ratio T_{max}/P_x à partir duquel le coefficient de frottement local μ_l entre deux surfaces peut être déterminé (Eq. 6.10). Des essais ont ensuite été réalisés selon plusieurs conditions : la force de traction, la vitesse de glissement et la température. Les résultats du coefficient μ_l sont disponibles Tab. 8.1. Il convient également de noter que la plage $\mu_l \epsilon [0.3 \ 0.6]$ équivaut partiellement à la plage $\mu_g \epsilon [0.88 \ 1.75]$ si l' Eq. 6.10 est considérée pour $\alpha = 40$ degrés (courroie EDIT). Cela valide l'utilisation des coefficients μ_l et μ_g obtenus par deux méthodes différentes, néanmoins équivalentes, dans les calculs des pertes de puissance.

TABLE 8.1 – Résumé des résultats de mesures du coefficient local de frottement.

					Pulleys roughness R_a = 0.3 µm	Pulleys roughness R_a = 0.8 µm
Initial Normal load	Sliding normal load	Axial traction force	Sliding velocity	Temperature	Local friction coefficient	Local friction coefficient
1000 N ≈ 0.5 MPa	950 N	437 N	1 mm/s	20 °C	0.46	0.66
1500 N ≈ 0.7 MPa	1350 N	594 N	1 mm/s	20 °C	0.44	0.68
2000 N ≈ 1 MPa	1950 N	839 N	1 mm/s	20 °C	0.43	0.75
400 N ≈ 0.2 MPa	350 N	154 N	0.5 mm/s	20 °C	0.44	0.62
2100 N ≈ 1 MPa	1935 N	813 N	0.5 mm/s	20 °C	0.42	0.64
4200 N ≈ 2 MPa	3850 N	1540 N	0.5 mm/s	20 °C	0.40	0.64
400 N ≈ 0.2 MPa	375 N	154 N	0.1 mm/s	20 °C	0.41	0.61
2100 N ≈ 1 MPa	1900 N	741 N	0.1 mm/s	20 °C	0.39	0.59
4200 N ≈ 2 MPa	3850 N	1425 N	0.1 mm/s	20 °C	0.37	0.59
400 N ≈ 0.2 MPa	320 N	147 N	0.01 mm/s	20 °C	0.46	0.56
2100 N ≈ 1 MPa	1800 N	720 N	0.01 mm/s	20 °C	0.40	0.52
4200 N ≈ 2 MPa	3700 N	1332 N	0.01 mm/s	20 °C	0.36	0.52
400 N ≈ 0.2 MPa	350 N	140 N	0.1 mm/s	80 °C	0.40	0.45
2100 N ≈ 1 MPa	1850 N	611 N	0.1 mm/s	80 °C	0.33	0.44
4200 N ≈ 2 MPa	3625 N	1196 N	0.1 mm/s	80 °C	0.33	0.46
2000 N ≈ 1 MPa	1825 N	657 N	1 mm/s	80 °C	0.36	
2000 N ≈ 1 MPa	1850 N	611 N	0.1 mm/s	80 °C	0.33	
2000 N ≈ 1 MPa	1800 N	468 N	0.01 mm/s	80 °C	0.26	

6.4. Caractérisation des tendeurs

Afin de caractériser la dissipation des tendeurs, le montage expérimental représenté Fig. 8.33 a été mis en place.

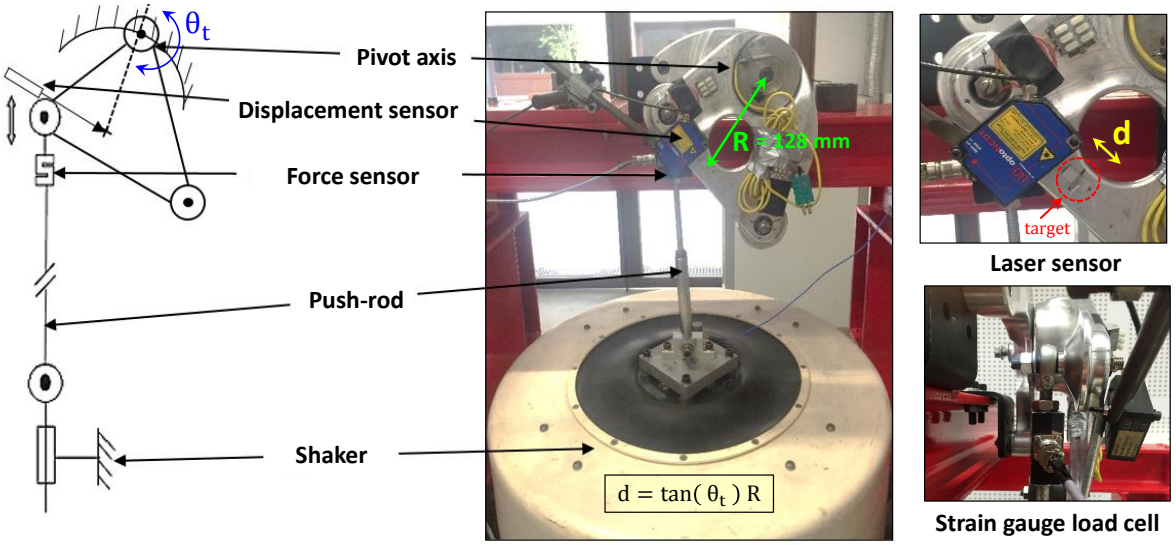

FIGURE 8.33 – Montage expérimental utilisé pour la caractérisation du tendeur.

Deux modèles de tendeurs correspondant aux façades EURO-6 et EDIT ont été testés. Grâce au pot vibrant (shaker) et au système bielle-manivelle (push-rod) une force mesurée par le capteur de force (force sensor Fig. 8.33) a été appliquée à différentes fréquences et amplitudes d (i.e. angle de rotation). Ensuite, le couple de frottement du tendeur a été mesuré et tracé en fonction de l'angle de rotation θ_t mesuré par le capteur de déplacement (displacement sensor Fig. 8.33). Des courbes, telles que le couple de frottement en fonction de l'angle de rotation du tendeur (Fig. 8.34), présentant de l'hystérésis, ont été tracées pour les tendeurs des façades EURO-6 et EDIT au chapitre 6 et dans les annexes $A10$ et $A11$. A partir de ces courbes d'hystérésis, la perte de puissance dans le tendeur peut être quantifiée (Eq. 2.57).

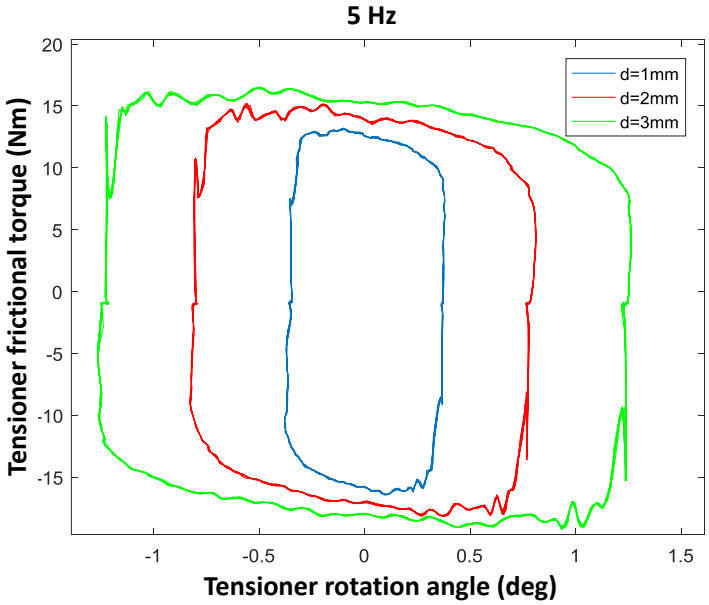

FIGURE 8.34 – Courbe d'hystérésis du tendeur EDIT soumis à une excitation de 5 Hz.

6.5. Amortisseur de vibration en torsion

L'amortisseur de vibration en torsion (Torsional Vibration Damper TVD Fig. 8.35) est responsable de l'amortissement des vibrations de torsion du vilebrequin du moteur à combustion interne.

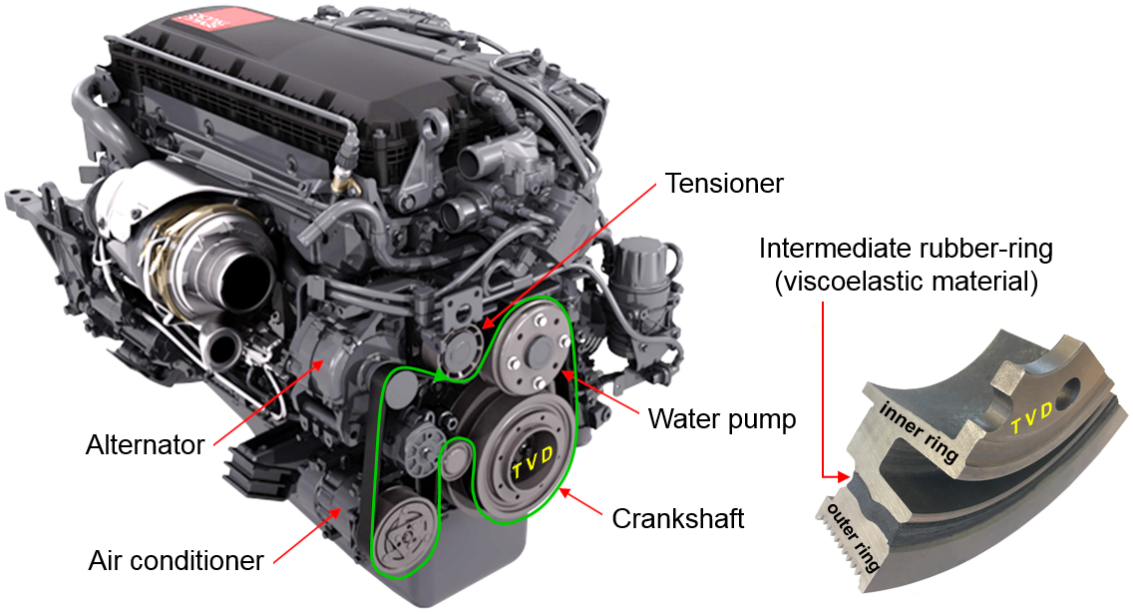

FIGURE 8.35 – Façade accessoire de camion avec la poulie damper du vilebrequin.

6.5.1. Simulations

La prise en compte des propriétés dissipatives de l'anneau en caoutchouc dans la réponse du TVD (Fig. 8.36) a également fait l'objet de plusieurs analyses (chapitre 6) et d'une caractérisation DMA du caoutchouc du TVD. Cette dernière ressemble à ce qui a été fait pour la prédiction des pertes de puissance par hystéresis du caoutchouc de la courroie.

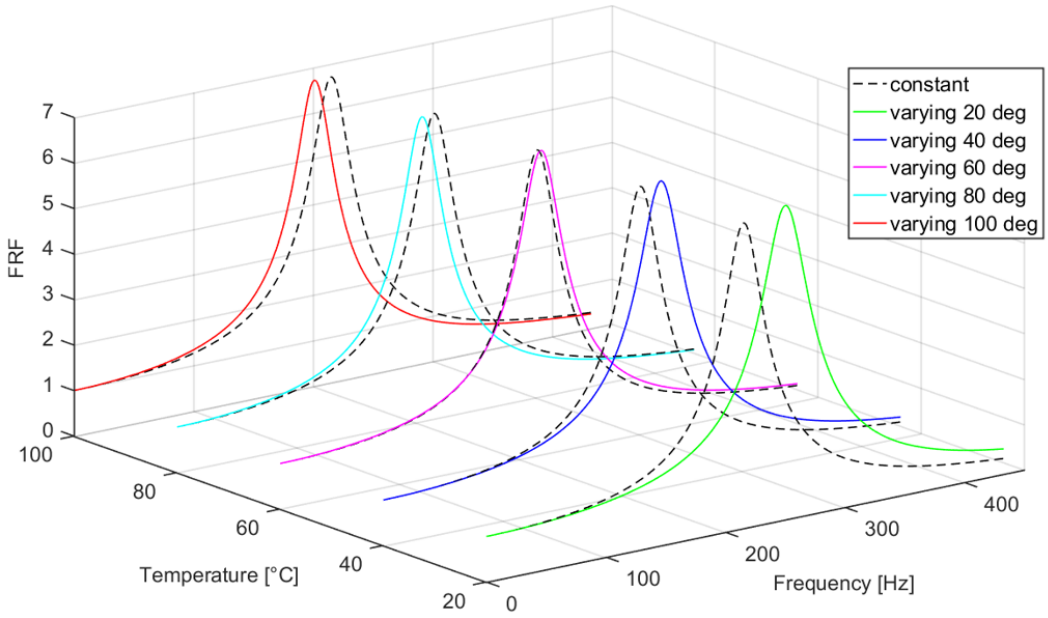

FIGURE 8.36 – Réponse en fréquence de l'amplitude du TVD pour plusieurs températures.

La réponse dynamique du TVD change selon la température de fonctionnement du moteur, la fréquence et l'amplitude (des déformations dans le caoutchouc du TVD) des acyclismes imposés par le moteur thermique (Fig. 8.36).

6.5.2. Vérification expérimentale

Afin de vérifier l'efficacité des modélisations et des simulations concernant le TVD, le montage expérimental Fig. 8.37 a été mis en place.

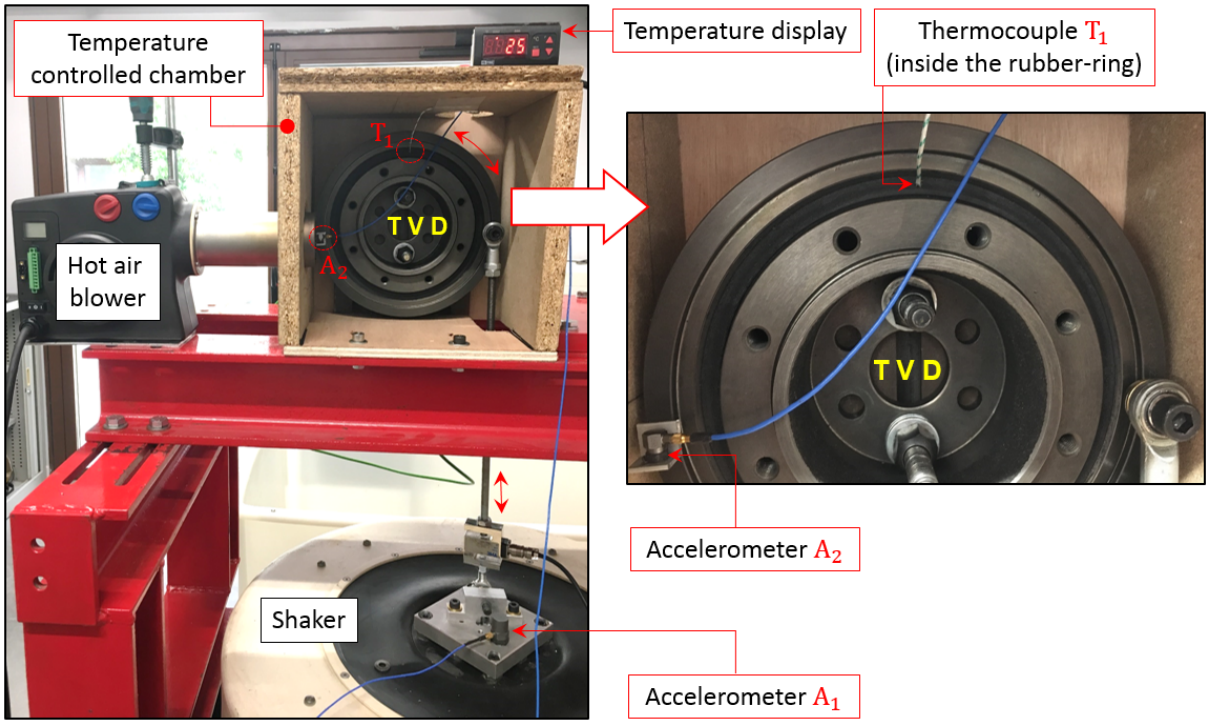

FIGURE 8.37 – Montage expérimental utilisé pour les tests du TVD sous conditions spécifiques.

Les résultats sont satisfaisants (Fig. 8.38) ; la direction (vers la gauche) et l'amplitude en fréquence en Hertz (Hz) du décalage de la FRF (Fonction de Réponse en Fréquence) issue des essais et des simulations sont équivalents (Tab. 6.7). Par contre, au niveau de l'amplitude de l'accélération des FRFs (Fig. 8.38), il y a un effet adoucissant (smoothing). Cela peut être dû aux difficultés expérimentales, comme par exemple isoler parfaitement l'excitation du TVD en rotation et l'obtention de sa réponse.

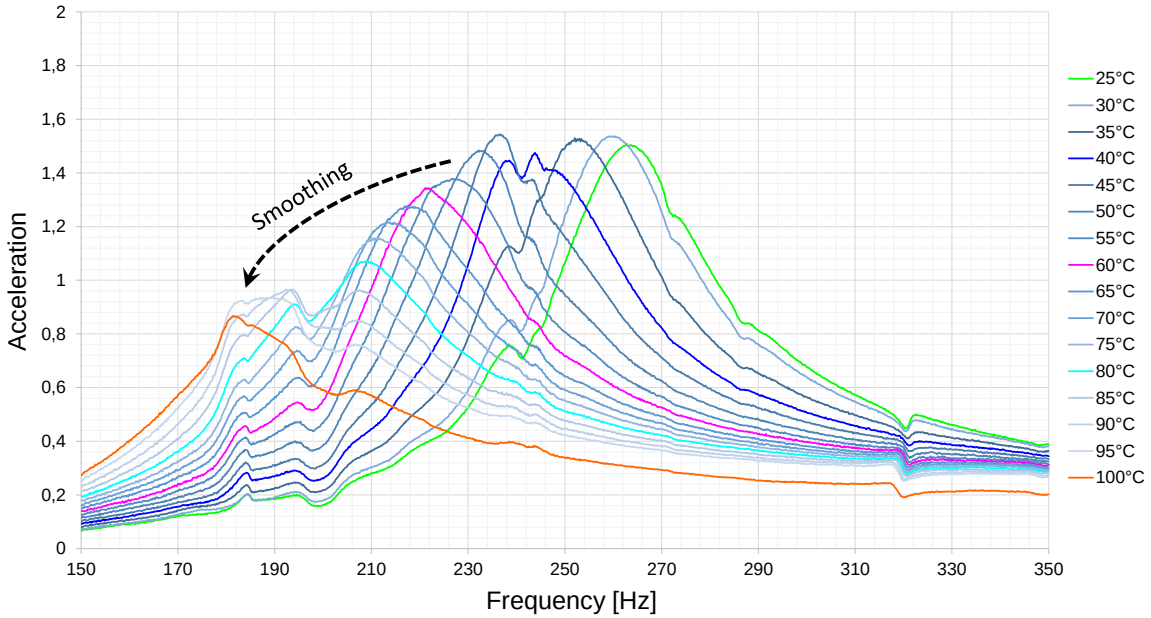

FIGURE 8.38 – FRF expérimentale (amplitude) de la poulie damper pour plusieurs températures.

Chapitre 7. Conclusions et futurs travaux

Le chapitre 7 résume les travaux accomplis et présentés lors des chapitres précédents. Il présente également des suggestions pour les futurs travaux concernant la modélisation et l'optimisation des pertes de puissance dans les façade accessoires des moteurs de véhicules.

7.1. Résumé et Conclusions

Le modèle, détaillé dans le chapitre 2, décrit les lieux et l'origine des pertes de puissance dans une façade accessoire de moteur de véhicule. L'équation 2.1 représente le modèle mathématique pour la prédiction des pertes de puissance, ainsi que la fonction qui doit être optimisée par les méthodes d'optimisation détaillées et validées dans le chapitre 3.

Les modèles des pertes de puissance modélisées et optimisées, respectivement dans le chapitre 2 et 3, ont été vérifiées expérimentalement dans le chapitre 4.

Dans le chapitre 3, les algorithmes génétique, de programmation dynamique et de "brute force" ont été considérés pour la réduction des pertes de puissance. Pourtant, seuls les algorithmes génétique et de programmation dynamique sont considérés comme des méthodes d'optimisation. Selon les analyses du chapitre 3, l'algorithme génétique est plus rapide pour la recherche de la meilleure solution.

Le chapitre 5 présente l'outil logiciel PLFead dans lequel les modèles des pertes de puissance ainsi que les algorithmes d'optimisation génétique et de programmation dynamique sont implémentés, ce chapitre expose la structure et les interfaces du logiciel.

Le chapitre 6 présente : (1) les méthodes utilisées pour l'identification expérimentale des paramètres nécessaires aux calculs des pertes de puissance ; (2) la caractérisation de deux tendeurs (EURO-6 et EDIT) ; ainsi que (3) la simulation et la vérification expérimentale de la réponse dynamique sous forme de FRFs de l'amortisseur de vibrations en torsion TVD utilisé dans les moteurs des camions Renault Trucks.

Entre autres, il a été démontré dans le chapitre 6 qu'un sous ensemble mécanique, tel que l'amortisseur de vibrations en torsion TVD, peut parfois ne pas fonctionner comme prévu dans les modélisations soutenues par des hypothèses trop simplificatrices. Il est donc indispensable de prendre en compte un minimum d'effets. Dans le cas du TVD, il est nécessaire de considérer les effets viscoélastiques du caoutchouc afin de représenter réellement son comportement en dynamique.

7.2. Futurs travaux

Concernant les futurs travaux, il faudrait considérer expérimentalement la génération de fluctuations de couple (acyclisme). Cela se fait par l'ajout d'un joint de cardan ou d'une poulie non-circulaire sur le banc d'essais. La génération d'acyclismes serait utile pour la validation des modèles des pertes de puissance (chapitre 2) liées aux vibrations : pertes sur le pivot des tendeurs et dans les brins de la courroie dues aux fluctuations de tensions.

Il faudrait également affiner les modèles existants des pertes de puissance, inclure d'autres paramètres dans l'optimisation ainsi que d'autres modèles de pertes de puissance, e.g. un modèle décrivant la perte de puissance dans l'anneau en caoutchouc du TVD.

Bibliography

[1] L. E. Hawker, A vibration analysis of automotive serpentine accessory drive systems, Ph.D. thesis, University of Windsor (1991).

[2] S. Hwang, N. Perkins, A. Ulsoy, R. Meckstroth, Rotational response and slip prediction of serpentine belt drive systems, Journal of Vibration and Acoustics 116 (1994) 71–78. doi:10.1115/1.2930400.

[3] T. Kraver, G. Fan, J. Shah, Complex modal analysis of a flat belt pulley system with belt damping and coulomb-damped tensioner, Journal of Mechanical Design 118 (1996) 306–311.

[4] R. Beikmann, N. Perkins, A. Ulsoy, Design and analysis of automotive serpentine belt drive systems for steady state performance, Journal of Mechanical Design 119 (1997) 162–168.

[5] R. S. Beikmann, Static and dynamic behavior of serpentine belt drive systems: theory and experiment, Ph.D. thesis, University of Michigan (1992).

[6] R. Beikmann, N. Perkins, A. Ulsoy, Free vibration of serpentine belt drive systems, ASME J. Vib. Acoust 118 (1996) 406–413.

[7] R. Parker., Efficient eigensolution, dynamic response, and eigensensitivity of serpentine drive belts, Journal of Sound and Vibration 270 (2004) 15–38. doi:https://doi.org/10.1016/S0022-460X(03)00259-1.

[8] S. Chowdhury, R. K. Yedavalli, Dynamics of belt-pulley-shaft systems, Mech. Mach. Theory 98 (2016) 199 – 215. doi:http://dx.doi.org/10.1016/j.mechmachtheory.2015.11.011.

[9] Y. Pan, X. Liu, Y. Shan, G. Chen, Complex modal analysis of serpentine belt drives based on beam coupling model, Mech. Mach. Theory 116 (2017) 162 – 177. doi:http://dx.doi.org/10.1016/j.mechmachtheory.2017.05.016.

[10] N. Srivastava, I. Haque, A review on belt and chain continuously variable transmissions (cvt): Dynamics and control, Mech. Mach. Theory 44 (1) (2009) 19 – 41. doi:http://dx.doi.org/10.1016/j.mechmachtheory.2008.06.007.

[11] V. A. Lubarda, Determination of the belt force before the gross slip, Mech. Mach. Theory 83 (2015) 31 – 37. doi:http://dx.doi.org/10.1016/j.mechmachtheory.2014.08.015.

[12] S. Amijima, Some basic problems about the belts, The science and engineering review of Dashisha of University 3(3-4) (1962) 13–21.

[13] S. Amijima, Some problems associated with the friction between belt and pulley, The science and engineering review of Dashisha of University 3(3-4) (1962) 9–21.

[14] G. Gerbert, Traction Belt Mechanics, Chalmers Univ of Technology, 1999.

[15] T. H. C. Childs, D. Cowburn, Power transmission losses in v-belt drives. part 2: effects of small pulley radii, Proc Institution of Mechanical Engineers 201 (1987) 41–53.

[16] I. M. Ward, D. W. Hadley, An introduction to the mechanical properties of solid polymers, John Wiley & Sons Ltd.; John Wiley & Sons, Inc., 1993.

[17] T. Chen, D. Lee, C. Sung, An experimental study on transmission efficiency of a rubber v-belt cvt, Mech. Mach. Theory 33 (4) (1998) 351 – 363. doi:http://dx.doi.org/10.1016/S0094-114X(97)00049-9.

[18] A. D. Almeida, S. Greenberg, Technology assessment: energy-efficient belt transmissions, Energy and Buildings 22 (3) (1995) 245 – 253. doi:http://dx.doi.org/10.1016/0378-7788(95)00926-0.

[19] L. Manin, G. Michon, D. Remond, R. Dufour, From transmission error measurement to pulley belt slip determination in serpentine belt drives: Influence of tensioner and belt characteristics, Mech. Mach. Theory 44 (2009) 813 – 821. doi:http://dx.doi.org/10.1016/j.mechmachtheory.2008.04.003.

[20] G. Cepon, L. Manin, M. Boltezar, Experimental identification of the contact parameters between a v-ribbed belt and a pulley, Mech. Mach. Theory 45 (10) (2010) 1424 – 1433. doi:http://dx.doi.org/10.1016/j.mechmachtheory.2010.05.006.

[21] B. Balta, F. O. Sonmez, A. Cengiz, Speed losses in v-ribbed belt drives, Mech. Mach. Theory 86 (2015) 1 – 14. doi:http://dx.doi.org/10.1016/j.mechmachtheory.2014.11.016.

[22] B. Balta, F. O. Sonmez, A. Cengiz, Experimental identification of the torque losses in v-ribbed belt drives using the response surface method, J Automobile Engineering 229 (2014) 1070–1082. doi:10.1177/0954407014555150.

[23] L. Manin, X. Liang, C. Lorenzon, Power losses prediction in poly-v belt transmissions: application to front engine accessory drives, in: P. Velex (Ed.), International Gear Conference 2014: 26th-28th August 2014, Lyon, Chandos Publishing, Oxford, 2014, pp. 1162 – 1171. doi:http://dx.doi.org/10.1533/9781782421955.1162.

[24] H. Zhu, Y. Hu, W. Zhu, Dynamic response of a front end accessory drive system and parameter optimization for vibration reduction via genetic algorithm, J. Vib. Control 24 (2016) 2201–2220. doi:10.1177/1077546316680543.

[25] J. Zhang, J. W. Zu, Non-linear vibrations of viscoelastic moving belts, Journal of Sound and Vibration 216 (1998) 93–105. doi:https://doi.org/10.1006/jsvi.1998.1689.

[26] H. Ding, L. Q. Chen, Nonlinear models for transverse forced vibration of axially moving viscoelastic beams, Shock and Vibration 18 (2011) 281–287. doi:10.3233/SAV20100586.

[27] L. Q. Chen, H. Ding, Steady-state transverse response in coupled planar vibration of axially moving viscoelastic beams, ASME 132 (2010) 1–9. doi:10.1115/1.4000468.

[28] K. Marynowski, Non-linear dynamic analysis of an axially moving viscoelastic beam, J. Theor. Appl. Mech. 40 (2002) 465–482.

[29] K. Marynowski, T. Kapitaniak, Zener internal damping in modelling of axially moving viscoelastic beam with time-dependent tension, J. Non-Linear Mech. 42 (2007) 118–131.

[30] L. Manin, G. Michon, Entrainements par courroie striees: Architecture et dynamique globale, Techniques de l'Ingenieur 1 (2010) 1–16.

[31] [link].
URL https://www.hutchinsontransmission.com/products-solutions/products/poly-v

[32] H. Stief, R. Pflug, T. Schmidt, C. Fechler, Belt drive systems, in: Schaeffler SYMPOSIUM, 2010.
URL https://www.schaeffler.com/remotemedien/media/_shared_media/08_media_library/01_publications/schaeffler_2/symposia_1/downloads_11/Schaeffler_Kolloquium_2010_19_en.pdf

[33] L. Manin, R. Dufour, S. Schultz, Pulley torsional vibration damper characterization, Mechanics and Industry 14 (2013) 151–155. doi:10.1051/meca/2013057.

[34] G. Michon, L. Manin, R. Dufour, Hysteretic behavior of a belt tensioner: modeling and experimental investigation, Journal of Vibration and Control 11 (2005) 1147–1158. doi:https://doi.org/10.1177/1077546305055539.

[35] C. Monternot, Comportement dynamique des transmissions de puissance par courroie dentee, Ph.D. thesis, INSA Lyon (1998).

[36] F. Grashof, Teoretische Maschinenlehre, Leopold Voss, 1883.

[37] L. Euler, Remarque sur l'effet du frottement dans l'equilibre, Tech. Rep. pp. 265-278, Academie des sciences de Berlin (1762).

[38] R. S. Lakes, Viscoelastic Materials, Cambridge University Press, 2009.

[39] J. Meaud, T. Sain, G. M. Hulbert, A. M. Waas, Analysis and optimal design of layered composites with high stiffness and high damping, Journal of Solids and Structures 50 (9) (2013) 1342 – 1353. doi:http://dx.doi.org/10.1016/j.ijsolstr.2013.01.014.

[40] P. Butaud, Contribution a l utilisation des polymeres a memoire de forme pour les structures a amortissement controle, Ph.D. thesis, Universite de Franche Comte (2015).

[41] M. Chawla., Mechanical Behavior of Materials, Prentice Hall, 1999.

[42] [link].
URL http://www.skf.com/binary/77-121486/SKF-rolling-bearings-catalogue.pdf

[43] G. Gerbert, On flat belt slip, Vehicle tribology 18 (1991) 333–340. doi:10.1016/S0167-8922(08)70149-4.

[44] C. R. Barker, L. R. Oliver, W. F. Breig, Dynamic analysis of belt drive tension forces during rapid engine acceleration, in: SAE Technical Paper, SAE International, 1991. doi:https://doi.org/10.4271/910687.

[45] T. H. C. Childs, J. K. Parker, Power transmission by flat, v and timing belts, Tribological design of machine elements Tribology series 14 (1989) 133–142.

[46] C. A. F. Silva, L. Manin, R. G. Rinaldi, D. Remond, E. Besnier, M. A. Andrianoely, Modeling of power losses in poly-v belt transmissions: hysteresis phenomena (enhanced analysis), Mech. Mach. Theory 121 (2018) 373–397. doi:https://doi.org/10.1016/j.mechmachtheory.2017.10.008.

[47] C. A. F. Silva, L. Manin, R. G. Rinaldi, D. Remond, E. Besnier, M. A. Andrianoely, Modeling of power losses in poly-v belt transmissions: hysteresis phenomena (standard analysis), JSME 11 (2017) 1–15. doi:10.1299/jamdsm.2017jamdsm0085.

[48] R. Bellman, Dynamic programming, Princeton University Press, 1957.

[49] E. F. Moore, The shortest path through a maze, Bell Telephone System, 1959.

[50] M. Sniedovich, Dynamic Programming: Foundations and Principles, CRC Press, 2010.

[51] M. A. Andrianoely, Analyse structurale par les donnees en vue de l optimisation d une unite de production de zinc, Ph.D. thesis, INSA Toulouse (1984).

[52] D. Kim, H. Peng, S. Bai, J. Maguire, Control of integrated powertrain with electronic throttle and automatic transmission, IEEE transactions on control systems technology 15 (2007) 474–482. doi:10.1109/TCST.2007.894641.

[53] H. Luu, L. Nouveliere, S. Mammar, Dynamic programming for fuel consumption optimization on light vehicle, IFAC Symposium advances in automotive control 43 (2010) 372–377. doi:10.3182/20100712-3-DE-2013.00097.

[54] R. W. Anderson, M. Conrad, Hans j. bremermann: a pioneer in mathematical biology, Bio Systems 34 (1995) 1–10. doi:10.1016/0303-2647(94)01442-A.

[55] A. L. S. Chua, N. A. Benedek, L. Chen, M. W. Finnis, A. P. Sutton, A genetic algorithm for predicting the structures of interfaces in multicomponent systems, Nature Materials 9 (2010) 418–422. doi:10.1038/nmat2712.

[56] S. Sasaki, A. J. Comber, H. Suzuki, C. Brunsdon, Using genetic algorithms to optimize current and future health planning - the example of ambulance locations, International Journal of Health Geographics 9 (2010) 4. doi:10.1186/1476-072X-9-4.

[57] C. Darwin, On the Origin of Species, John Murray, 1859.

[58] K. J. Binkley, M. Hagiwara, Applying self-adaptive evolutionary algorithms to two-dimensional packing problems using a four corners heuristic, European Journal of Operational Research 183 (2007) 1230–1248. doi:10.1016/j.ejor.2004.12.029.

[59] A. J. Umbarkar, P. D. Sheth, Crossover operators in genetic algorithms: a review, Journal on Soft computing 6 (2015) 1083–1092. doi:10.21917/ijsc.2015.0150.

[60] T. D. Gwiazda, Genetic Algorithms Reference, TOMASZGWIAZDA E-BOOKS, 2006.

[61] V. Krishnamurthy, Partially Observed Markov Decision Processes: from filtering to controlled sensing, Cambridge University Press, 2016.

[62] C. A. F. Silva, M. A. Andrianoely, L. Manin, S. Ayasamy, C. Santini, E. Besnier, D. Remond, Optimization of power losses in poly-v belt transmissions via genetic algorithm and dynamic programming, Mech. Mach. Theory 128 (2018) 169–190. doi:https://doi.org/10.1016/j.mechmachtheory.2018.05.016.

[63] S. Braun, D. Ewins, S. S. Rao, Encyclopedia of vibration, Academic Press, Oxford, 2001. doi:http://dx.doi.org/lO.1006/rwvb.2001.

[64] M. Lalanne, P. Berthier, J. D. Hagopian, Mechanical Vibrations for ENGINEERS, John Wiley & Sons Inc, 1984.

[65] K. T. Amijima, Fuji, Inukai, Study on v-ribbed belt: the relation between rib deformation and transmitted force of the v-ribbed belt, JSME 29 (1986) 2317–2322.

[66] D. Tonazzi, Macroscopic frictional contact dynamics, Ph.D. thesis, INSA Lyon and Sapienza Universita di Roma (2014).

[67] J. Abdo, M. Tahat, The effect of frequency and amplitude of vibration on the coefficient of friction for metals, WSEAS Transactions on applied and theoretical mechanics 3 (2008) 265–274.

[68] X. LI, The experimental characterization of the belt tensioner in order to modify its model in cae tool, Tech. rep., INSA Lyon (2016).

[69] H. Blanc, Dynamique des rotors en torsion : Etude des amortisseurs de torsion, Techniques de l'Ingenieur BM5124 V1 (2000) 1–9.

[70] P. P. Hujare, A. D. Sahasrabudhe, Experimental investigation of damping performance of viscoelastic material using constrained layer damping treatment, AMME Procedia Materials Science 5 (2014) 726–733. doi:https://doi.org/10.1016/j.mspro.2014.07.321.

[71] A. Q. Bhatti, H. Varum, Comparison between the visco-elastic dampers and magnetorheological dampers and study the effect of temperature on the damping properties, WCEE 19 (2012) 1–9.

[72] J. C. Jauregui, J. A. Becerril, A. L. Guzman, Viscoelastic torsional damper model, Power Transmission and Gearing Conference, ASME 88 (1996) 777–780.

[73] J. M. Kelly, Moving load problems in the theory of viscoelasticity, Ph.D. thesis, Stanford (1962).

[74] K. Wakabayashi, Y. Honda, T. Kodama, K. Shimoyamada, Torsional vibration damping of diesel engine with rubber damper pulley, JSME 38 (1995) 670–678.

[75] M. Kinoshita, T. Sakamoto, An experimental study of a torsional/bending damper pulley for an engine crankshaft, Society of Automotive Engineers, SAE Paper n. 891127 (1989) 1605–1615.

[76] R. N. Jazar, Advanced Vibrations A Modern Approach, Springer, New York, 2013. doi:10.1007/978-1-4614-4160-1.

[77] A. G. Piersol, T. L. Paez, Harris Shock and Vibration Handbook, McGraw Hill, New York, 2010.

[78] M. Thomas, F. Laville, Simulation des vibrations mecaniques, Presses de l Universite du Quebec, 2007.

[79] S. Cantournet, R. Desmorat, J. Besson, Mullins effect and cyclic stress softening of filled elastomers by internal sliding and friction thermodynamics model, International Journal of Solids and Structures 46 (2009) 2255 – 2264. doi:https://doi.org/10.1016/j.ijsolstr.2008.12.025.

[80] P. Saad, Modelisation et identification du comportement non lineaire des cales en caoutchouc, Ph.D. thesis, Ecole Centrale de Lyon (2003).

[81] M. Schulz, Elastic creep in serpentine belt drives and adopting a suitable strain measure, Mechanical Engineering Science 218 (2004) 1421–1433.

APPENDICES

A1: Hysteresis loop area analysis

Based on linear algebra, Eq. 1.5 corresponds to the equation of the ellipse in Fig. 1.39 whose major and minor axes coincide with the cartesian axes.

$$\frac{x^2}{a^2} + \frac{y^2}{b^2} = 1 \tag{1.5}$$

The area of the ellipse in Fig. 1.39 is equal to four times its hatched area which can be calculated by Eq. 1.6, where from equation 1.5 the function $g(x)$ describing the ellipse upon the hatched area of the ellipse in Fig. 1.39 can be obtained (Eq. 1.7).

$$A_{ellipse} = 4 \int_0^b g(x)\,\mathrm{d}x \tag{1.6}$$

$$g(x) = b \cdot \sqrt{1 - \frac{x^2}{a^2}} \tag{1.7}$$

Changing the variables of the Eq. 1.6 as in Eq. 1.8, where θ is the ellipse polar angle coordinate taken in the anticlockwise direction.

$$x = \sin\theta \cdot a \tag{1.8}$$

The integral 1.6 can be rewritten as in Eq. 1.9a.

$$A_{ellipse} = 4\ b\ a\ \int_0^{\frac{\pi}{2}} \sqrt{1 - \sin\theta^2} \cdot \cos\theta\,\mathrm{d}\theta \tag{1.9a}$$

Developing Eq. 1.9a, then solving the integral analytically:

$$A_{ellipse} = 4\ b\ a\ \int_0^{\frac{\pi}{2}} \cos\theta^2\,\mathrm{d}\theta \tag{1.9b}$$

$$A_{ellipse} = 2\ b\ a\ \int_0^{\frac{\pi}{2}} 1 + \cos 2\theta\,\mathrm{d}\theta \tag{1.9c}$$

Finally, the area of the generic ellipse in Fig. 1.39 is equal to Eq. 1.10.

$$A_{ellipse} = \pi\ a\ b \tag{1.10}$$

Note that if $a = b = r$, it comes back to the classical formula for calculating the area of a circle of radius r ($A_{ellipse} = A_{circle} = \pi \cdot r^2$).

In the case of viscoelastic materials [38], the hysteresis loop (Fig. 1.40) is often considered. From the left and right triangles in Fig. 1.40, respectively, Eqs. 1.11, 1.12 are obtained. Arranging the Eqs. 1.11, 1.12 and the relation $\tan\delta = E'$ leads to Eq. 1.13. Hence, from Eqs. 1.10 and 1.13 the area of the hysteresis loop in Fig. 1.40 is obtained by Eq. 1.14.

$$\cos\delta = \frac{a}{E'' \cdot \varepsilon_a} \tag{1.11}$$

$$\sin\delta = \frac{E' \cdot \varepsilon_a}{b} \tag{1.12}$$

$$a \cdot b = E'' \cdot {\varepsilon_a}^2 \tag{1.13}$$

$$A_{loop} = \pi \cdot E'' \cdot {\varepsilon_a}^2 \tag{1.14}$$

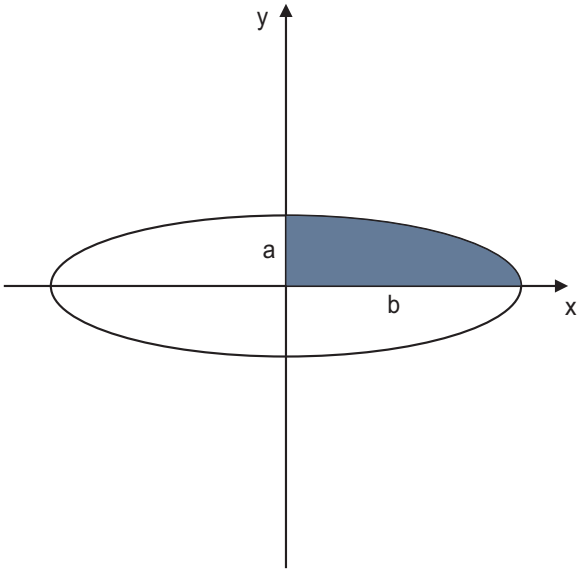

Figure 1.39 – Generic ellipse.

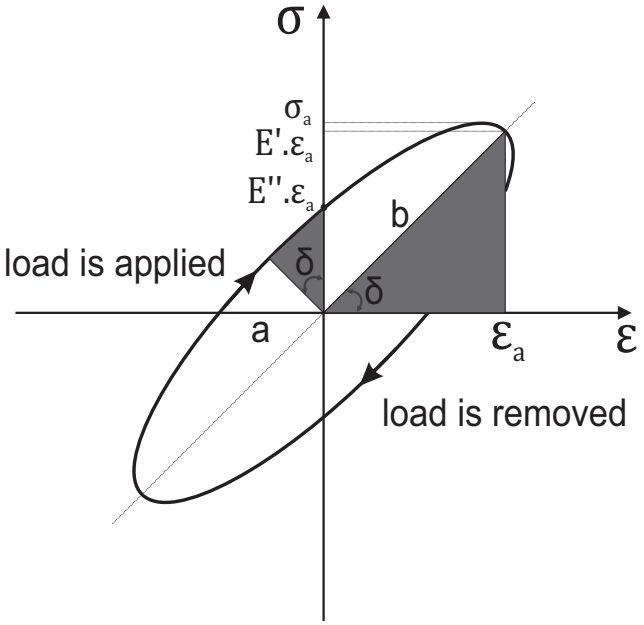

Figure 1.40 – Hysteresis loop analysis.

A2: Belt/pulley contact pressure

Considering the infinitesimal poly-V belt element in Fig. 1.41 and the distribution of forces acting on the small belt element in Fig. 1.42.

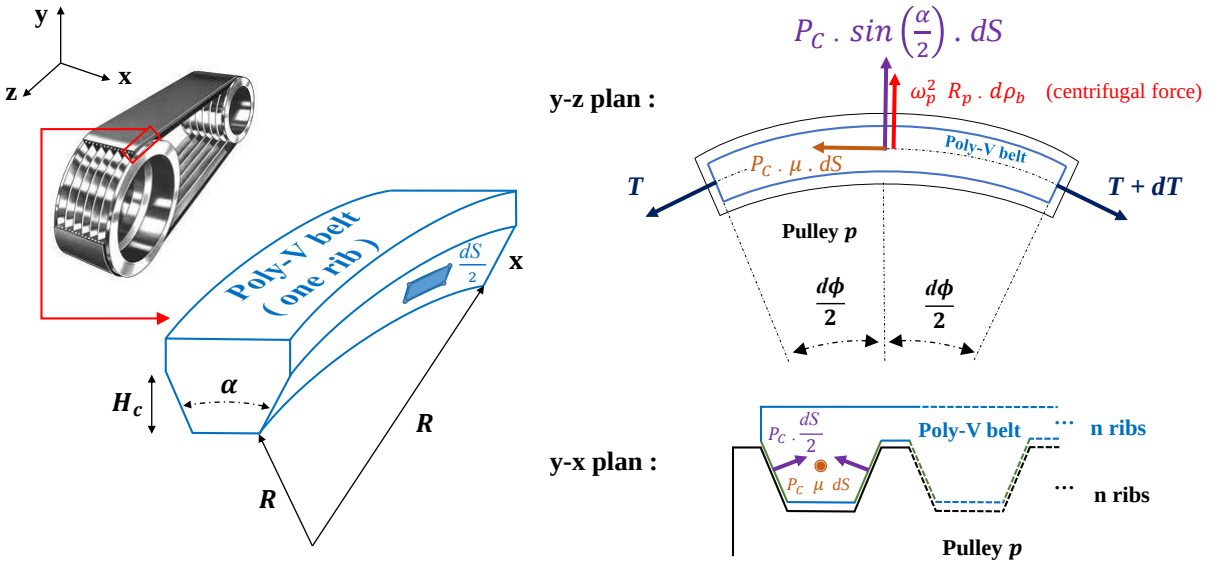

Figure 1.41 – Infinitesimal poly-V belt element analysis.

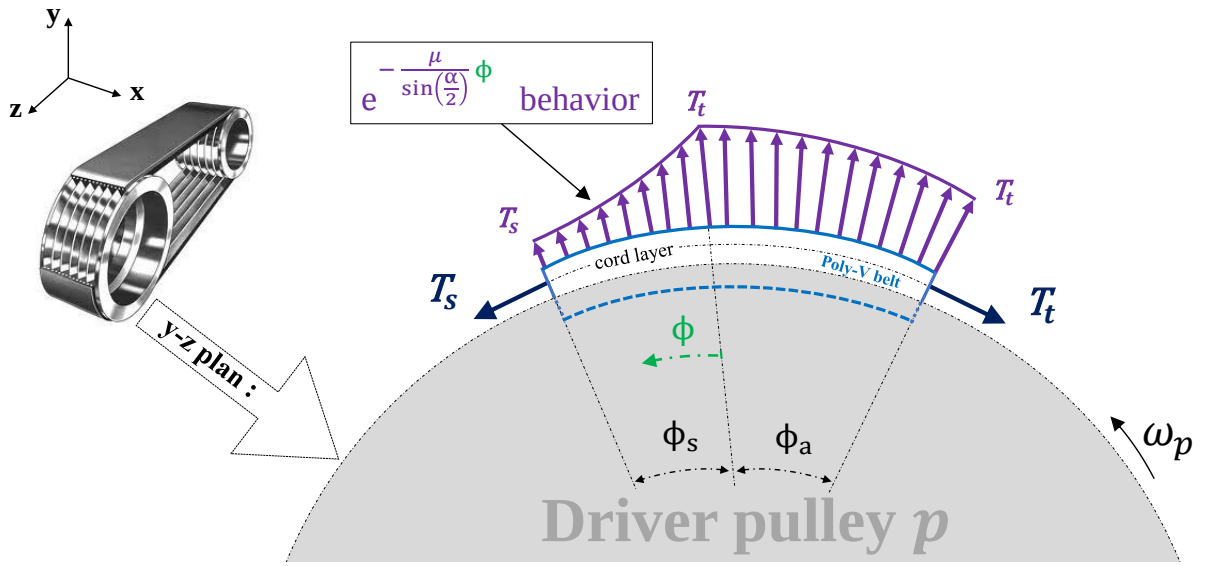

Figure 1.42 – Distribution of forces acting on a small belt element.

The sum of forces in the **z-direction** (Fig. 1.41) without the centrifugal action T_c gives:

$$T \cdot cos(\frac{d\phi}{2}) + P_c \cdot \mu \cdot dS = (T + dT) \cdot cos(\frac{d\phi}{2}) \tag{1.15}$$

If the $d\phi$ is infinitesimal, it can be assumed that $[cos(\frac{d\phi}{2}) = 1]$. Thus, simplifying and neglecting the high order (≥ 2) therms (e.g. $dT \cdot d\phi$) leads to Eq. 1.16.

$$dT = P_c \cdot \mu \cdot dS \tag{1.16}$$

The sum of forces in the **y-direction** (Fig. 1.41) without the centrifugal action T_c gives:

$$P_c \cdot sin(\frac{\alpha}{2}) \cdot dS + \omega_p^2 \cdot R_p \cdot d\rho_b = T \cdot sin(\frac{d\phi}{2}) + (T + dT) \cdot sin(\frac{d\phi}{2}) \tag{1.17}$$

If the $d\phi$ is infinitesimal, $[sin(\frac{d\phi}{2}) = \frac{d\phi}{2}]$ can be assumed. Then, Eq. 1.17 can be rewritten as in Eq. 1.18.

$$P_c \cdot sin(\frac{\alpha}{2}) \cdot dS + \omega_p^2 \cdot R_p \cdot d\rho_b = T \cdot \frac{d\phi}{2} + (T + dT) \cdot \frac{d\phi}{2} \tag{1.18}$$

Or else

$$P_c \cdot sin(\frac{\alpha}{2}) \cdot dS + \omega_p^2 \cdot R_p \cdot d\rho_b = 2 \cdot T \cdot \frac{d\phi}{2} + dT \cdot \frac{d\phi}{2} \tag{1.19}$$

Simplifying and neglecting the high order (≥ 2) therms (e.g. $dT \cdot d\phi$) leads to Eq. 1.20.

$$P_c \cdot sin(\frac{\alpha}{2}) \cdot dS = (T - T_c) \cdot d\phi \tag{1.20}$$

From Eqs. 1.16 and 1.20:

$$\frac{dT}{(T - T_c)} = \frac{\mu}{sin(\frac{\alpha}{2})} \cdot d\phi \tag{1.21}$$

Integrating on both sides (See Fig. 1.42) for a driver pulley:

$$\int_{T_t}^{T} \frac{dT}{(T - T_c)} = \frac{\mu}{sin(\frac{\alpha}{2})} \cdot \int_0^{\phi} d\phi \tag{1.22}$$

The force acting on the poly-V belt as a function of the wrap angle ϕ is equal to Eq. 1.23.

$$T(\phi) = T_t \cdot e^{-\frac{\mu}{sin(\frac{\alpha}{2})} \cdot \phi} + T_c \cdot (1 - e^{-\frac{\mu}{sin(\frac{\alpha}{2})} \cdot \phi}) \tag{1.23}$$

In the Eq. 1.23, the boundary conditions 1.24 can be verified (Fig. 1.42).

$$\begin{cases} T(\phi) = T_t \\ for : \phi = 0 \end{cases} \tag{1.24}$$

To get the contact pressure as a function of the wrap angle. Let us consider Eq. 1.25 which can be demonstrated from Eq. 1.20 (with the centrifugal action T_c).

$$P_c(\phi) = \frac{(T(\phi) - T_c)}{sin(\frac{\alpha}{2})} \cdot \frac{d\phi}{dS_{poly-V}} \tag{1.25}$$

As illustrated in Fig. 1.41 (left), the infinitesimal element of area $\frac{dS}{2}$ (Eq. 1.26) of a V belt can be obtained through trigonometrical relationships.

$$\frac{dS}{2} = \frac{H_c}{cos(\frac{\alpha}{2})} \cdot R_p \cdot d\phi \tag{1.26}$$

Then, the poly-V belt infinitesimal element of area considering two sides and n ribs:

$$dS_{poly-V} = 2 \cdot n \cdot \frac{dS}{2} = \frac{2 \cdot n \cdot H_c}{cos(\frac{\alpha}{2})} \cdot R_p \cdot d\phi \tag{1.27}$$

Finally, the belt-pulley contact pressure for a **driver** pulley as a function of the wrap angle can be calculated by Eq. 1.28.

$$P_c(\phi) = \frac{(T_t - T_c) \cdot e^{-\frac{\mu}{sin(\frac{\alpha}{2})} \cdot \phi}}{2 \cdot n \cdot H_c \cdot R_p \cdot tan(\frac{\alpha}{2})} \tag{1.28}$$

Similarly, the belt-pulley contact pressure for a **driven** pulley as a function of the wrap angle can be calculated by Eq. 1.29.

$$P_c(\phi) = \frac{(T_s - T_c) \cdot e^{\frac{\mu}{sin(\frac{\alpha}{2})} \cdot \phi}}{2 \cdot n \cdot H_c \cdot R_p \cdot tan(\frac{\alpha}{2})} \tag{1.29}$$

A3: Poly-V belt Finite Element Analysis

The objective of this Finite Element simulation is firstly to validate that, in poly-V belts, the strain has a linear behavior $\varepsilon = \frac{x}{R}$ according to the beam bending theory. Where $\frac{1}{R}$ is the curvature and x the through-thickness distance from neutral axis of the belt, where the strain equals zero. Secondly, to confirm that the neutral axis as in the beam bending theory coincides with the center of the poly-V belt tension-cords layer as considered in Chapter 2. To demonstrate this, a simplification is made, consistent material properties were chosen to the Poly-V belt layers and simulations are performed to conclude about the neutral axis location by analyzing the through-thickness stress and strain results of the poly-V belt, when the it is subjected to a 3 point bending test.

Details on the poly-V belt FEA and associated results are presented hereafter.

Modeling

Thanks to the symmetry between the poly-V belt ribs, the analysis of the full belt with several ribs is simplified to the analysis of a single rib (Fig. 1.43).

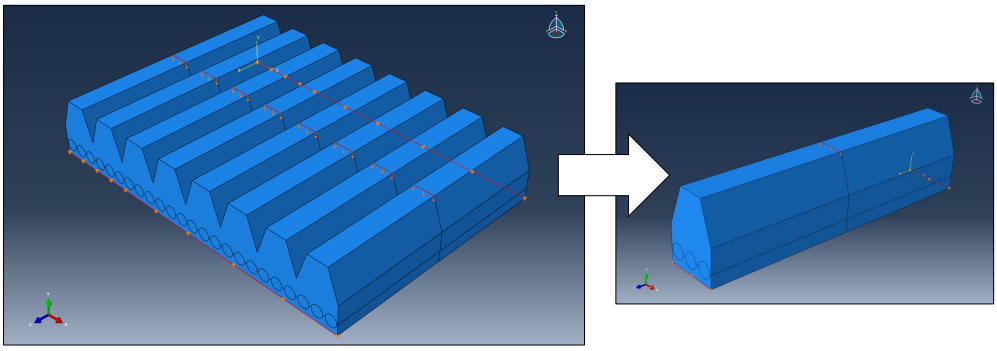

Figure 1.43 – Simplification of a poly-V belt with several ribs.

Representative belt materials, with belt-cords much stiffer than other layers, are assigned to each layer: (1) soft and hard rubbers are assigned to the rib and top layers; and (2) a stiff material (fiber) with a high storage modulus is assigned to the cords layer (Fig. 1.44)

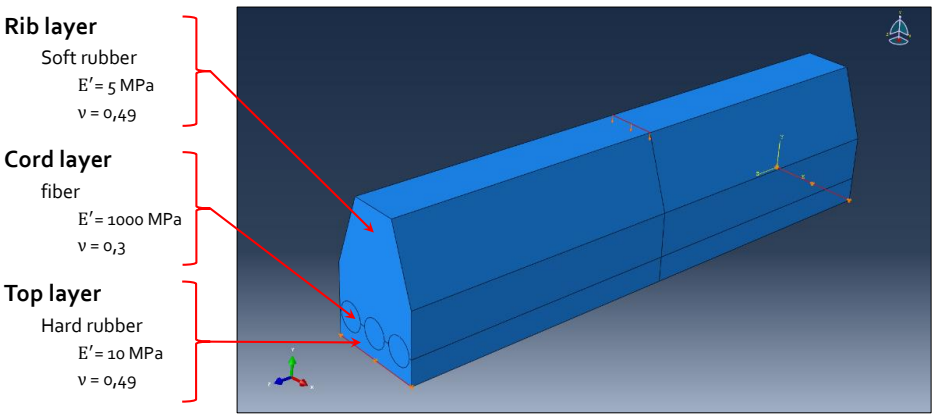

Figure 1.44 – Assigning of material properties to the poly-V belt layers.

To obtain the poly-V belt (stress and strain) behavior a 3 point bending test is virtually set up, i.e. adapted boundary conditions are declared to the extremities and the middle of the rib as in Fig. 1.45. Next, a FEA is done and the results are given in the next section.

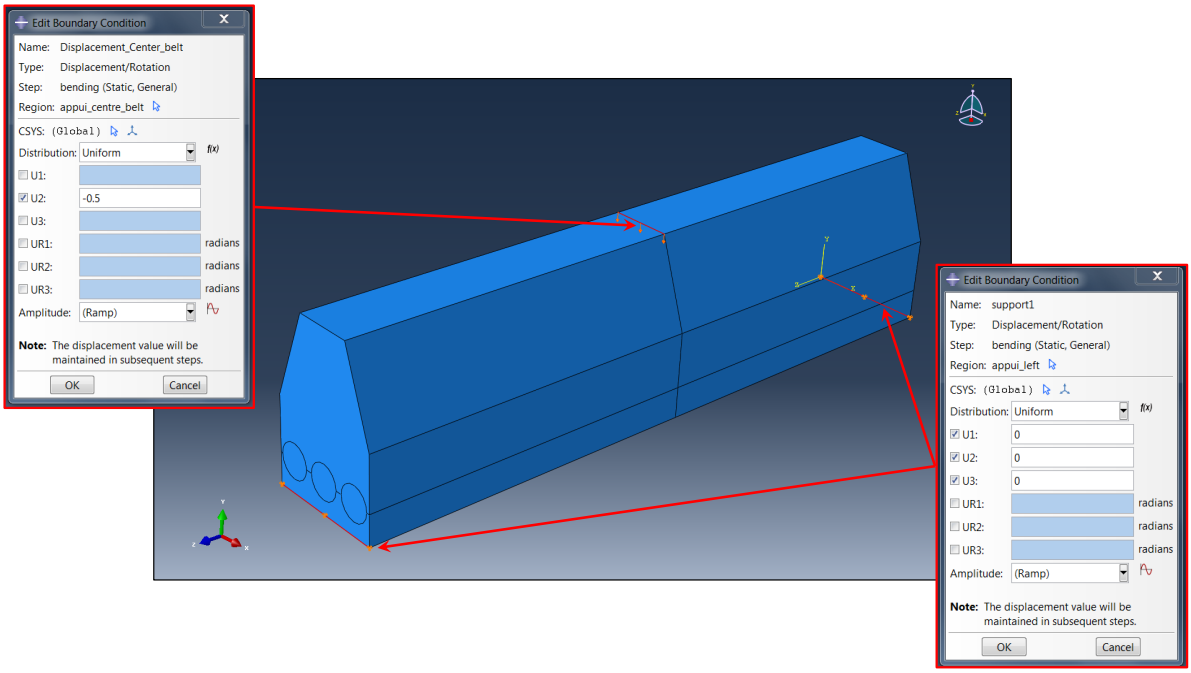

Figure 1.45 – Boundary conditions to perform a 3-point bending test.

Results

Results are presented for stress in the through-thickness direction (Fig. 1.46).

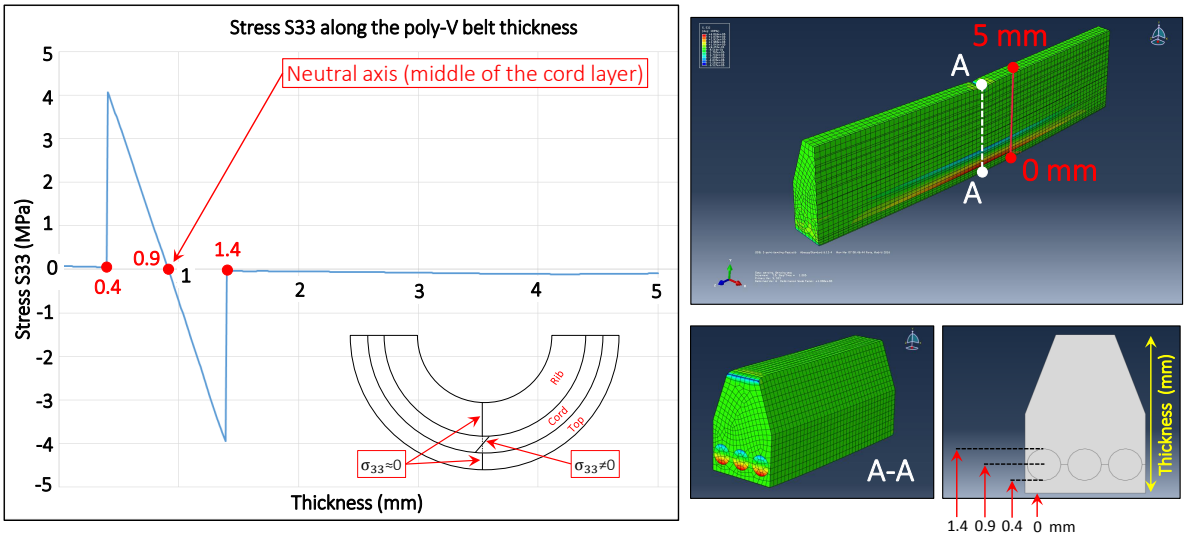

Figure 1.46 – Poly-V belt Stress (S33) along its through-thickness distance.

Remember that the goal here is to find out, independently of the magnitude, the behavior of stress along to the through-thickness direction of the poly-V belt. Similarly, results are also presented for strain in the through-thickness direction (Fig. 1.47).

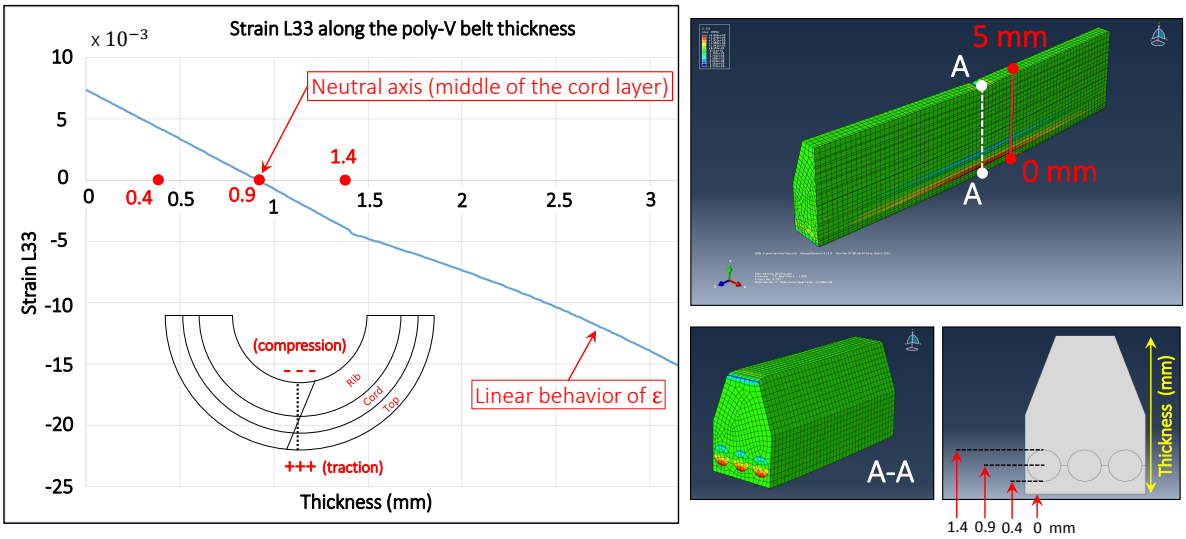

Figure 1.47 – Poly-V belt Strain (L33) along its through-thickness distance.

Fig. 1.47 also confirms that one side of the rib is subjected to compression, the other side is subjected to traction and the null strain coincides with the center of the poly-V belt tension-cords layer (i.e. neutral axis as in the beam bending theory).

Conclusions

Based on the poly-V belt FEA, one can conclude about

the through-thickness stress (Fig. 1.46):

- In the cord layer the stress along the through-thickness direction changes notably. This is due to the difference between the storage modulus of the rubber and cord layer materials;
- The major part of the stress in the longitudinal direction is supported by the tension cords. This can be verified visually in Fig. 1.46 through the significant variation in Stress between 0.4 and 1.4 mm;
- Outside the cord layer (i.e. $]0.4, 1.4[$ mm) the stress can be neglected since $S33 \approx 0$.

the through-thickness stress (Fig. 1.47):

- It is observed that the top layer is subjected to traction $\varepsilon(+)$;
- It is observed that the middle and rib layers are subjected to compression $\varepsilon(-)$;
- The strain is also nil in the middle of the cord layer (i.e. along the neutral axis).

These results should be kept in mind for a better understanding of the belt bending-hysteresis power losses.

A4: Belt elastomer characterization

Elastomeric materials are often described as hyperelastic materials, with the ability to undergo without dissipation large reversible deformation.

However, filled elastomers exhibit dissipative behaviors when deformed. Indeed, complex matrix-fillers interaction phenomena such as the Payne and the Mullins effects trigger the macroscopic (dissipative) viscoelastic behavior.

Payne and Mullins effects are important and they will be analyzed for the belt elastomeric constituent (rubber) used in FEAD applications.

Mullins effect

The Mullins effect is a particular behavior of filled elastomers submitted to deformation cycles. Macroscopically, the system is seen to irreversibly soften till a steady state regime and the amount of softening depends on the maximum deformation experienced by the sample (Cantournet [79]). Thus, since the poly-v belt will periodically travel within the FEAD, the account for the Mullins effect consists in measuring the materials viscoelastic properties of pre-conditionned samples.

In our modeling, the Mullins effect was not strictly studied, it was simply considered by taking the loss and storage moduli after a sufficient period of time (several loading cycles) to reach a stationary state with constant stress amplitude and stabilized hysteresis loop in order to better match the steady-state engine operation point (Fig.1.48).

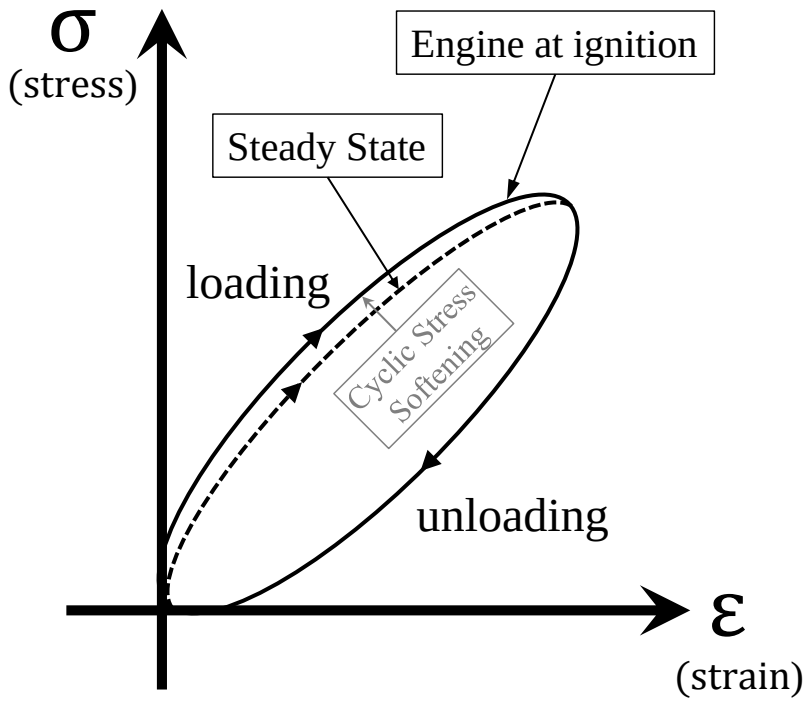

Figure 1.48 – Belt rubber stress-strain curve with cyclic stress softening (Mullins effect).

Payne effect

Depending on testing conditions (varying dynamic strain) the Payne effect can be noticed by analyzing experimental data such as those in Fig.1.49.

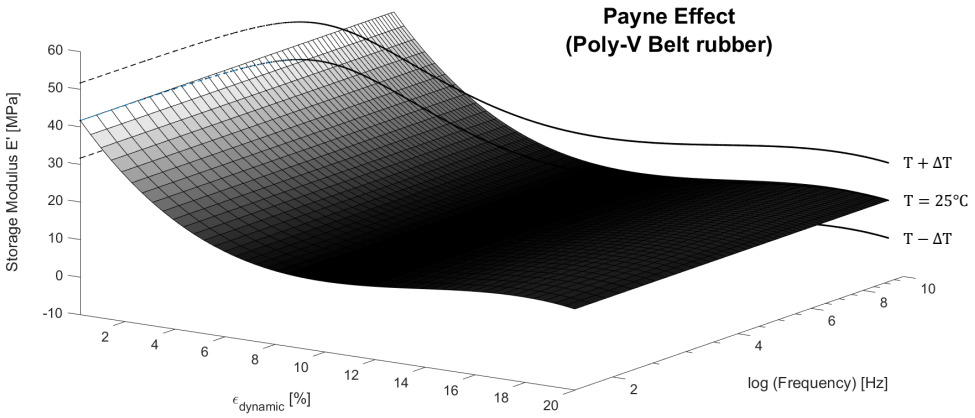

Figure 1.49 – Storage modulus $E' = F(\theta_{exp}, f_{exp}, \varepsilon_{exp})$ from DMA tests.

The Payne effect observed in filled elastomers (e.g. rubber) coincides with a reversible viscoelastic behavior that is a non linear function of the periodic strain amplitude. See the mechanical response curves (Fig.1.50) of a Poly-V belt backside EPDM-rubber.

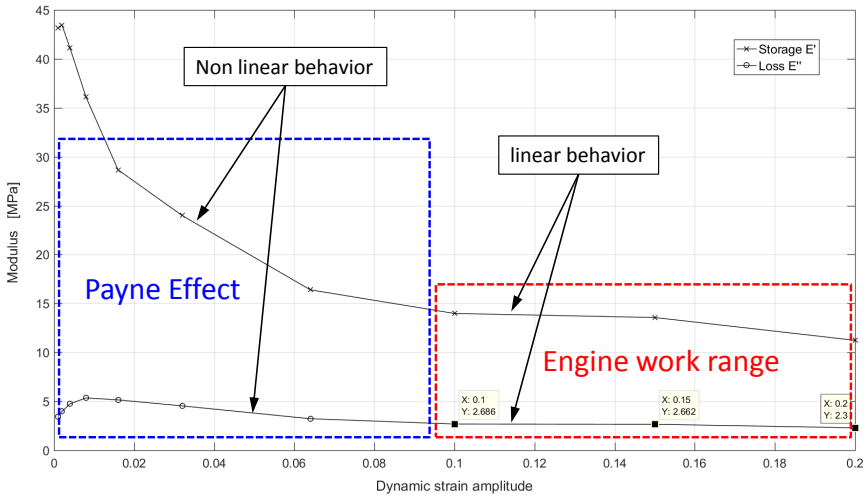

Figure 1.50 – Belt rubber modulus at temperature $(25°C)$ and frequency $(1Hz)$ fixed.

Yet, the reversibility time constant is demonstrated to be longer than the time needed for the belt to complete a FEAD cycle. Consequently, the account for the Payne effect consists in considering the storage and loss moduli measured for the largest strain value experienced by the elastomeric material throughout a complete cycle. Ultimately, the strain dependence is neglected.

It is worth noting that the direct consequence of neglecting the Payne effect is the assumption that DMA tests can be performed at a fixed strain representative of the poly-V belt cyclic loading modes. Also, note that Fig. 1.50 is similar to a 2D version of Fig.1.49.

A5: Belt-hysteresis enhanced analysis

So far we have considered the analysis relatively straightforward when finding the FEAD strain magnitudes (Eqs. 2.14, 2.20, 2.26 (or 2.30) and 2.37), it comprises the classical analysis such as Gerbert [14]. However, changing some aspects while modelling would give more accurate results.

1st aspect According to Saad [80], in Eqs. 2.14, 2.20, 2.26 (or 2.30) and 2.37 the complex E^* instead of storage E' modulus should be used. For example, the Eq. 1.30 should be considered instead of the classical one containing E' (Eq. 2.14).

$$\varepsilon_{a_{st}} = \frac{\Delta T}{\sum E_k^* \cdot A_k} \tag{1.30}$$

Also, knowing that the absolute value of the E^* is slightly larger than E', depending on how much viscous a material is, the new $\varepsilon_{a_{st}}$ will be slightly smaller than before. In engineering applications, how materials are designed to dissipate a right (small) quantity of energy, that difference can be neglected. That is why, strains measures from the classical approach is often used. In this work, the analyses with E' are here assumed to be sufficient, but strain measures could be theoretically refined by using E^* instead of E'.

2nd aspect Moreover, according to Schulz [81], considering a logarithmic (Eq. 1.31) instead of the linear strain measure (Eqs. 2.14, 2.20, 2.26 (or 2.30) and 2.37) would contribute to improve the accuracy of results, and therefore, to enhance classical analyses.

$$\varepsilon_{a_{log}} = \ln(1 + \varepsilon_{a_{linear}}) \tag{1.31}$$

According to Schulz linear strain measures do not respect the system mass conservation law, i.e. while this condition is violated for the linear strain measure together with Hooke's law, whereas it holds for the logarithmic strain measure. In this thesis, linear strain measures are assumed, because of small train amplitudes taking place in the belt transmission (FEAD). In this case, the linear and logarithmic relations are equivalent, with a small (acceptable) relative error. However, logarithmic strain measures could be taken into account to further improve accuracy throughout a supposed enhanced analysis.

3rd aspect Finally, up to now, we have considered isolated hysteresis phenomena, but in solid mechanics, the strain fields are commonly represented by vectors with direction, magnitude and orientation. Thus, concerning the belt transmissions considered in this thesis, in the belt longitudinal direction an overlapping of Bending-Stretching-Shear (BSS) strains might occur. It takes place along the arc of contact ϕ (Fig. 1.51). An improved model would consider not only each isolated phenomena, but also their interaction (overlapping). To this aim, the total BSS strain magnitude might be considered (Eq. 1.32). Consequently, the strain in Eq. 2.10 should be replaced by Eq. 1.32 while choosing + or − signs to the place of the ±. These signs depend on working conditions.

Finally, Eq. 1.32 inside Eq. 2.10 will represent the total BSS hysteresis energy loss equation for Bending, Stretching and Shear (BSS).

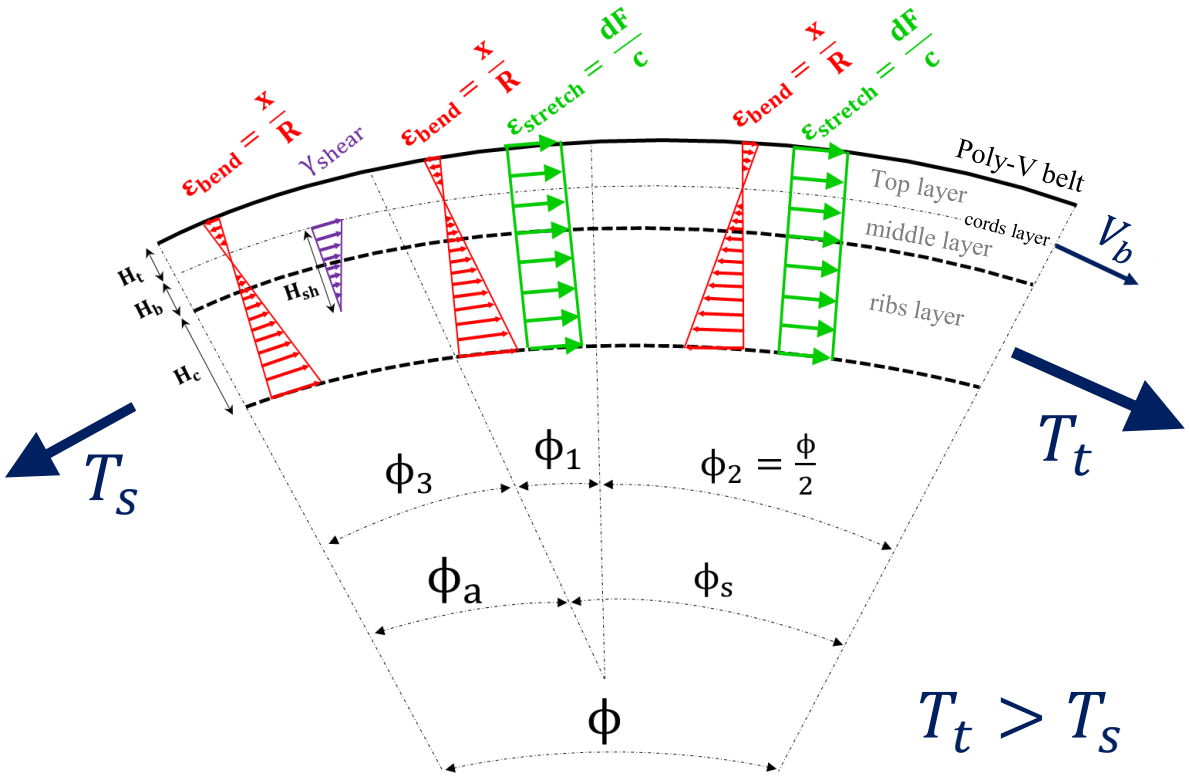

Figure 1.51 – Bending-Stretching-Shear strains overlapping in the case of a DN pulley.

The total Bending-Stretching-Shear (BSS) strain magnitude (general case in Eq. 1.32):

$$\begin{aligned}\varepsilon_{BSS} &= (\varepsilon_{a_{bend}} \pm \varepsilon_{a_{st}}) \cdot \frac{\phi_1}{\phi} + (\varepsilon_{a_{bend}} \pm \varepsilon_{a_{st}}) \cdot \frac{\phi_2}{\phi} + \left(\varepsilon_{a_{bend}} \pm \frac{\gamma_{a_{sh}}}{\sqrt{2 \cdot (1+\nu)}}\right) \cdot \frac{\phi_3}{\phi} + \\ &+ \left(\varepsilon_{a_{bend}} \pm \frac{\gamma_{a_{sh}}}{\sqrt{2 \cdot (1+\nu)}}\right) \cdot \frac{\phi_4}{\phi} \end{aligned} \tag{1.32}$$

Note that in the case of the DN pulley in Fig. 1.51 the work conditions provide the following coefficients ϕ_1, ϕ_2, ϕ_3 and ϕ_4 for Eq. 1.32.

$$\begin{cases} \phi_1 = \phi_s - \frac{\phi}{2} \\ \phi_2 = \frac{\phi}{2} \\ \phi_3 = \phi_a \\ \phi_4 = 0 \end{cases} \tag{1.33}$$

In the belt transverse or pulley radial direction there is no strain overlapping, since the different belt (rib, middle and top) layers are compressed due to the flank and radial compression. In this case, each phenomenon is independent and the correspondent power loss measures do not interfere with each other.

A6: GABO EPLEXOR®, DMA machine

The goal of the apparatus in Fig. 1.52 is to obtain through Dynamic Mechanical Analysis (DMA) the following viscoelastic-material properties of the poly-V belt:

- The complex modulus E^*
- The storage modulus E'
- The loss modulus E''

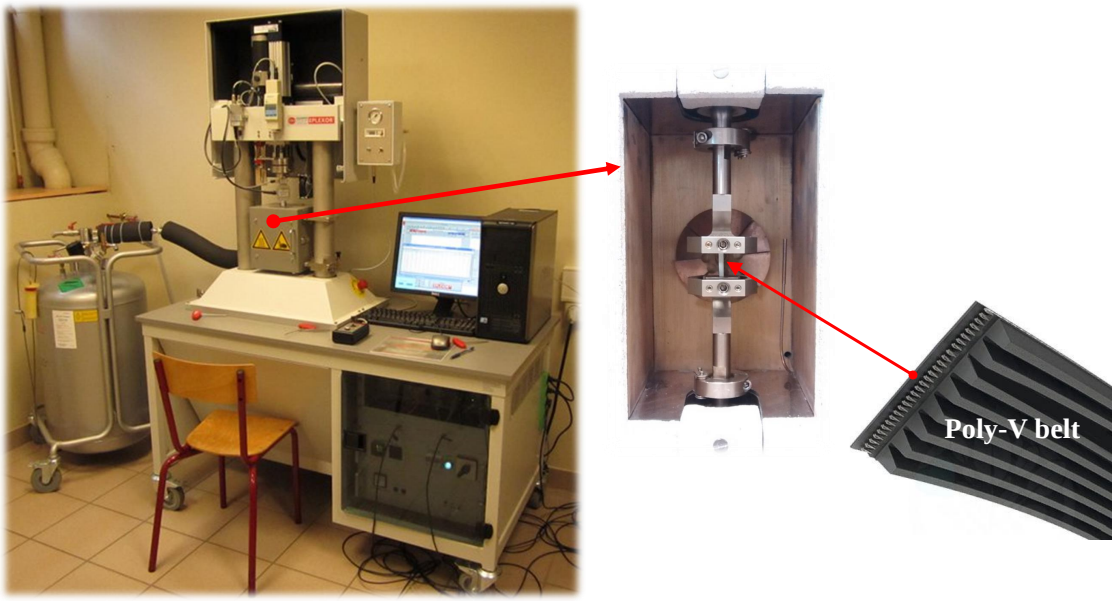

Figure 1.52 – Experimental set-up

The DMA tests are performed under the following conditions:

- The temperature equal to the wanted engine-room-temperature
- The frequency equivalent to the engine speed (Tab. 2.3)
- The belt static-strain equivalent to the FEAD setting tension
- The belt dynamic-strain equal to the cyclic loading modes strains

A7: Development of the sliding velocity

The sliding velocity V_{sl} responsible for the power losses by slip is defined as in Eq. 1.34.

$$V_{sl} = V_b - V_p = V\ (1+\varepsilon) - R\omega\left(1 - \frac{x_{cp}}{R}\right) \tag{1.34}$$

However, it is possible to rearrange Eq. 1.34 as a function of primary system parameters. Thus, dividing Eq. 1.34 by the belt linear velocity V (Eq. 1.35).

$$\frac{R\omega}{V} = \frac{1}{\left(1 - \frac{x_{cp}}{R}\right)}\left[1 + \varepsilon + \frac{V_{sl}}{V}\right] \tag{1.35}$$

Next, considering the Maclaurin serie in Eq. 1.36 and the ratio x_{cp}/R as a small quantity.

$$\frac{1}{\left(1 - \frac{x_{cp}}{R}\right)} = 1 + \frac{x_{cp}}{R} + \left(\frac{x_{cp}}{R}\right)^2 + \left(\frac{x_{cp}}{R}\right)^3 + ... + \left(\frac{x_{cp}}{R}\right)^\infty \tag{1.36}$$

Neglecting the high order terms (≥ 2) and developing, Eq.1.35 can be rewritten (Eq.1.37).

$$\frac{R\omega}{V} = 1 + \varepsilon + \frac{x_{cp}}{R} - \frac{V_{sl}}{V} \tag{1.37}$$

On the driven pulley, at the beginning of the sliding arc, slack side conditions prevail [14], i.e. $V_{sl} = 0$, $\varepsilon = \varepsilon_s$ and $x_{cp} = x_{cp_s} = T_s/(R\,K)$. Applying these conditions to Eq. 1.37 leads to Eq. 1.38.

$$\frac{R\omega}{V} = 1 + \varepsilon_s + \frac{x_{cp_s}}{R} \tag{1.38}$$

To obtain the sliding velocity V_{sl} as a function of primary system parameters, Eq. 1.38 can be rearranged by eliminating $(R\omega)/V$ through subtracting Eq. 1.38 from Eq. 1.37 leading to Eq. 1.39.

$$\frac{V_{sl}}{V} = \varepsilon - \varepsilon_s + \frac{x_{cp} - x_{cp_s}}{R} \tag{1.39}$$

Note that in Eq. 1.39 one can see clearly the contribution of the belt stretching $(\varepsilon - \varepsilon_s)$ and radial compression $(x_{cp} - x_{cp_s})$. Nevertheless, it is still possible to rearrange Eq. 1.39 in a more convenient way by applying the definition of x_{cp} and ε leading to Eq. 1.40.

$$V_{sl} = V\left(\frac{1}{EA} + \frac{1}{K\,R^2}\right)(T - T_s) \;=\; V(1 + C_*)\,\frac{T - T_s}{EA} \tag{1.40}$$

Where V_{sl} is the belt-pulley sliding velocity and C_* a dimensionless quantity (Eq. 1.41).

$$C_* = \frac{EA}{K\,R^2} \tag{1.41}$$

A8: FEAD optimization via Genetic Algorithm (GA)

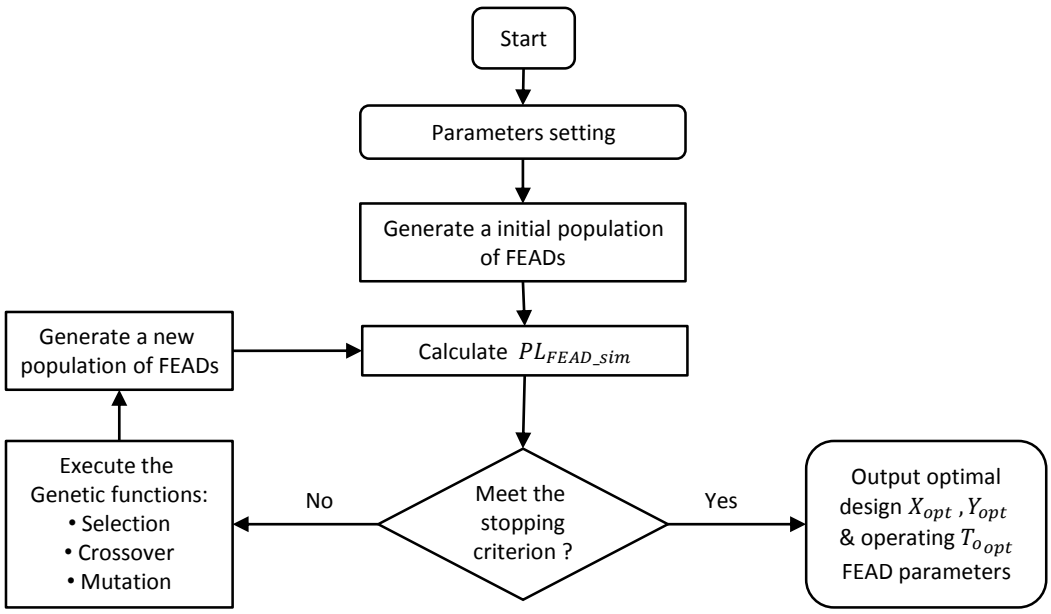

Figure 1.53 – Flowchart of the optimization via a genetic algorithm.

A9: FEAD optimization using Dynamic Programming (DP)

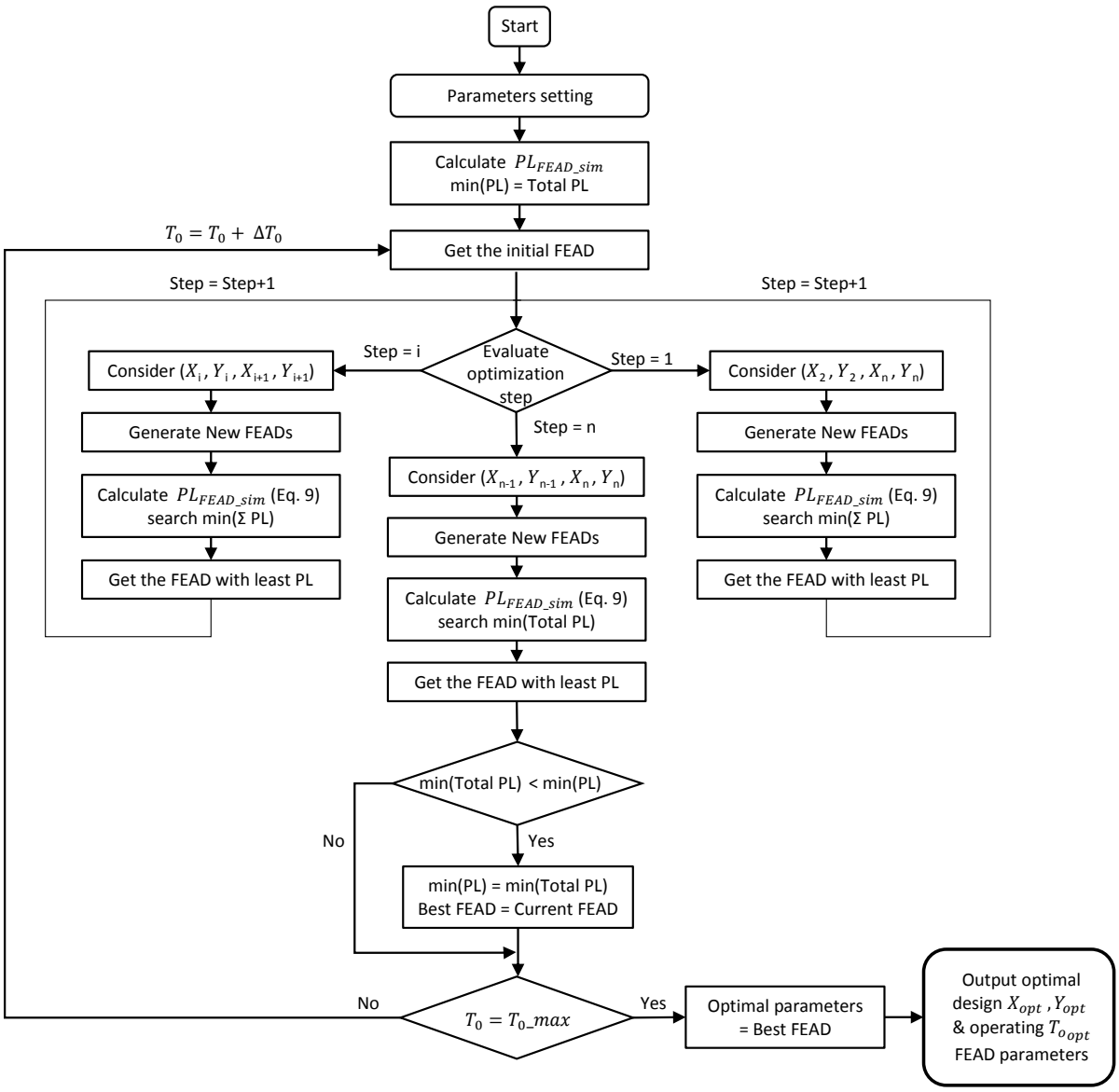

Figure 1.54 – Flowchart of the optimization using dynamic programming.

Where PL is the power loss coming from the evaluation of the dynamic programming sub-problems, i.e. a generic step between the first and the last optimization step n.

A10: EDIT tensioner hysteresis curves

For the same linear amplitude (2 mm) and several excitation frequencies (Fig. 1.55).

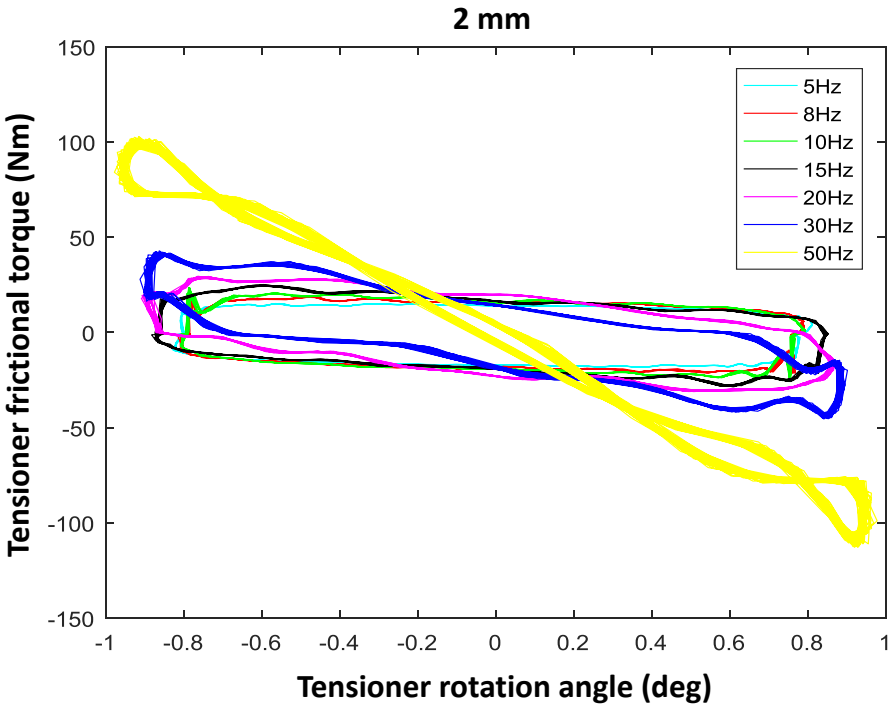

Figure 1.55 – EDIT tensioner hysteresis curves with the shaker amplitudes of 2 mm.

For the same linear amplitude (3 mm) and several excitation frequencies (Fig. 1.57).

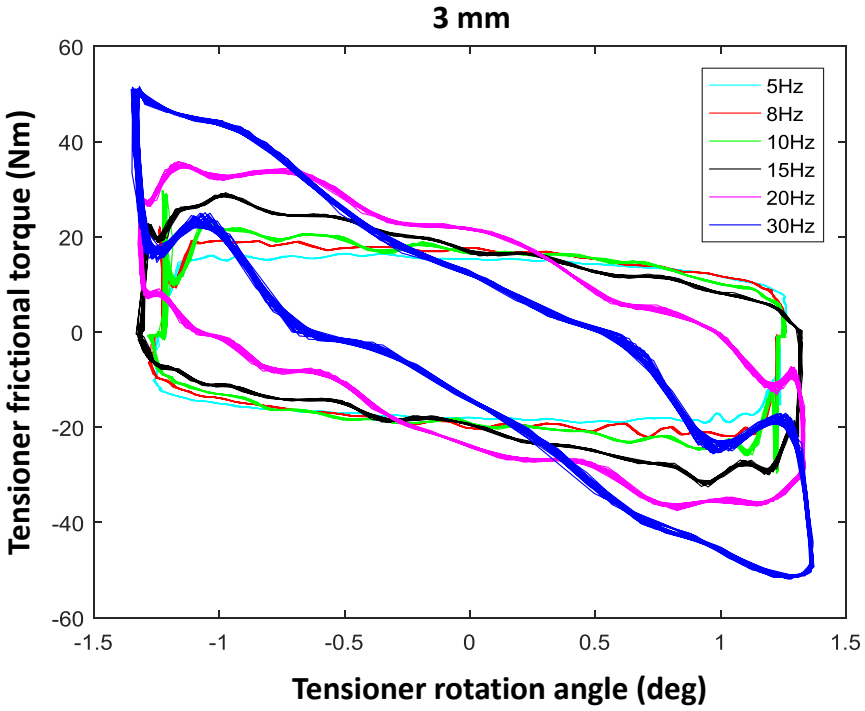

Figure 1.56 – EDIT tensioner hysteresis curves with the shaker amplitudes of 3 mm.

For the same frequency (5Hz), 1mm of linear amplitude and 5 tightening torques (Fig.1.57).

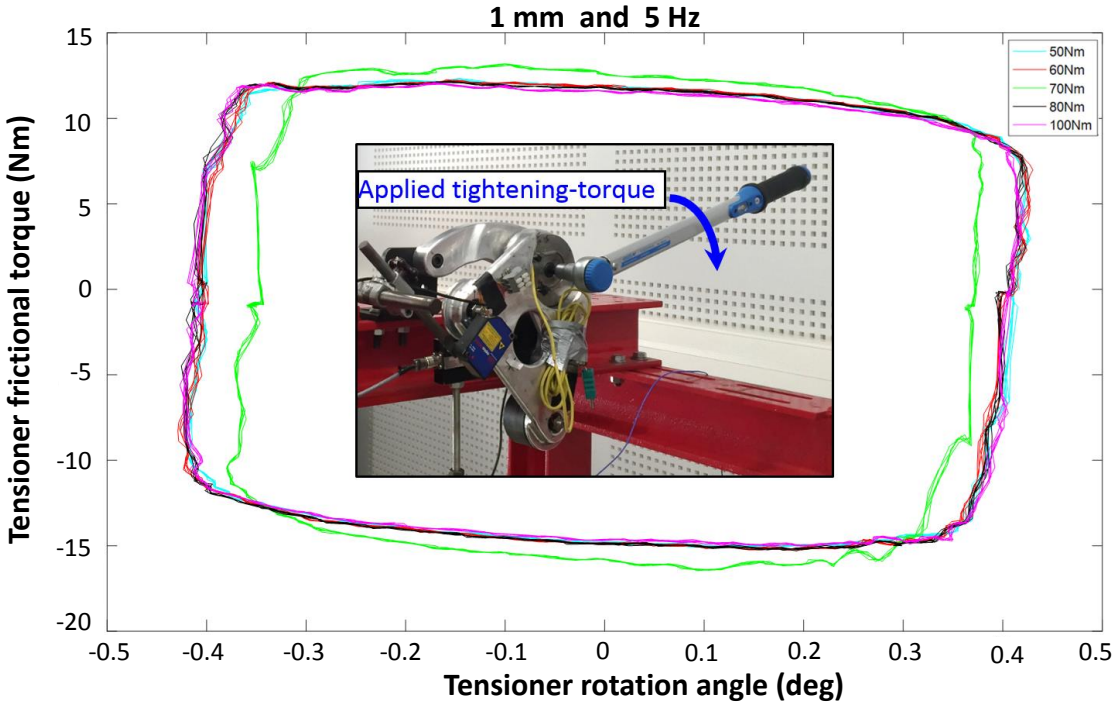

Figure 1.57 – EDIT tensioner hysteresis curves, linear amplitude of 1mm and frequency of 5Hz.

For the same frequency (5Hz), 2mm of linear amplitude and 5 tightening torques (Fig.1.58).

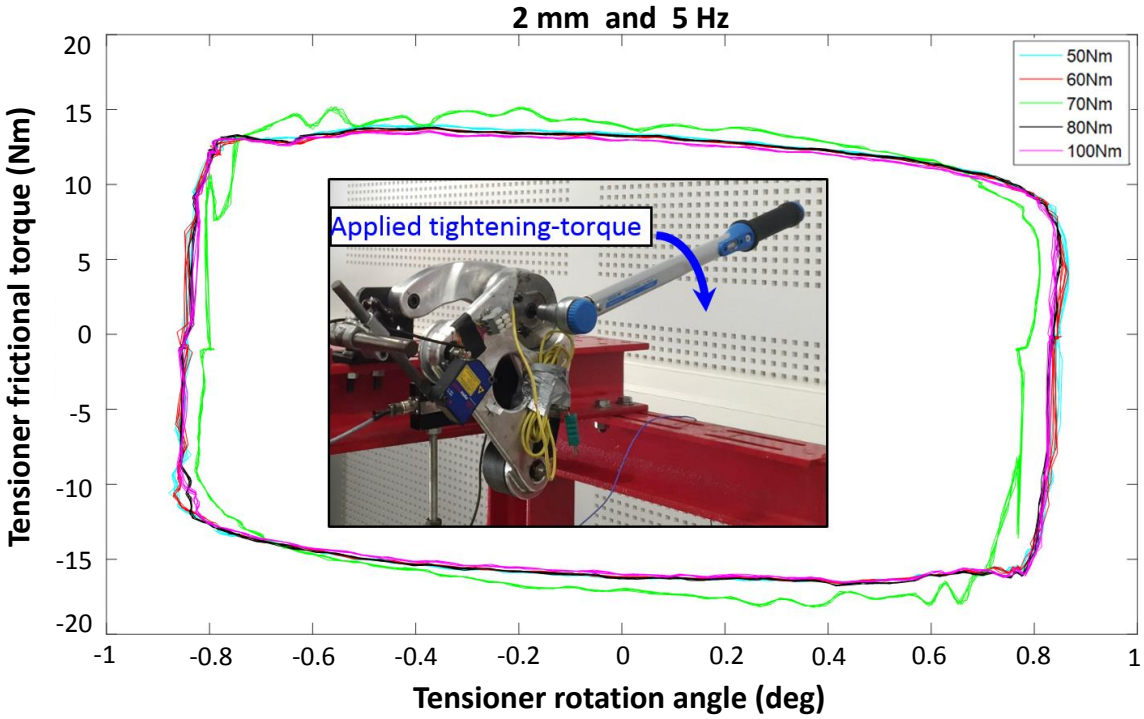

Figure 1.58 – EDIT tensioner hysteresis curves, linear amplitude of 2mm and frequency of 5Hz.

Finally, with the shaker excitation frequency ranging from 8 to 20 Hertz, several linear amplitudes (d) imposed by the shaker resulting in various rotation angles (Fig. 1.59)

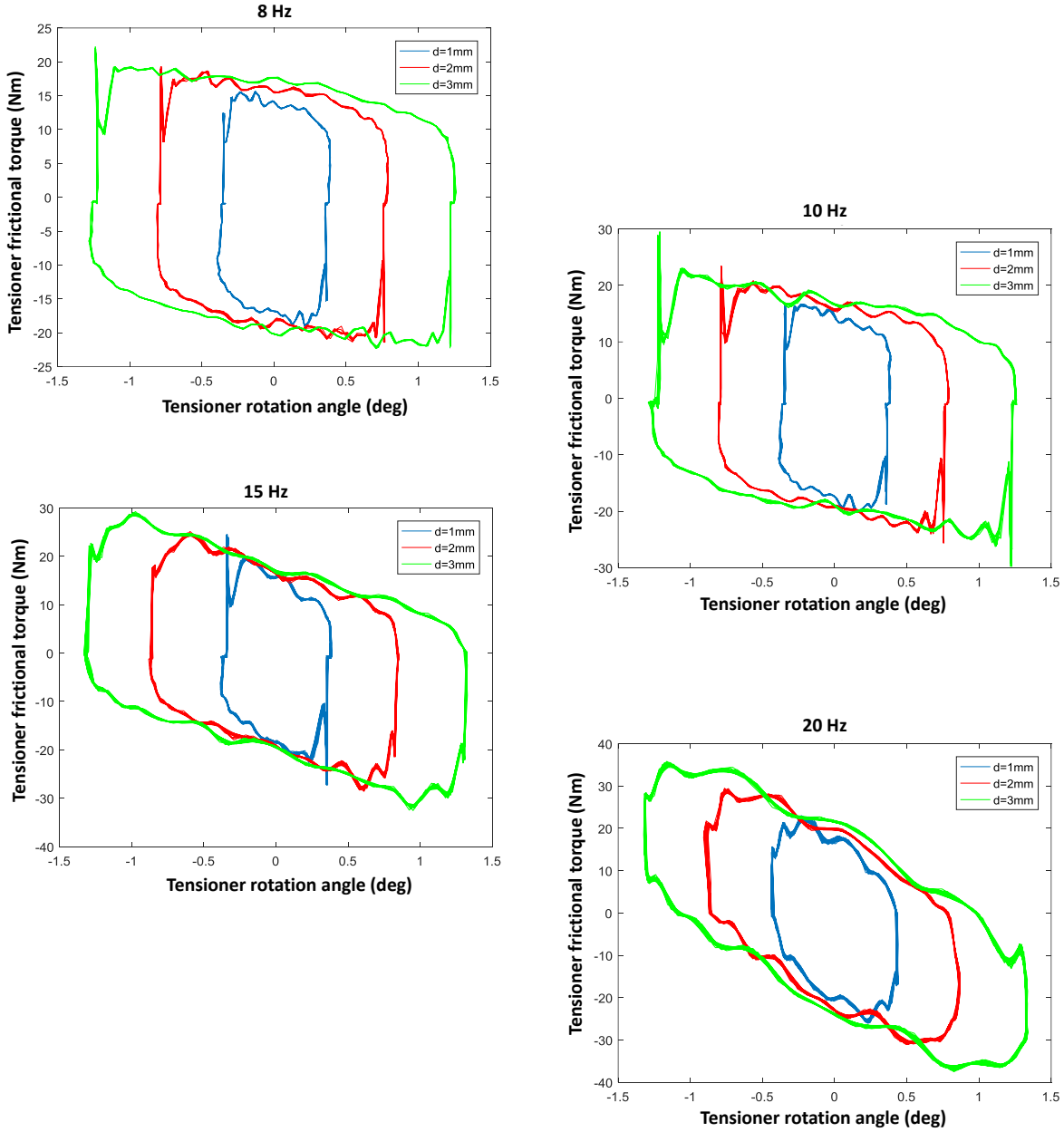

Figure 1.59 – EDIT tensioner hysteresis curves for several frequencies and linear amplitudes (d).

A11: EURO-6 tensioner hysteresis curves

For the same tensioner rotation angle (4.1°) and several excitation frequencies (Fig. 1.60).

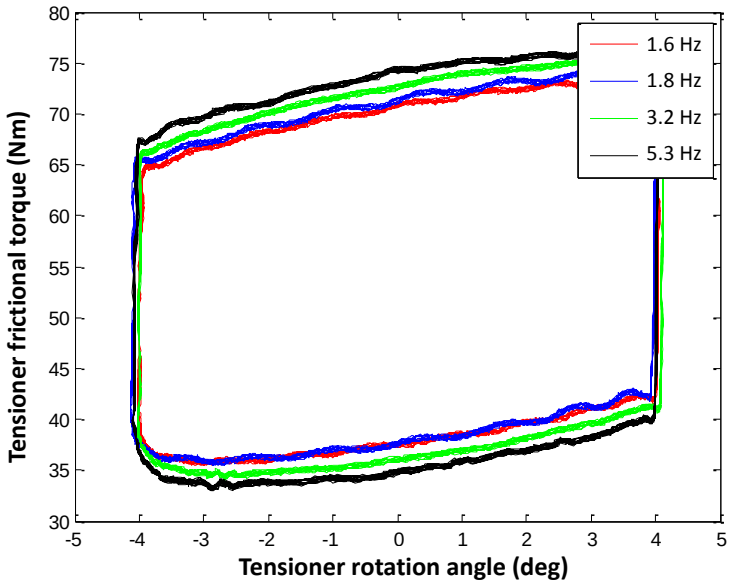

Figure 1.60 – EURO-6 tensioner hysteresis curves with tensioner rotation angle of 4.1°.

For the same 2 by 2 frequencies and various tensioner rotation angles (Fig. 1.61).

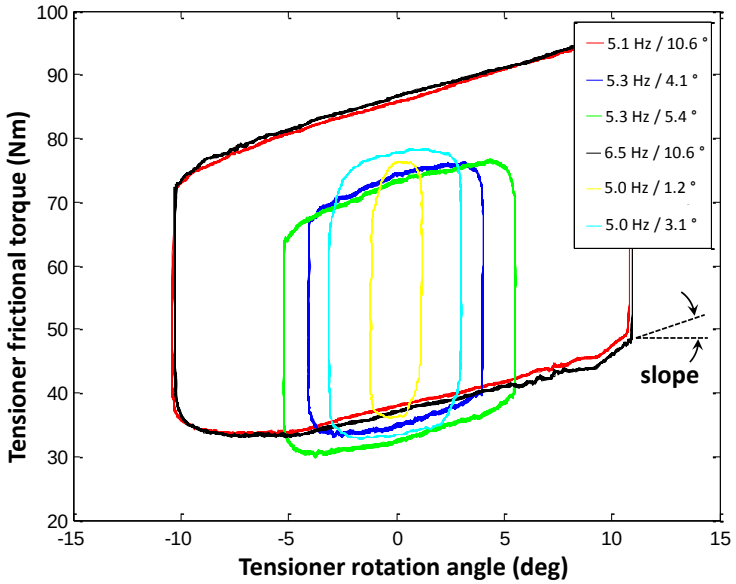

Figure 1.61 – EURO-6 tensioner hysteresis curves for various frequencies and rotation angles.

Figures 1.60 and 1.61 globally represent the characterization of the EURO-6 tensioner performed during the internship of LI [68], where no different tightening torques were considered since the current version of the EURO-6 tensioner manufactured by Dayco does not permit adjusting this parameter directly proportional to the tensioner damping.

Moreover, the EURO-6 hysteresis curves in Figs. 1.60 and 1.61 are not horizontal-lines (not nil slope as in Fig. 1.61) differently to the theoretical hysteresis curves of the EDIT tensioner. This is because the EURO-6 tensioner has a counter-spring, and therefore, not nil tensioner arm stiffness.

More details on the characterization of the EURO-6 tensioner can be found in [68].

FOLIO ADMINISTRATIF

THESE DE L'UNIVERSITE DE LYON OPEREE AU SEIN DE L'INSA LYON

NOM : FERREIRA DA SILVA DATE de SOUTENANCE : 25 / 10 / 2018

Prénoms : Carlos Alexandre

TITRE : Modélisation et optimisation des pertes de puissance dans les transmissions par courroie poly-v : application aux façades accessoires des moteurs de camions

NATURE : Doctorat Numéro d'ordre : 2018LYSEI079

Ecole doctorale : ED 162, MECANIQUE, ENERGETIQUE, GENIE CIVIL, ACOUSTIQUE (MEGA) Spécialité :

Génie Mécanique

RESUME :

Ces travaux s'inscrivent dans le cadre du projet EDIT (Efficient Distribution Truck, FUI19), piloté par le groupe Volvo Trucks, dont l'objectif de réduction de consommation pour 2020 est fixé à 13% par rapport à un véhicule actuel EURO-6. Le projet EDIT porte sur cinq axes techniques d'amélioration dont un consiste en l'obtention d'un système optimisé de transmission par courroie poly-V au regard des pertes de puissance. Actuellement les faces avant de moteur sont perfectionnées sur le plan mécanique ; cela signifie que la durée de vie de ses composants est optimisée, et que les nuisances vibratoires sont réduites. Par contre, des améliorations peuvent être apportées sur le plan énergétique. Cette thèse, qui a pour objectif d'investiguer les possibilités de réduction et d'optimisation des pertes de puissance sur les façades accessoires, se décline en trois parties : une caractérisation par l'analyse mécanique dynamique des matériaux viscoélastiques des courroies poly-V et des composantes de façade ; une modélisation, une optimisation et une implémentation logicielle des modèles de pertes de puissance ; validées par une dernière partie expérimentale sur banc d'essais. Les pertes de puissances dans une face avant moteur sont de plusieurs types : des pertes internes à la courroie poly-V (hystérésis du caoutchouc), des pertes externes à la courroie (glissement poulie/courroie) et des pertes internes aux composants (frottement dans les roulements). Ces pertes peuvent désormais être quantifiées et optimisées grâce aux modèles développés durant cette thèse. Ces modèles ont été validés et implémentés dans un outil de simulation (PLFead, Power Loss Front engine accessory drive), qui a été développé pour optimiser les pertes de puissance en tenant compte des paramètres de design et de fonctionnement des faces avant moteur.

MOTS-CLÉS :

Transmission par courroie poly-V. Pertes de puissance. Faces avant moteur. Optimisation. Caractérisation. Matériau viscoélastique. Modélisation. Validation sur banc d'essais. Simulation.

Laboratoire (s) de recherche : Laboratoire de Mécanique des Contacts et des Structures (LaMCoS)
Campus LYON TECH La DOUA
Bâtiment Sophie GERMAIN
27 bis Avenue Jean Capelle
69621 Villeurbanne Cedex - France

Directeur et co-directeur de thèse: Didier REMOND et Lionel MANIN

Président de jury : Guilhem Michon

Composition du jury : Robert Parker, Julien Ameil, Miha Boltezar, Guilhem Michon, Lionel Manin, Thouraya Nouri Baranger, Didier Remond